UNIVERSITY OF SOUTHAMPTON

Faculty of Physical Sciences and Engineering
School of Electronics and Computer Science

Modelling of Arcing Phenomena During Opening Contacts in Novel Circuit Breakers

by

Jing Nan

Thesis for the degree of Doctor of Philosophy

November 2025

University of Southampton

Abstract

Faculty of Physical Sciences and Engineering
School of Electronics and Computer Science

Doctor of Philosophy

Modelling of Arcing Phenomena During Opening Contacts in Novel Circuit Breakers

by Jing Nan

The increasing adoption of renewable energy and DC-based loads has renewed interest in DC transmission systems. Unlike AC networks, DC systems lack natural current zero-crossings and exhibit rapid fault propagation, making interruption highly challenging. Reliable and scalable DC protection is essential for future power systems, with mechanical DC circuit breakers providing the most cost-effective approach to managing DC faults. Maximising their performance depends on accurate prediction of arc behaviour.

This study primarily focuses on compact LC commutator-based DC circuit breakers operating at voltage levels between 1–5 kV. The research investigates the reignition phenomenon observed after current commutation and reveals that the key factor governing reignition is the temperature of the boundary layer between the arc plasma and the electrode surface. Conventional breakdown models, such as Paschen's law and streamer theory, are inadequate for describing reignition because they assume uniform gas temperature at room conditions. In reality, the air temperature within the contact gap varies non-uniformly as the electrodes separate. To address this limitation, a hybrid breakdown voltage model was developed based on non-uniform temperature distribution and dynamically changing electrode gap. The model covers the full temperature range of 300–5000 K and quantitatively reproduces published experimental data with a prediction error within 20%. The analysis also provides a physical interpretation for the transition between the Townsend and streamer breakdown mechanisms. The applicability of the arc model is further examined in low-voltage DC switches ($<$ 100 V, typical for electric traction systems). By simulating the influence of external electric field and electrode opening velocity on the arc behaviour across different stages, the model predicts arc extinction time within $\pm$15% accuracy under multiple experimental conditions.

Overall, this work provides a unified modelling framework that bridges the gap between fundamental arc physics and practical circuit breaker design. The developed model offers predictive capability for evaluating the influence of different parameters on arc extinction performance. These findings contribute physical insight into arc dynamics and establish design guidelines for optimising compact DC interrupters across different voltage ranges. The modelling approach can be extended to higher-voltage systems to support future DC protection technologies.

Contents

List of Figures

List of Tables

Abbreviations

2T Two-Temperature

AC Alternating Current

BL Boundary Layer

CCI Counter Current Injection

CFD Computational Fluid Dynamics

DC Direct Current

DCCB Direct Current Circuit Breaker

EMF Electromotive Force

HVAC High Voltage Alternating Current

HVDC High Voltage Direct Current

IGBTs Insulated Gate Bipolar Transistor

IGCTs Integrated Gate-Commutated Thyristors

LCS Load Commutation Switch

LTE Local Thermodynamic Equilibrium

LVDC Low Voltage Direct Current

MCCB Molded Case Circuit Breaker

MHD Magnetohydrodynamic

MOSA Metal-oxide Surge Arrester

MOV Metal Oxide Varistor

MRTB Metallic Return Breaker

MT Multi-Terminal

MTDC Multi-Terminal Direct Current

MVDC Medium Voltage Direct Current

NEC Net Emission Coefficient

NLTE Non-Local Thermodynamic Equilibrium

PV Photovoltaic

TIV Transient Interruption Voltage

UFD Ultra-Fast Disconnector

UV Ultraviolet

V-J Voltage-Current Density

VAC Volt-Ampere Characteristic

VCB Vaccum Circuit Breaker

Symbols

Symbol	Description	Unit
A_f	Work function of electrode material	eV
A_i	Ionisation energy	eV
D	Characteristic length or diameter for Reynolds number	m
E_0	Externally applied electric field between the electrodes	$\mathrm{V/m}$
$E_{\mathbf{critical}}$	Critical electric field required for breakdown	$\mathrm{V/m}$
$E_{\mathbf{red}}$	Reduced electric field strength	$\mathrm{V\,m^2/K}$
$E_{\mathbf{sc}}$	Electric field induced by the space charge in the avalanche head	$\mathrm{V/m}$
F_c	Residual or decreasing contact force during contact separation	N
H	Dynamic enthalpy	$\mathrm{J/kg}$
I_{R4}	Current through resistor R_4 in the circuit	A
$I_{\mathbf{column}}$	Current flowing through the arc column	A
I	Circuit current	A
$J_{\mathbf{ar}}$	Current density at the arc root	$\mathrm{A/m^2}$
L	Inductance of the circuit	H
N_e	Electron number density	$\mathrm{cm^{-3}}$
N	Total neutral gas number density	$\mathrm{m^{-3}}$
$P_{\mathbf{arc}}$	Power consumed by arc itself	W
$P_{\mathbf{supply}}$	Power from power supply	W
P	Pressure	Pa
$Q_{\mathbf{boundary}}$	Conductive heat flux to the wall through natural gas	W

Symbol	Description	Unit
$Q_{\mathbf{internal}}$	Internal power losses due to the gas collision	W
$Q_{\mathbf{kinetic}}$	Convective power losses due to the heating of surrounding gas	W
Q_j	Joule heating	$\mathrm{W/m^3}$
Q_η	Viscous dissipation term	$\mathrm{W/m^3}$
$Q_{\mathbf{rad}}$	Radiative energy losses	$\mathrm{W/m^2}$
$Q_{\mathbf{tran}}$	Energy transported by thermal diffusion drift in plasma	$\mathrm{W/m^3}$
R_a	Characteristic radius of the hot gas	mm
R_p	Plasma radius in radiation calculation	m
$R_{\mathbf{column}}$	Electrical resistance of the arc column	Ω
Re	Reynolds number	–
R	Resistance of the circuit	Ω
T_0	Reference temperature	K
$T_{\mathbf{back}}$	Background temperature of the surronding gas	K
$T_{\mathbf{max}}$	Maximum initial temperature	K
T_e	Electron temperature	eV
T_g	Gas temperature in the arc or gap	K
T_h	Temperature of heavy particles	K
T_l	Temperature of the lower boundary between arc and electrodes	K
T_u	Temperature of the upper boundary between arc and electrodes	K
T_{pa}	Average plasma temperature	K
T	Temperature	K
U_c	Voltage drop across the cathode sheath	V
U_s	System voltage	V
$U_{\mathbf{arc}}$	Arc voltage across the circuit breaker	V
V_B	Breakdown voltage	V
$V_{\mathbf{th\_run}}$	Critical voltage for thermal runaway	V
V_s	Electric potential on the cathode side	V

Symbol	Description	Unit
$V_{\mathbf{LTE}}$	Electric potential on the LTE plasma side	V
$V_{\mathbf{arc}}$	Total arc voltage	V
$V_{\mathbf{ar}}$	Voltage drop across the arc root	V
$V_{\mathbf{sheath}}$	Voltage drop across the sheath	V
V	Electric potential	V
ΔV_a	Anode voltage fall	V
ΔV_c	Cathode voltage fall	V
ΔV	Arc sheath voltage	V
Δy	Thickness of the arc root layer	m
α	First Townsend ionisation coefficient	m^{-1}
γ_{se}	Secondary electron emission coefficient	–
$\hat{\pi}$	Viscous stress tensor accounting for internal friction in the fluid	Pa
κ_e	Thermal conductivity of electrons	$\mathrm{M}/(\mathrm{mK})$
κ_{hp}	Thermal conductivity of heavy particles	$\mathrm{M}/(\mathrm{mK})$
λ	Thermal conductivity	$\mathrm{W}/(\mathrm{mK})$
$\mathbf{A}$	Magnetic vector potential	Wb/m
$\mathbf{B}$	Magnetic flux density	Wb/m^2
$\mathbf{E}$	Electric field vector	V/m
$\mathbf{F}_{\mathrm{L}}$	Lorentz force	N
$\mathbf{I}_{cr}$	Critical current of the sheath regime transition	A
$\mathbf{J}_a$	Particle flux of neutral atoms	$\mathrm{m}^{-2}\mathrm{s}^{-1}$
$\mathbf{J}_e$	Particle flux of electrons	$\mathrm{m}^{-2}\mathrm{s}^{-1}$
$\mathbf{J}_i$	Particle flux of positive ions	$\mathrm{m}^{-2}\mathrm{s}^{-1}$
$\mathbf{J}_c$	Current density vector at the cathode surface	A/m^2
$\mathbf{V}_{\mathbf{break,sh}}$	Breakdown voltage of sheath layer	V
$\mathbf{V}$	Velocity vector of plasma flow	m/s
$\mathbf{j}$	Current density vector	A/m^2
$\mathbf{q}_e$	Heat flux carried by electrons	$\mathrm{W}/\mathrm{m}^2\mathrm{K}$
$\mathbf{q}_h$	Heat flux carried by heavy particles	$\mathrm{W}/\mathrm{m}^2\mathrm{K}$
μ_1	Magnetic permeability of free space or non-magnetic medium	H/m
μ	Dynamic viscosity	$\mathrm{kg}/(\mathrm{ms})$

Symbol	Description	Unit
ν	Kinematic viscosity	m^2/s
ρ_{cr}	Contact resistivity at the arc–electrode interface	$\Omega \cdot \mathrm{m}^2$
ρ	Density	kg/m^3
σ_u	Electrical conductivity in the arc root region	S/m
σ	Electrical conductivity	S/m
ξ	Theoretical coefficient for fully ionized plasma	–
c_p	Specific heat capacity at constant pressure	$\mathrm{J}/(\mathrm{kg}\,\mathrm{K})$
d	Gap distance between contacts	cm
h	Static enthalpy	J/kg
k_B	Boltzmann constant	J/K
m	Mass of neutral particle	kg
p	Pressure	Torr
q_a	Total energy flux to the anode	W/m^2
$q_{\mathbf{LTE,w}}$	Normal energy flux from the LTE plasma to the boundary layer	W/m^2
$q_{\mathbf{nl,w}}$	Normal energy flux from the boundary layer to the cathode	W/m^2
$q_{\mathbf{to\ cathode}}$	Energy flux deposited on the cathode surface	W/m^2
$q_{\mathbf{to\ plasma}}$	Energy flux lost to the plasma from the cathode sheath	W/m^2
t	Time	s
u	Flow velocity	m/s
v	Average velocity	m/s
$w_{\mathbf{rad}}$	Radiative energy loss per unit volume	–

Declaration of Authorship

I, Jing Nan, declare that this thesis and the work presented in it is my own and has been generated by me as the result of my own original research.

I confirm that:

1. This work was done wholly or mainly while in candidature for a research degree at this University;
2. Where any part of this thesis has previously been submitted for a degree or any other qualification at this University or any other institution, this has been clearly stated;
3. Where I have consulted the published work of others, this is always clearly attributed;
4. Where I have quoted from the work of others, the source is always given. With the exception of such quotations, this thesis is entirely my own work;
5. I have acknowledged all main sources of help;
6. Where the thesis is based on work done by myself jointly with others, I have made clear exactly what was done by others and what I have contributed myself;
7. Parts of this work have been published as:

    - **J. Nan**, G. Chen, I. Golosnoy, *Temperature-Segmented Hybrid Arc Model for Breakdown Voltage Prediction from 300 K to 5000 K: Arc-to-Gas Phase Transition Analysis and Sheath Cooling Effects for Reignition Suppression in Air Circuit Breakers*, accepted (in press), *IET High Voltage*.
    - **J. Nan**, G. Chen, I. O. Golosnoy, *Analysis of Breakdown Mechanisms in Heated Short Air Gaps During Contact Opening in Compact DC Circuit Breakers*, in *2024 IEEE 69th Holm Conference on Electrical Contacts (HOLM)*, IEEE, 2024.
    - **J. Nan**, G. Chen, I. O. Golosnoy, *Identification of Key Mechanism Behind Arc Re-Ignition in LC Commutator-Based DC Circuit Breakers*, in *2024 7th International Conference on Electric Power Equipment – Switching Technology (ICEPE-ST)*, IEEE, 2024.
    - **J. Nan**, G. Chen, I. Golosnoy, *Modelling of Arcing Phenomenon During Contact Opening in Novel Circuit Breaker*, in *Proceedings of the International Symposium on High Voltage Engineering (ISH 2023)*, IET, 2023.

Signed:..... Date:.....

Acknowledgements

The completion of this thesis would not have been possible without the support and encouragement of many people over the past few years.

First and foremost, I would like to express my deepest gratitude to my primary supervisor, Dr. Igor Golosnoy, for his continuous guidance, valuable insights, and unwavering support throughout my PhD. His mentorship has been crucial both academically and personally.

I am also sincerely thankful to my second supervisor, Prof. George Chen, for his encouragement during difficult times and for generously supporting my participation in international conferences. I would also like to thank Prof. Paul Lewin for his consistent support and kind encouragement throughout my PhD, especially his recognition and kind words following each of my academic achievements and awards. My thanks also go to Prof. Suleiman Sharkh for his encouragement and helpful suggestions on revising my journal manuscript.

I gratefully acknowledge the contribution of Mr. Mingli Yan and Prof. John McBride, who provided experimental data that significantly supported my research. I also appreciate the discussions and assistance offered by Dr. Kevin Goddard and Dr. Sunny Chaudhary during the modelling and writing process.

I am also grateful to Dr. George Callender and Dr. Thomas Andritsch for acting as my viva examiners and for their valuable comments and suggestions, which helped improve the final version of this thesis.

I would like to extend my thanks to all my colleagues and friends for their companionship and encouragement during this journey. Finally, I am deeply grateful to my parents for their unconditional love and support.

This PhD journey has been both challenging and rewarding. I am thankful for every experience and for everyone who played a part in it.

Chapter 1

Introduction

To ensure clarity and consistency throughout this thesis, the key terms are defined as follows:

- **Arc Reignition:** This term refers specifically to the re-establishment of the arc path after current zero due to a failure of the dielectric recovery strength of the gap. It is the primary phenomenon investigated in this work and will be used exclusively.
- **Arc Root:** The localized area on the electrode surface where the arc column attaches and through which current flows.
- **Arc Sheath (or Electrode Sheath):** The thin, non-equilibrium plasma region adjacent to the arc root, characterized by strong electric fields and space charge effects, which is responsible for a significant portion of the voltage drop near the electrodes.

1.1 Background and Motivation

In modern society, although conventional Alternating Current (AC) generation and transmission systems still dominate, the increasing integration of renewable energy sources and the growing prevalence of Direct Current (DC) loads have renewed interest in DC transmission systems [1–3]. Many renewable sources (e.g., solar photovoltaic (PV)) and emerging loads (e.g., electric vehicles, energy storage systems, and electronic devices) are inherently DC, whereas traditional AC systems are often inefficient in supporting these applications. As a result, there is a growing focus on developing reliable and efficient DC transmission networks.

However, a major obstacle to the advancement of DC systems lies in the difficulty of interrupting DC faults, which lack natural current zero-crossings [4–6]. DC fault interruption technologies have thus become a critical research area. Broadly, existing approaches can be categorized into grid-side and device-side strategies.

Grid-side strategies include interrupting the fault from the AC side using AC breakers or blocking the fault through converters [7, 8]. However, these methods have significant limitations. For instance, interrupting faults on the AC side can shut down the entire grid, while converter-based

isolation requires complex coordination between multiple switches, potentially affecting healthy lines [9, 10]. In contrast, device-side solutions, particularly DC circuit breakers (DCCBs), offer more effective and flexible fault isolation without causing widespread outages. Furthermore, DCCBs facilitate interconnection across different voltage levels, enhancing overall grid flexibility. In Multi-Terminal DC (MTDC) networks, they also help reduce infrastructure costs by minimizing the number of required converter stations [11]. In addition, the recent publication [12] explores the feasibility of using LC DCCB as the fault current limiter with AC distribution systems. As such, DCCBs are the central focus of this doctoral research.

DCCBs exhibit varying interruption characteristics depending on the voltage level. Widely used low-voltage, high-current electromechanical switches—such as those found in hybrid and electric vehicles—must interrupt large DC currents. These devices typically rely on self-induced magnetic fields, gas blasts, insulation barriers, or metal splitter plates to quench the arc [13, 14]. However, in low-current applications such as relays, the self-induced magnetic field is relatively weak, necessitating auxiliary arc control strategies. Techniques such as hydrogen filling, externally applied magnetic fields, and high-speed contact separation have been explored [15]. Yet, challenges in experimental control—such as difficulties in capturing transient arc evolution, particularly rapid variations in gas flow direction and intensity (due to limited camera frame rates and diagnostic constraints), as well as maintaining ideal test conditions (including uniform magnetic fields, constant contact velocity, stable contact force, and unoxidised electrode surfaces)—undermine the reproducibility and reliability of the results [16]. Consequently, the fundamental dynamics of arc behaviour in such systems remain insufficiently understood, highlighting the need for modelling to aid in their understanding.

For medium-voltage DCCBs, mechanical breakers offer several advantages over solid-state or hybrid designs, including low conduction losses, compact structure, and reduced cost. Recent studies have demonstrated the potential of mechanical DCCBs incorporating LC commutation circuits to achieve fast and cost-effective fault interruption [17–19]. These breakers can reroute fault current into a capacitor within microseconds, thereby shortening the arcing time and reducing contact wear. However, extending these designs to handle higher currents or voltages remains challenging due to the persistent issue of arc re-ignition. For instance, [17] observed that arc commutation could be achieved at lower current levels, whereas increasing the current under constant voltage led to reignition, even without changes in circuit conditions. In contrast, [18] reported that arc extinction was possible at higher currents, while re-ignition could still occur at low current levels following successful commutation. These findings suggest that arc behaviour is influenced by more complex factors beyond just voltage and current magnitude. Variables such as current slope near zero-crossing [18, 20], contact cooling effectiveness [21], and gap evolution [22] all contribute to inconsistent experimental outcomes. This complexity poses a major barrier to scaling mechanical DCCBs for higher-voltage or more demanding applications. Hence, a model is needed to aid in the understanding of arc re-ignition phenomena, identify the root causes, and develop mitigation strategies.

To overcome these challenges, numerical simulation is essential for investigating the underlying physical processes and guiding the design of reliable, high-performance DCCBs. In particular, understanding re-ignition phenomena requires careful consideration of the possibility of breakdown occurring in post-commutation stage. This necessitates tracking temperature evolution within the narrow air gap, as thermal conditions critically affect dielectric strength. Experimental studies have shown that breakdown voltage is temperature-dependent [23, 24], emphasizing the importance of including thermal effects in predictive models.

Traditional models, such as Paschen's Law and Critical Field Theory, are commonly used to estimate breakdown thresholds [25, 26]. However, these models often fall short in capturing the dynamics of DC arc extinguishment, where the contact gap changes rapidly and the temperature distribution is highly non-uniform. Such transient and spatial variations fall outside the assumptions of classical models, limiting their ability to accurately explain the observed re-ignition behaviour. Hence, a more predictive model needs to be proposed that takes these factors into consideration.

Therefore, this thesis aims to develop a physics-based and scalable modelling framework capable of addressing re-ignition, breakdown prediction, and arc extinguishment optimisation across different voltage levels.

1.2 Aims and Objectives

The primary aim of this research is to formulate an efficient and scalable modelling methodology for mechanical DCCBs, with a strong emphasis on understanding and predicting key arcing phenomena—including arc decay, arc extinction, and arc re-ignition. Through a combination of physical modelling, numerical simulation, and experimental validation, the study seeks to bridge gaps in current understanding and provide guidance for improved breaker design.

To achieve this, the following specific objectives are established:

- Validate the arc modelling methodology through 2D simulation and ensure the initial condition of the simulation is reasonable.
- Investigate re-ignition mechanisms in LC commutation-based breakers and evaluate mitigation strategies under different cooling conditions.
- Develop a temperature-segmented hybrid breakdown model that integrates Paschen's Law and Critical Field Theory to predict dielectric recovery under elevated temperatures.
- Apply the developed models in practical scenarios, including LC commutation frameworks and low-voltage DC switches, to assess model flexibility and identify design guidelines.

1.3 Novel Contributions

The main contributions of this thesis are summarised as follows:

1. Provided an enhanced understanding of arc thermal runaway and re-ignition mechanisms, and proposed corresponding mitigation strategies. Previous studies have primarily analysed arc re-ignition based on circuit-level voltage and current waveforms (e.g., di/dt), without exploring the underlying physical mechanisms. This is largely due to experimental challenges, as the arc near-electrode layer is small in size and reaches high temperatures, making detailed diagnostics difficult. This thesis addresses the gap by investigating the physical-level processes contributing to thermal runaway arc reignition.

2. Developed a hybrid breakdown model that captures transitions across the 300–5000 K range in compact DC switches, and elucidates the underlying physics in the transition regime. Existing approaches for predicting breakdown voltage, such as Paschen's Law and the Critical Field Theory, are not applicable to practical DC circuit breaker conditions, where the arc exhibits non-uniform temperature distribution and the electrode gap dynamically changes during contact motion. No single model in the literature has been able to cover the full temperature range of 300–5000 K with consistent physical interpretation. This thesis proposes a unified hybrid breakdown model to address this limitation.

3. Conducted a detailed analysis of the effects of magnetic field and contact motion at different stages of the arc extinguishment process, and proposed an analytical equation to predict arc extinguishing time, offering practical guidance for DC switch design. Most existing low-voltage air arc models focus on gas flow fields under fixed electrodes, or attribute arc extinction solely to elongation effects. In contrast, this work establishes a stage-based analysis framework based on arc position, systematically examining the influence of contact velocity and external magnetic field at each stage. Energy distribution is also analysed, providing design insights for arc control in DC fault management.

4. Demonstrated that the proposed model is compatible across devices operating at different voltage levels, and can serve as a predictive tool for real-world DC switch designs. The model simplifies the arc near-electrode boundary without explicitly resolving sheath effects or metal vapour dynamics, yet retains high predictive accuracy.

1.4 Thesis Structure

This thesis is structured into eight chapters, as outlined in Figure 1.1, to systematically investigate arc phenomena in compact DC switching devices across different voltage levels.

Chapter 1 introduces the motivation and background for studying DC arc phenomena, highlighting both the potential of DC systems and the complexity of arc behaviour. Chapter 2 reviews the literature on DC circuit breakers and explains why a physics-based arc model is essential. Chapter 3 focuses on the simulation methodology and outlines the general assumptions made in

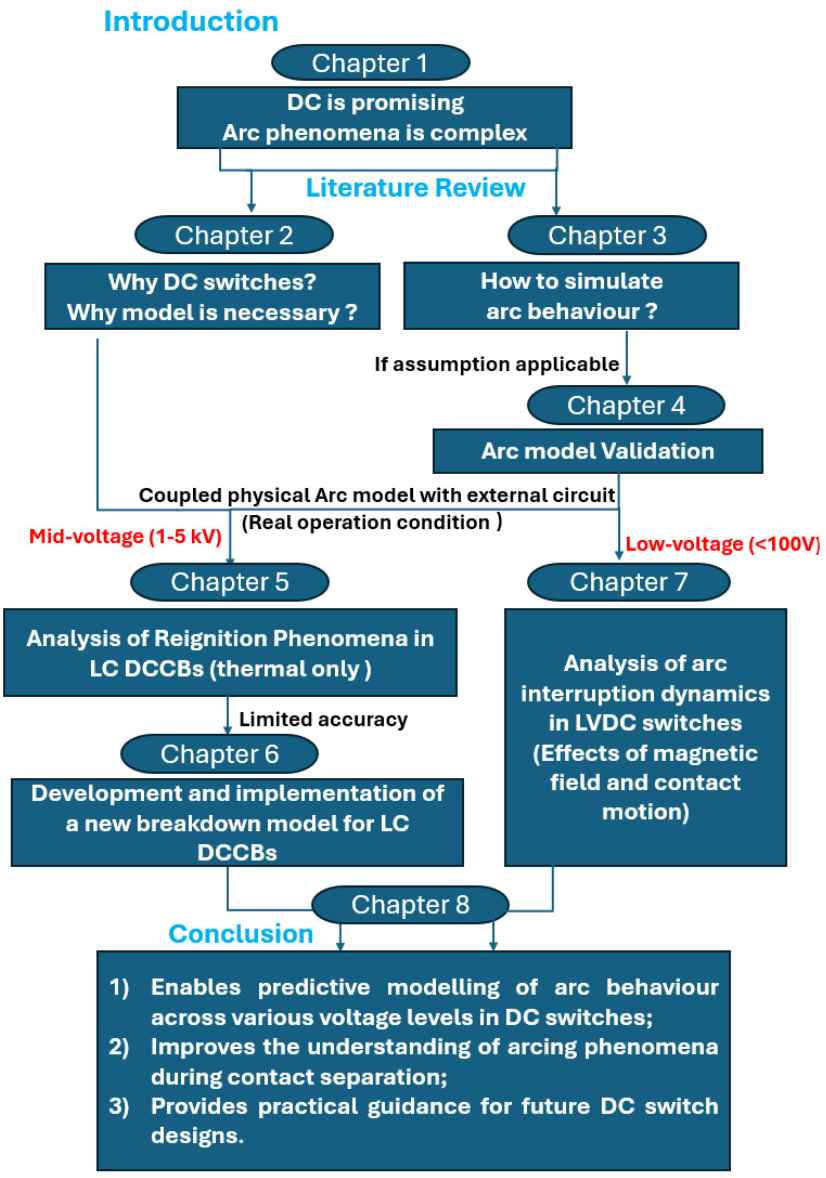

FIGURE 1.1: Overview of the thesis structure and chapter interconnections

arc modelling. To verify the implementation and applicability of these assumptions, Chapter 4 validates the arc behaviour using a 2D physical model without circuit coupling, thereby laying the foundation for later applications.

Building on this foundation, the model is then coupled with external circuits to simulate real operating conditions at different voltage levels: medium-voltage (1–5 kV) in Chapters 5 and 6, and low-voltage (< 100 V) systems in Chapter 7.

Specifically, Chapter 5 investigates the mechanism of arc reignition in LC-type DC circuit breakers, attributing it to residual heat in the boundary layer. However, the model shows limited accuracy due to the absence of an electrical breakdown mechanism. To address this, Chapter 6 develops a new breakdown voltage prediction model for the post-arc phase, covering the temperature range from 300 K to 5000 K. It also bridges two classical breakdown theories—Townsend

avalanche and streamer—by offering a unified physical interpretation. Then the model is implemented and validated in LC-commutated DC circuit breakers.

Chapter 7 shifts focus to low-voltage DC switches, analysing the stage-dependent effects of magnetic fields and contact velocity based on arc position between two contacts. Also analyse the energy distribution of the whole system in different stages, which gives the insight of the DC switches design. Another aim of this chapter is to examine the scalability of the proposed model.

Finally, Chapter 8 concludes the thesis by summarising the major findings and future works.

Chapter 2

DC Circuit Breakers

2.1 Overview of DC Protection and Scope of This Study

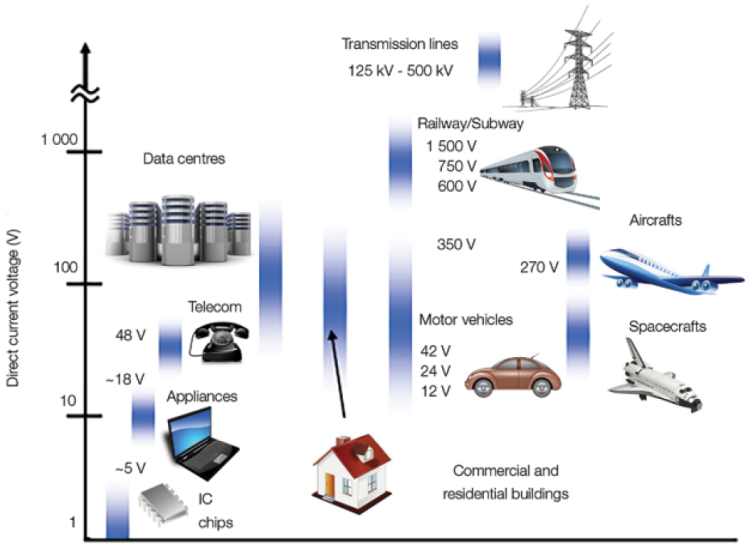

FIGURE 2.1: Voltage range for typical DC applications today [27];the vertical axis represents typical DC voltage levels, while the horizontal placement has no quantitative meaning .

Direct current (DC) systems have existed since the earliest electric networks deployed by Edison in the late nineteenth century [27]. Although alternating current (AC) later dominated long-distance transmission due to convenient voltage transformation, DC distribution has remained important in industry, transportation, and electronic systems. Figure 2.1 summarises the voltage range of representative modern DC applications [27]. Driven by renewable integration and the demand for high-efficiency power conversion, DC grids have recently regained attention across multiple voltage levels. High-voltage DC (HVDC) links enable bulk power transmission and interconnection of asynchronous systems [4, 5], while low-voltage DC (LVDC) networks support distributed energy resources, electric traction, and residential microgrids [27, 28]. Across these

applications, the absence of natural current zero-crossings makes fault interruption inherently difficult [29].

DC networks nonetheless provide distinct benefits, including reduced conversion losses, direct coupling of renewables and storage units, and elimination of reactive power flow and skin effects [5, 30]. However, the lack of natural fault current limitation requires specially designed protection systems capable of interrupting high di/dt currents within milliseconds. Unlike AC faults that extinguish naturally at zero current, DC arcs must be forced to extinction by creating a counter-voltage greater than the driving source. This fundamental difference means that many conventional AC protection schemes—such as overcurrent, differential, or distance protection—perform poorly in DC networks, where fault currents rise too quickly for threshold-based detection [30, 31].

To address these issues, various system-level DC protection strategies have been proposed, including converter blocking, handshaking coordination with AC breakers, and DC-DC chopper limiting [8–10]. Although these approaches can temporarily suppress fault propagation, they do not completely interrupt the fault current in the DC grid and often disturb healthy lines or converter operation. Such limitations highlight the necessity for a dedicated and fast-acting interruption device—namely the DC circuit breaker (DCCB)—which can isolate faulted sections within a few milliseconds while maintaining power continuity elsewhere [4, 32].

Accordingly, this thesis concentrates on low- and medium-voltage DC breakers operating in the 1–5 kV and sub-100 V ranges, which are most relevant to compact protection applications. HVDC breaker technologies are briefly mentioned for completeness but not analysed in detail, as their converter-based architectures lie beyond the scope of this study. The following sections review representative DC circuit breaker topologies and explain their interruption principles, including current commutation, voltage evolution across branches, and energy dissipation mechanisms.

2.1.1 Key Differences between AC and DC Interruption

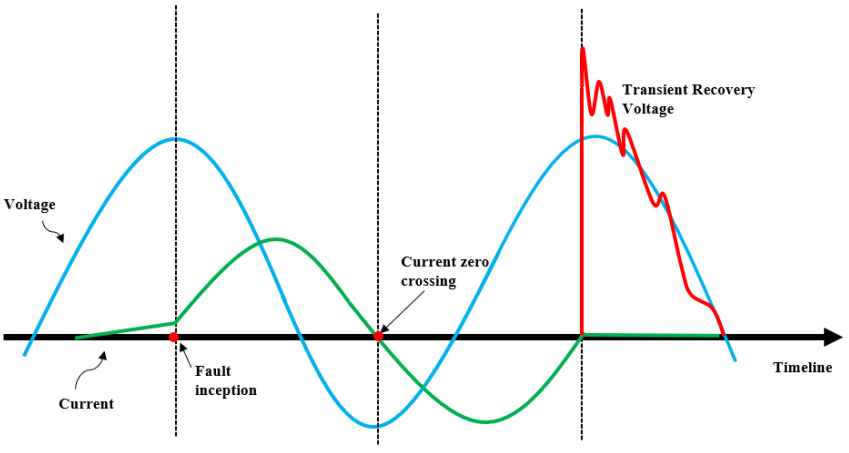

FIGURE 2.2: Schematic of AC fault current interruption [7]

In AC interruption, the arc extinguishing process leverages the natural zero crossing of the AC waveform, as shown in Figure 2.2. It needs four cycles of about 80 to 100 *ms* to interrupt the fault current [4]. However, in DC networks, there are no such zero-crossings, making it more difficult to extinguish the arc formation between two moving contacts. In the AC systems, the arc is quenched when the fault current hits the zero point, coinciding with the system voltage entering a high voltage region. The phase shift of the AC supply causes the arc voltage to decrease along with the system voltage, effectively preventing the arc from reigniting. Additionally, the reactance of the transmission line and transformers in AC grids inherently limits the increase of fault currents, adding protecting against rapid current escalation during faults. Contrastingly, in DC systems, the commutation and interruption processes are combined. After artificially creating a current zero crossing, the DC system lacks an inherent mechanism like the AC phase shift to eliminate arc voltage. When contacts open in DC, the system voltage merges with the arc voltage, making it challenging to prevent contact breakdown and sometimes it causes the occurrence of reignition [6]. Furthermore, in DC grids, the slope of the fault current post-fault is mainly limited by the line inductances. The influence of ohmic resistances on the amplitude of fault currents is almost negligible [33], which means that the spread of faults can pose a significant challenge for fault clearing in DC grids [6, 34].

From an energy perspective, the zero-crossing in the AC system coincides with a minimum of magnetic energy, facilitating interruption. Conventional HVAC networks can facilitate the arc extinguishment by two current zero crossings per cycle in fault condition. Think of it as having a pause in the action. But in DC systems. There's no such pause so a DC circuit breaker has to handle all the built-up energy [5, 35, 36]. For a specific example, an HVDC breaker dealing with a large fault current of around 15 kA flowing in a 100 km overhead line has to manage the energy equivalent to stopping a 30-ton train going at 100 km/h in just a split second [7].

In summary, the key differences between fault interruption in AC and DC grids are primarily due to their distinct electrical characteristics including natural zero crossing, arc voltage behaviour, fast fault current propagation and the requirement of energy dissipation. Fault interruption in AC grids is facilitated by natural zero crossings and phase shifts that aid in arc extinction, while DC grids face greater challenges due to this absence and require more complex interruption technologies.

2.1.2 DC Interruption Principle

The function of a circuit breaker is to interrupt the fault current flow within a circuit, a process often referred to as 'interruption,' 'switching,' or 'breaking' [37, 38]. Understanding current interruption in DC networks requires analyzing the sample circuit shown in Figure 2.3, along with its corresponding Equation (2.1).

$$U_s(t) = I(t)R + L\frac{dI(t)}{dt} + U_{\text{arc}}(t) \tag{2.1}$$

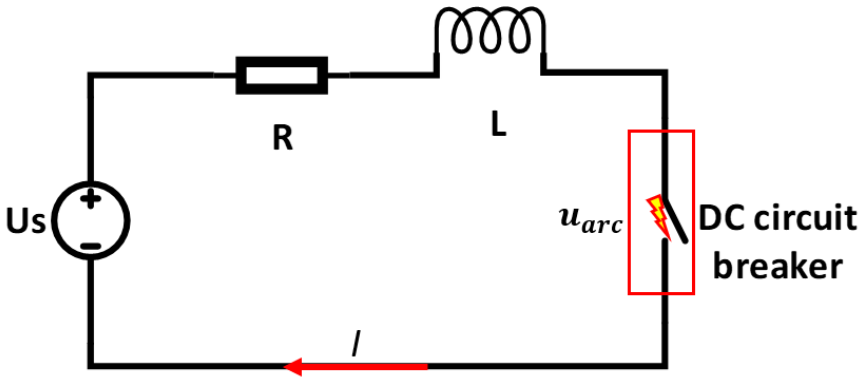

FIGURE 2.3: Basic circuit layout for DC interruption [37]

Here, U_s is the system voltage, I is the current, R is the resistance, L is the inductance and U_{arc} is the arc voltage. To reduce the fault current $\frac{dI(t)}{dt} < 0$ in Equation (2.1), the voltage across the circuit breaker U_{arc} must be higher than the system voltage U_s. The general working principle for DC breaker is based on this equation, which creates a counter voltage that stays above the system voltage and holds for a while to suppress the fault current to zero [5, 32].

Low Voltage DC Interruption

To investigate the process of DC interruption, we need to look through the current-voltage characteristic of the circuit as shown in Figure 2.4. The inclination of the linear path (L1) signifies the resistance R, while the curved line (L2) portrays the relationship between voltage and current of the arc. The enclosed region between the straight and curved lines represents the Electromotive Force (EMF) in the inductance L. The points where the derivative of the current concerning time equals zero are labelled as P1 and P2. They both represent arcing points, however, P1 is an unstable arcing point as it is highly susceptible to fluctuations with changes in current [37]. P2 is considered as a more stable arcing point.

Therefore, successful interruption of the DC arc necessitates the removal of the stable arcing point P2. As depicted in Figure 2.5, two primary strategies to circumvent this stable point are introduced: steepening the slope of the straight line (L3) or elevating the curved line (L4). In particle terms, these strategies can be achieved by amplifying the resistance and boosting the arc voltage [40].

These methods (L3 and L4) are mainly used for public and traction applications, aiming to interrupt current by generating a counter voltage through elongation and cooling, exceeding the system voltage to force the arc current to zero. Techniques to increase arc voltage include: extending the arc length, cooling the arc column, reducing arc diameter by increasing pressure and adding metallic plates to segment the arc into short arcs, but this can increase device size and initial cost. In practical applications, steep slopes require large loads, which is unfeasible for DC grids due to increasing power losses and complex management. Typically, this method is most applicable to systems with voltages below 1.5 kV [38, 39]. In medium-voltage DC systems (1.5–3 kV), arc extinguishment becomes more complex than at low voltages. Simple arc elongation

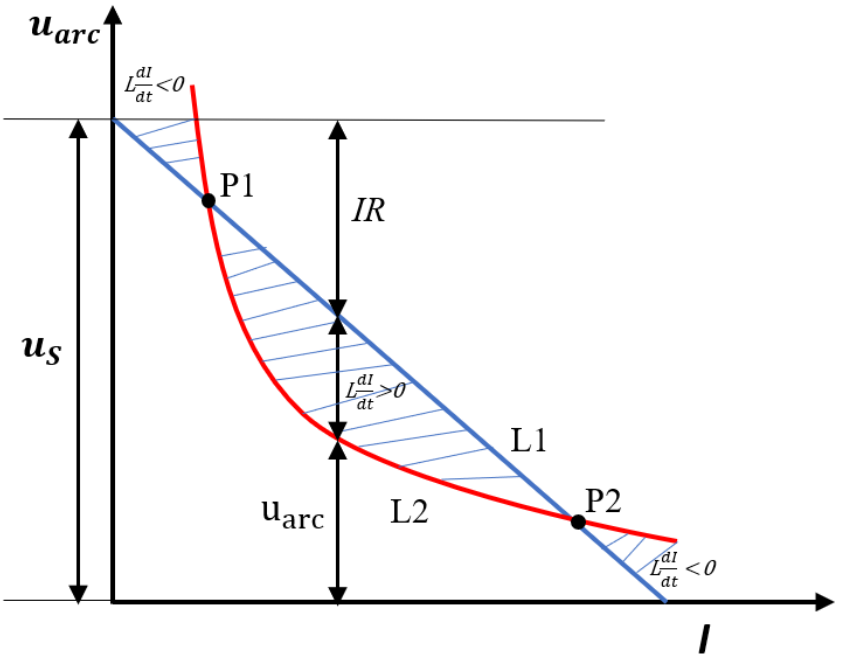

FIGURE 2.4: Current-voltage relationship in a DC circuit [37, 39]

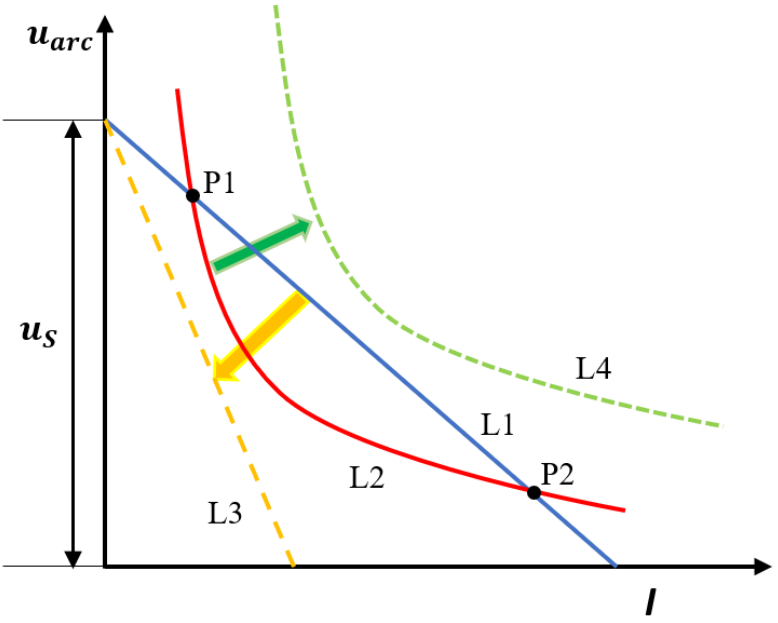

FIGURE 2.5: Principle of interrupting DC arc [37, 39]

and cooling often fail to generate sufficient arc voltage to exceed the system voltage, requiring enhanced techniques such as intensified cooling, magnetic blowing, or arc segmentation. Higher fault currents lead to stronger arc sustainment and increase the risk of reignition due to elevated recovery voltages. Furthermore, greater thermal and mechanical stresses demand more robust materials and interrupter designs. While these methods can still be adapted for medium-voltage DC, their limitations become critical in high-voltage DC grids, necessitating new interruption approaches.

High Voltage DC Interruption

For high-voltage DC interruption, the most common approach is to employ an LC-based circuit structure. HVDC circuit breakers typically consist of three main branches, as illustrated in Figure 2.6. The continuous current branch, designed with low resistance, minimizes conduction losses under normal operating conditions. The commutation branch generates a high resistance to create the required Transient Interruption Voltage (TIV) when the current is transferred into it. The energy absorption branch stabilizes the TIV and absorbs the magnetic energy released during interruption [7].

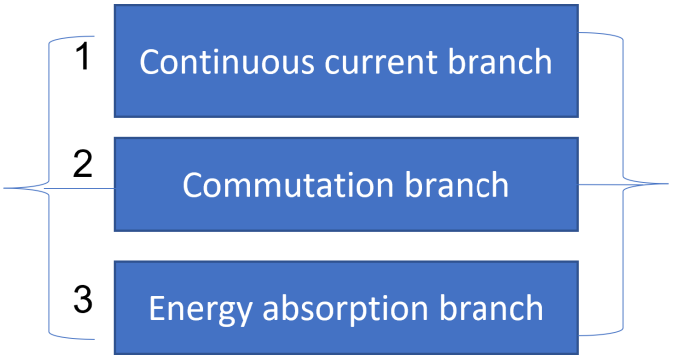

FIGURE 2.6: Basic layout of HVDC circuit breaker [7]

To provide a clear understanding of the operating behavior of each branch, the switching sequence is explained in Figure 2.7.

The fault handling process of a DC circuit breaker consists of four sequential stages based on the working sequence outlined in [7]. In the **fault detection stage** ($t_0 \rightarrow t_1$, relay time), a fault causes a sudden increase in current within the main circuit. The detection system takes a few milliseconds to identify the abnormality due to relay delays and then sends a trip signal to the circuit breaker. In the **mechanical preparation stage** ($t_1 \rightarrow t_2$, breaker operation time), the breaker receives the signal and starts physically separating its contacts, creating the necessary conditions to establish isolation voltage. Next, during the **current transfer stage** ($t_2 \rightarrow t_3$, voltage rise time), a semiconductor or RLC resonant circuit rapidly generates a TIV, forcing the current to shift from the main circuit to the commutation branch. This commutation process typically takes around 1-2 milliseconds. The TIV continues to increase until it reaches a level that safely triggers the Metal-Oxide Surge Arrester (MOSA). Finally, in the **energy dissipation**

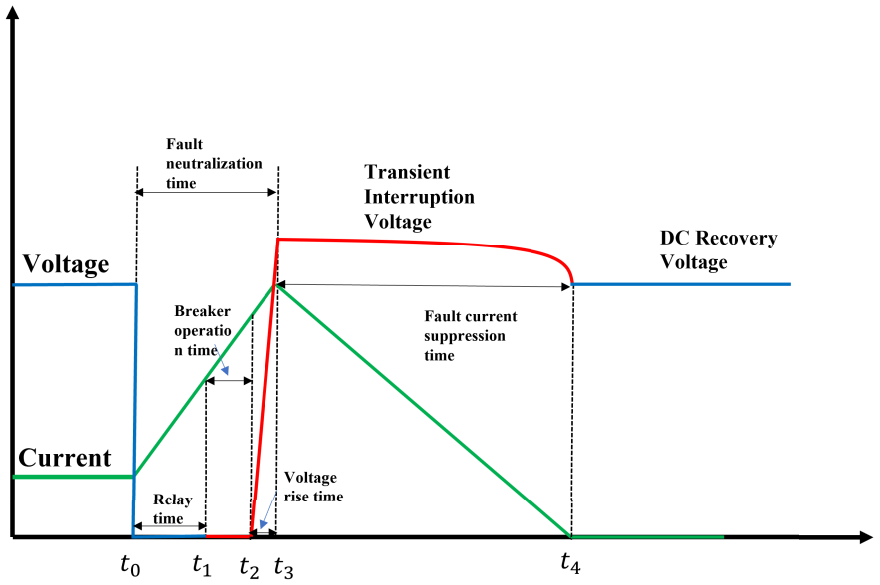

FIGURE 2.7: Timing diagram of HVDC interruption process [41]

stage ($t_3 \rightarrow t_4$, fault current suppression time), the MOSA absorbs the electromagnetic energy, gradually reducing the current to zero over a few milliseconds. At the end of this process, the system voltage is fully restored to normal.

Counter Current Injection Technology

In addition to conventional LC-based HVDC interruption methods, active Counter Current Injection (CCI) techniques have been developed to enhance interruption reliability—particularly in systems lacking a natural current zero [42–44]. These methods inject a high-frequency oscillating current into the fault current path to artificially create a current zero in vacuum [18] or air gaps [9, 17, 45], enabling arc extinction under purely DC conditions. The high-frequency injection current is superimposed on the fault current immediately after contact separation, forming the basis for successful current interruption. A widely adopted implementation of CCI relies on a pre-charged capacitor bank forming a resonant LC circuit to generate the injection current [46–49]. The dynamic voltage and current behaviors of each circuit branch during this process are illustrated in Figures 2.8 and 2.9.

At the time t_0, a fault is detected; the current in the continuous branch rises, and system voltage decreases but does not drop to zero due to the EMF caused by the line inductance. As the circuit breaker starts to open at t_1, an arc forms along with the sheath voltage, continuing the rise in fault current until t_2. Here, the commutation circuit, energized by a pre-charged interrupter, starts diverting the current, leading to a decrease in the continuous branch. By t_3, the current in the continuous branch hits zero, the discharge continues in the capacitor until it triggers the energy absorption branch at t_s, after which the MOSA dissipates the fault current until completion at t_4. The majority of descriptions about interruption processes missed the t_S about the detailed action

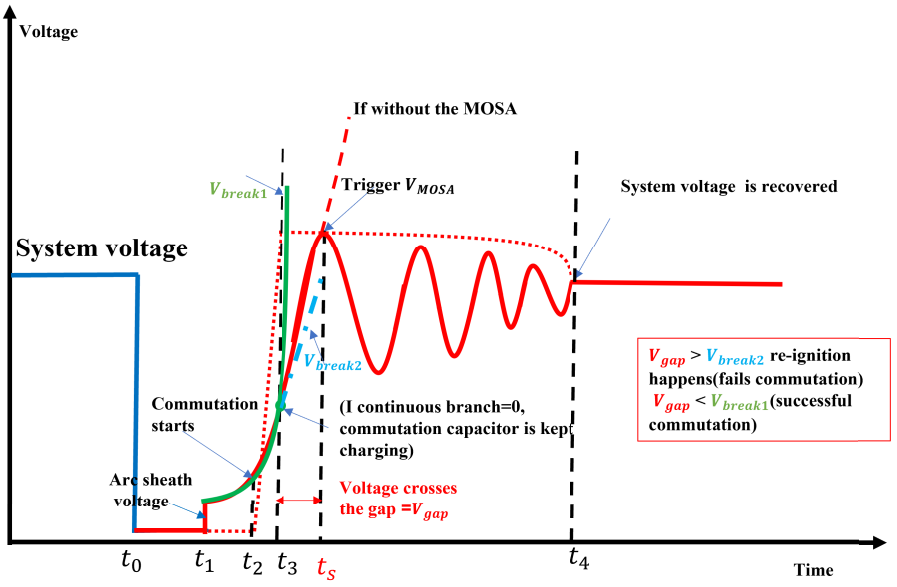

FIGURE 2.8: Voltage behaviors for DC commutative DC circuit breaker. V_{break1} and V_{break2} are conceptual boundaries representing cases on successful interruption and reignition respectively.

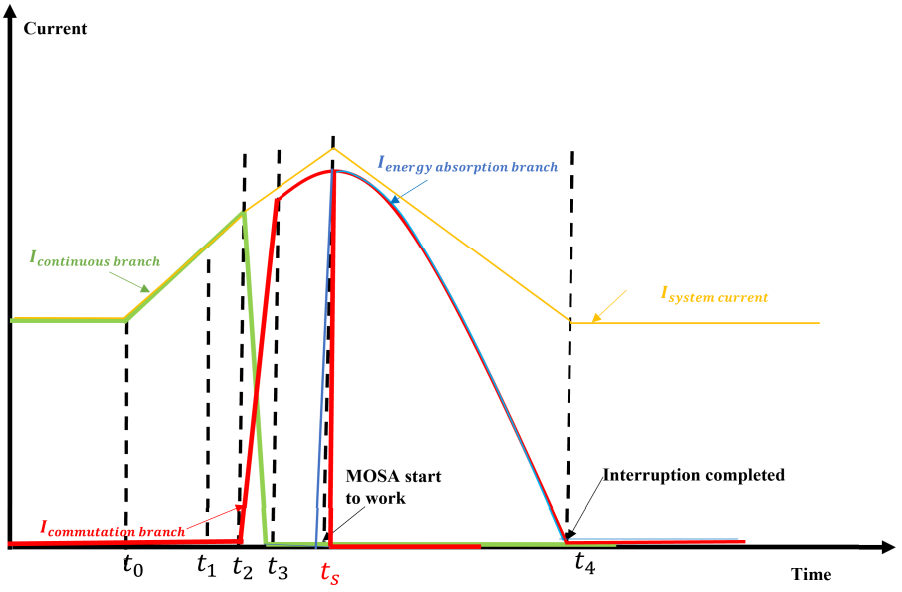

FIGURE 2.9: Current behaviours for counter-current injection technology

of the surge arrester triggering. If the circuit does not have the surge arrester, the voltage will keep increase as shown in Figure 2.8.

Look through the voltage behaviours, after the current goes to 0 at t_3, there is noticeable voltage across the hot air gap of circuit breakers (the voltage increases up to the opening voltage of the surge arrester). Once the arrestor is open, after several damping oscillations, the system recovers back to the normal. Here another critical phenomenon of the circuit breaker emerges during time t_3 to t_s, after the current interruption between two contacts, the gas is stressed by a very steep voltage spike originating from the large inductance of DC circuit. The reignite phenomenon happens when the breakdown voltage is lower than the actual voltage across of the gap, it is shown as the blue dashed line V_{break2} on Figure 2.8. Conversely, the reignition could be avoided if the breakdown voltage follows the green solid line on Figure 2.8 as V_{break1}. If an analytical model for V_{break} is developed, it helps with the design optimisation.

Successful interruption using CCI requires satisfying several conditions: keeping the arcing current below a certain threshold before the forced zero [50], maintaining a low current change rate (di/dt) near zero-crossing [43, 51], and ensuring a sufficient contact gap distance to withstand the post-interruption voltage [7, 50]. When properly implemented, this technique enables bidirectional fault current interruption and has been realized in both MVDC and HVDC systems using vacuum or air interrupters [9, 17, 18].

2.2 Review of Existing DC Circuit Breakers

DC circuit breakers can generally be categorized based on their interruption principles into three main types: mechanical, solid-state, and hybrid breakers [4]. Mechanical DCCBs that use both passive and active resonance circuits, Solid-state DCCBs that exclusively utilize electronic switches, and Hybrid DCCBs that merge electronic components with mechanical disconnectors. This classification applies to both high voltage and low voltage systems.

Although the underlying interruption principles are similar, differences in application scale, current ratings, and design constraints lead to distinct breaker implementations in HVDC versus LVDC. This section outlines the operating principles of the main DC circuit breaker types, then contrasts their strengths, limitations, and typical applications. We also reference successful deployments—e.g., the $\pm$160 kV Nan'ao three-terminal project [42, 52], the $\pm$200 kV Zhoushan island link [53], and the $\pm$500 kV Zhangbei meshed HVDC grid [54, 55]—to illustrate real-world practice.

Mechanical DC Circuit Breakers

Mechanical DC breakers operate via physical contact separation and interrupt fault currents by initiating and extinguished an arc [38]. Figure 2.10 illustrates the operation of a mechanical DCCB.

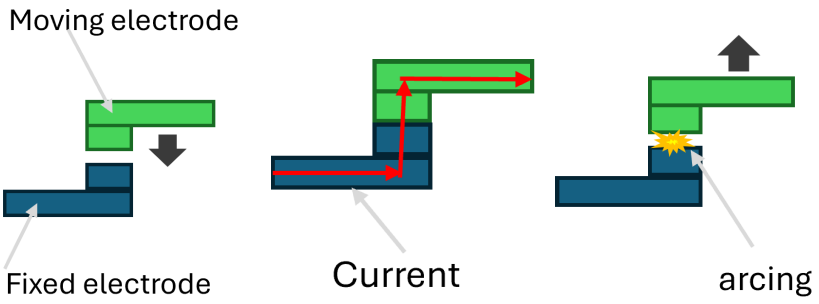

(A) Making current

(B) Carrying current

(C) Breaking current

FIGURE 2.10: Mechanical DC switching functions

Figure 2.10 illustrates the operating sequence of a mechanical DC circuit breaker. During making (A), the moving contact closes onto the fixed contact to establish conduction. During carrying (B), current flows through the closed metallic path. During breaking (C), the moving contact is driven open and an arc forms across the opening gap; the high fault current generates Lorentz forces that stretch and drive the arc away from the contacts (into the arc chute), increasing its voltage and cooling the plasma until conduction collapses and the current is interrupted [38].

Molded Case Circuit Breaker (MCCB)

MCCBs are the most common mechanical DCCBs, which are commonly used in low-voltage DC and AC systems, especially for high-current protection. They are typically enclosed in an insulated plastic housing and may adopt dual arc quenching chambers to enhance interruption performance, as shown in Figure 2.11. They use both thermal and magnetic trip units, and they exhibit electrodynamic auto-protection. Under short-circuit conditions, the high fault current and contact geometry generate a Lorentz repulsion that separates the movable contact before the trip unit releases the mechanism; this effect is especially pronounced at the high fault currents typical of MCCBs [56]. This self-initiated contact motion significantly influences the arc ignition process and the timing of arc formation in MVDC switching devices.

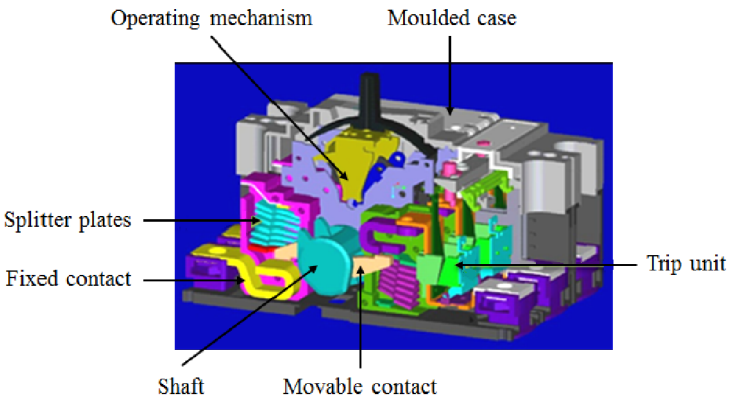

FIGURE 2.11: Example of a MCCB with dual arc chambers.

While MCCBs are widely used in low-voltage DC systems and offer fast, compact protection against short circuit current, for higher voltage and current ratings more advanced mechanical DC breakers are required to achieve reliable fault interruption.

Passive Oscillation DC Circuit Breakers

This type of breaker operates based on a passive resonance principle. As illustrated in Figure 2.12, the design consists of a main circuit breaker connected in parallel with an inductance (L_p), a capacitance (C_p), a MOSA. When a fault occurs, the breaker opens, initiating a resonant LC oscillation across the arcing gap. This oscillatory current (I_p) counteracts the fault current, helping to drive it toward zero. Meanwhile, the surge arrester absorbs the excess energy.

The current and voltage behavior during interruption is shown in Figure 2.12(B). After the breaker opens, the voltage across the contacts (V_a) rises rapidly, and an oscillating current is generated, which gradually decays as the fault is cleared [57, 58].

This method is typically applied in Mechanical Return Transfer Breakers (MRTB) used in HVDC systems, where the current can reach several kiloamperes. The oscillation frequency usually ranges between 1–3 kHz, and the total interruption time is approximately 20–40 ms [18].

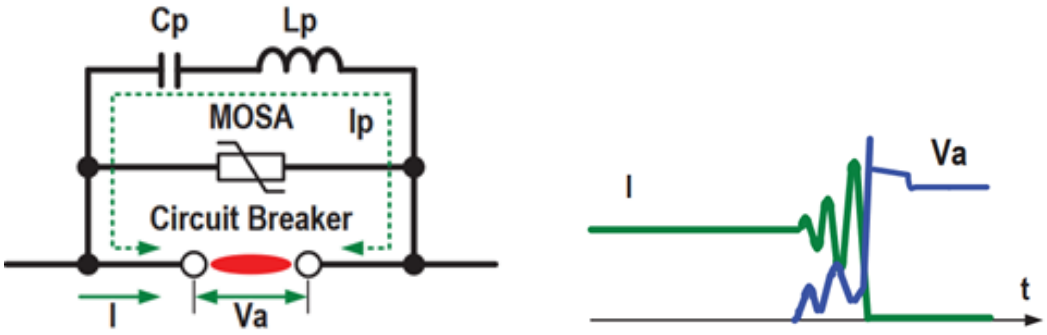

(A) Passive resonance circuit breaker (B) Current and voltage waveform

FIGURE 2.12: Passive resonance circuit breaker interruption phenomena and capability [18]

Active Current Injection DC Circuit Breakers

Unlike passive schemes, active current injection breakers incorporate a DC power source to pre-charge a capacitor and use a thyristor switch or a triggering gap in the resonant circuit, as shown in Figure 2.13. When a fault occurs, the thyristor or triggering gap is activated, allowing the pre-charged capacitor to discharge through the inductor (L_p). This discharge generates a high-frequency oscillating current (I_p), which is designed to flow in the opposite direction of the fault current, helping to bring the total current to zero.

The superimposed oscillation rapidly reduces the net current through the circuit breaker to zero, enabling successful interruption. As shown in the voltage and current waveforms, once the thyristor is triggered, the voltage (V_a) across the breaker rises sharply, followed by a high-frequency oscillation in current that quickly decays to zero [5, 18, 59].

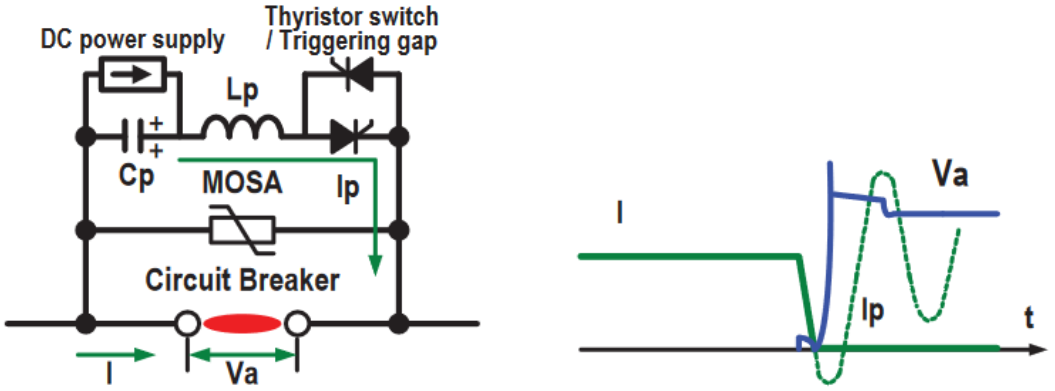

(A) Active resonance circuit breaker (B) Current and voltage waveform

FIGURE 2.13: Active resonance circuit breaker interruption phenomena and capability [18]

A key distinction from passive methods is that the capacitor is pre-charged in advance, enabling a forced zero-crossing of the current rather than relying on natural oscillation. This method typically achieves current interruption within 8–10 ms and is suitable for both fault and nominal current clearing in HVDC systems [18].

Comparison Summary: In summary, the active current injection breaker enables faster interruption, as demonstrated by the current and voltage waveforms. Comparing Figure 2.12(B) and Figure 2.13(B), the passive system exhibits a natural, gradual decay of current leading to a zero-crossing. In contrast, the active system produces a rapid, forced current drop to zero, achieved through the discharge of a pre-charged capacitor.

Solid-State DC Circuit Breaker

Solid-state DC circuit breakers are a class of DC interruption devices that rely entirely on power electronic components to rapidly interrupt fault currents without generating arcs [60–63]. These breakers use devices such as thyristors, IGBTs, or Integrated Gate-Commutated Thyristors (IGCTs) to control the flow of current in the system. Upon fault detection, the semiconductor switches are rapidly turned off, interrupting the current almost instantaneously.

As illustrated in Figure 2.14, a typical topology consists of two main branches [9]. The primary path includes high-voltage electronic switches arranged in a back-to-back configuration to support bidirectional current interruption. An auxiliary parallel branch, often incorporating a surge arrester or energy-dissipating element, is used to absorb the magnetic energy induced by the system's inductance, such as from transmission lines or DC reactors [4].

To achieve bidirectional interruption, solid-state breakers typically employ two sets of high-voltage valves—each made up of hundreds of IGBTs modules—arranged in an anti-parallel configuration. During normal operation, current flows through the semiconductor devices with minimal control effort. When a fault occurs, the IGBTs immediately cease conduction, while a parallel Metal Oxide Varistor (MOV) limits the transient overvoltage across the switches. For high current ratings, multiple IGBTs are paralleled to handle thermal load, whereas series

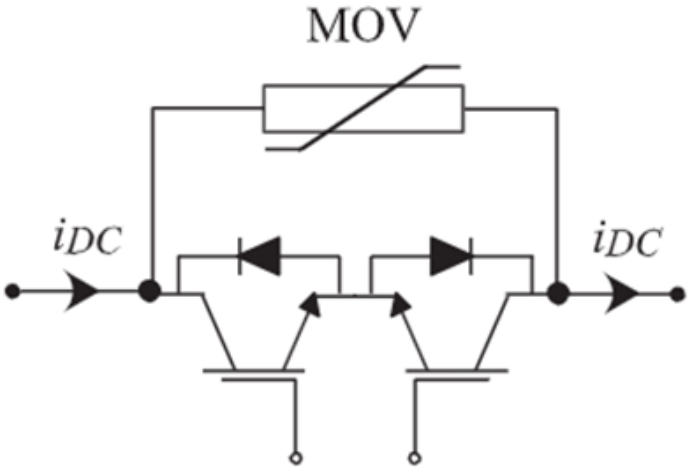

FIGURE 2.14: Typical structure of solid-state circuit breaker [4]

connection is used to meet voltage withstand requirements. Example layouts are presented in Figure 2.15.

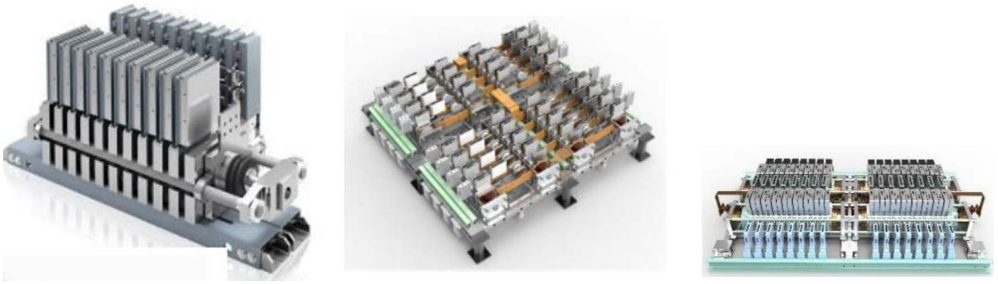

(A) Example 1 [64] (B) Example 2 [65] (C) Example 3 [66]

FIGURE 2.15: Various configurations of power electronic switches used in solid-state circuit breakers

Advantages and Limitations: Solid-state DC circuit breakers offer extremely fast response times—often in microseconds—making them suitable for protecting sensitive systems and enabling selective protection in meshed DC grids. They operate without arcing and experience no mechanical wear, which increases their longevity and allows for frequent operation.

However, these advantages come at the cost of continuous conduction losses during normal operation due to the on-state voltage drop of power electronic devices [9, 67]. Solid-state breakers also face challenges related to the thermal limitations of IGBTs switches and the complexity of ensuring equal voltage distribution among series-connected devices, especially in the context of future MTDC systems where voltage ratings may exceed several hundred kilovolts [4]. This typically requires long chains of IGBTs, increasing both system cost and power loss.

Moreover, overcoming thermal stress in these semiconductors often demands complex and costly cooling systems, further enlarging the device footprint and system complexity. Due to

these limitations, current assessments suggest that purely solid-state circuit breakers may not be the most suitable option for wide deployment in MTDC grid architectures [4, 68].

Hybrid DC Circuit Breakers

Hybrid DC circuit breakers combine mechanical and solid-state switches to leverage the benefits of both technologies. They offer faster interruption times, higher current breaking capacity, and reduced power losses compared to pure solid-state or mechanical breakers [36, 69, 70].

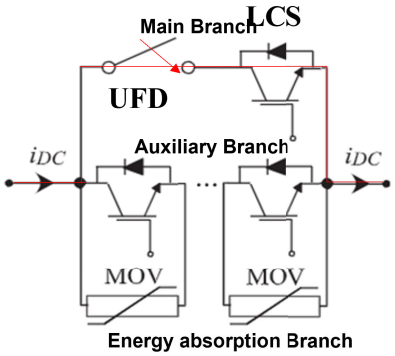

(A) Under normal working condition

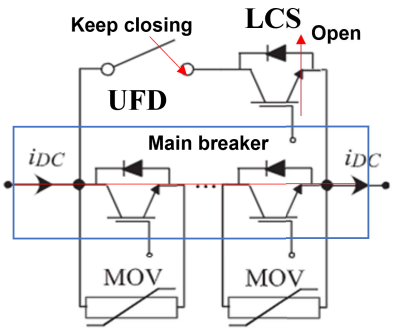

(B) Under fault condition – Step 1

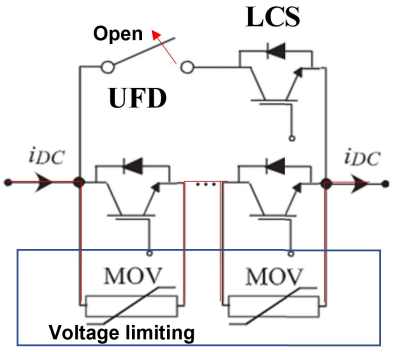

(C) Under fault condition – Step 2

FIGURE 2.16: Structure and working principle of hybrid circuit breaker

As shown in Figure 2.16, a hybrid breaker typically consists of three branches: a main branch,an auxiliary branch and an energy absorption branch. The main branch includes a mechanical switch—known as the Ultra-Fast Disconnector (UFD)—in series with a limited number of power semiconductor devices called the Load Commutation Switch (LCS). Due to its mechanical nature and low on-state resistance, this path carries current during normal operation with minimal conduction losses, as depicted in Figure 2.16(A). Running parallel to this configuration is an auxiliary branch, comprised of a series connection of multiple power electronic switches, commonly IGBTs with anti-parallel diodes, which is the main breaker for this type of circuit breaker, the difference compared to the mechanical circuit breaker is the interruption process happens in main breaker (auxiliary branch) not the main branch. Alongside these, a voltage-limiting device like MOV is also connected in parallel to help with the energy dissipation.

When a fault is detected, the hybrid breaker initiates its interruption sequence by activating the main breaker (auxiliary branch) and turning off the LCS. This action diverts the fault current into the auxiliary path, allowing the UFD to open under zero-current conditions—eliminating arcing and enabling faster disconnection [35]. Once the UFD opens fully, the auxiliary IGBTs breaker turns off, and the MOV clamps the voltage to extinguish the residual current, as shown in Figures 2.16(B) and (C). This staged process enables fault interruption within a few milliseconds [18].

Currently, hybrid DC breakers represent the most widely deployed HVDC circuit breaker type. Products have been commercialized by ABB [36, 71], Alstom [72], and Siemens [73].

Advantages and Limitations: Hybrid circuit breakers combine the low-loss characteristics of mechanical switches with the fast-switching capabilities of power electronics. However, their dependence on a significant number of solid-state components still results in high cost and increased system complexity. This raises concerns about their economic scalability, especially for large-scale MT- MVDC systems, where both capital expenditure and conduction losses must be minimized [18, 74].

Comparison of Different DC Circuit Breakers

According to the technical specifications for DC switching equipment [75], Table 2.1 summarizes key performance metrics of representative circuit breakers from literature. These include mechanical (both passive and active resonance), solid-state, and hybrid types.

- **Mechanical Circuit Breakers (Passive Oscillation):** These breakers use air blast or SF_6 as the interruption medium and feature long commutation times (12–14 ms). While they exhibit negligible conduction losses and low cost, they are limited by low fault interruption capacity and slow clearing speeds, and arc hazards are present [58, 76].
- **Mechanical Circuit Breakers (Active Current Injection):** Incorporating vacuum interrupters, these breakers achieve faster commutation (less than 5–8 ms) and improved interruption capacity (up to 16 kA), while maintaining low cost and negligible losses. However, arcing risk remains [18, 77].
- **Solid-State Circuit Breakers:** Using IGBTs-based switches, these breakers interrupt current in under 0.5 ms and can handle high fault currents (up to 19.2 kA) [78]. However, they suffer from high conduction losses and significant cost due to large arrays of semiconductor devices.
- **Hybrid Circuit Breakers:** By combining IGBTs or thyristors with mechanical switches, hybrid breakers achieve a balanced performance—moderate commutation times (2–3 ms), high interruption capacity (7.5–16 kA), and lower losses than solid-state breakers. Nevertheless, their cost and system complexity remain high [79–81].

TABLE 2.1: The summary of HVDC circuit breaker comparison

Type	Interruption medium	Internal current commutation time	Conduction losses	Interruption Capability	Cost	Fault clearing speed	Arcing hazard	Reference
Mechanical (Passive oscillation)	Air blast	12ms	Negligible	4kA	Low	Low	Yes	[76]
	SF6	14ms		2.2kA				[58]
Mechanical (Active current injection)	Vacuum 1	less than 5ms	Negligible	2kA	Low	Low	Yes	[77]
	Vacuum 2	less than 8ms		16kA				[18]
Solid state	IGBT based	0.4ms	High	19.2kA	Very High	Very high	No	[78]
Hybrid	IGBT	2.4ms	Moderate	16kA	High	High	No	[79]
	Thyristor	2ms		7.5kA				[80]
	Full bridge	3ms		15kA				[81]

In summary, mechanical breakers remain cost-effective and reliable, making them attractive for applications where slower fault-clearing times and arcing risks are acceptable. Solid-state and hybrid breakers offer faster performance and arc-free interruption but at a higher financial and technical cost.

Given this trade-off, mechanical DC circuit breakers still hold significant practical value. Therefore, enhancing their arc extinguishment performance—particularly through techniques such as magnetic blowout, increased contact velocity, or optimized arc runners—is a crucial direction for improving their suitability in future DC grids.

Strategies of Arc Extinction in Mechanical DC Circuit Breakers

To address the limitations of mechanical circuit breakers—particularly their slower interruption speeds and the risk of prolonged arcing—various arc extinction strategies have been developed. These strategies aim to stretch, cool, or segment the arc to increase its voltage drop and accelerate its extinction. The following are the most commonly employed methods:

Magnetic blowout: This method uses self-induced or external permanent magnetic fields to exert a Lorentz force on the arc plasma. The resulting force drives the arc into splitter plates or arc runners, where it becomes elongated, increasing its voltage and facilitating heat dissipation. This technique is widely used in DC contactors and MCCBs) [14, 82–84].

Recent experimental studies by Tokumitsu et al. [85] further validated the effectiveness of magnetic blowout in reducing arc duration. In their tests, contact pairs made of $AgSnO_2$, AgC, and pure Ag were evaluated under DC inductive load conditions (14 V–12 A and 20 V–7 A) with an inductor of 5.7 mH and varying contact opening speeds ranging from 1 to 200 mm/s. A 120 mT magnetic field was applied near the contact gap using a neodymium permanent magnet placed 0.5 cm away.

As shown in Fig. 2.17, applying a 120 mT external magnetic field elongates and lifts the arc away from the contacts, enhancing cooling and thereby accelerating extinction compared with the no-field case where the arc remains confined; the reduction in arcing time is especially evident at higher opening speeds.

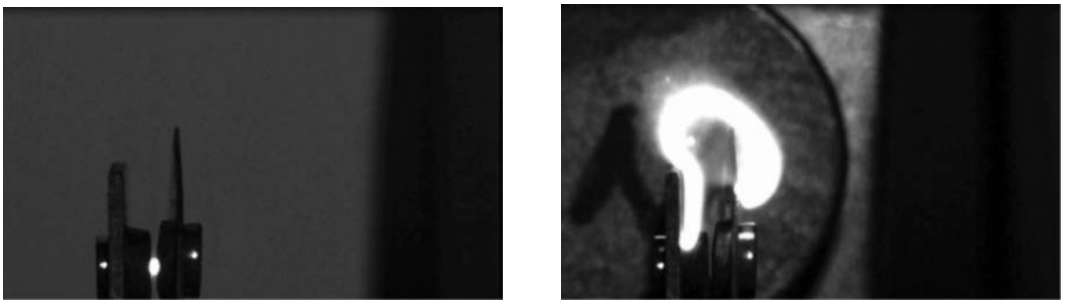

(A) Without magnetic field (B) With 120 mT magnetic field

FIGURE 2.17: Experimental evidence of arc behaviour with and without magnetic blowout under a 14 V–12 A load and 50 mm/s opening speed [85].

Another study by Yan et al. [16], the influence of an external magnetic field on low-voltage DC arc extinguishment was systematically investigated using experiments The experimental setup (as shown in Figure 2.18) consisted of a controlled-opening DC switch operating under resistive loads (up to 45 A, 75 V), with contact velocities ranging from 10 to 500 mm/s. A uniform 40 mT magnetic field was applied using a pair of Helmholtz coils, enabling arc imaging under well-defined and repeatable conditions. The arc's length and diameter were extracted from high-speed camera images, from which the arc conductance and conductivity were estimated. Their results demonstrated that the magnetic field significantly reduced arc duration—by a factor of 5 to 25—due to enhanced convective cooling and a corresponding drop in arc conductivity. The study also provided parametric insights into how contact velocity and arc geometry evolve during the interruption process. These experimental datasets and trends are used in Chapter 7 of this thesis for validation and further modeling analysis of arc cooling mechanisms under external magnetic fields.

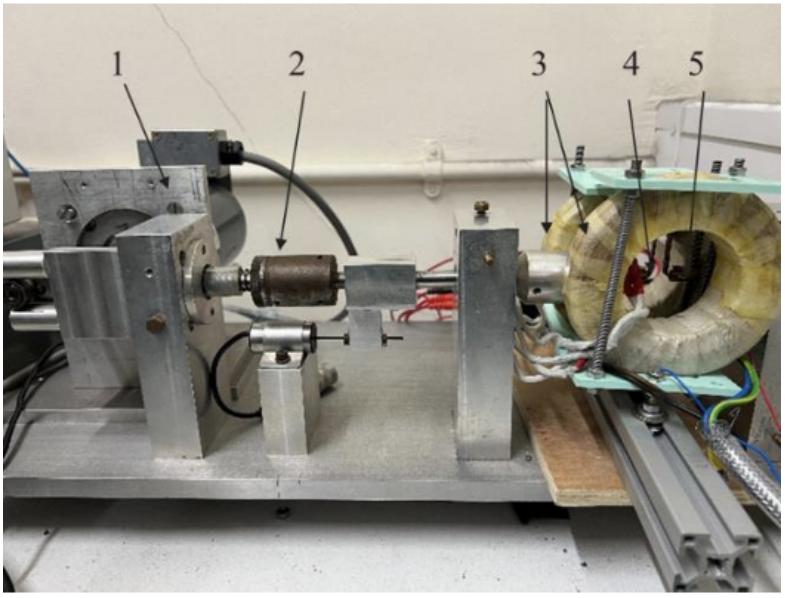

FIGURE 2.18: The test rig of experimental [16], 1- Stepping motor, 2- Contact force spring, 3-Helmohltz coils, 4- Movable, 5-Static contact.

These findings provide a solid experimental basis for the use of magnetic blowout in practical DC switching applications, particularly where fast, compact arc extinction is desired. However, the interaction between magnetic fields and arc dynamics remains complex and further investigation is needed—especially regarding how these effects evolve under different opening speeds, magnetic field, and load conditions.

Splitter plates: Splitter plates are a series of parallel metal plates installed within the arc chamber to enhance arc extinction. When the arc is driven into this region—typically by magnetic or aerodynamic forces—it is segmented into multiple shorter arcs across adjacent plates. This segmentation increases the total arc voltage and promotes arc cooling via surface interaction, thereby accelerating the current decay process [83, 84].

Figure 2.19 illustrates both the structural design of the arc chamber and the dynamic behavior of the arc as captured by high-speed imaging. Subfigure (A) shows the simulation model of the arc chamber, while subfigure (B) presents experimental images of arc motion within a 110 mm-wide chamber [86].

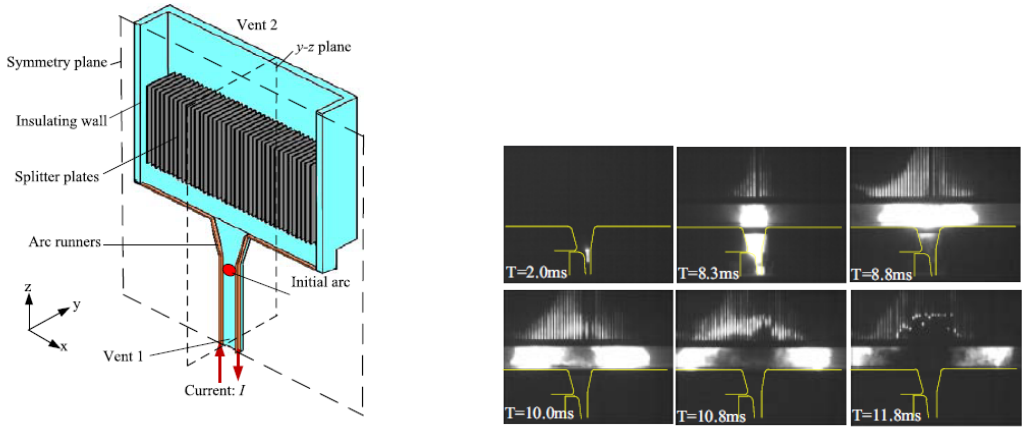

(A) Schematic diagram of the arc chamber adopted in simulation

(B) High-speed imaging of arc motion in a 110 mm-wide chamber

FIGURE 2.19: Simulated structure and experimental observation of arc movement and extinction using splitter plates in air DC circuit breakers [86].

Experimental and numerical studies have demonstrated that splitter plates play a critical role in the final arc extinction phase. In air DCCB, once the arc reaches the horizontal runners, it elongates into the splitter plate region, causing the arc voltage to rise rapidly—often exceeding 1300 V—which results in a steep reduction in arc current and enables successful interruption [86].

However, high-speed camera observations reveal that the arc may stagnate temporarily at the entrance of the chamber, undergoing back commutation before fully engaging the splitter plates. This delay can prolong arc duration and increase thermal stress on the electrodes. Simulation results further indicate that chamber geometry strongly influences arc motion: in wider arc chambers (e.g., 190 mm), the arc tail remains extended and prone to reignition, whereas narrower chambers (e.g., 110 mm) promote faster arc compression and more effective segmentation.

These findings suggest that key factors such as chamber width, pressure distribution, and arc root displacement significantly affect this process. Therefore, optimizing the arc path geometry is essential to fully realize the arc-quenching potential of splitter plates in compact DC breaker designs.

However, the use of splitter plates also presents practical challenges. Their effectiveness often requires wide arc chambers and extended arc runners, which limit the size of switching devices. The added volume and structural complexity pose constraints for modern DC applications—such as electric vehicles (EVs), battery systems, and modular LVDC protection—where space and integration are critical.

These limitations highlight the need for alternative or complementary arc control strategies that enable fast and reliable to predict arc extinction. In this context, understanding how external magnetic fields and dynamic contact motion jointly affect arc behaviors becomes essential.

Air blast or gas propulsion: Air blast interruption is a well-established arc control method that uses a high-velocity stream of air or gas to forcefully remove the arc from the contact region and cool the plasma. This technique rapidly increases the dielectric strength of the gap and facilitates arc extinction. The airflow can be externally supplied—such as from a pressurized tank—or internally generated by mechanisms such as spring-loaded plungers or piston-actuated nozzles.

In LVDC circuit breakers, this method is often implemented through built-in gas chambers and fast-opening contacts that channel air across the arc path. These compact air-driven quenching mechanisms are being increasingly explored for modular protection devices in photovoltaic and battery storage applications [15].

Experimental investigations of air-blast arc extinguishing systems have shown that the direction, velocity, and timing of the airflow are critical to successful interruption. As shown in earlier studies [87], axial-flow designs in high-voltage air-blast breakers enabled fault current extinction up to 2740 A within a single half-cycle. In such configurations, the arc is immediately exposed to a blast of air as the contacts separate, rapidly elongating and cooling the arc column.

Despite its strong cooling effect and fast response time, air-blast interruption presents practical challenges. The need for compressed air sources, valves, nozzles, and energy storage elements limits the size and integration of this method into compact or embedded DC systems. Moreover, the coordination of mechanical motion and timing of the air blast requires precise actuation control, which increases system complexity and cost.

These constraints suggest that while air-blast techniques are highly effective for medium- and high-power applications, their applicability in compact LVDC environments is limited. This highlights the importance of exploring alternative arc control methods that can achieve rapid interruption method—such as combining magnetic blowout with dynamic contact actuation.

2.3 Research Gap

2.3.1 Incomplete Understanding of Re-ignition Behavior in LC commutator based DCCBs

The two experimental studies presented above reveal critical and partially conflicting observations regarding the interruption behavior of LC-based active current injection HVDC circuit breakers. In the vacuum interrupter-based tests [18], successful current interruption was achieved at high fault current levels (up to 16 kA). However, at lower fault currents such as 0.5 kA, reignition events occurred, and interruption only succeeded after multiple oscillations.

This suggests that a low rate of current change (di/dt) at the zero-crossing point is crucial for successful interruption.

Conversely, in the air interrupter-based tests [9, 17], failure was observed when the fault current magnitude slightly increased from 400 A to 430 A, even under otherwise identical circuit conditions. Here, the interruption failure appeared more sensitive to the absolute fault current magnitude rather than the current slope. This apparent contradiction—where one case shows sensitivity to current slope, and the other to fault current magnitude—highlights a deeper uncertainty: the fundamental mechanisms leading to re-ignition, and their dependence on fault conditions and medium properties, are not yet fully understood. Additionally, the air interrupter tests assumed cold air conditions, further complicating the interpretation of results under real operating environments where thermal effects are significant.

These inconsistencies underscore a major research gap: the lack of a unified and predictive understanding of re-ignition behavior in LC commutator based DC circuit breakers. Without such understanding, it is difficult to ensure scalability, robustness, and reliability of these devices across a wide range of system conditions. Addressing this gap requires a physics-based model that captures the full interruption process and enable to predict re-ignition phenomenon under different operation conditions, which can assist the future DC circuit breaker design.

2.3.2 Limited Understanding of Arcing Phenomena in DC Power Relays, Switches, and Circuit Breakers

Despite extensive advancements in DC circuit breaker technologies, a critical limitation remains in the fundamental understanding of arcing phenomena—particularly under conditions involving both external magnetic fields and dynamic contact motion.

Magnetic fields are known to promote arc elongation, commutation onto arc runners, and enhanced plasma cooling [14, 82–84, 88, 89]. Experimental studies further confirm that magnetic fields can reduce arc conductance [90], while increased contact opening speeds have been shown to shorten arc durations via elongated the arc length [14, 82, 91].

However, the combined influence of magnetic field and contact separation velocity remains poorly understood. Most existing models and simulations focus on stationary arc or fixed contacts [13, 92], often oversimplifying arc motion dynamics in practical systems. This is limited for compact mechanical DC devices, where fast actuation and permanent magnets are jointly employed in compact geometries.

The synthetic effect between magnetic fields and contact motion and its impact on arc elongation, arc decay, and overall interruption success has not been adequately addressed in existing studies. This gap in physical understanding limits further optimization of low-voltage DC circuit breakers, especially for compact devices. To address this issue, this thesis will develop a multi-physics arc model that captures the coupled effects of magnetic forces, contact motion, and thermal processes.

Chapter 3

Physics of Arcs

3.1 DC Circuit Breaker Operation and Arc Stages

The following section presents two representative implementations of active current injection HVDC circuit breakers and examines the critical phenomenon of re-ignition that can occur during the current interruption process.

Case 1: Scheme with Vacuum interrupter

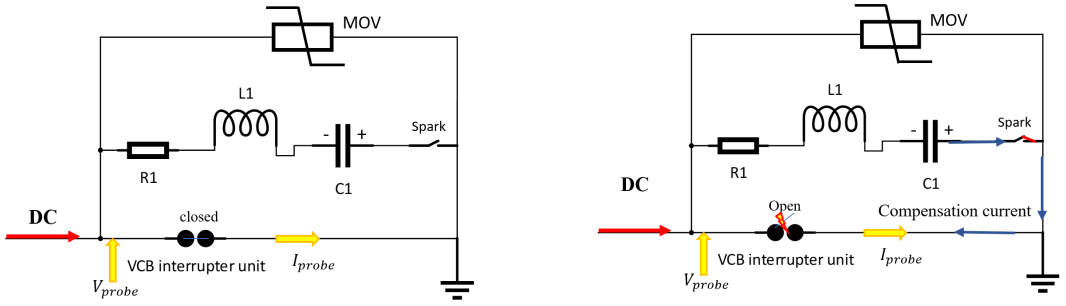

(A) Normal working condition

(B) Under faults condition

FIGURE 3.1: Testing circuit of a Vacuum interrupter based circuit breaker adapted from [18]

The study [18] has been proposed to test how well a mechanical DCCB could stop the fault current up to 16 kA. A simplified schematic of the circuit is given by Figure 3.1: the circuit setup included a pre-charged capacitor, an inductor, a spark gap (as a switch function) and a surge arrestor all linked to the vacuum interrupter in parallel. During the testing phase of the breaker, it was observed that the time it took for the charged capacitor to discharge was consistently just a few milliseconds after the vacuum circuit breaker contacts had separated. The current required for the interruption test was drawn from an AC source capable of simulating the equivalent DC conditions encountered by the DCCB during a typical power frequency short circuit event. As shown in Figure 3.1, under normal working conditions, the Vacuum Circuit Breaker (VCB) is closed and the spark is open, the current goes through the interrupter to the ground.

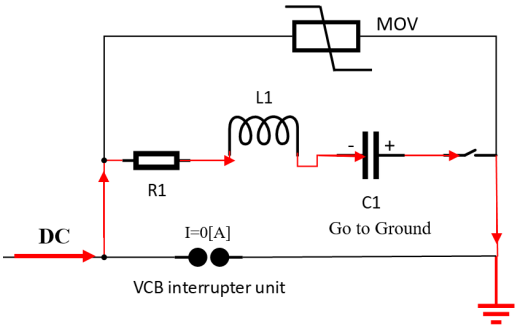

(A) circuit behavior for successful commutation case

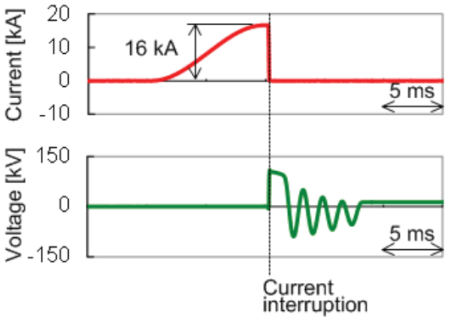

(B) waveform of whole test sequence for 16kA

FIGURE 3.2: Test results of big current commutation for case 1 [18]

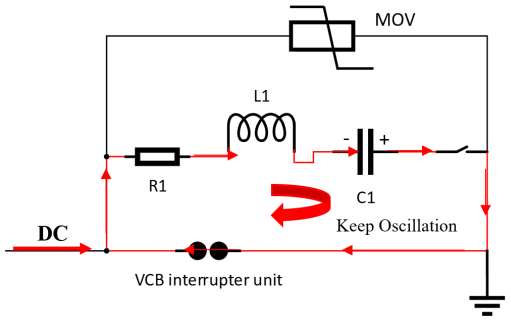

(A) circuit behavior for unsuccessful commutation case

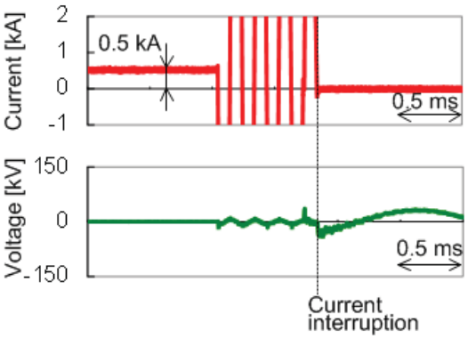

(B) Waveform of whole test sequence for 0.5kA

FIGURE 3.3: Test results of small current commutation for case 1 [18]

When the faults happen, the VCB is open with arcing and the spark is closed to connect the resonant circuit to the system, the pre-charged capacitor will generate the compensation current in the reverse direction to offset the fault current. The test conditions were set based on the insulation standards needed for a high-voltage AC circuit breaker. The DC currents attempted to interrupt varied from 0.5 kA, which is the standard operating current, to 16 kA, matching the highest short-circuit current anticipated in the modelled HVDC network with a radial multi-terminal layout. Based on the test results, it is observed that if the commutation is successful, the current going through the VCB will be zero, and the current will go to the ground, but the capacitor is still charged which causes the voltage oscillation as shown in Figure 3.2.

If the commutation is unsuccessful, the current oscillation is within the commutation circuit and there are several times oscillations until it goes to zero currents because the voltage jumps are observed before the final current zero, which reduced the slop of current changing, as in Figure 3.3. Testing has shown that the current injection circuit breaker is capable of effectively interrupting large currents, successfully handling initial zero crossing points at levels of 16 kA and 5 kA. However, when it comes to lower currents, such as 0.5 kA, a reignition event is observed. The interruption at this lower current level only becomes successful after the current undergoes several oscillations, reducing the rate of current change to a sufficiently low level.

These observations underscore that the rate of current change at the zero crossing is a critical factor in determining the success of the interruption process.

Case 2: Scheme with air interrupter

Another example is using the air interrupter to fast commutate the DC into a capacitor. Figure 3.4 illustrates a detailed schematic of the LC-based experiment testing circuit with a mechanical air interrupter. The circuit setup includes switches (S1), inductors (Ldc), capacitors (Cs), energy-dissipating components (SA) and an AC breaker denoted as S2 is implemented to stop LC oscillations post commutation. The capacitor bank is strategically placed in proximity to the commutation switch. S1, which serves as a rapid disconnector, operates swiftly, achieving separation within 1-2 ms and creating a 3 mm gap in the air.

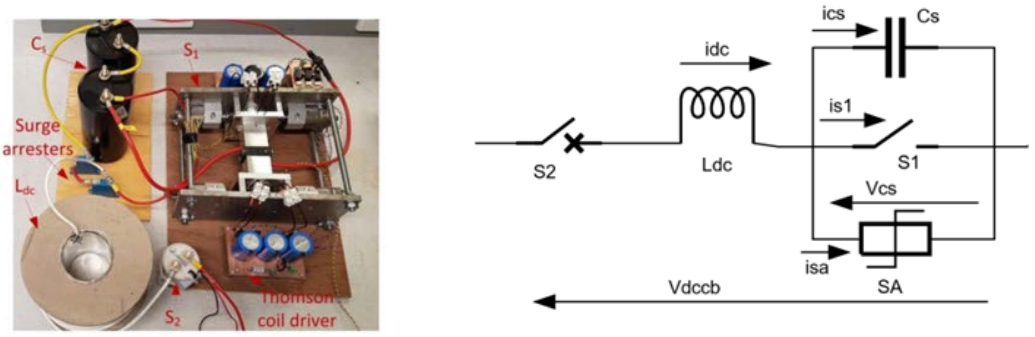

(A) Experimental circuit configuration

(B) Schematic of series LC DC CB

FIGURE 3.4: An example of LC-based with mechanical air interrupter for case 2 [17]

In Figure 3.5(A), a remarkable observation was made: a 400 A current was swiftly redirected from a switch to a capacitor. The voltage of the switch soared to 1.3 kV in about 1 millisecond, notably without any arcing. Voltage spikes were effectively managed by protective arresters. The test also noted that the commutation typically occurred around 350 microseconds after the sliding of contact, and it successfully interrupted the 400 A fault current. However, as depicted

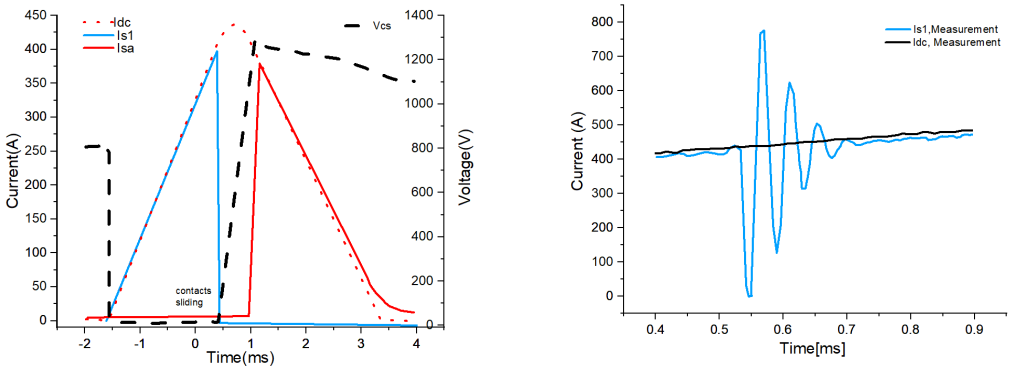

(A) 400A successful commutation case

(B) 430A fails commutation case

FIGURE 3.5: Test results of LC-based with mechanical air interrupter for case 2 [9]

in Figure 3.5(B), when the fault current was marginally increased to 430A while keeping other parameters constant, a different outcome was observed. The switch current I_{s1} decreased rapidly, but it did not drop to zero and persisted in oscillating. This behaviour indicated a failed interruption, physically manifesting as an arcing reignition phenomenon. This difference in results underlines that the success of an interruption heavily depends on the fault current's magnitude. Maintaining the same voltage but increasing the current at the interruption point revealed a threshold beyond which the interruption process is unsuccessful. These tests correlate with the scenario in Figure 2.8, suggesting that a successful interruption depends on the breakdown voltage being higher than the voltage across the gap post-commutation.

This chapter is divided into two sections: arc theory and arc simulation. The arc theory section covers key aspects such as arc structure, arc characteristics, initiation, sustainment, and reignition. The arc simulation section introduces conventional modelling approaches, including simplified assumptions, governing equations, and relevant material properties.

3.2 Arc Theory

3.2.1 Arc Structure

The arc structure consists of an arc column and two near-electrode regions. These near-electrode regions are also referred to as the arc root zones or arc sheath regions [37, 38, 93]. However, the term arc sheath region is not entirely accurate, as these zones comprise more than just the arc sheath layer. A typical arc structure is illustrated in Figure 3.6. Most volume of the arc is occupied by the arc column, whereas the arc root regions are relatively narrow. The electric potential along the arc column remains nearly constant, while a steep voltage drop occurs across the arc root areas [38]. This voltage drop is primarily attributed to the sheath, which has a space charge region.

Arc Column: Within the arc column region, it has been shown experimentally and theoretically [38] that the electron density is equal to the ion density, based on the quasi-neutrality condition in plasma under Local Thermodynamic Equilibrium (LTE). In this state, the plasma is sufficiently dense and collisional such that deviations from charge neutrality are negligible over macroscopic scales. As a result, the number of positive ions approximately balances the number of free electrons. The main ionisation mechanism in the column is thermal ionisation. Due to LTE, all species (ions,electrons, and neutral particles) are assumed to have the same temperature, which simplifies the modelling of the arc column as a thermally ionised, quasi-neutral plasma [38]. And it can be regarded as a single, high-temperature gas that satisfies the conservation equations of mass, momentum and energy. By applying the principles of Magnetohydrodynamic (MHD), it is the common methods used to develop the model of stable electric arc. Owing to its high electrical conductivity, the arc column is capable of carrying substantial currents with minimal a voltage drop. Although the voltage along the arc column remains relatively constant, it can still be influenced by parameters such as current magnitude, temperature and gas pressure [37].

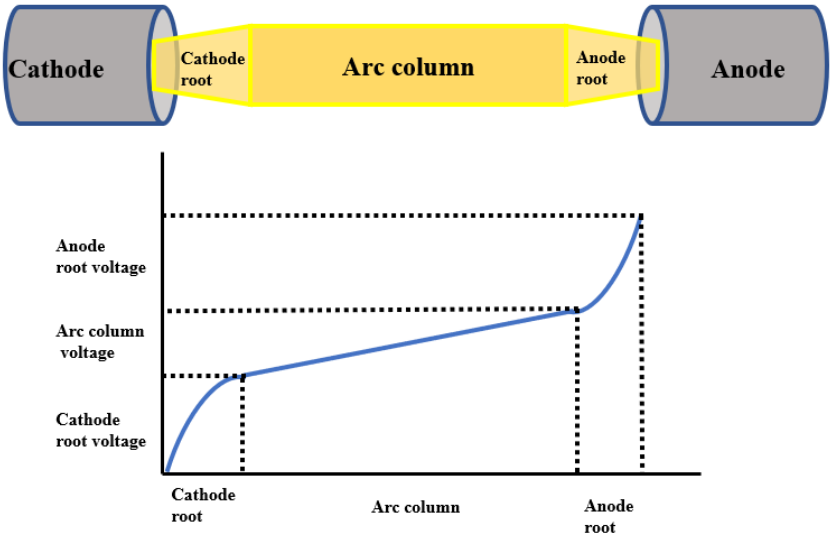

FIGURE 3.6: Schematic of the air arc with the corresponding voltage drop [37]

Arc Root: The narrow region between an arc column and an electrode is referred to as the arc root [37, 94, 95]. The regions adjacent to the electrodes are of critical importance, as they govern the exchange of current and energy between the metallic surfaces and the surrounding plasma-referred to as plasma-electrode interactions, which includes all the physical and chemical reactions happening on the electrode surfaces and nearby. The regions where plasma properties change rapidly and the plasma is no longer in LTE are called the near-cathode and near-anode zones [94]. The behaviour of the arc near the anode and cathode differs significantly due to the different mechanisms of current maintenance and the distinct roles of the space-charge sheath [96].

On the cathode side, most of the current is carried by electrons emitted from the electrode surface, predominantly through Schotty-enhanced thermionic emission. To sustain this emission, significant electrical power must be deposited within the space-charge sheath, which plays a dominant role in regulating current flow and heating the cathode [96]. In contrast, on the anode side, the current is primarily sustained by electrons arriving from the plasma, and the required electron density in the ionization layer is maintained by electron heat conduction from the thermal non-equilibrium region [96]. As a results, the anode sheath contributes little to energy transfer and exhibits only a minor voltage drop. The small and negative voltage drop near the anode has been confirmed by multiple numerical studies. For instance, under comparable electrode surface temperature (around 3000K) but different ambient pressures and gases (Hg at 30 bar vs. Ar at 1 bar), the simulated near-anode voltage drop remained within the same negative range (-0.4V to -0.3V) [96, 97].

Electrodes influence the arc plasma over multiple length scales, giving rise to distinct near-electrode layers with different physical mechanisms [93, 96]. From the arc column towards the

electrode surface, the near-electrode region can be subdivided into: the constricted plasma region, the thermal perturbation layer (TP), the thermal non-equilibrium layer (TN), the ionization layer (IL), and the space-charge sheath (SH) [96], as illustrated in Figure 3.7.

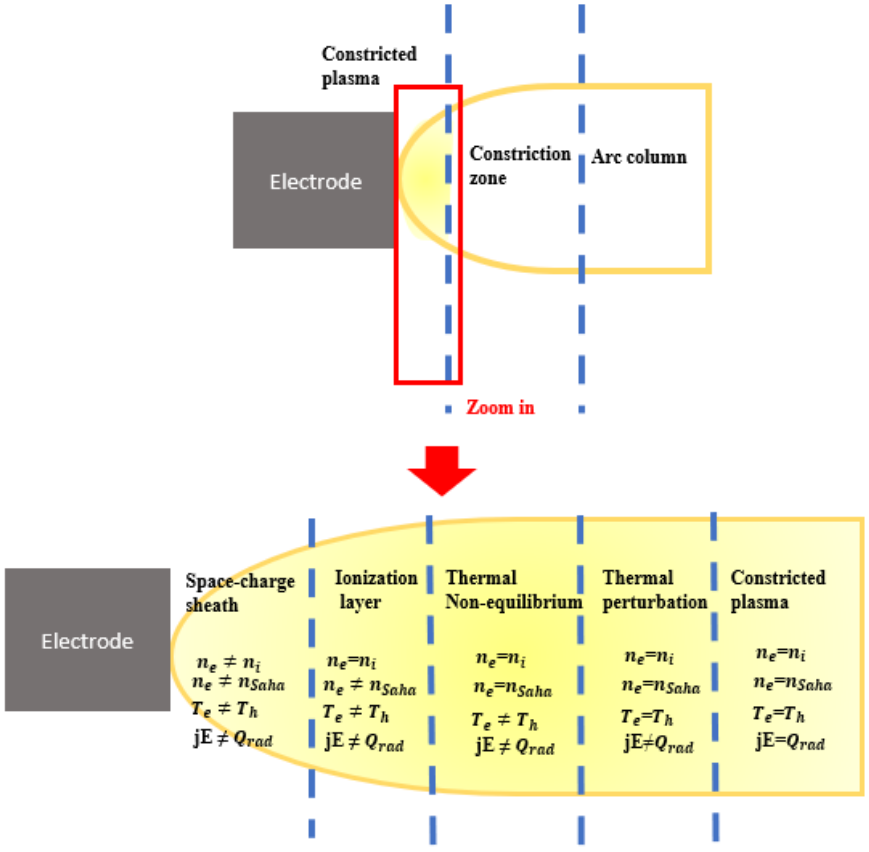

FIGURE 3.7: Structure of the near-electrode perturbation region [96]

The arc root exhibits a complex multi-layer structure extending from the electrode surface into the quasi-neutral plasma column. Proceeding outward, these include: a thin space-charge sheath where quasi-neutrality breaks down; an ionization layer where the Saha equilibrium begins to fail; a thermal non-equilibrium layer where electron and heavy-particle temperatures decouple; and finally, the constricted plasma region in local thermal equilibrium (LTE). Due to the extreme gradients and strong non-equilibrium effects, fully resolving this region is computationally challenging. Therefore, in this work, a simplified approach based on a boundary layer power balance is adopted to model the arc-electrode interaction effectively[96–98].

3.2.2 Arc Electrical Characteristic

The electrical characteristic of an arc typically follows a U-shaped Volt-Ampere Characteristic (VAC), where the arc voltage initially decreases with increasing current and then stabilizes or rises slightly. This behaviour results in a negative differential resistance region, as illustrated in Figure 3.8. The overall arc voltage consists of three primary components: voltage drops at the

cathode and anode roots (ΔV_c and ΔV_a), and the voltage across the arc column, which behaves like a resistive plasma channel. Mathematically, the total arc voltage V_{arc} can be expressed as [99]:

$$V_{\text{arc}} = \Delta V_a + \Delta V_c + R_{\text{column}} \times I_{\text{column}} \tag{3.1}$$

Here, R_{column} represents the resistance of the arc column and I_{column} denotes the current passing through it. As current increases, the arc voltage initially drops, indicating a negative differential resistance ($\frac{dV}{dI} < 0$), until the arc enters a high-current saturation regime as shown in Figure 3.8.

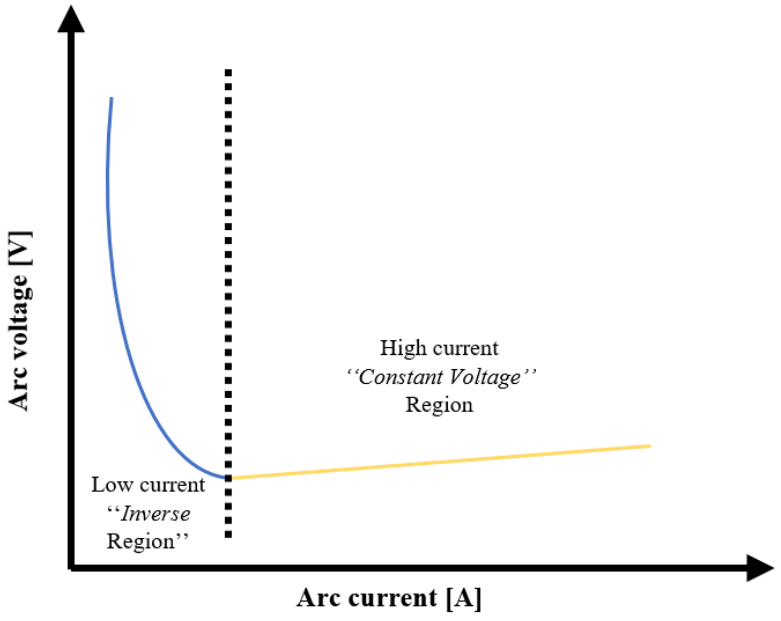

FIGURE 3.8: Free-burning arc volt-ampere characteristic [37, 99]

Mentel et al. [100] conducted experiments using Langmuir probes to quantify the individual contributions to arc voltage in an argon arc at 0.26 MPa, over a current range of 1–10 A. A Langmuir probe is a diagnostic tool used to measure local plasma parameters such as electron temperature, plasma potential, and electron density [101]. Their findings, shown in Figure 3.9, reveal that the cathode voltage drop varies significantly with current, whereas the anode voltage remains relatively constant. At lower currents, the increase in total arc voltage is primarily attributed to the rising cathode fall [37].

The volt-ampere characteristic of a DC arc can generally be divided into two distinct regions. In the low-current regime, the arc voltage decreases with increasing current, exhibiting negative differential resistance due to enhanced ionization and conductivity. Conversely, in the high-current regime, the arc voltage rises more gradually or reaches a plateau as the arc approaches thermal saturation. At this stage, the arc temperature nears its upper limit of approximately 20,000 K, beyond which further increases in current do not raise the temperature. Instead, the arc expands in cross-sectional area to accommodate the higher current density while maintaining

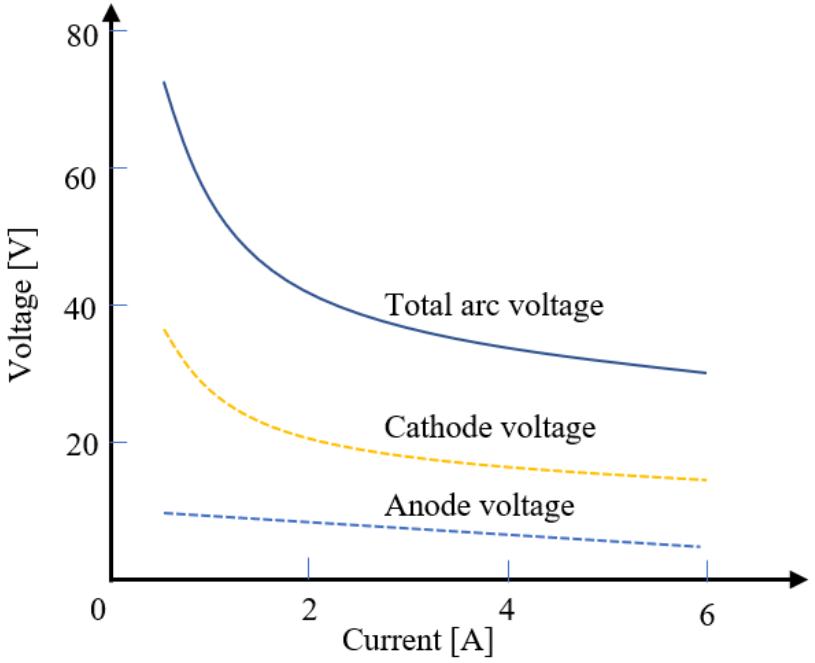

FIGURE 3.9: Measured arc voltage components in 0.26 MPa argon, including cathode, anode, and arc column voltage drops [37, 99]

nearly constant electrical conductivity. This expansion is primarily governed by radiative heat losses, which dominate the energy dissipation mechanisms at high currents [37, 99].

Arc Root Voltage and V–J Characteristic

The arc root region, located at the interface between the arc column and the electrode surface, plays a pivotal role in determining arc attachment behavior and the overall voltage profile during interruption. Due to its highly localized, non-equilibrium nature, directly resolving the sheath dynamics and plasma–electrode interactions is computationally expensive. As a practical alternative, a nonlinear Voltage–Current Density (V-J) characteristic is often adopted to model the arc root behavior [37, 102], as shown in Figure 3.10.

There are two widely used numerical approaches to implement this behavior. The first is the thin mesh layer method, where a virtual interface (typically 0.1 mm thick) is added in front of the electrode surface. The local electrical conductivity in the arc root region σ_u in this mesh is defined as:

$$\sigma_u = J_{\text{ar}} \frac{\Delta y}{V_{\text{ar}}},$$

where J_{ar} is the current density, V_{ar} is the voltage drop across the arc root, and Δy is the layer thickness [37].

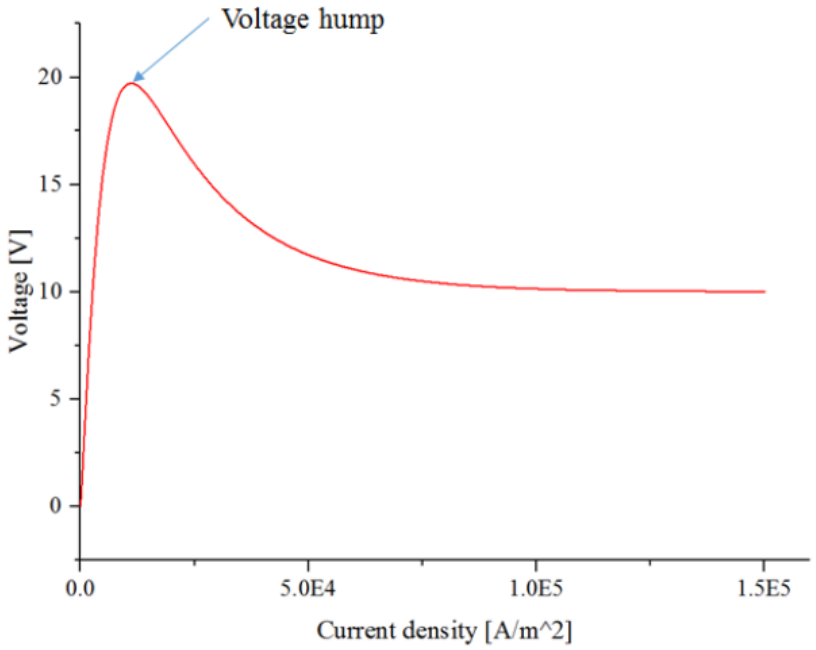

FIGURE 3.10: Nonlinear relationship between the voltage drop and current density in the arc root region (V-J curve) [102]

The second method is to define a contact resistivity at the arc-electrode interface (ρ_{cr}) expressed as:

$$\rho_{cr} = \frac{V_{ar}}{J_{ar}}$$

Compared to the thin-layer approach, the contact resistance method is numerically more stable and avoids mesh deformation issues during contact motion. It is particularly suitable for simulating arc splitting on splitter plates in low-voltage DC systems [37, 102].

The V-J curve itself is typically derived from empirical data [103], showing a peak voltage (19.7 V) at a threshold current density (10^4–10^5 A/m^2), followed by a saturation region at approximately 10 V. This relationship captures the transition from arc ignition to stable root attachment and is critical for modeling voltage increases during arc splitting [37]. As shown in Figure 3.10, the curve facilitates realistic arc behavior in simulations without resolving microscopic sheath phenomena.

3.2.3 Arc Initiation during Contact Opening

There are several methods to initiate an arc. One common approach is to apply a high voltage across the electrodes, causing a breakdown of the gas in the gap between two fixed electrodes. To sustain a stable arc, the external circuit and power supply must be appropriately configured to support continuous current flow. A standard 220V power supply is typically sufficient to initiate low-pressure arcs, such as those found in mercury lamps [24]. However, one of the simplest and most widely used methods for arc initiation involves connecting two electrodes to a power

source capable of delivering high current, then physically bringing the electrodes into contact and rapidly separating them. This action generates intense localized heating and ionisation at the contact point, which is sufficient to establish an arc. This approach is commonly employed in welding applications and circuit breakers [24, 38]. Figure 3.11 illustrates the arc ignition process occurring between opening contacts.

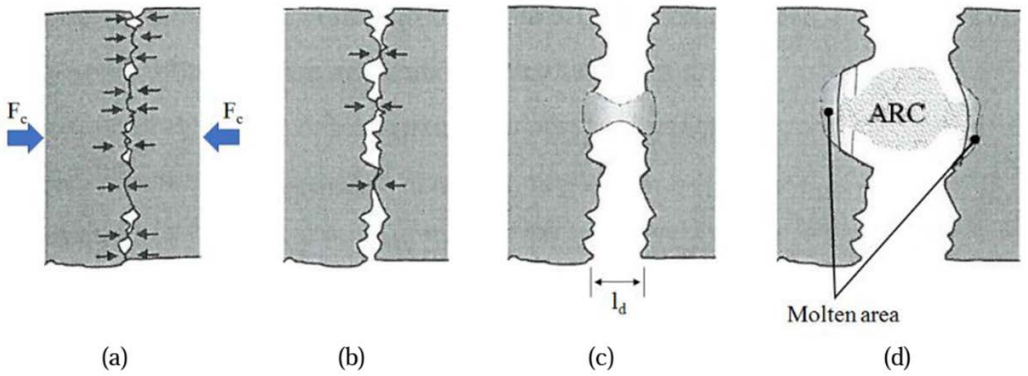

FIGURE 3.11: Process of the arc ignition between opening contacts [104]

The process of arc formation can be divided into four distinct stages [38]:

- A contact force F_c presses the two electrodes together, establishing physical contact and allowing current to flow through the closed circuit.
- As the contacts begin to separate, the contact force F_c decreases, leading to an increase in contact resistance. This causes localized heating at the contact interface due to ohmic losses, and visible hot spots may form on the electrode surfaces.
- As the separation increases further, a molten metal bridge forms between the electrodes and stretches. The narrowing of this bridge leads to a further rise in temperature due to increased current density. At this stage, contact erosion and metal evaporation become significant.
- Eventually, the molten bridge breaks down and the gap is filled with ionized gas, forming a plasma. Metal vapour is released as the surface temperature exceeds the melting and boiling points of the electrode material, sustaining the arc discharge.

As discussed above, arc ignition between two electrodes involves complex, coupled, and transient physical phenomena. To approximate this process numerically, many studies have employed a pre-defined hot gas channel with a Gaussian temperature distribution to initiate the arc [37, 93, 105, 106]. This approach captures the key thermal and plasma characteristics of arc formation, where temperature—and consequently electron and ion densities—peaks at the core and gradually decreases toward the periphery. The Gaussian profile is widely used, as it reflects not only empirical observations but also the steady-state solution of the heat conduction equation in cylindrical symmetry, where localized heating and radial diffusion naturally produce such distributions. A similar strategy is adopted in this study.

3.2.4 Arc Sustainment

Ionisation is the fundamental mechanism responsible for the initiation and maintenance of an electric arc, as illustrated in Figure 3.12. When an incident electron carries sufficient energy to overcome the ionisation energy—the energy required to liberate the most weakly bound electron—the result is the formation of a positive ion and the release of two free electrons. This process transforms neutral gas into a plasma composed of charged particles. In circuit breakers, ionisation is primarily driven by thermal energy and electric fields. In this section, two ionisation mechanisms are introduced: thermal ionisation and field ionisation.

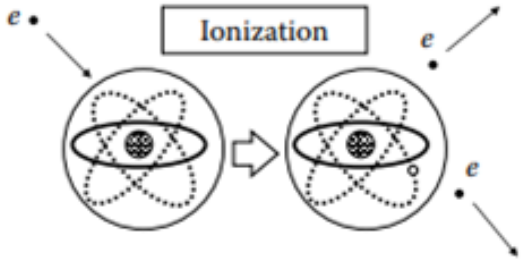

FIGURE 3.12: The schematic of ionisation process which releases an electron from the atom leaving a positive ion [38]

When a gas is continuously heated, its particles acquire increasing kinetic energy. Once this energy exceeds the molecular binding energy, molecular dissociation occurs—breaking the gas into constituent atoms. With further heating, these atoms can lose electrons, becoming ionised. This sequence of processes is referred to as thermal ionisation [38]. The relationship between the thermal and kinetic energy of gas particles is described by:

$$\frac{1}{2}mv^2 = \frac{3}{2}kT \tag{3.2}$$

where m is the particle mass, v is its average velocity, k_B is Boltzmann's constant, and T is the absolute temperature.

Figure 3.13 illustrates how gas composition in dry air evolves with increasing temperature at 1 atm. Molecular oxygen (O_2) begins to dissociate into atomic oxygen at approximately 1500 K, while nitrogen (N_2) dissociates at higher temperatures around 2500 K. With continued heating beyond 6000 K, both oxygen and nitrogen atoms become ionised, producing charged species such as O^+ and N^+, along with free electrons.

The degree of ionisation increases sharply with temperature. At around 15,000 K, the plasma is nearly fully ionised. At even higher temperatures, doubly ionised species such as O^{2+} and N^{2+} appear. These ionisation processes result in a conductive medium—a state referred to as *air plasma*. This transformation imparts significant electrical conductivity to the gas, which is critical in the formation and sustainment of electric arcs.

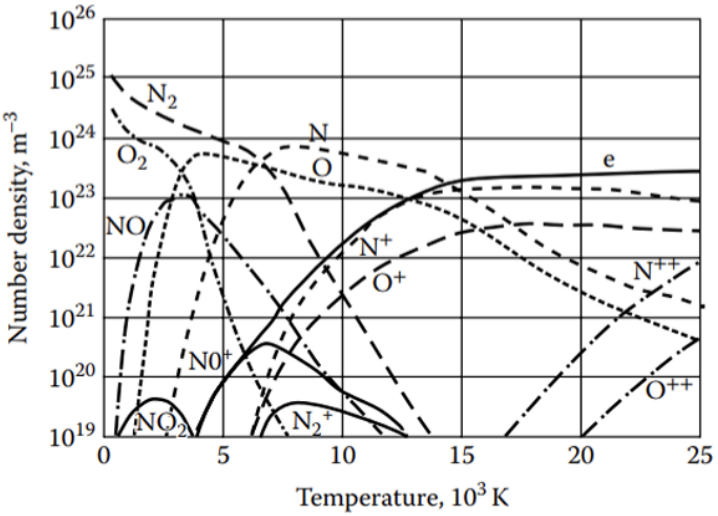

FIGURE 3.13: Number density of different species in dry air at 1 atm as a function of temperature [107]

For example, the first ionisation energies of atomic nitrogen and oxygen are approximately 14.5 eV and 13.5 eV, respectively [38]. Since these two elements dominate air composition, their ionisation properties largely determine arc plasma behaviour.

In low-voltage switching devices, the formation of an electric arc between two contacts creates a conductive plasma channel, sustained predominantly by ohmic heating. Thermal ionisation is therefore a key mechanism that maintains arc conductivity. Typical arc temperatures in such systems range from 6000 K to 20,000 K, depending on current magnitude and breaker geometry [37, 108].

Ionisation Driven by Electric Field

In addition to thermal ionisation, strong electric fields can also initiate and sustain ionisation in gaseous media. This process, known as field ionisation, occurs when free electrons in the gas are accelerated by an applied electric field and collide with neutral gas molecules [38].

As electrons move through the gas under an applied electric field, they frequently collide with neutral atoms or molecules. These collisions can be either elastic or inelastic [37]. In elastic collisions, because the mass of the electron is much smaller than that of neutral particles, the electron transfers only a negligible amount of its kinetic energy. As a result, the electron effectively retains its energy after each elastic collision and continues to gain energy from the electric field over successive interactions. This mechanism enables the electron to accumulate sufficient energy to eventually cause inelastic collisions such as excitation, dissociation, or ionisation [38].

With increasing energy, electrons may eventually cause inelastic collisions, triggering three possible outcomes:

- **Dissociation**: The electron breaks a molecule into its atomic constituents.

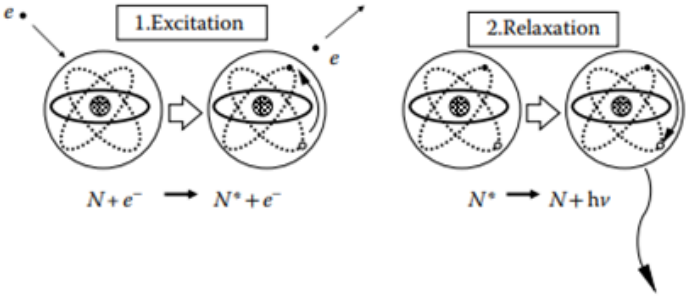

FIGURE 3.14: Excitation and relaxation mechanisms in plasma [38]

- **Excitation**: The electron promotes an inner electron of the gas molecule to a higher energy level. The excited molecule is unstable and rapidly returns to its ground state through relaxation, often releasing photons in the process (see Figure 3.14).
- **Ionisation**: If the kinetic energy of the electron exceeds the ionisation energy of the molecule, the collision ejects another electron, resulting in a positive ion and an additional free electron.

This last process is critical, as it leads to an exponential increase in charge carriers—a phenomenon known as an ionisation avalanche. This mechanism sustains and enhances plasma conductivity, particularly in arcs where thermal energy alone may be insufficient.

Wendelstorf et al. [109] highlighted that an increased cathode voltage plays a pivotal role in maintaining arc discharge, especially at low current levels. As shown in Figure 3.15, a higher electric field at the cathode surface enhances ion bombardment, which raises the surface temperature and boosts thermionic emission. Simultaneously, the field accelerates emitted electrons, improving their ability to ionise neutral species and sustain the arc plasma.

These synergistic effects are particularly important in low-current or transient arc conditions, where thermal energy alone may be insufficient for stable discharge [37].

3.2.5 Foundations of Breakdown Mechanisms

Arc Re-ignition

Re-ignition refers to the phenomenon in which previously non-conductive air transitions into a conductive state, allowing the re-establishment of an electrical discharge between two electrodes immersed in a gas. This transformation is inherently complex, involving multiple stages that ultimately lead to the formation of a new arc [24]. The overall process is illustrated in Figure 3.16.

Electric Breakdown: Townsend Mechanism

Initial Electron Generation:
At the initial stage t_1, the air is electrically neutral. However, when exposed to Ultraviolet (UV)

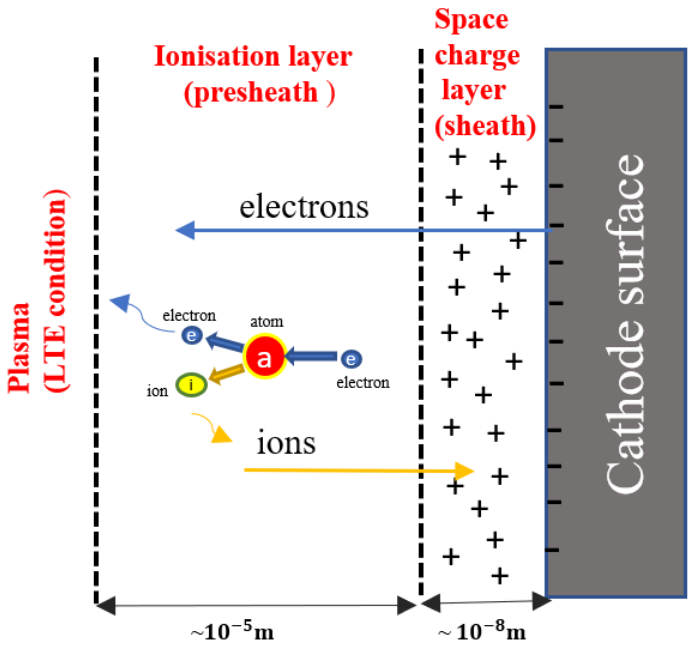

FIGURE 3.15: Structure of the cathode root region: ionisation and sheath layers [37, 109]

radiation, some gas molecules absorb photons with sufficient energy to liberate electrons from atomic or molecular orbitals. These initial electrons, known as seed electrons, may also originate from natural background radiation, cosmic rays, or the photoelectric effect. At this stage, the seed electrons remain embedded within the gas and possess relatively low kinetic energy.

Electron Acceleration:

At t_2, upon application of an external electric field, the seed electrons begin to accelerate. The field imparts kinetic energy to the electrons as they drift toward the anode.

Ionisation and Avalanche Formation:

As electrons gain energy from the field, their collisions with gas molecules become more energetic. When these collisions are sufficiently forceful, they ionise neutral molecules, releasing additional electrons. These newly freed electrons are also accelerated, causing further ionisation. This initiates a self-sustaining chain reaction called an electron avalanche. As time progresses to t_4, the avalanche grows exponentially, provided the electric field remains strong and the electrons have sufficient mean free path to continue ionising. This process is characterised by the Townsend ionisation coefficient α, and the resulting cascade can produce electron densities on the order of 10^{13} m^{-3} [24].

Ion Bombardment and Cathode Effects:

At t_5, the heavier positive ions generated in the avalanche begin moving slowly toward the cathode. Upon reaching the cathode surface, they bombard it with high kinetic energy. This bombardment can induce the emission of secondary electrons from the cathode, a phenomenon known as secondary emission.

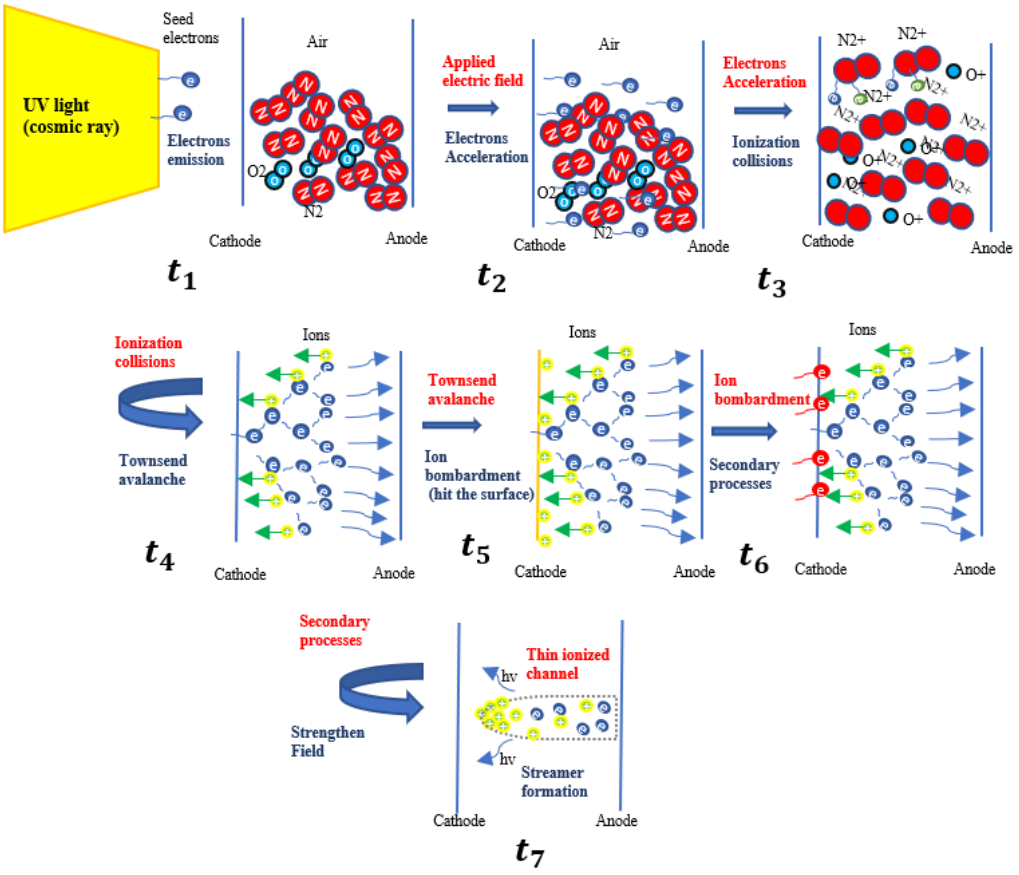

FIGURE 3.16: The schematic of breakdown process in air [24]

Secondary Processes and Field Enhancement:

At t_6, the secondary electrons emitted from the cathode enter the gap with initial kinetic energy and are rapidly accelerated by the electric field. These electrons contribute to the growth of the avalanche and increase the discharge current. As the charge carrier density rises, the local electric field is further enhanced by the space charge effect. Secondary processes are especially important when they contribute to electron emission from the cathode, thereby sustaining and amplifying the breakdown process [24].

Streamer Formation:

When the applied electric field is sufficiently strong and the product (pd) of pressure P and electrode gap distance d, exceeds a certain threshold (typically $pd > 4000$ Torr $\cdot$ cm, corresponding to a gap length of approximately 5–6 cm in air [24]), a weakly ionized but conductive channel, known as a streamer, can develop around t_7. The streamer bridges the electrode gap on a timescale of microseconds or less, enabling a sudden increase in current flow. This process involves the accumulation of space charges, especially at the streamer head, which strongly disturbs and enhances the local electric field. This localized field enhancement promotes further ionization ahead of the tip, sustaining streamer propagation. The entire transition depends on

various parameters such as electric field strength, pressure, gas composition, and the initial level of free electrons. The final outcome is the formation of a conductive path through the air, which may ultimately lead to a full electrical breakdown.

Streamer Mechanism

Under low pressures and shorter electrode gaps, the Townsend mechanism prevails, relying heavily on secondary electron emissions from the cathode in a parallel plate configuration [110]. However, when considering atmospheric pressures, the streamer or spark mechanism provides a more accurate physical description of breakdown [111]. In this streamer mechanism, ionisation avalanches play a fundamental role, with particular emphasis on their collective interactions. Electrons at the leading edge of an avalanche move significantly faster than the heavier positive ions trailing behind due to their much higher mobility. This separation of charge results in the formation of a strong localized space charge region. The corresponding space charge field, denoted E_{sc}, combines with the externally applied electric field E_0, leading to a local amplification of the electric field ahead of the avalanche front. This local field enhancement at the streamer head accelerates ionisation in the adjacent region, as the ionisation coefficient α increases exponentially with the electric field E_0, leading to the formation of new secondary avalanches. When the space charge field E_{sc} becomes comparable in magnitude to the applied field E_0, the avalanche transitions into a streamer—defined as a narrow, highly conductive ionised channel bridging the gap between the electrodes [24, 110]. This transition marks the threshold for streamer formation.

Paschen's Law

For a basic configuration involving two electrodes separated by a gas, Paschen's law describes the breakdown voltage V_B required to initiate an electrical discharge in a uniform electric field. This empirical relationship expresses the breakdown voltage as a function of the gas pressure p, the electrode gap distance d, and the gas composition [25]:

$$V_B = \frac{Bpd}{\ln(Apd) - \ln\left[\ln\left(1 + \frac{1}{\gamma_{se}}\right)\right]} \tag{3.3}$$

In this equation, γ_{se} represents the secondary electron emission coefficient, which depends on the electrode material. The empirical constants A and B are specific to each gas. For air, typical values are $A = 15$ [1/cm/Torr], $B = 365$ [V/cm/Torr], and γ_{se}= 0.01 [24].

At moderate gap distances and pressures, the breakdown voltage is approximately proportional to the product of pressure and gap distance (pd). However, at extremely low values of pd, Paschen's law suggests that a discharge might never occur. In practice, however, breakdown can still take place due to additional effects such as field emission at small gaps at normal temperature (=300K) or high temperature at d $\leq$ 1mm, which are not initially accounted for in Paschen's law [112].

To address this, a modified Paschen's law incorporating thermal effects is introduced [113]:

$$V_{B_1} = \frac{Bpd\frac{T_0}{T_g}}{\ln(Apd\frac{T_0}{T_g}) - \ln\left[\ln\left(1+\frac{1}{\gamma_{se}}\right)\right]} \tag{3.4}$$

Here, T_0=300 K is the reference temperature, and T_g is the gas temperature in the gap.

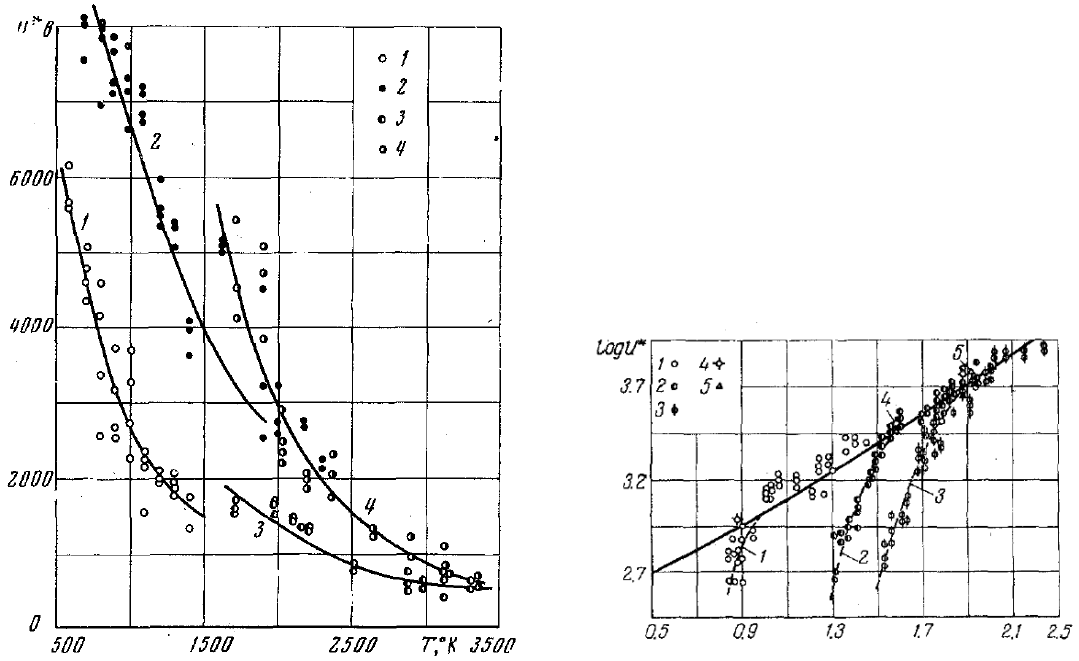

(a) Temperature dependence of breakdown potential of air

(b) Breakdown voltage as a function of the parameter pdT_0/T

FIGURE 3.17: Experimental studies from [113] illustrating the influence of gas temperature and electrode gap on breakdown voltage in air. (a) shows how the breakdown potential decreases with temperature, for different gap distances d and electrode cooling conditions. (b) reorganizes the breakdown voltage data against the parameter pdT_0/T, confirming the scaling used in modified Paschen models. These results validate the thermal dependence of breakdown voltage and the need to adjust Paschen's law under high-temperature conditions.

Experimental results from Dandaron et al.[113] provide direct measurements of breakdown voltage in air as a function of temperature and electrode gap. As shown in Figure 3.17, the breakdown voltage decreases nonlinearly with increasing temperature, and the results differ between cooled and uncooled electrodes. Furthermore, by rescaling the voltage using the parameter pdT_0/T, a clearer trend is observed, supporting the use of temperature-compensated Paschen models in high-temperature arc environments. Despite this modification, experimental studies suggest that Paschen's law holds primarily at around 2200 K.

In practical arcing conditions, especially post-current commutation, the gas temperature often exceeds this threshold. Thus, alternative breakdown mechanisms must be considered. Moreover, for millimeter-scale gaps, Paschen's law loses accuracy due to the growing influence of

field emission effects [114], which surpass Townsend avalanche mechanisms. Accurate modeling under these conditions requires deeper consideration of field emission-dominated breakdown.

Streamer and Breakdown Threshold

As breakdown transitions from a Townsend avalanche to a streamer, the availability of background ionisation becomes essential, and breakdown is governed primarily by the critical electric field across the gap. For dry air, the reduced critical dielectric strength remains relatively constant up to 2000 K, as verified by experimental data [18, 26, 115].

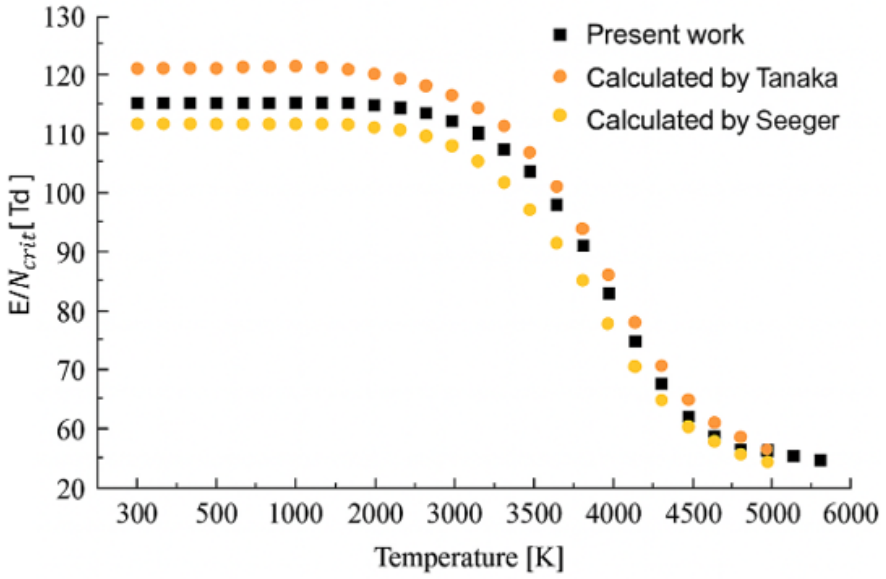

FIGURE 3.18: Critical reduced electric field strengths as a function of temperature [26]

The reduced electric field strength, denoted as E_{red}, reflects the ratio of electric field intensity to gas number density and governs the balance between electron attachment and detachment. It is typically expressed in Townsend units:

$$1\ \text{Td} = 1 \times 10^{-21}\ \text{V} \cdot \text{m}^2 \tag{3.5}$$

As shown in Figure 3.18, simulations indicate that the critical reduced field strength $(E/N)_{\text{crit}}$, where N denotes the total neutral gas number density, remains nearly constant up to 2000 K, then decreases sharply with rising temperature. Breakdown typically occurs at field strengths close to the critical value E_{critical}, which ensures a sufficient ionisation rate to sustain the discharge. This drop is attributed to thermal dissociation of species such as O_2 and CO_2, and the formation of NO and NO_2, which possess lower ionisation potentials and thereby enhance ionisation efficiency. The results underscore the need to account for detailed plasma chemistry—especially at elevated temperatures and under high-pressure conditions—for accurate modelling of breakdown behaviour.

Spark, Gap Heating, and Thermal Plasma Formation

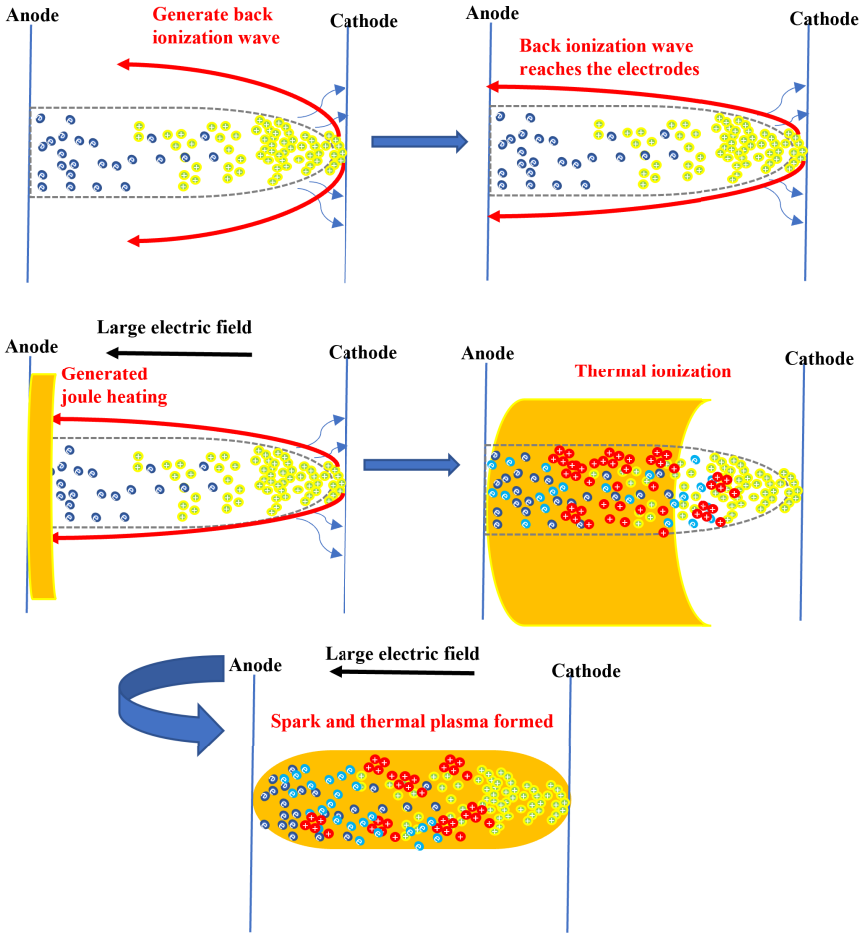

FIGURE 3.19: The demonstration of the process from streamer to spark [24]

As illustrated in Figure 3.19, a streamer initially forms a weakly ionised path through the air. Although this channel is conductive, its degree of ionisation remains relatively low. When the streamer connects with the cathode, it initiates a return ionisation wave that propagates back toward the anode, marking the onset of spark formation. This spark develops once the streamer establishes contact with one of the electrodes [24].

In comparison, the Townsend mechanism involves an electron avalanche that reaches the electrode, leading to reduced conductivity. A similar back-propagating ionisation wave occurs, but the key distinction lies in whether the path is formed through a weakly ionised streamer or a denser, more strongly ionised channel. Nevertheless, both processes eventually lead to spark formation via this backward-moving ionisation front.

This return ionisation wave is an inevitable consequence when either a streamer or a Townsend avalanche reaches an electrode under high voltage. Although both processes involve only a small current—typically fractions of a milliampere—a much larger current is required to form a spark. This increase is enabled by the return ionisation, which significantly boosts charge carrier density.

When the back ionisation front reaches the opposite electrode, a highly ionised thermal plasma is formed. Although the initial ionisation level—around $10^{15}\,\mathrm{m}^{-3}$—is relatively modest, it is insufficient for significant electrical conductivity [24, 107]. In other words, the ionisation produced by the streamer or avalanche is not adequate to convert the air into a good conductor. However, under a strong electric field, substantial Joule heating Q_j occurs, which drives thermal ionisation in poorly conducting regions. It is important to emphasise that electrical breakdown alone does not immediately produce thermal plasma. Rather, thermal plasma generally forms in areas with low conductivity, where resistive heating is most intense. Therefore, analyses of thermal runaway should be included, as localized resistive heating in such regions can rapidly escalate to intense ionisation and trigger the formation of thermal plasma.

This thermal ionisation phase is a critical prerequisite for arc initiation. Once the streamer forms, a return ionisation wave develops rapidly, and intense localised heating follows. As a result, the transition from streamer to thermal arc occurs swiftly, typically with only a brief delay before arc formation.

In summary, the transition from streamer to spark to arc follows a sequence: the formation of a low-ionisation conductive channel, the propagation of a back ionisation wave, and the subsequent development of thermal plasma due to Joule heating in poorly conducting regions. While the present study does not focus on modelling the avalanche or streamer phases, it specifically targets the transition from spark to thermal arc. This is particularly relevant in small-gap configurations (on the order of millimetres), where this transition occurs almost instantaneously. Once breakdown is initiated under high-temperature or high-current conditions, the formation of a thermal arc can proceed rapidly, even if contact separation is attempted. In such cases, if breakdown has already occurred, an arc is likely to form regardless [38]. Therefore, my work centres on two key phenomena: arc extinguishment dynamics and arc re-ignition phenomena. Both must be accurately captured within the arc simulation model. The following section introduces the methods and modelling strategies employed in this work.

3.3 Arc Simulation

3.3.1 Review of Arc Modelling

Arc simulation plays a pivotal role in evaluating the performance of DC switching devices [101, 103, 117]. The arc that forms between two separating contacts is governed by a tightly coupled cycle of physical processes (see Figure 3.20): first, the electric potential establishes a current density distribution, which generates Ohmic heating and magnetic forces; these in turn drive the gas dynamics (combined heat transfer and fluid flow), producing local temperature and pressure fields; and the resulting plasma parameters (e.g. electrical conductivity) feed back to the electric potential. Because each link influences and depends on the others, all of these interdependent phenomena must be solved simultaneously for an accurate arc model.

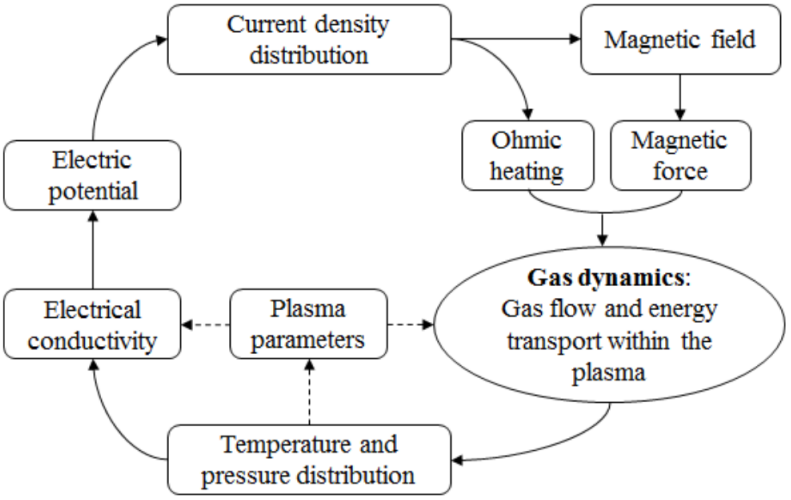

FIGURE 3.20: Interaction of physical processes in the arc column [116]

Figure 3.20 illustrates the interaction pathways among the governing physical domains in the arc column. The process begins with the electric potential distribution, which determines the current density. This current flow produces magnetic fields and generates Ohmic heating, which acts as the primary energy input to the arc. Concurrently, the magnetic field induces Lorentz forces that influence the gas dynamics, especially the velocity field and vortex structures around the arc.

Ohmic heating adds energy to the gas, increasing its internal energy and thus raising its temperature. This shift in the local thermodynamic state alters key plasma parameters—such as pressure, enthalpy, and specific heat—which in turn change the electrical conductivity that governs current flow. The new conductivity then updates the electric field and current-density solution, closing the self-consistent feedback loop.

Meanwhile, temperature and pressure distributions drive *gas dynamics*, including fluid convection and diffusion of charged and neutral particles. These flows significantly affect the arc shape, position, and cooling efficiency. The evolving thermodynamic conditions also influence the ionisation and recombination processes within the plasma.

Due to this strong coupling between electrical, thermal, fluid, and plasma behaviours, arc simulations are inherently multi-physics in nature. Solving these coupled equations typically requires iterative numerical methods and robust computational resources. With the advancement of Computational Fluid Dynamics (CFD) tools and multi-physics platforms such as COMSOL Multi-physics, it has become feasible to model these complex interactions under practical operating conditions [105, 118, 119].

In the following sections, the modelling strategies and governing equations for simulating the arc column and arc root regions are introduced in detail.

3.3.2 Arc Column Modelling

The modelling of the arc column is based on MHD theory, which combines the conservation laws governing gas-plasma dynamics with Maxwell's equations describing the electromagnetic field. In this section, we present the mathematical formulation used to represent the bulk plasma of the arc. The plasma domain is comprehensively described using a set of partial differential equations that account for the conservation of mass, momentum, energy, and the behaviour of electromagnetic fields [37, 93, 108, 116, 120].

Governing Equations for Arc Column Modelling

Mass Conservation Equation

$$\frac{\partial \rho}{\partial t} + \nabla \cdot (\rho \mathbf{V}) = 0 \tag{3.6}$$

This equation expresses that the net mass flow out of a control volume is equal to the rate of decrease of mass within it. Here, ρ is the mass density ($\mathrm{kg/m^3}$), $\mathbf{V}$ is the flow velocity vector ($\mathrm{m/s}$), and t is time (s).

Momentum Conservation Equation

$$\frac{\partial (\rho \mathbf{V})}{\partial t} + \nabla \cdot (\rho \mathbf{V} \otimes \mathbf{V}) = -\nabla P - \nabla \cdot \hat{\pi} + \mathbf{j} \times \mathbf{B} \tag{3.7}$$

The momentum Equation (3.7) is a statement of Newton's second law applied to a moving fluid. The left-hand side represents the product of mass and acceleration per unit volume, while the right-hand side accounts for the net forces acting on the gas. These forces include body forces, such as the Lorentz force, and surface forces, such as pressure gradients and viscous stresses. The Lorentz force arises from the interaction between the current flowing through the arc and the magnetic field generated by the arcing current itself.

The viscous stress tensor $\hat{\pi}$ characterizes internal frictional forces within the plasma caused by shear flow between adjacent fluid layers. Pressure P is expressed in pascals (Pa), current density $\mathbf{j}$ in amperes per square meter ($\mathrm{A/m^2}$), and magnetic flux density $\mathbf{B}$ in webers per square meter ($\mathrm{Wb/m^2}$).

Energy Conservation Equation

$$\frac{\partial (\rho H)}{\partial t} + \nabla \cdot (\rho H \mathbf{V}) = \nabla \cdot (\lambda \nabla T) + \frac{\partial p}{\partial t} + Q_j - Q_{\text{rad}} + Q_\eta + Q_{\text{tran}} \tag{3.8}$$

Equation (3.8) describes the conservation of energy within a compressible, electrically conducting fluid. On the left-hand side, the transient term $\frac{\partial (\rho H)}{\partial t}$ denotes the local rate of change of total enthalpy, while the convective term $\nabla \cdot (\rho H \mathbf{V})$ accounts for enthalpy transport due to fluid motion. The right-hand side includes several source and sink terms: $\nabla \cdot (\lambda \nabla T)$ represents heat conduction; $\frac{\partial p}{\partial t}$ accounts for pressure work; Q_j is the Joule heating due to current flow; Q_{rad} represents radiative losses; Q_η is the viscous dissipation term, which redistributes but does not

generate heat and is often neglected [116]; and Q_{tran} convective enthalpy flux due to the drifted motion of charge carriers under electromagnetic forces.

The Joule heating term is defined as:

$$Q_j = \sigma \mathbf{E}^2 \tag{3.9}$$

where σ is the electrical conductivity ($\mathrm{S/m}$) and $\mathbf{E}$ is the electric field intensity ($\mathrm{V/m}$).

The thermal drift term is expressed as:

$$Q_{\text{tran}} = \frac{5}{2}\frac{k_B T}{e}\mathbf{j} \tag{3.10}$$

with k_B being the Boltzmann constant ($\mathrm{J/K}$), T the absolute temperature (K), and $\mathbf{j}$ the current density ($\mathrm{A/m^2}$).

The total enthalpy H includes both kinetic and thermal components:

$$H = \tfrac{1}{2}\rho \|\mathbf{V}\|^2 + h \tag{3.11}$$

where $\mathbf{V}$ is the plasma velocity vector and $V = \|\mathbf{V}\|$ is its magnitude (speed).

Here, h is the static enthalpy ($\mathrm{J/kg}$), obtained by integrating the specific heat capacity at constant pressure:

$$h = \int c_p \, dT \tag{3.12}$$

where c_p is in $\mathrm{J/(kg \cdot K)}$. The term λ in Equation (3.8) denotes thermal conductivity ($\mathrm{W/(m \cdot K)}$), governing the rate of conductive heat transfer within the plasma.

The electromagnetic aspects of the simulation consider the electric potential V, current density $\mathbf{j}$, and magnetic flux density $\mathbf{B}$. These are governed by Maxwell's equations, which form a complex system of partial differential equations. To make the model computationally tractable, the following simplifying assumptions are adopted [116]:

- **Neglect of Induced Currents:** In arc plasma flows, the plasma behaves as a moving conductor in a magnetic field. It is a reasonable approximation to assume that the induced currents are negligible compared to the externally applied or injected current. As such, time-varying magnetic flux and the resulting induced electric fields are ignored. The dominant driving force for current distribution is the electric potential applied at the electrodes, which generates a magnetic field that interacts with the current to produce the Lorentz force, propelling the arc plasma.
- **Non-Magnetic Medium Assumption:** The simulation assumes that all materials involved are non-ferromagnetic, thereby avoiding the nonlinearities associated with magnetic saturation. Consequently, the magnetic permeability is treated as a constant value, denoted by μ_1, which simplifies the computation of magnetic fields.

Current Continuity and Electromagnetic Field Model

The electric field $\mathbf{E}$ in the plasma is calculated as the negative gradient of the electric scalar potential:

$$\mathbf{E} = -\nabla V \tag{3.13}$$

where V is the electric potential (in V). Assuming a quasi-static condition and neglecting displacement current, the current continuity equation reduces to:

$$\nabla \cdot \mathbf{j} = 0 \tag{3.14}$$

The current density $\mathbf{j}$ is related to the electric field via Ohm's law:

$$\mathbf{j} = \sigma \mathbf{E} \tag{3.15}$$

This simplified Ohm's law neglects time-dependent and convective electromotive terms, such as $\partial \mathbf{j}/\partial t$ and $v \times \mathbf{B}$, which are typically small in low-inertia arc simulations and thus often excluded for numerical efficiency [121].

To compute the magnetic field $\mathbf{B}$ associated with the Lorentz force, the vector potential $\mathbf{A}$ is introduced:

$$\nabla^2 \mathbf{A} = -\mu \mathbf{j} \tag{3.16}$$

$$\mathbf{B} = \nabla \times \mathbf{A} \tag{3.17}$$

where μ_1 is the magnetic permeability of free space (in H/m). The Coulomb gauge condition,

$$\nabla \cdot \mathbf{A} = 0 \tag{3.18}$$

is applied to ensure uniqueness of the vector potential. This magnetostatic approximation avoids solving the full set of Maxwell's equations and is valid when the characteristic timescales of the arc evolution are much larger than the electromagnetic wave propagation time [37].

The above electromagnetic field expressions are used to calculate the source terms in the momentum and energy conservation equations through the Lorentz force ($\mathbf{F}_\mathrm{L} = \mathbf{j} \times \mathbf{B}$) and Joule heating ($Q_j = \mathbf{j} \cdot \mathbf{E}$).

Material Properties

The arc simulation domain is composed of two primary materials: air (as the plasma medium) and copper (as the electrode material). All relevant thermophysical properties of air are obtained from the widely cited work by Murphy [122]. These properties—including thermal conductivity, electrical conductivity, specific heat capacity, and dynamic viscosity—are all strong functions of temperature, as shown in Figures 3.21–3.24. Incorporating accurate, temperature-dependent data is essential for capturing the dynamic behaviour of arc plasma in simulations.

As temperature rises, air exhibits distinct non-linear trends in its material properties due to molecular dissociation and successive stages of ionisation. These transitions directly influence the governing equations of mass, momentum, and energy conservation.

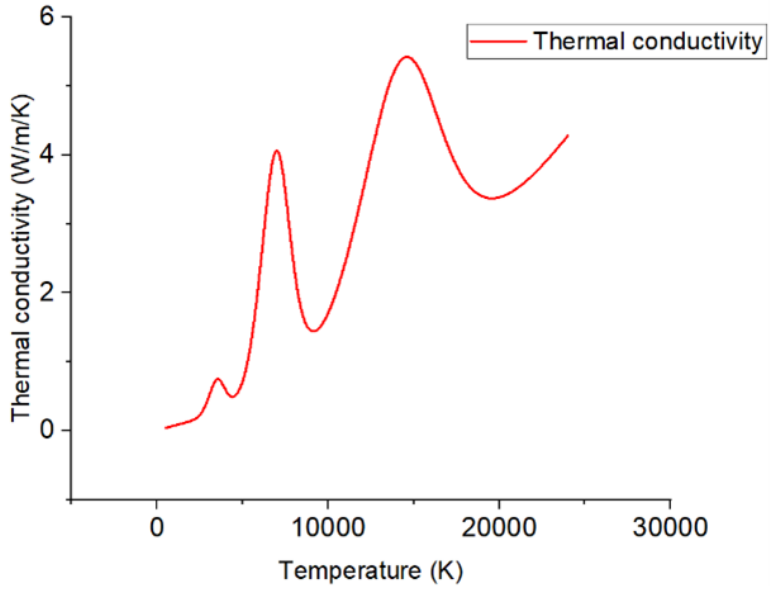

FIGURE 3.21: Air thermal conductivity as a function of temperature [122]

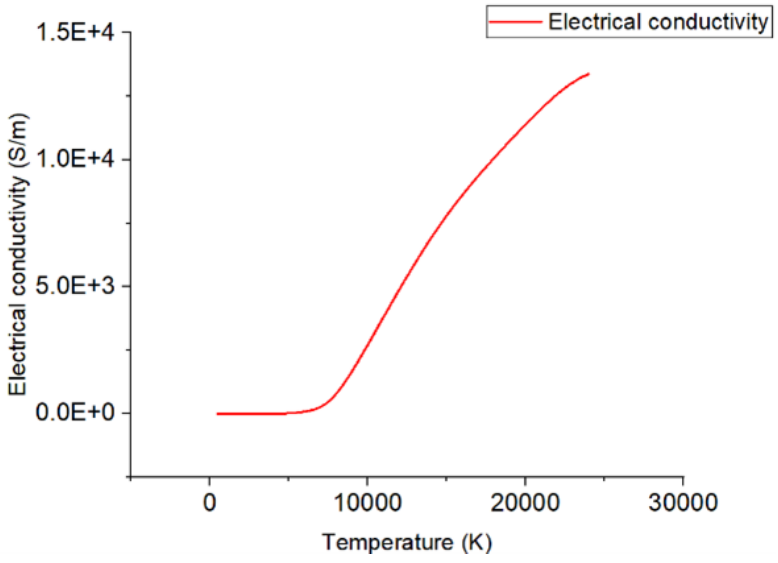

FIGURE 3.22: Air electrical conductivity as a function of temperature [122]

- Thermal conductivity (Figure 3.21) shows multiple peaks between 8000 K and 20,000 K, which coincide with the dissociation of diatomic molecules (such as O_2 and N_2) and the onset of ionisation. These transitions contribute to the overall increase in thermal conductivity and influence the $\nabla \cdot (\lambda \nabla T)$ term in the energy conservation equation, affecting how heat is conducted within the plasma column [123].

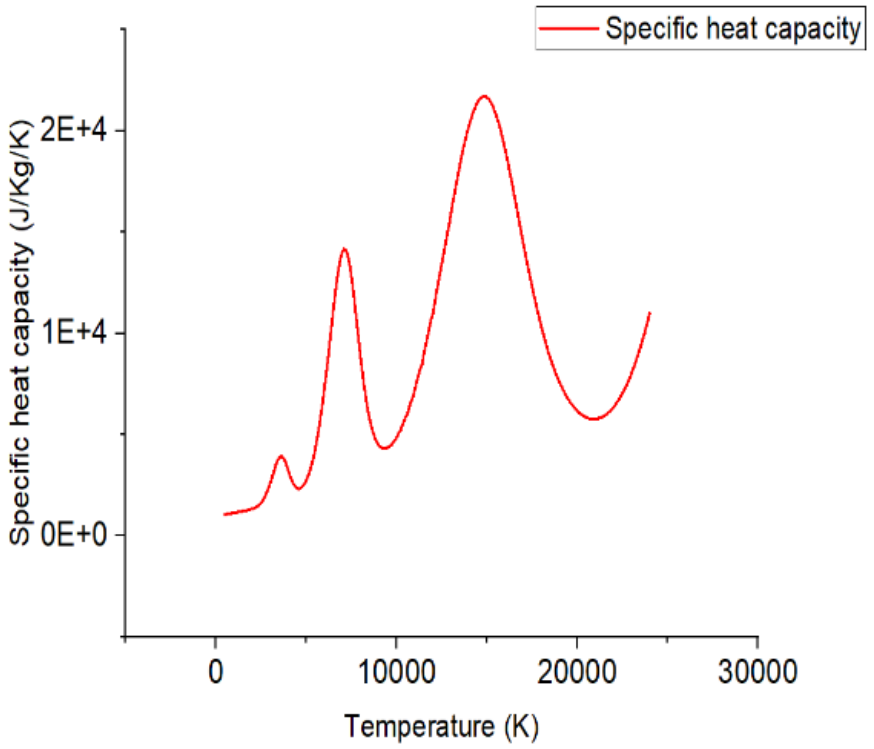

FIGURE 3.23: Air specific heat capacity as a function of temperature [122]

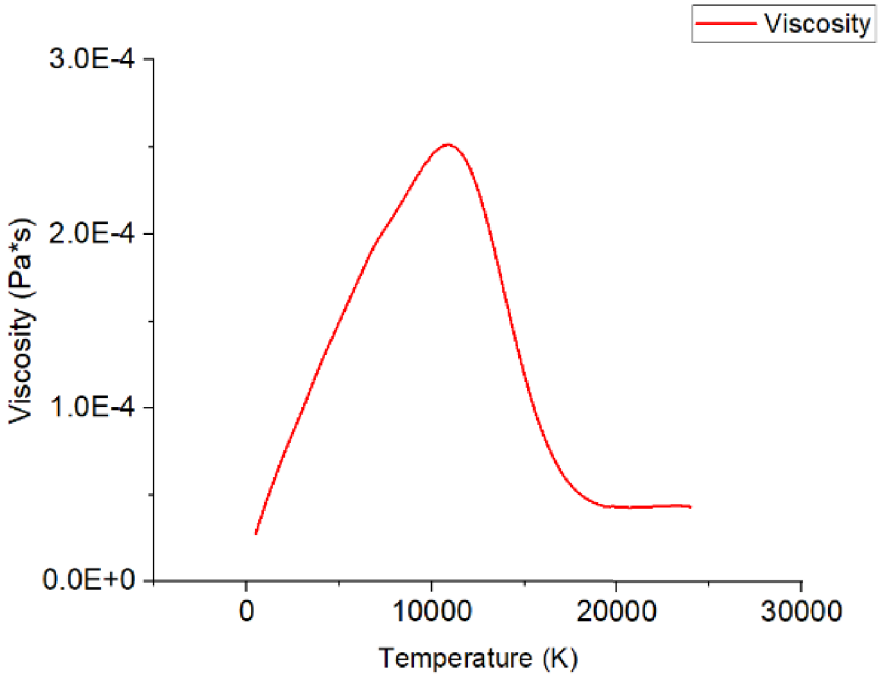

FIGURE 3.24: Air viscosity as a function of temperature [122]

- Electrical conductivity (Figure 3.22) increases sharply around 8000 K, indicating the transition from a weakly ionised gas to a highly conductive plasma. Although high electrical

conductivity reduces local Joule heating density Equation (3.9) for a given current, it facilitates more uniform current distribution across the arc column, which in turn affects the electromagnetic force and overall energy dissipation profile in the model.

- Specific heat capacity (Figure 3.23) exhibits two pronounced peaks, the first around 9000 K due to the dissociation of molecular species such as N_2 and O_2, and the second around 16000 K associated with the ionisation of atomic species like N and O [122].The presence of these peaks ensures that significant energy input does not immediately raise temperature, which is critical for accurately capturing delayed thermal responses in arc formation.
- Viscosity (Figure 3.24) initially increases with temperature, peaking near 10,000 K, and then gradually decreases. This trend reflects the competition between molecular agitation and free electron effects. Viscosity governs internal momentum diffusion ($\nabla \cdot \hat{\pi}$), influencing arc jet stability and arc root attachment [122]. High viscosity in mid-temperature regimes increases damping, reducing flow instabilities, which is particularly important near the cathode spot region.

In summary, the strong temperature dependence of these properties defines the arc's thermal-electrical behaviour. Accurately modelling such non-linearities is critical for simulating realistic arc initiation, movement, and extinction processes. Therefore, these temperature-dependent profiles are incorporated into the arc simulation to ensure fidelity in predicting heat flow, plasma conductivity, and viscous dissipation across different phases of arc evolution.

3.3.3 Arc Root Modelling

Although the majority of the arc plasma is dense and exhibits high temperature, ensuring thermal equilibrium within the bulk, deviations occur near the electrodes and at the arc's edges. These near-electrode regions—critical for current and energy exchange between plasma and electrodes—are collectively referred to as plasma–electrode interactions. These zones typically deviate from LTE, and are thus subdivided into near-anode and near-cathode regions, each exhibiting unique behaviours [96]. A physically consistent treatment of these zones is essential to connect the LTE arc column with the boundaries. The following subsections describe both plasma–anode and plasma–cathode interactions and their simplified implementations in this work.

Plasma–Anode Interaction

In this work, the LTE arc column is matched to the metal anode via a non-equilibrium Boundary Layer (BL), which includes sublayers such as the ionisation layer, thermal non-equilibrium region, and the space-charge sheath (Figure 3.25), ensures energy and current transfer between the anode and LTE arc column. Within the boundary layer, conservation of energy can be described by [95]:

$$\nabla \cdot \left(\frac{5k_B T_h}{2} \mathbf{J}_a + \frac{5k_B T_h}{2} \mathbf{J}_i + \left(\frac{5k_B T_e}{2} + A_i \right) \mathbf{J}_e + \mathbf{q}_e + \mathbf{q}_h \right) = \mathbf{j} \cdot \mathbf{E} - w_{\text{rad}} \tag{3.19}$$

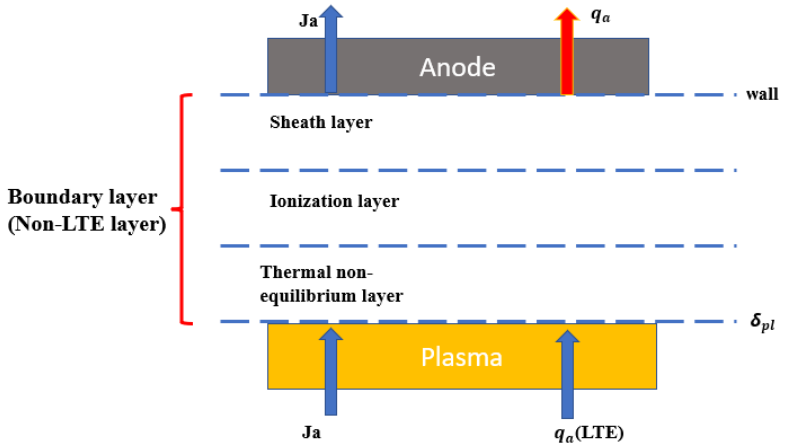

FIGURE 3.25: Schematic representation of the plasma–anode interface

Here, $\mathbf{J}_a$, $\mathbf{J}_i$, and $\mathbf{J}_e$ are the fluxes of atoms, ions, and electrons; T_h and T_e denote the temperatures of heavy particles and electrons; and A_i is the ionisation energy. $\mathbf{q}_e$ and $\mathbf{q}_h$ represent energy flux due to electron and heavy-particle thermal conduction. The loss term w_{rad} accounts for radiation. The heat fluxes carried by electrons and heavy particles, $\mathbf{q}_e$ and $\mathbf{q}_h$, respectively, can be written as [95]:

$$\mathbf{q}_e = -\kappa_e \nabla T_e + k_B T_e N_e \left[A_i^{(e)} (\mathbf{v}_e - \mathbf{v}_i) + A_a^{(e)} (\mathbf{v}_e - \mathbf{v}_a) \right], \tag{3.20}$$

$$\mathbf{q}_h = -\kappa_{\text{hp}} \nabla T_h + k_B T_h \left[n_i A_i^{(h)} (\mathbf{v}_i - \mathbf{v}_a) + n_a A_a^{(h)} (\mathbf{v}_a - \mathbf{v}_i) \right]. \tag{3.21}$$

The second terms in both expressions represent energy transfer due to the relative drift between species, which are typically negligible compared to the conductive terms when diffusion velocities are small in weakly ionized plasmas or when species temperatures are similar. Therefore, only the thermal conduction terms are retained in later equations.

Using the current continuity equation:

$$\nabla \cdot (\mathbf{J}_i - \mathbf{J}_e) = 0, \tag{3.22}$$

we multiply by $(A_i - A_f)$, where A_f is the anode work function, to derive a composite conservation law:

$$\nabla \cdot \left[(A_i - A_f)\mathbf{J}_i + \left(\frac{5k_B T_e}{2} + A_f \right) \mathbf{J}_e + \mathbf{q}_e + \mathbf{q}_h \right] = \mathbf{j} \cdot \mathbf{E} - w_{\text{rad}} \tag{3.23}$$

The above Equation (3.23) is the energy conservation of all the species in the whole electrode layer. Taking into account the geometry of Figure 3.25, the energy flux from the plasma to the anode surface could be expressed as

$$q_a = -\left[\left(\frac{5k_B T_e}{2} + A_f \right) J_e + q_e + (A_i - A_f) J_i + q_h \right]_w \tag{3.24}$$

Since $J_e \gg J_i$, the ion term is often neglected. Assuming constant $\mathbf{j}$ across the boundary layer and 1D transport, we simplify further:

$$\frac{d}{dz}\left[\left(\frac{5k_BT_e}{2}+A_f\right)\frac{j}{e}-q_e-q_h\right]=jE_z-w_{\text{rad}} \tag{3.25}$$

Integrating across the boundary yields the net heat flux to the anode:

$$q_a=\left[\left(\frac{5k_BT_e}{2}+A_f\right)\frac{j}{e}-q_e-q_n\right]_w \tag{3.26}$$

where the values of all the variables should be taken on the anode surface w. Among them, the electron contributions q_e is neglected at the boundary due to weak temperature gradients and the relatively small electron current density. This expression captures the main convective and conductive mechanisms governing energy transfer to the anode in the non-equilibrium layer. Additionally, the radiative energy loss w_{rad} is often omitted from the anode energy balance, as the boundary layer is typically thin and the residence time of hot particles is short, resulting in minimal net radiation within this region.

Plasma–Cathode Interaction

The boundary conditions for plasma–electrode interactions depend significantly on the choice of bulk plasma model [124]. In a Non-Local Thermodynamic Equilibrium (NLTE) model—where deviations from ionisation equilibrium and different temperatures between electrons and heavy particles are considered—accurate representation of the near-electrode sheath is required. This approach offers greater physical fidelity but requires considerable computational resources [125]. Conversely, the 2T model acknowledges thermal non-equilibrium but assumes ionisation equilibrium and quasi-neutrality, thus requiring boundary conditions that account for both the ionisation layer and the space-charge sheath [96].

In this work, we aim to establish simplified boundary conditions to couple the LTE arc column to the cathode, consistent with previous non-equilibrium arc root models [93, 125]. A schematic of the near-cathode interaction region is shown in Figure 3.26.

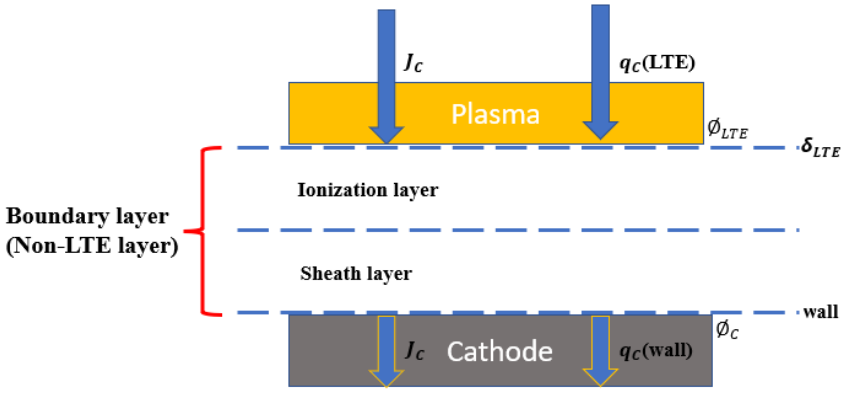

FIGURE 3.26: Schematic representation of the plasma–cathode interface

The simplified implementation omits explicit modelling of the non-equilibrium layers and instead applies boundary conditions that ensure continuity of electrostatic potential and energy across the plasma–electrode interface. The electrostatic potential exhibits a finite drop near the interface, which is expressed as:

$$V_s - V_{\mathrm{LTE}} = U_c \tag{3.27}$$

Here, V_s and V_{LTE} denote the electric potential on the cathode and the LTE plasma sides of the interface, respectively. U_c is the voltage drop across the cathode sheath, which may vary along the surface.

The corresponding energy balance at the cathode interface is given by:

$$q_{\mathrm{nl,w}} - q_{\mathrm{LTE,w}} = \mathbf{J}_c U_c - \frac{\mathbf{J}_c A_f}{e} \tag{3.28}$$

where $q_{\mathrm{LTE,w}}$ and $q_{\mathrm{nl,w}}$ are the energy fluxes from the LTE plasma and from the sheath to the cathode, respectively. $\mathbf{J}_c$ is the current density at the electrode surface, and A_f is the work function of the cathode material. The right-hand side terms represent the electric power supplied to the sheath and the energy needed to extract electrons from the cathode surface.

The overall energy exchange mechanism is summarised in Figure 3.27, which illustrates how the energy stored in the boundary layer is split—part is returned to the plasma, while the remainder is transferred to the cathode.

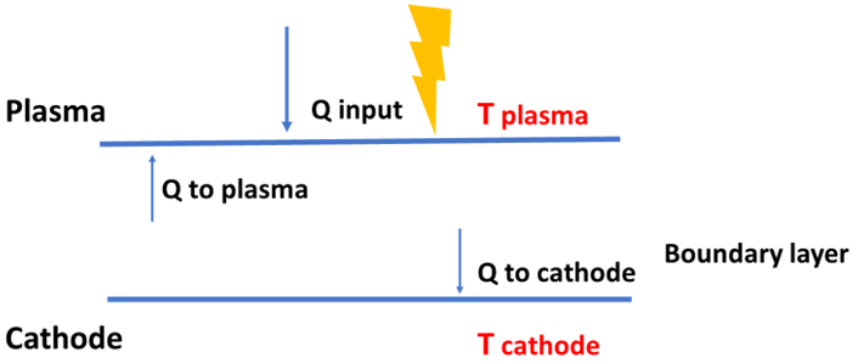

FIGURE 3.27: Schematic representation of energy balance in the boundary layer

The energy loss from the sheath to the plasma is expressed as:

$$q_{\text{to plasma}} = \left(\frac{\mathbf{J}_c}{e}\right)\left(\frac{5}{2}k_B T_e + \xi k_B T_e\right) \tag{3.29}$$

Here, $\xi = 0.7$ is a theoretical coefficient for fully ionized plasma representing the contribution of thermal diffusion [106].

The energy flux transferred to the cathode surface is given by:

$$q_{\text{to cathode}} = \mathbf{J}_c(U_c - A_f) - \left(\frac{\mathbf{J}_c}{e}\right)(3.2 k_B T_e) \tag{3.30}$$

In the later stages of the simulation, boundary heat transfer to the cathode is implemented using Equation (3.30).

3.3.4 Assumptions and Justifications

To facilitate arc simulation in DC circuit breakers, several simplifications and physical assumptions are introduced:

- **LTE**
  At 1 atm, the arc column is often treated as a quasi-neutral, thermally equilibrated plasma composed of high-temperature electrons, ions, atoms, and molecules which is referred to as the Local Thermodynamic Equilibrium (LTE) condition. The validity of LTE is typically evaluated using the electron density criterion derived by [126], expressed as:

$$n_e \geq 10^{14} \cdot T_e^{1/2} \cdot (E_k - E_i)^3 \, [\mathrm{cm}^{-3}] \tag{3.31}$$

  where T_e is the electron temperature in eV, and $E_k - E_i$ is the energy gap (e.g., between ground and first excited states). For example, in argon plasma with $E_2 - E_1 = 11.5\,\mathrm{eV}$ and $T_e = 1\,\mathrm{eV}$, the required electron density would be $n_e \geq 10^{17}\,\mathrm{cm}^{-3}$. Similar thresholds have been confirmed by [127].

- **Arc Ignition Initialization**
  Since modeling the melted bridge ignition process between contacts is complex, this step is omitted. Instead, the arc is initialized as a high-temperature column using a Gaussian distribution to mimic initial arc formation, following the practice in MCCB studies with 2 mm contact gap [128].

- **Laminar Flow Assumption**
  The nature of gas flow is evaluated using the Reynolds number:

$$Re = \frac{\rho u D}{\mu} = \frac{u D}{\nu} \tag{3.32}$$

  where ρ is the gas density ($\mathrm{kg/m^3}$), u is the characteristic flow velocity ($\mathrm{m/s}$), D is the characteristic length or hydraulic diameter (m), μ is the dynamic viscosity ($\mathrm{kg/(m\,s)}$), and ν is the kinematic viscosity defined by $\nu = \mu/\rho$ ($\mathrm{m^2/s}$). The Reynolds number Re is dimensionless.

  Flow is considered laminar when $Re < 2000$. In this model, simulation results consistently show $Re < 100$, validating the laminar flow assumption. This aligns with earlier arc modelling literature [129–131].

- **High Mach Number Flow (HMNF)**
  Arc-induced heating causes rapid gas expansion and high-speed flow, requiring compressible flow treatment. The HMNF model (comsol Library) accounts for coupled conservation of mass, momentum, and energy—essential in resolving transient plasma dynamics under arc conditions [132].

- **Radiation Loss via NEC**
  Air plasma emits significant radiation, and the Net Emission Coefficient (NEC) method offers a practical way to estimate radiative losses without solving the full radiative transfer equation. The radiative heat loss is estimated as:

$$Q_{\text{rad}} = 4\pi \cdot NEC \tag{3.33}$$

  where NEC $W/m^3 sr$ accounts for wavelength-integrated emission assuming an optically thin plasma. In this work, COMSOL's default radiation data is scaled by 10 times to reflect a plasma radius $R_p = 1\,\text{mm}$, consistent with experimental comparisons from [133], as shown in Figure 3.28.

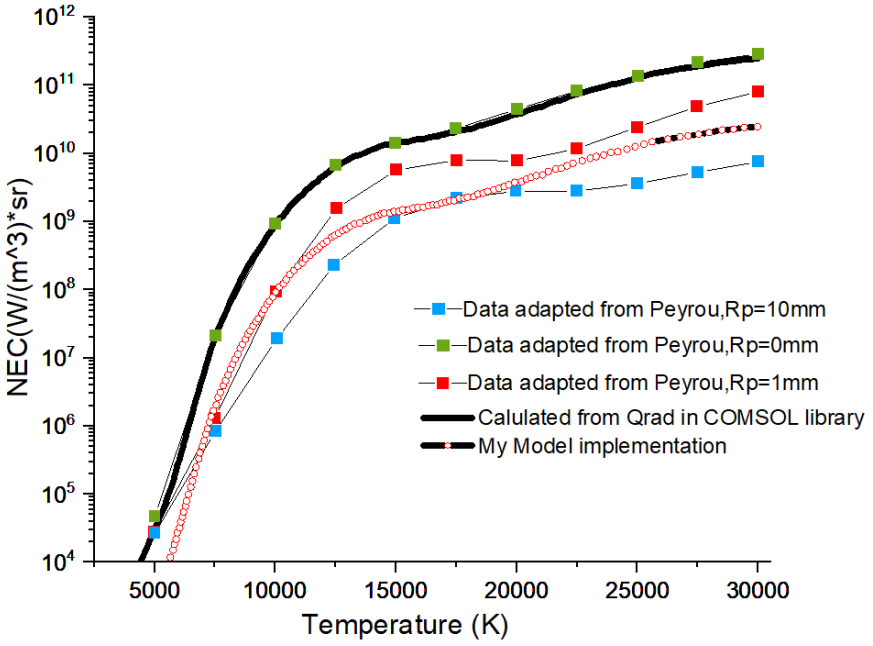

FIGURE 3.28: NEC data verification and implementation for air at 1 atm [133]

Note that the NEC method best approximates radiation losses in the arc core but does not account for reabsorption in cooler boundary regions, thus providing an upper-bound estimate.

3.3.5 Research Gap 3: Insufficient Predictive Models for Breakdown Voltage in Compact DC Air Gaps

This section establishes a comprehensive theoretical and numerical foundation for understanding electric arc phenomena in air circuit breakers. It begins with a description of arc structure, distinguishing between the arc column and arc root regions. The arc's voltage–current characteristic demonstrates a negative differential resistance, a typical signature of plasma behaviour. Arc initiation mechanisms are reviewed, including both high-voltage breakdown and the mechanical separation of contacts. The arc's sustainment is attributed to thermal ionisation and electric field ionisation, both of which are essential for plasma maintenance and arc re-ignition.

The breakdown process is modelled using classical mechanisms such as the Townsend avalanche and the Meek criterion. These are used to describe the progression from initial electron multiplication to streamer formation and gap heating, leading to a fully developed arc.

On the numerical side, this section introduces the major assumptions adopted in arc simulation, including LTE, laminar flow, and high Mach number compressible fluid behaviour. Governing equations for mass, momentum, energy, and electromagnetic fields are presented. The treatment of radiation loss via the NEC method is also discussed and compared the model implemented data with referenced literature review. Electrode boundary conditions will be implemented using physically justified semi-analytical models for both the cathode and anode, providing interface constraints for charge and energy continuity.

Despite the historical success of Paschen's law and the Critical Field Theory in predicting breakdown voltages in uniform temperature and constant gap, these models fall short when applied to compact DC circuit breakers where the contact gap evolves dynamically during opening and the air temperature exhibits non-uniformed. This gap becomes particularly critical in the sub-centimeter regime (0.1–0.5 cm), where rapid contact separation and localized heating due to residual arc energy result in a transient, dense plasma. Under such conditions, neither Paschen's law nor the Critical Field Theory provides reliable predictions, as they fail to capture the breakdown voltage variation arising from the nonlinear dependence of ionisation and electron mobility on temperature and field strength. The mechanisms governing this transition, including the interplay between local N_e, temperature gradients, and ionisation potential, remain poorly understood.

Moreover, there is a lack of predictive frameworks capable of incorporating multi-zone temperature coupling or describing the evolving breakdown path as the air gap cools non-uniformly. This limits our ability to design reliable DCCB, especially those operating at sub-millimetre scales (compact size). Therefore, a gap exists in developing a physically interpretable, temperature-dependent breakdown model that accounts for thermal non-equilibrium and variable electrode separation during DC interruption.

Chapter 4

Validation of Arc Simulation Framework

This chapter validates the arc simulation framework introduced in Chapter 3 through its application to two representative cases: welding arcs and switching arcs. These scenarios were selected due to their shared physical foundation, a conductive plasma channel formed by gas ionization under electrical excitation, governed by Magnetohydrodynamics (MHD), conservation laws, and radiation-based heat transfer [93, 134].

The welding arc case is first used to verify the accuracy of the core physical model, while the switching arc is employed to assess its applicability to circuit breaker conditions involving short interruption durations, typically on the order of microseconds [7]. The validation strategy aims to address the following key questions: The validation strategy aims to address the following key questions:

1. Whether the electrode–plasma coupling implementation accurately captures the essential physics, including energy and mass transfer at the boundaries, Local Thermodynamic Equilibrium (LTE) core behaviour governed by Joule heating and radiation transport, and deviations from Non-Local Thermodynamic Equilibrium (NLTE) or two-temperature descriptions in the near-electrode regions.

2. What constitute reasonable and physically consistent initial conditions for simulating arcing phenomena, and how long the model requires to settle (i.e., for the arc to evolve from artificial initial conditions to physically realistic profiles).

3. What mesh resolution is most suitable to ensure both computational efficiency and sufficient accuracy of the model.

4.1 Welding Arc Simulation: Benchmark Validation

The study begins with validating the rod-plane geometry, chosen primarily due to its large inter-electrode gap (10 mm) and strongly non-uniform electric field. These features induce high convective velocities, making it easy to implement while providing an effective benchmark for stressing thermal arc models. The computational domain (Figure 4.1) represents a direct current (DC) argon discharge at atmospheric pressure. Argon is used to enable direct comparison with existing experimental and numerical studies [93, 117, 125, 135], as its thermophysical properties are well established and it is commonly employed in welding applications. The material data are adopted from [117, 136].

4.1.1 Computational Domain and Boundary Condition

The computational geometry used in the simulation is consistent with the experimental configuration described in [117, 137] and the setup outlined in [93], as illustrated in Figure 4.1. The cathode consists of a tungsten rod, 12 mm in length, with a hemispherical tip of 1mm radius. The anode is a flat copper plate measuring 30 mm in width and 4 mm in height. The gap between two electrodes is set to 10 mm.

The computational domain, labeled ACDEH, is filled with argon. To improve numerical resolution in the arc region, a virtual semi-circle boundary is introduced between points A and H. This local mesh refinement enhances the accuracy of the simulated thermal and flow characteristics in the inter-electrode gap, which are critical for the analysis of arc dynamics.

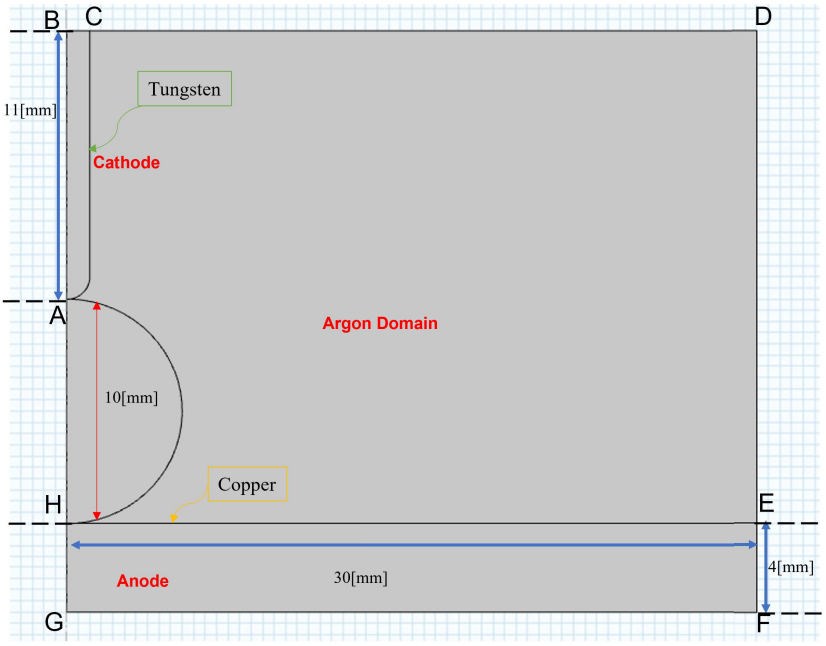

FIGURE 4.1: Details of the computational domain of rod-plane geometry

Boundary Conditions

TABLE 4.1: Summary of boundary conditions for the welding arc simulation

Category	Boundary	Condition
Thermal	BC, CD, DE, EF, FG, GH, HA, AB Electrode-plasma interfaces (AC,HE)	Fixed temperature at 300 K [93, 106, 108] Convective heat flux with heat transfer coefficient $500\,\mathrm{W}/(\mathrm{m}^2\cdot\mathrm{K})$ [93, 124]
Fluid Flow	AC, CD, EH DE	No-slip wall Outlet with constant pressure (1 atm) [93]
Electrical	BC EF, GF BD, DF, FG, GB	Electric current injection Grounded terminals [93] Zero normal current density (electrical insulation)

Here, the "no-slip wall" is a standard fluid dynamics boundary condition meaning that the fluid velocity at that boundary is zero (i.e., the fluid "sticks" to the wall).

The boundary conditions listed in Table 4.1 are adopted based on prior simulation and experimental studies [93, 117], ensuring consistency with established modeling practices. These settings are widely used in thermal arc simulations to provide reliable thermal, electrical, and fluid flow behavior between arc and electrodes. The models presented in this section are based on a stationary study formulation.

The material properties for copper and tungsten, including electrical conductivity, are sourced from the built-in material library in COMSOL Multiphysics [138]. The boundaries BC and GF are where the current is injected, and the solution within the electrode domains is computed based on their defined conductivity.

4.1.2 Calculation Results and Discussion

In this section, the primary focus is on validating the temperature distribution of the welding arc to assess the reliability of LTE framework. This is a key step in confirming the physical consistency of the simulation model. In addition, the gas flow characteristics under large-gap conditions are examined to provide a reference baseline for subsequent analysis of switching arcs, which operate under more compact geometries.

Temperature

The system of equations, along with the boundary conditions and matching expressions at the cathode and anode interfaces in last chapter, is solved numerically under steady-state conditions for a wide range of current values. Representative results are shown in Figure 4.2. The temperature distribution within the arc column exhibits a typical bell-shaped profile, consistent with previous studies [93, 117, 139], with the peak temperature located near the cathode tip and gradually decreasing along the arc axis toward the anode. This indicates strong energy concentration

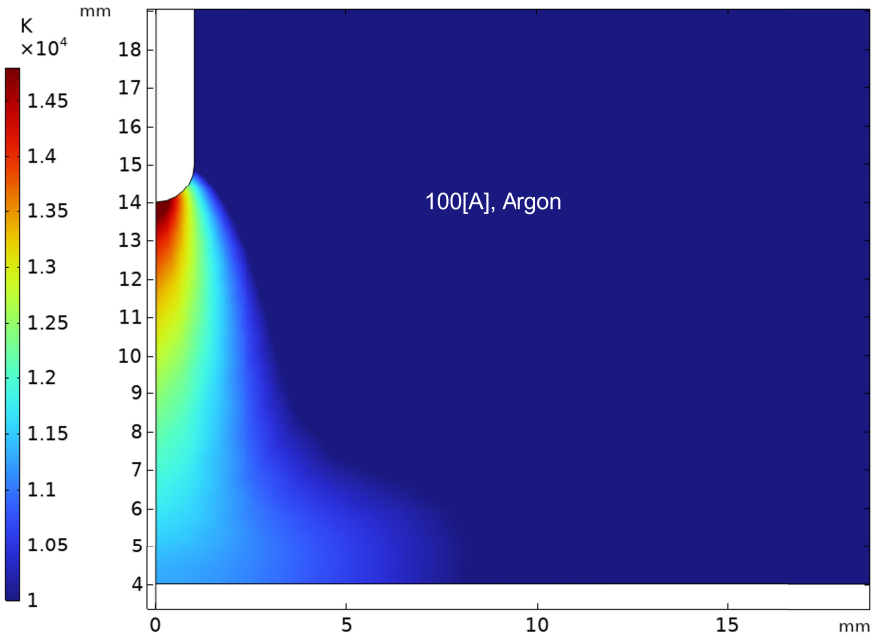

(A) I=100A

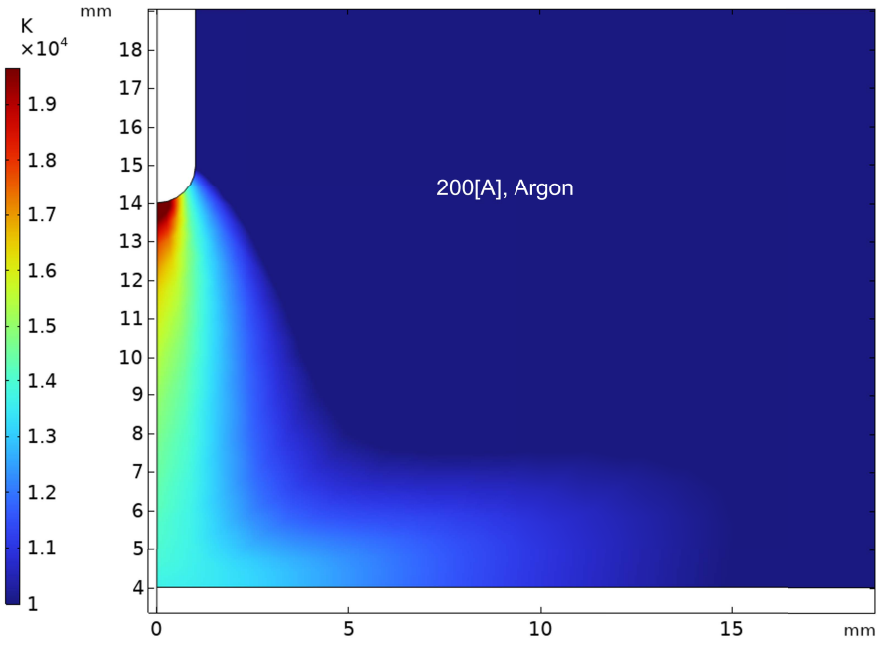

(B) I=200A

FIGURE 4.2: Temperature distributions in LTE arc; 1atm argon, tungsten cathode (rod), copper anode (plane), for stationary arc;Color legend represents the Temperature in K; the y-axis refer to the gap length in *mm*

near the cathode and progressive thermal diffusion downstream. At 100 A, the peak temperature reaches approximately 15,000 K as shown in Figure 4.2a, while at 200 A, it increases to about 20,000 K (in Figure 4.2b).This temperature rise is primarily attributed to increased Joule heating, as power dissipation scales quadratically with current ($P = I^2R$). Additionally, higher temperatures enhance electrical conductivity through thermal ionization. As temperature

increases, more particles gain sufficient energy to ionize, resulting in an exponential rise in conductivity, approximately following $\sigma \propto e^{-A_i/k_B T}$, where A_i is the ionization energy and k_B is the Boltzmann constant.

The computed axial temperature profiles are further compared with results from two-temperature (2T) [135] and NLTE models [125], as shown in Figure 4.3 for 100 A and for 200 A. A detailed view near the cathode is presented in Figure 4.4. The agreement is generally good in the arc core region for both current levels. However, noticeable discrepancies appear near the electrodes, particularly between the computed LTE temperature and the heavy-particle temperature T_h predicted by non- LTE models.This deviation is a key feature of the proposed approach: the rapid decrease in T_h near the electrode surfaces is not resolved by solving bulk LTE equations alone, but rather captured through physically informed boundary conditions at the plasma-electrode interfaces. Compared with conventional LTE models [140], which often neglect near-electrode layers or impose artificial cut-offs, the current approach better represents the thermal behavior at the boundaries without introducing mesh-dependent artifacts or cut-off distances. This not only improves physical accuracy, but also ensures numerical stability and adaptability in simulating the near-electrode regions.

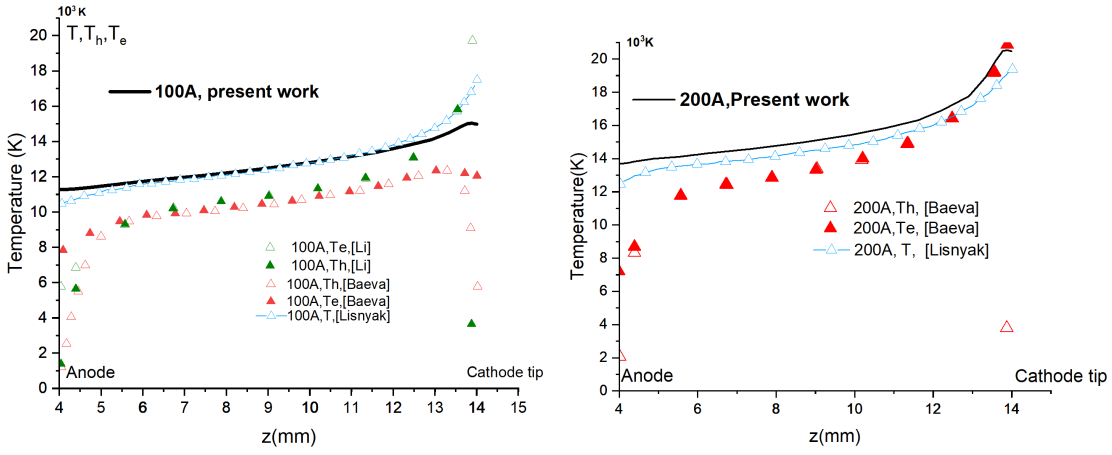

(A) 100 A (B) 200 A

FIGURE 4.3: Comparison of axial temperature distributions at 100A and 200A from different sources. Experimental data are represented by triangles [125, 135]. Simulation results from [93] are shown as blue lines with triangular markers. The results from the present model are represented by solid black lines.

Gas behaviour

Compared to the temperature field, gas flow behaviour within the arc has been less extensively investigated. Although experimental approaches—such as Doppler-shifted plasma scattering [141]—have successfully quantified axial flow velocities in high-current arcs, such measurements are challenging due to their complexity and precision requirements. The method infers macroscopic gas velocity from frequency shifts in scattered light along a predefined optical path, typically resolving only the axial component, and thus cannot capture the full spatial distribution of velocity within the arc column. This limitation constrains the direct validation of

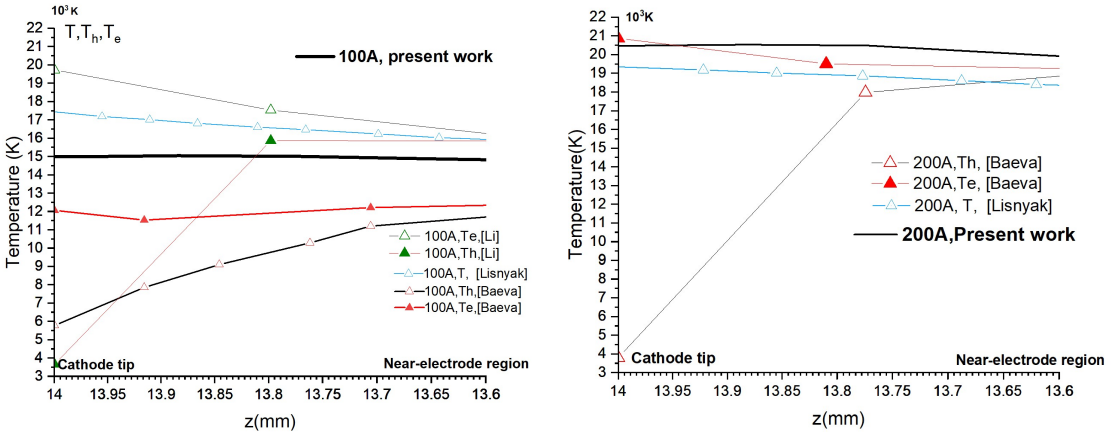

(A) Near electrode region temperature distribution at 100 A

(B) Near electrode region temperature distribution at 200 A

FIGURE 4.4: Comparison of arc temperature distributions under different current levels for near-electrode region (around 0.4mm).experimental data from [125, 135], simulation results from [93], and current simulation from the present model

detailed numerical flow fields, making modelling a valuable complementary tool. Previous numerical studies of welding arcs [93] report that the gas accelerates along the cathode surface, reaches its peak velocity within the arc core a few millimetres downstream of the cathode tip, and then decelerates toward the anode, with typical magnitudes in the range of 80–220 m/s. The present simulations reproduce these key features as shown in Figure 4.5: gas acceleration along the cathode surface (Space 1), a peak velocity of approximately 200 m/s in the central arc gap, gradual deceleration along the axis (Space 2), and near-zero velocity at the anode due to the no-slip condition (Space 3). The predicted peak velocities and their axial positions agree closely with the reference results, and the overall acceleration–deceleration pattern is preserved. These agreements confirm that the current numerical method reliably captures the dominant gas flow characteristics in welding arcs.

Axial velocity and temperature profiles along the cutline for the 100 A and 200 A cases as shown in Figure 4.6 that the gas velocity is relatively low in the near-electrode regions, increases rapidly within the arc core, and reaches a maximum at approximately 2 mm downstream of the cathode tip. Beyond this point, the velocity gradually decreases toward the anode, approaching zero at the surface due to the no-slip condition. This behaviour is consistent with previous simulations [93], in which the high-velocity core is driven by strong Joule heating and electromagnetic compression, while viscous dissipation and geometric confinement suppress near-surface acceleration [93]. In narrow-gap configurations, the reduced flow channel height increases near-wall viscous shear and limits the effective action length of both the pressure gradient and Lorentz force. These effects confine the acceleration zone to the arc core, lowering the attainable peak velocity compared with larger-gap designs. Such geometric constraints are particularly critical in compact electrode systems, as they influence arc cooling efficiency and set physical limits on arc-induced flow development. In addition, the present results demonstrate smooth continuity of

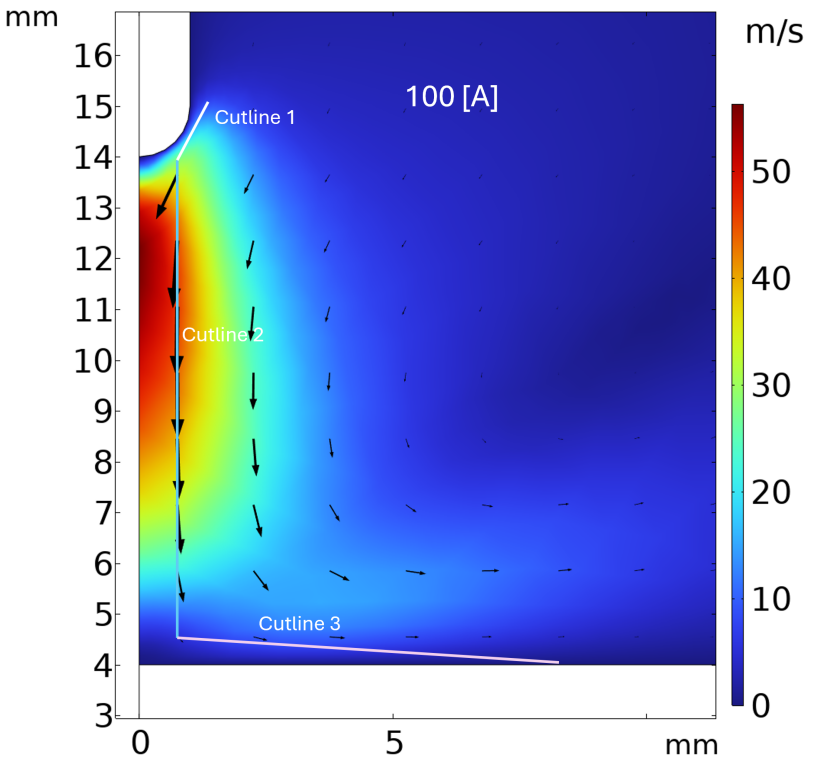

(A) I=100A

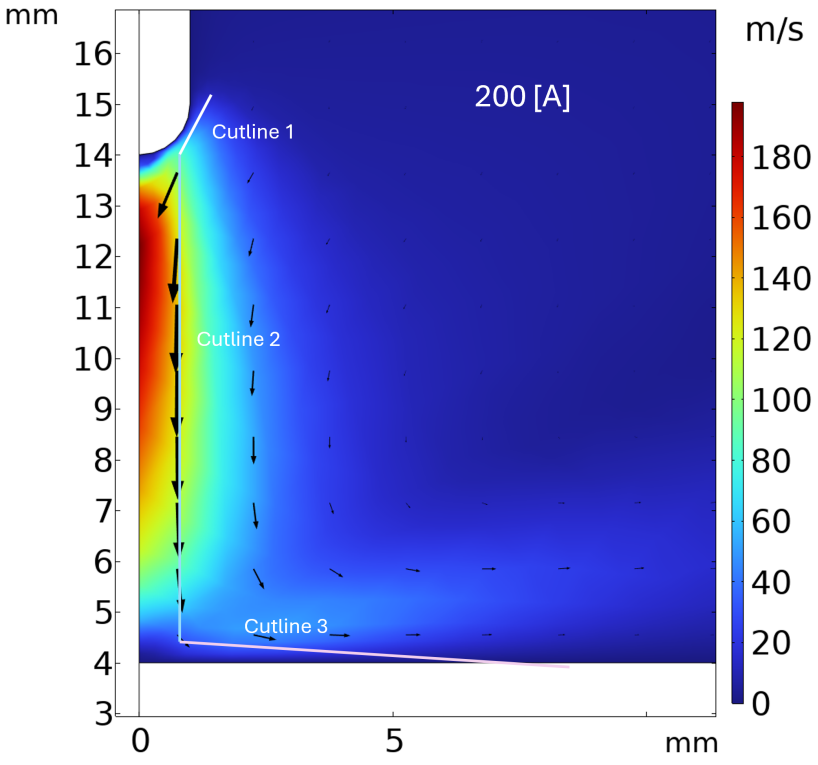

(B) I=200A

FIGURE 4.5: Velocity distributions in LTE arc; 1atm argon, tungsten cathode (rod), copper anode (plane), for stationary arc; Color legend represents the air velocity in m/s; the y-axis refer to the gap length in *mm*

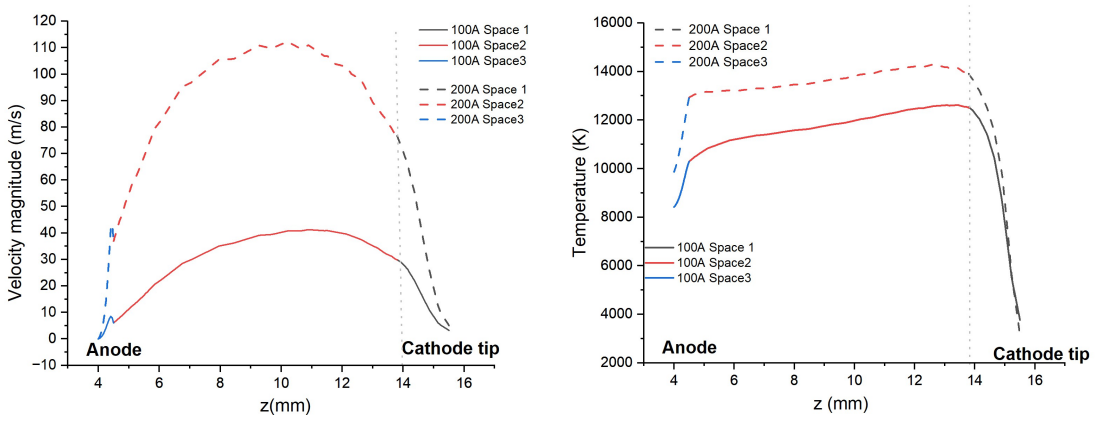

(A) Velocity

(B) Temperature

FIGURE 4.6: Temperature and velocity distribution along the three cutline drawn in Figure 4.5, I=100 A and 200 A

velocity and temperature profiles across the electrode–arc interfaces, indicating that the numerical approach accurately resolves boundary-layer behaviour and enforces consistent coupling between the plasma domain and electrode surfaces.

4.2 Switching Arc Simulation

After validating the simulation methodology using welding arcs, this section focuses on the main research objective — the simulation of switching arcs. The aim is to establish a validated baseline of physical conditions for subsequent studies on arc behaviour during contact separation. Compared to welding arcs, switching arcs are typically formed in compact electrode geometries with short inter-electrode gaps (2-5 mm), resulting in limited space for gas flow development and more intense thermal gradients. These characteristics are representative of arc conditions in compact DC circuit breakers.

In this chapter, the electrodes are assumed to remain fixed, allowing the analysis to focus on the steady-state distributions of temperature and gas flow under constant current. The main aim is to test if the initial condition in my model is reasonable.

4.2.1 Computational Domain and Boundary Condition

The rod-to-rod configuration used in this simulation is based on a symmetric cylindrical geometry, corresponding to the experimental setup described in [9]. As shown in Figure 4.7, the air domain is a cylindrical region with a length of 40 mm and a width of 20 mm. Both the anode and cathode are made of copper, each with a height of 9 mm and a hemispherical tip of 3 mm in radius. The gap between the electrodes is set to 2 mm.

Boundary conditions

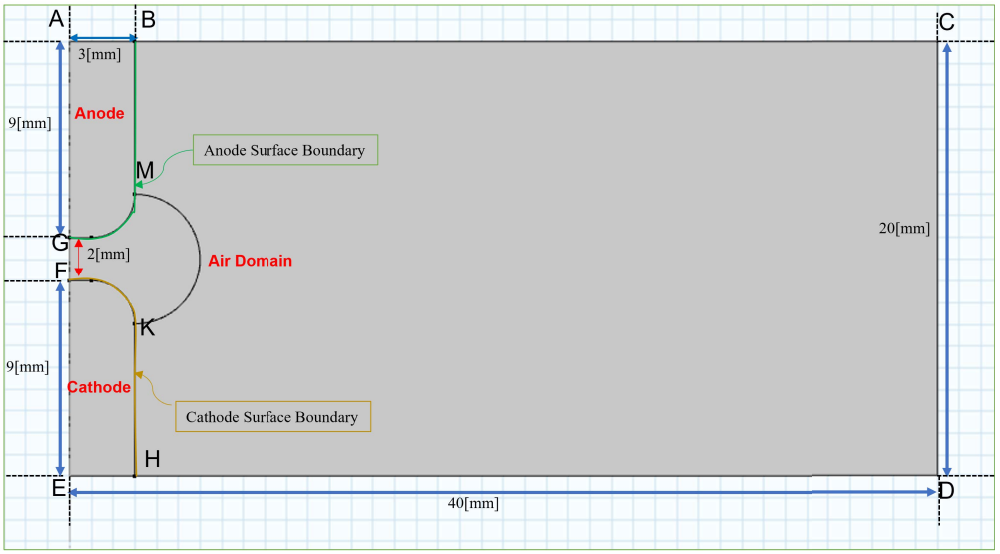

FIGURE 4.7: Details of the computational domain of rod-to-rod geometry

Table 4.2 summarises the boundary conditions used in the switching arc simulation. The convective heat flux q_0 applied along the electrode surface is calculated based on the heavy particle conduction, with a boundary layer thickness of 0.1 mm as suggested in [21, 142, 143]. The corresponding formulation is given in Equations (4.1) and (4.2).

$$q_0 = h_{\text{heavy}} \times (T_{\text{external}} - T_{\text{plasma}}) \tag{4.1}$$

$$h_{\text{heavy}} = -\lambda_{\text{plasma}}(T_a) \times \frac{1}{\Delta d} \tag{4.2}$$

Here, T_a is the average temperature between the plasma and electrodes, Δd represents the thickness of the boundary layer.

TABLE 4.2: Boundary conditions applied in switching arc simulation

Category	**Boundary**	**Condition**
Electrical	AB, EH	AB: applied voltage; EH: grounded (Provides stable reference potential, mitigates leakage currents, and aligns with experimental practices [9])
Thermal	AB, EH BC, CD, DH BG, FH	External temperature set to 300 K External temperature set to 1000 K (Represents thermal boundary layer saturation [142]) Convective heat flux q_0 applied (Convective flux q_0 (Eqs. 4.1-4.2) models heavy-particle conduction across $\Delta d =$ 0.1 mm sheath [143])
Fluid (Flow)	GB, BC, FH, HD CD	No-slip wall boundary condition Pressure outlet set to 1 atm[108, 140]

Initial conditions: The initial velocity field in both radial and axial directions is set to zero $(u_r = 0, u_z = 0)$, and the pressure is uniformly initialized at $p = 1$ atm. The temperature distribution is prescribed using a Gaussian profile:

$$T(r) = (T_{\max} - T_{\text{back}}) \exp\left(-\frac{r^2}{R_a^2}\right) + T_{\text{back}} \tag{4.3}$$

where $T_{\max}$=10,000 K is the maximum initial temperature at the arc axis ($r = 0$), T_{back} =1000 K is the background temperature of the surrounding gas, and R_a=3 mm is the characteristic radius controlling the width of the hot gas column (normally equal to the radius of electrodes). This configuration mimics a pre-heated arc channel embedded in an ambient environment.

4.2.2 Calculation Results and Discussion

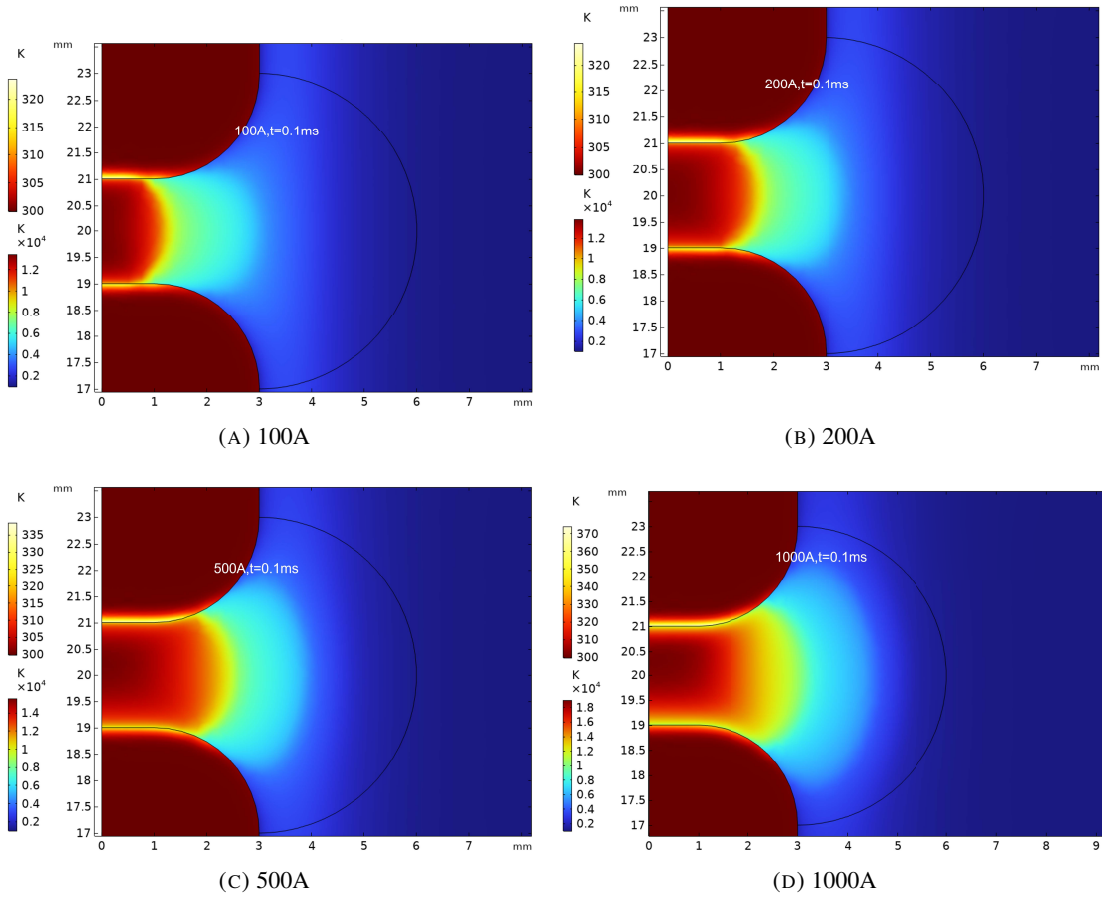

(A) 100A (B) 200A

(C) 500A (D) 1000A

FIGURE 4.8: Temperature distributions in LTE arc under different applied currents (100–1000 A). Simulations conducted with 1 atm air plasma and copper electrodes.

In the symmetric electrode configuration, an intriguing phenomenon is observed when the current increases from 100 A to 1000 A as shown in Figure 4.8: the peak arc temperature rises only modestly from 14,000 K to 18,000 K (an increase of about 28%), whereas the arc channel width nearly doubles (from an initial 1.2 mm to 2.8 mm). This temperature saturation effect stands in stark contrast to the prediction of the classical Joule heating model ($P \propto I^2$), in which

a doubling of current should lead to a pronounced temperature increase. The underlying physical cause lies in a radiation-dominated energy balance: the radiative loss of high-temperature plasma ($Q_{\text{rad}} \propto T^4$) escalates sharply with temperature, effectively limiting further temperature increase under operating currents above 500 A. Meanwhile, electromagnetic expansion driven by the Lorentz force ($\mathbf{F}_{\text{L}} \propto I^2$) becomes the primary driver of size growth, continuously pushing the plasma boundary outward and forcing the arc channel to widen in order to accommodate the increased energy flux.

These characteristics directly challenge the validity of artificially prescribed thermal channels: if the steady-state temperature is insensitive to current variations, could the choice of initial values distort physical realism? To address this question, the time dimension must be examined—specifically, measuring the transition time from the prescribed thermal channel to steady state. If the model, starting from a common initial condition, converges to a unique steady state for a given current within a few millisecond timescale, the thermal channel assumption remains valid for that specific operating condition. Otherwise, the full spark initiation process must be simulated to determine the appropriate initial state.

Validation of the initial conditions

Within this time frame (0-0.1 ms), the arc reaches a stable state, but different applied currents exhibit varying characteristics that warrant further investigation.

Figure 4.9 (left) shows the temperature profiles at selected times during the early phase. As time progresses, the temperature rises and stabilises, with the profile evolving from a relatively flat shape to a more peaked form—indicating progressive heating of the inter-electrode space. In Figure 4.9 (right), the overlap of profiles at later times confirms that the system quickly reaches and maintains a stable thermal distribution.The 500A case (in Figure 4.10) exhibits a similar trend, although the convergence is slightly less complete than at 100A, suggesting that higher currents may introduce more thermal variability and require marginally longer times to stabilise. The temperature distribution shown in both case stabilises within an extremely short time of 0.1 ms, with curves obtained at different time steps (10^{-7} s and 10^{-4} s) overlapping closely for $t \geq 0.1$ ms. This indicates that the hot-channel initial condition rapidly reaches steady state, while the operating timescale of an actual circuit breaker (on the order of milliseconds) is much longer than this convergence time. Therefore, the chosen setup fully captures the key evolutionary stages of the physical process without omitting any thermal conduction characteristics.

These results demonstrate that the preset hot-channel configuration is both physically valid and computationally efficient.The brevity of the transient phase within our simulations indicates its negligible impact on the overall arc behaviour in the context of circuit interruption. They support the approach of using an initial spark with a fixed channel as a viable initial condition for arc simulation models.

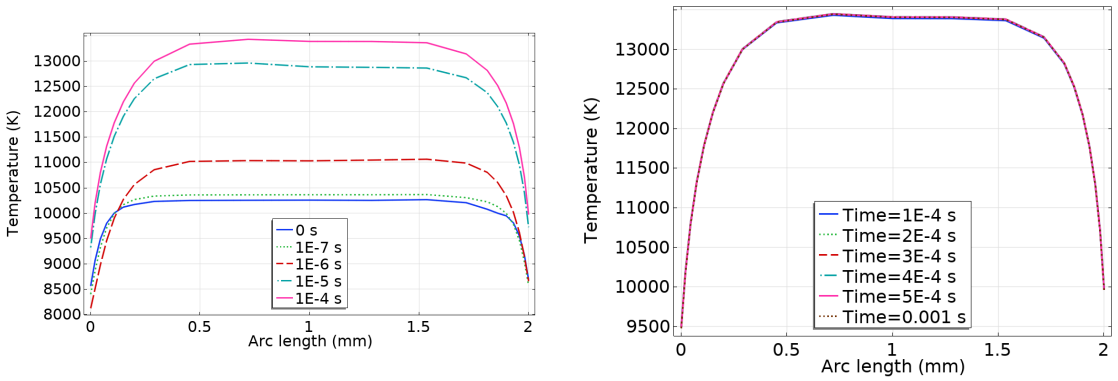

FIGURE 4.9: Temperature distribution between two electrodes when applied current is 100A in small time-step (each 10^{-7}s) and large time-step (each 10^{-4}s)

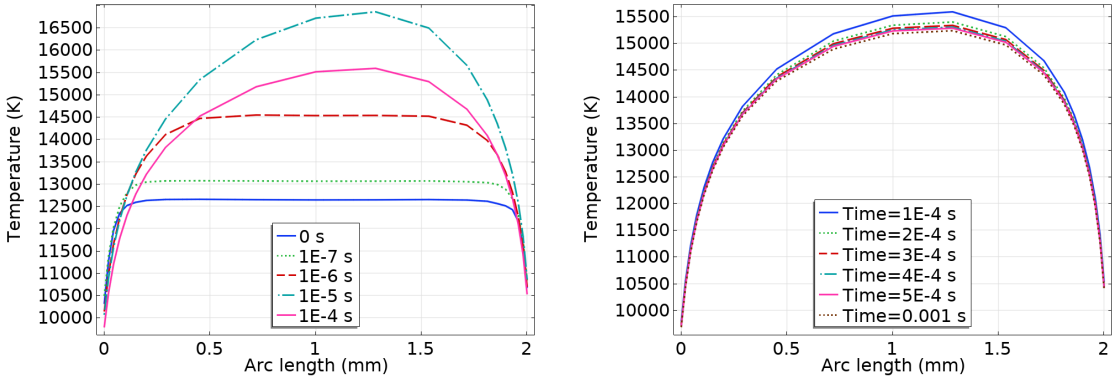

FIGURE 4.10: Temperature distribution between two electrodes when applied current is 500A in small time-step (each 10^{-7}s) and large time-step (each 10^{-4}s)

4.2.3 Mesh Sensitivity Analysis

The final step in preparing the simulation domain was the generation of a suitable numerical mesh. Accurate representation of the arc physics requires resolving steep gradients in temperature, velocity, electric field, particularly near the electrode surfaces where the small dimension but properties changes rapidly. Arc core and near-electrode boundary demand different mesh resolutions due to their distinct characteristic length scales. Hence, three mesh configurations were built as shown in Figure 4.11:

Mesh A (Coarse mesh): Physics-controlled mesh without special boundary layer settings, with a maximum element size of 2.68 mm and a minimum element size of 0.012 mm. Mesh B (Intermediate mesh): Custom refinement near the arc column and electrode surfaces, using a maximum element size of 0.26 mm, a minimum element size of 0.003 mm, and six boundary layer elements with a stretching factor of 1.2. Mesh C (Fine mesh): Further refinement based on Mesh B, with a maximum element size of 0.13 mm, a minimum element size of 0.0015 mm, and twelve boundary layer elements.The stretching factor of 1.2 specifies that the thickness of each successive boundary layer element increases by 20% relative to the preceding one, i.e., $t_n = t_1 \times (1.2)^{n-1}$, ensuring sufficient resolution of steep gradients near the wall while avoiding excessive element counts further from the surface.

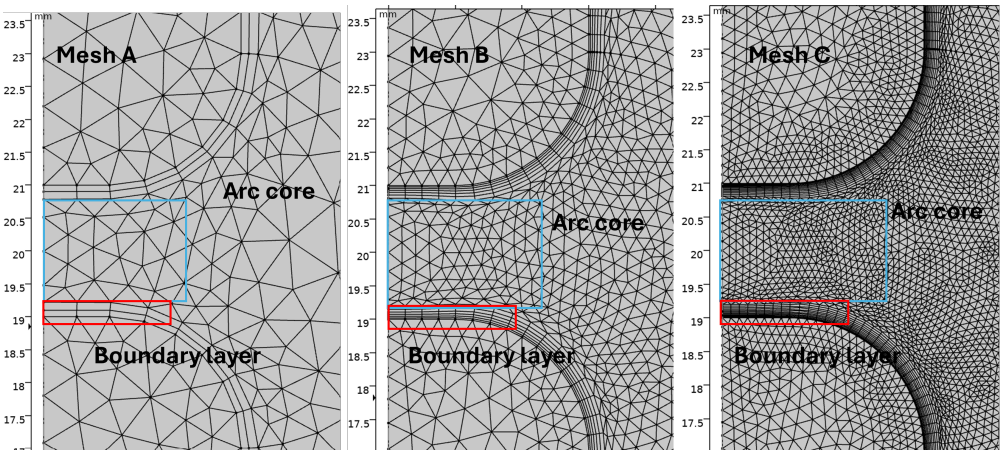

FIGURE 4.11: Comparison of three mesh configurations used in the sensitivity analysis: (a) Mesh A (coarse), (b) Mesh B (intermediate), and (c) Mesh C (fine). The blue boxes highlight the arc core region, while the red boxes indicate the electrode boundary layer.

The evaluation metrics included arc core temperature, boundary layer temperature gradient, and gas flow velocity. Mesh A failed to capture the steep gradients in the boundary layer, while Mesh B and C produced nearly identical results for key parameters such as arc core temperature and flow velocity, with maximum deviations below 5%. The corresponding computational times for Mesh A, B, and C were 17 min, 30 min, and 40 min, respectively. Based on these results, Mesh B was selected as the optimal configuration, offering high accuracy at a reasonable computational cost.

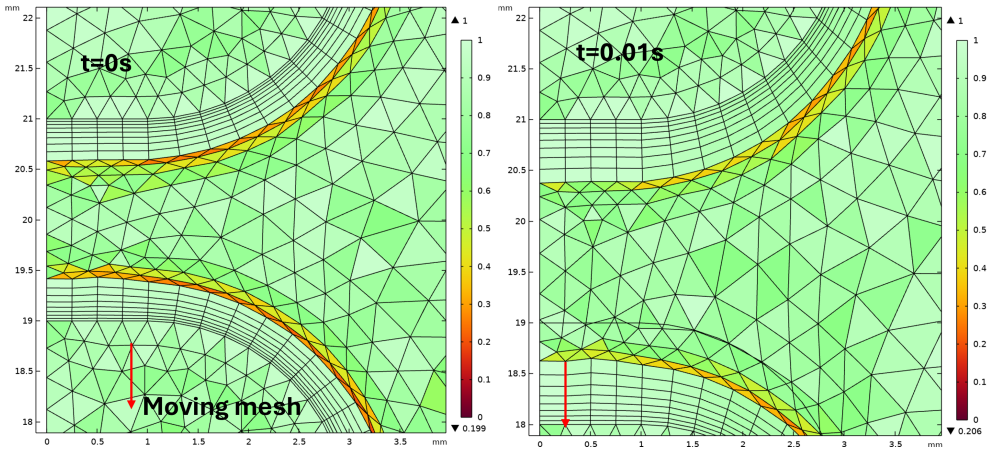

FIGURE 4.12: Mesh deformation during electrode motion from (left) $t = 0\,\mathrm{s}$ to (right) $t = 0.01\,\mathrm{s}$, showing the adaptive movement of elements in the arc core region and minimal distortion in the electrode boundary layer. The colour scale represents the element quality factor, where values close to 1 (green) indicate high-quality elements.

For simulations with moving arcs, building on the optimised static mesh configuration (Mesh B), a moving mesh technique was applied to accommodate electrode motion. During this process, elements in the arc core region undergo noticeable stretching as the contact gap changes, while

the mesh in the electrode boundary layer remains nearly unchanged in size, preserving the resolution of near-wall gradients. The mesh distortion rate was evaluated using the Jacobian determinant. More than 95% of the elements maintained a Jacobian determinant greater than 0.3, indicating acceptable element quality. In addition, 85% of the elements had a quality factor exceeding 0.8, confirming that most elements were close to the ideal value of 1, as indicated by the colour scale in Figure 4.12.

4.3 Summary

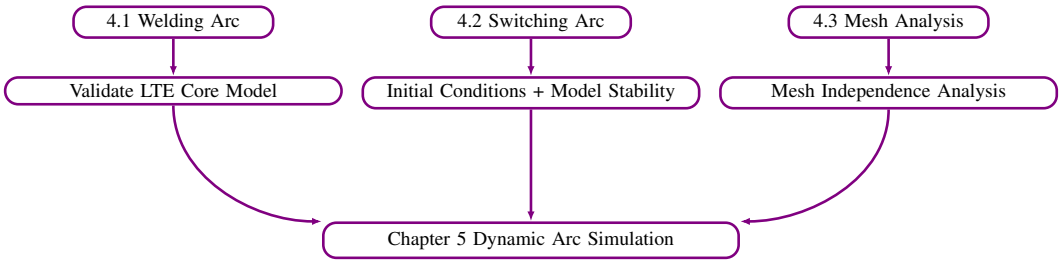

FIGURE 4.13: Summary of the links between Chapter 4 sections and their contribution to the dynamic arc simulation framework in Chapter 5.

Figure 4.13 summarises the logical structure of this chapter and its connection to the dynamic arc simulation framework developed in Chapter 5. Section 4.1 validates the LTE core model using a welding arc case, Section 4.2 examines the applicability of initial conditions and the stability of the model under switching arc conditions, and Section 4.3 presents the mesh independence analysis. Together, these components form the methodological foundation for the dynamic arc simulations in the next chapter. In specific, for the welding arc case (10 mm large gap), the model successfully reproduces the temperature field (bell-shaped profile, peak of 15,000–20,000 K at the cathode tip) and flow field (maximum axial velocity of 200 m/s, Figures 4.5–4.6). Comparison with Two-Temperature (2T)/ NLTE models shows that the near-electrode boundary condition adopted here ensures boundary continuity and provides a more realistic description of the electrode–plasma interface.

For switching arcs under circuit breaker conditions (2–5 mm compact gaps), it is observed that raising the current to 1000 A increases the peak temperature by only 28%, while the arc width doubles (Figure 4.8). This counterintuitive behaviour is attributed to the competing effects of radiative cooling ($Q_{\text{rad}} \propto T^4$) and Lorentz-force-driven expansion ($F_L \propto I^2$). The initial hot-channel assumption is verified as the arc reaches steady state within 0.1 ms (Figures 4.9–4.10), much faster than the millisecond-scale operation of the breaker, supporting the use of a Gaussian profile as the initial condition.

The mesh independence study confirms that the optimised mesh B (six-layer refined boundary layer with minimum size 0.003 mm) achieves accuracy within 5% (Figure 4.11) while reducing computation time by 25% (30 min) compared to the finer mesh C. During dynamic electrode motion, more than 85% of elements maintain a quality factor above 0.8, with overall distortion below 8% (Figure 4.12).

Overall, this chapter establishes a validated modelling approach with physically consistent boundary conditions, a reliable initialisation strategy, and an optimised meshing scheme. These elements form a solid basis for the dynamic arc simulations presented in Chapter 5.

Chapter 5

Investigation of Arc Re-ignition Mechanism in LC Commutator-based DC Circuit Breakers

The model developed in this chapter is a direct extension of the validated thermal arc framework established in Section 4.2. The foundational computational setup, including the electrode geometry, domain discretization, and the bulk of the boundary conditions, remains unchanged from the previous chapter to ensure consistency and build upon the established baseline.

The primary advancement introduced here is the coupling of the plasma model with an external LC commutation circuit, enabling the simulation of dynamic arc-circuit interactions during the current interruption process. To more accurately represent the physical conditions at the electrode interfaces, a key modification involves the implementation of a sheath resistance model, which is integrated as a circuit element to capture the characteristic voltage drop and electrical behavior of the near-electrode regions. Additionally, recognizing the critical role of thermal management, the model explores the sensitivity of the arc behavior to cooling efficiency by examining three distinct scenarios for the heat transfer coefficient at the electrode boundaries.

Building on the validated thermal arc modelling framework presented in Chapter 4, this chapter incorporates an LC commutation circuit into the plasma model to address the research gap identified in Section 2.3.1. Although LC commutator-based Direct Current (DC) circuit breakers have been widely investigated, the underlying mechanisms governing arc re-ignition in such systems remain insufficiently understood. To this end, an integrated arc–circuit model is employed to analyse the arcing stages during LC commutation and to identify the root causes of re-ignition.

5.1 Model Formulation

5.1.1 Thermal Plasma model

The LC-commutator circuit breaker system comprises multiple subsystems, including the power supply connection, the commutation branch, and the mechanical switches, consistent with the experimental setup described in [17]. In the simulations, the mechanical switches are replaced with an axisymmetric contact plasma model. The computational domain geometry and boundary conditions are identical to those in Chapter 4 (Figure 4.7 and Table 4.2). In brief, the arc core is modelled as a Magnetohydrodynamic (MHD) continuum governed by the conservation laws of mass, momentum, and energy, coupled with Maxwell's equations for electromagnetic fields. Radiation losses are calculated using the Net Emission Coefficient (NEC) method [144], while thermodynamic and transport properties of air are adopted from [122]. Internal source terms include Joule heating, radiation, Lorentz forces, and volume forces.

The electrode boundary layer is represented using a simplified sheath model [96, 142] to interface the equilibrium plasma with the electrode surfaces. Only the collisionless sheath is explicitly resolved, due to its dominant role in voltage drop and electrode heating; a constant voltage drop of $\Delta V = 16$ V is assumed for copper electrodes [24, 106]. Conduction across the contact gap is permitted only when the applied voltage exceeds ΔV, thereby focusing this study on thermal breakdown driven by Joule heating within the boundary layer. This approximation enables the investigation of cooling effects on the onset of re-ignition.

5.1.2 Circuit Configuration and Parameters

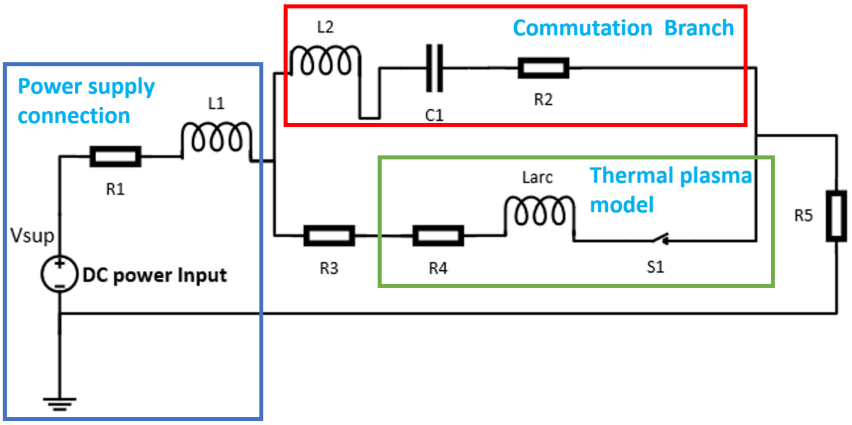

FIGURE 5.1: Schematic of the equivalent electric circuit of circuit breaker coupled with physic arc model

The simulation circuit, shown in Figure 5.1, is divided into three main parts: (i) the power supply branch (V_{sup}, R_1, L_1), (ii) the commutation branch (L_2, C_1, R_2), and (iii) the switching branch (S_1 thermal plasma model, R_3 electrode resistance, R_4 arc sheath resistance, (R_{arc} arc inductance, and R_5 ground resistance). The main components, their values, and physical meanings are summarised in Table 5.1.

TABLE 5.1: Circuit parameters and physical meanings for the LC-commutator breaker model

Component	Value	Physical meaning
V_{sup}	1000 V	DC supply voltage
R_1	2.1 Ω	Main circuit current-limiting resistor (line/load resistance)
L_1	10 mH	Main circuit inductance (system inductance)
Initial current	435 A	Steady-state current before interruption (via S_1)
L_c	227 nH	Commutation inductance (controls transfer speed/oscillation frequency)
C_c	208 μF	Commutation capacitance (controls stored energy/oscillation period)
R_2	0.0075 Ω	Damping resistor in commutation branch (parasitic/added damping)
S_1	–	Thermal plasma model representing the contact gap
R_3	0.001 Ω	Fixed resistor in arc branch (lead or shunt resistance)
R_4	$\frac{16\text{ V}}{\lvert i_{R_3}\rvert+1\times10^{-3}\text{ A}}$	Dynamic resistance modelling electrode sheath voltage drop
L_3	50 nH	Arc branch inductance (parasitic inductance)
R_5	0.01 Ω	Ground resistance (return path, measurement reference)

Operating principle: In the initial steady state ($t \leq 0$), a pre-established electric arc provides a conductive path between the electrodes. Current flows predominantly through the arc branch:

$$V_{\text{sup}} \to R_1 \to L_1 \to R_3 \to R_4 \to L_{\text{arc}} \to S_1 \to R_5 \to \text{GND}.$$

At $t = 0^+$, interruption is initiated by plasma cooling and/or contact separation, causing the arc resistance (S_1) to increase sharply. This diverts current into the commutation branch:

$$V_{\text{sup}} \to R_1 \to L_1 \to L_c \to C_c \to R_2 \to R_5 \to \text{GND}.$$

The L_c–C_c network generates a resonant counter-current pulse, driving the arc current toward zero-crossing.

5.1.3 Three Cooling Scenarios: Assumptions and Justifications

To investigate the influence of thermal conditions near electrodes on arc re-ignition, three distinct cooling scenarios are defined based on the heat transfer coefficient h at the electrode–plasma interface. This coefficient governs the heat flux $\mathbf{q}_h$ according to:

$$\mathbf{q}_h = h \cdot (T_{\text{plasma}} - T_{\text{electrode}})$$

where $T_{\text{electrode}} = 300\,\text{K}$ is assumed constant. The coefficient h is estimated from the plasma thermal conductivity λ and the boundary layer thickness Δ_d as:

$$h = \frac{\lambda(T_{pa})}{\Delta_d}, \quad \Delta_d = 0.1\,\text{mm}$$

where T_{pa} is the average plasma temperature. Figure 5.2 presents the thermal conductivity of air plasma, which forms the basis for the defined cooling scenarios.

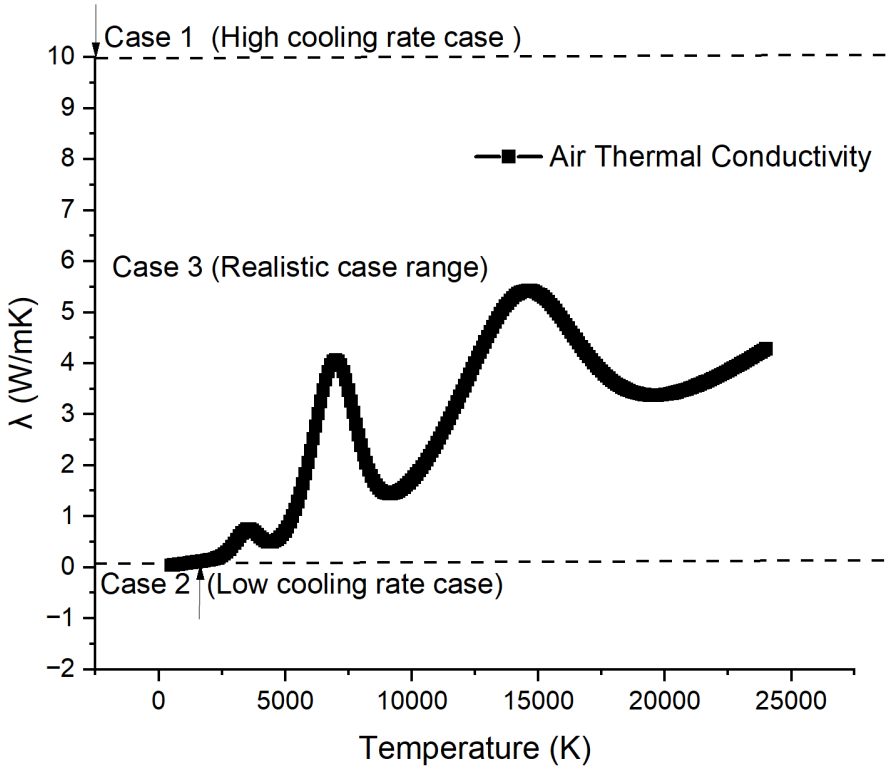

FIGURE 5.2: Thermal conductivity of air plasma as a function of temperature [122]. The dashed lines indicate the assumed thermal conductivity values for Case 1 (strong cooling, $\lambda = 10\,\mathrm{W/mK}$) and Case 2 (weak cooling, $\lambda = 0.1\,\mathrm{W/mK}$). Case 3 corresponds to the realistic temperature-dependent range of λ obtained from the data.

In the first scenario, referred to as high cool rate cooling, the plasma thermal conductivity is assumed to be $\lambda_1 = 10\,\mathrm{W/mK}$, representing a high thermal conductivity condition. With a boundary layer thickness of $\Delta_d = 0.1\,\mathrm{mm}$, the corresponding heat transfer coefficient is calculated as $h_1 = \frac{\lambda_1}{\Delta_d} = 100{,}000\,\mathrm{W/m^2K}$. This value exceeds the maximum thermal conductivity of air plasma ($\approx 6\,\mathrm{W/mK}$) and is intended to represent an enhanced cooling environment, such as that achieved through forced convection or active cooling (e.g. with air blast), where heat can be efficiently transferred from the plasma to the electrode.

The second scenario, low cooling rate case, assumes a much lower plasma thermal conductivity of $\lambda_2 = 0.1\,\mathrm{W/mK}$. Using the same boundary layer thickness, the resulting heat transfer coefficient is $h_2 = \frac{\lambda_2}{\Delta_d} = 1{,}000\,\mathrm{W/m^2K}$. This condition corresponds to the thermal conductivity of air plasma at approximately 2,500 K, representing the later stages of arc decay. Under such conditions, the limited heat transfer capability can result in heat accumulation near the electrode surface, potentially influencing the likelihood of arc re-ignition.

The third scenario, realistic case cooling, incorporates a temperature-dependent thermal conductivity, $\lambda_3 = \lambda_{\mathrm{plasma}}(T_{pa})$, to reflect realistic variations in cooling efficiency during the arc evolution. The corresponding heat transfer coefficient is given by $h_3(T_a) = \frac{\lambda_{\mathrm{plasma}}(T_a)}{\Delta_d}$.

This scenario captures the natural transition from strong cooling at high temperatures to weak cooling near extinction.

5.2 Result and Discussion

5.2.1 Case 1: High Cooling Rate $h = h_1$

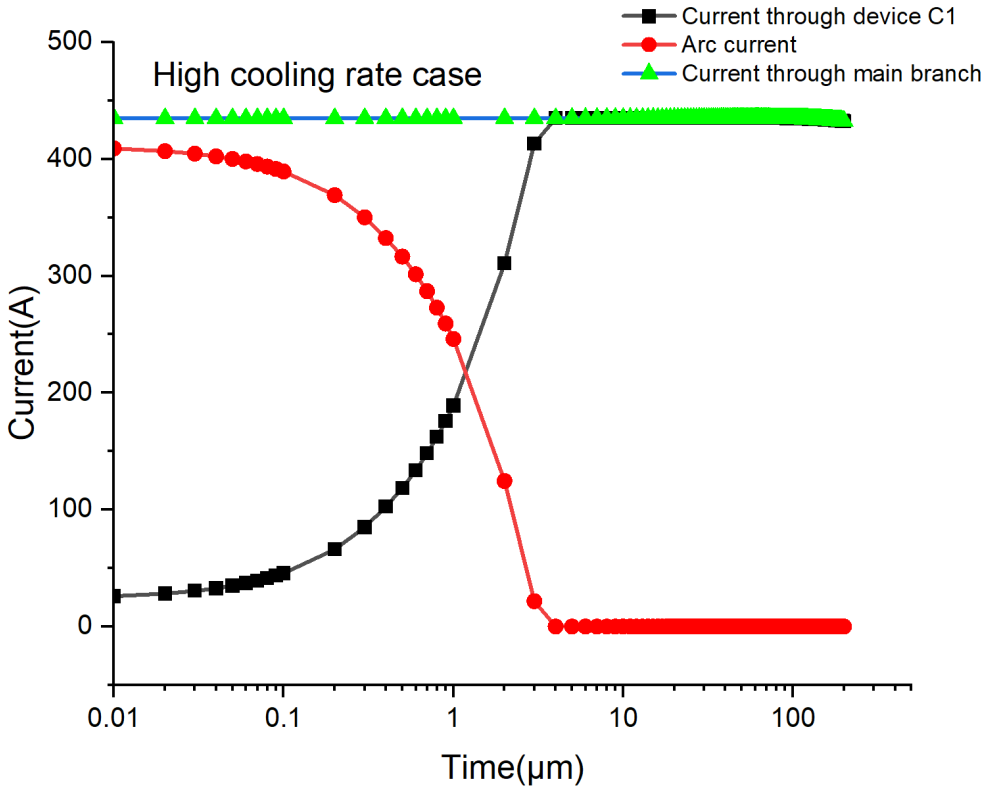

FIGURE 5.3: Current profile goes through the air gap and capacitor for high cooling rate case $h = h_1$

Circuit behaviours: As shown in Figure 5.3 and 5.4, in the initial steady state ($t \leq 0$), the pre-established arc path offers lower impedance, allowing the entire current (435 A) to flow through the arc branch: $V_{\text{sup}} \to R_1 \to L_1 \to R_3 \to R_4 \to L_{\text{arc}} \to S_1 \to R_5 \to \text{GND}$. When interruption is initiated at $t = 0^+$, the arc resistance increases sharply due to intensive cooling, forcing current transfer to the commutation branch with a ~ 1 μs delay. The commutation process completes within 3 μs, with the arc current reaching zero at approximately 4 μs. Subsequently, all current flows through the LC path ($V_{\text{sup}} \to L_1 \to L_c \to C_c \to R_2 \to R_5 \to \text{GND}$), the arc core voltage drops to 0 V, the air-gap voltage stabilises at 8.9 V (below the 16 V sheath threshold), and the capacitor voltage settles at 5.09 V.

The post–commutation voltage behaviour can be explained by the arc model physics. Once the current has been fully commutated to the LC branch, the arc-column drop collapses to zero because it is essentially an ohmic bulk drop, $V_{\text{core}} \approx I_{\text{arc}} R_{\text{plasma}}$ with $R_{\text{plasma}} \propto 1/\sigma$, and $I_{\text{arc}} \to 0$ as the plasma rapidly cools and its conductivity σ decays. The sheath (arc-fall) voltage exhibits

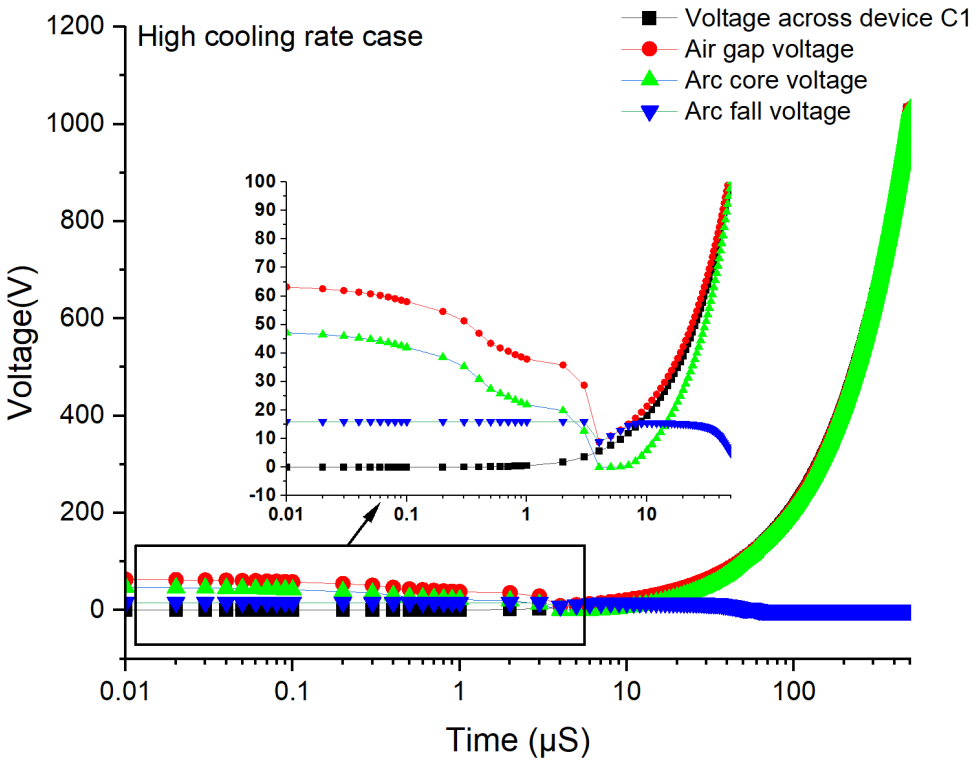

FIGURE 5.4: Voltage profile goes through the air gap and capacitor for high cooling rate case $h = h_1$

a short dip followed by a mild rise due to circuit and space-charge transients. In the boundary-layer model,

$$V_{\text{sheath}} \approx I_{\text{arc}} R_4 = I_{\text{arc}} \cdot \frac{16\ \text{V}}{|I_{\text{arc}}| + 10^{-3}\ \text{A}},$$

so as $I_{\text{arc}} \to 0$ the instantaneous conductive drop tends to zero and the sheath effectively becomes a very large resistance. During commutation, the L_c–C_c resonance produces a counter-current and a brief reverse gap field, which effectively neutralizing the energy state associated with the space charge region. After current extinction, no conduction path exists and the gap behaves as an open circuit; at this stage the circuit breaker is fully open, and the voltage across C_1 rises towards the system voltage while the same recovery potential appears across the air gap. In the strong-cooling case, this recovery level remains below the conduction threshold ($V_{\text{gap}} \approx 8.9\ \text{V} < \Delta V = 16\ \text{V}$), preventing arc reignition and ensuring that V_{core} stays at zero while the capacitor voltage settles.

Physics of the phenomena: To further understand why re-ignition does not occur under these conditions, it is essential to examine the near-electrode thermal state at the zero-current crossing. At $t = 4\ \mu$s in the high cooling rate case, a critical phenomenon emerges: the formation of an ultra-thin cold boundary layer (thickness ~ 0.05 mm) adjacent to the electrode surface, as shown in Figure 5.5. This layer, maintained at approximately 2000 K, acts as a high-resistance thermal barrier that significantly reduces the likelihood of electron emission and ionisation within the near-electrode region. The synergistic effect between this thermal barrier and the circuit's

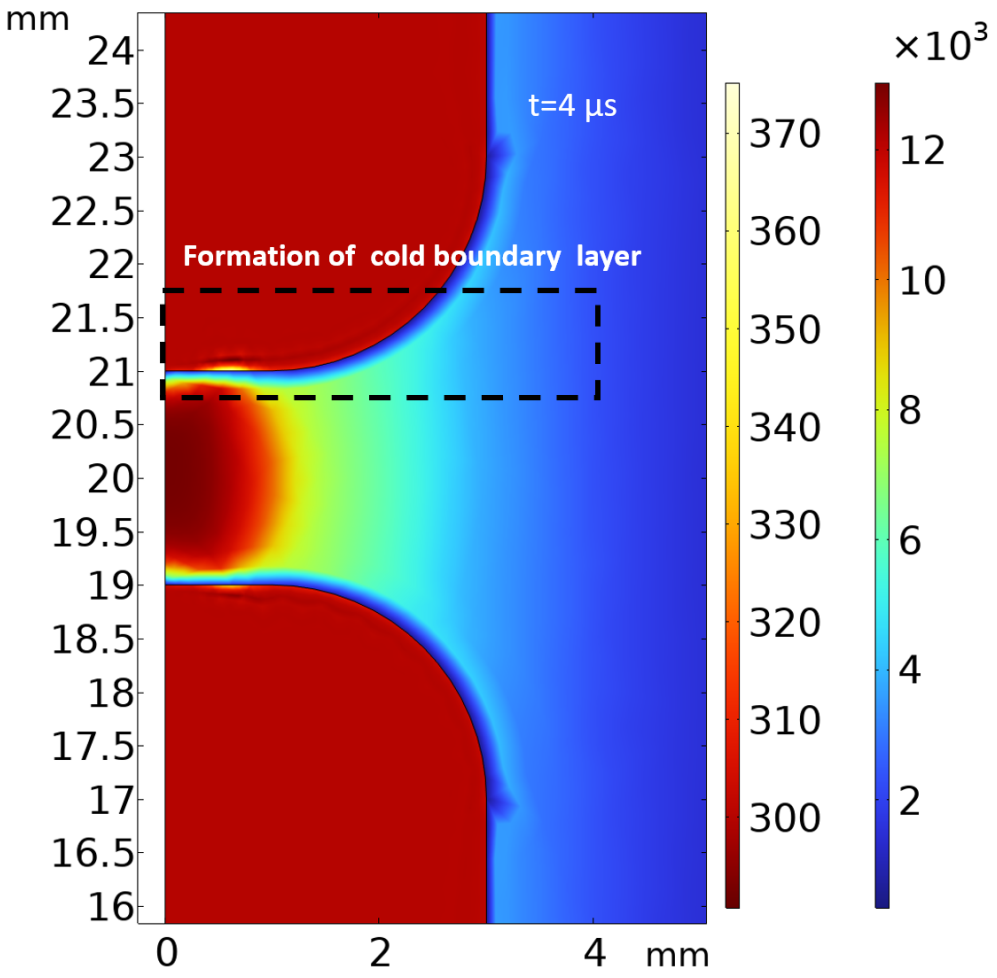

FIGURE 5.5: Temperature distribution showing cold boundary layer formation ($h = h_1$) at $t = 4\mu s$. The sub-millimeter cold zone (∼2000 K) at electrode interfaces provides critical dielectric strength.

commutation behaviour enables the gap to withstand transient recovery voltages up to 1000 V without re-ignition. In summary, for the high cooling rate case, commutation completes within 3 μs through combined thermal–electromagnetic action, and the resultant cold air gap (2000 K boundary layer) sustains a breakdown strength exceeding the applied recovery voltage, demonstrating effective and stable arc extinction.

5.2.2 Case 2: Low Cooling Rate $h = h_2$

Circuit behaviours: As shown in Figure 5.6 and 5.7, in the initial steady state ($t \leq 0$), the arc branch again presents the lower impedance path, carrying almost the entire load current of 435 A through the sequence $V_{\text{sup}} \rightarrow R_1 \rightarrow L_1 \rightarrow R_3 \rightarrow R_4 \rightarrow L_{\text{arc}} \rightarrow S_1 \rightarrow R_5 \rightarrow$ GND. After interruption is initiated at $t = 0^+$, the increase in arc resistance is more gradual than in Case 1 because of the weaker cooling rate. As a result, the commutation branch current rises slowly, peaking at only ~ 250 A (less than half of the Case 1 peak), while the arc current decays to near zero only at $t \approx 7$ μs.

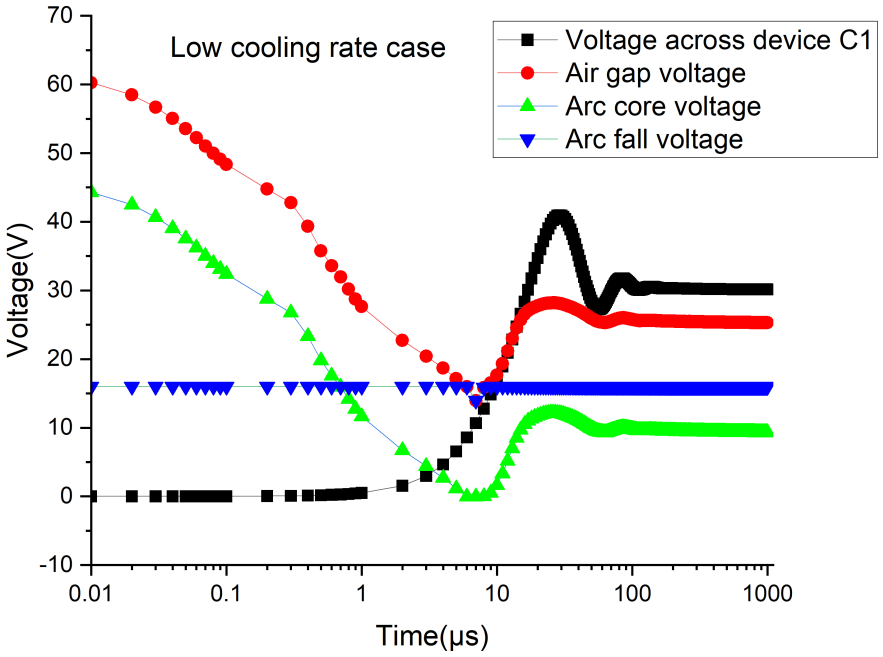

FIGURE 5.6: Voltage profile goes through the air gap and capacitor for low cooling rate case $h = h_2$

At this moment, the air-gap voltage exhibits a brief dip just below the 16 V sheath threshold before rising again. This quick drop is caused by the L_c–C_c resonant counter-current, which momentarily reverses the gap field and partially discharges the sheath space charge. However, because the boundary layer remains highly conductive, the dielectric strength does not improve, and the gap cannot sustain this low-voltage state. Consequently, the air-gap voltage rapidly climbs back to the sheath threshold within ~ 1 μs.

Subsequently, the air-gap voltage reaches 16 V at $t \approx 8$ μs, triggering re-ignition. The event is characterised by a renewed arc core voltage of about 0.5 V, a small arc current surge (~ 3.27 A), and stagnation of the capacitor voltage well below the system voltage. The post–re-ignition behaviour shows persistent current through the arc branch, preventing full voltage recovery across the capacitor.

Physics of the phenomena: At the apparent current zero around 7 μs, the weak cooling rate fails to produce a cold, high-resistance boundary layer; instead, the near-electrode region remains at ~ 9000 K as shown in Figure 5.8, with high residual conductivity and insufficient dielectric strength. The brief drop of the air-gap voltage below the sheath threshold is caused by the L_c–C_c counter-current partially discharging the sheath space charge, but the hot boundary layer quickly restores conduction. As a result, once the voltage recovers to the 16 V sheath threshold ($t \approx 8$ μs), re-ignition occurs, sustaining a low-level arc and preventing full recovery of the capacitor voltage.

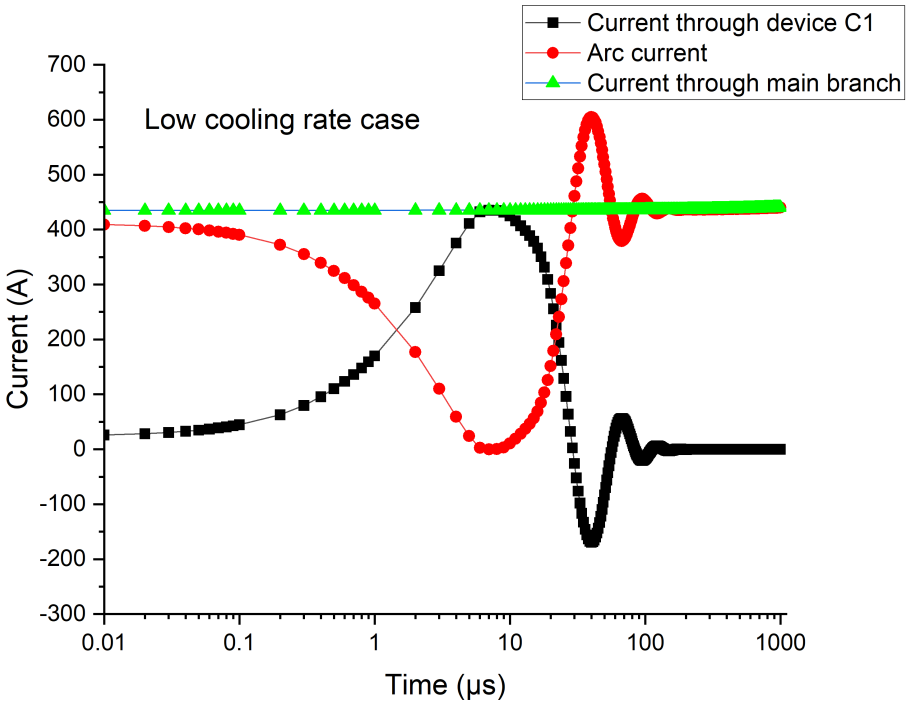

FIGURE 5.7: Current profile goes through the air gap and capacitor for low cooling rate case $h = h_2$

In summary, for the low cooling rate case, the delayed commutation and absence of a strong dielectric barrier permit re-ignition once the sheath threshold is exceeded, preventing complete arc extinction and full recovery voltage development across the capacitor.

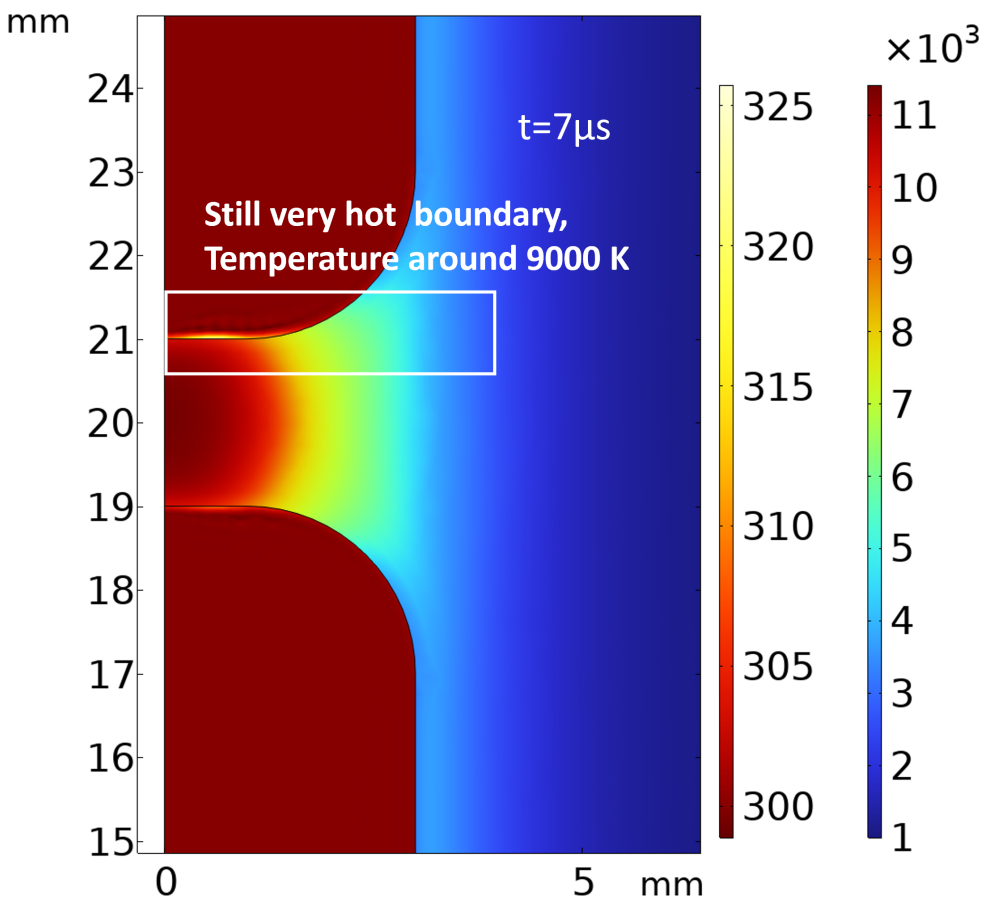

FIGURE 5.8: Temperature distribution for low cooling rate case of boundary layer h=h_2,t=7μs

5.2.3 Case 3: Realistic Cooling Rate $h = h_3$ based on T_{plasma}

Circuit behaviours: As shown in Figure 5.9 and 5.10, in the initial steady state, the current flows entirely through the arc branch, following the same path as in Case 1. When interruption begins at $t = 0^+$, the arc resistance rises and commutation to the LC branch proceeds quickly, reducing the arc current to ∼0.5 A by 4 μs. This pseudo-extinction is followed by a prolonged near–zero-current state lasting about 4 μs (6–10 μs), during which the air-gap voltage slowly increases from 11.8 V to the sheath threshold of 16 V. Unlike Case 2, where insufficient cooling causes almost immediate voltage threshold breach and re-ignition at 8 μs, here the current remains suppressed for a longer duration. However, recovery is still incomplete: a small current of ∼2 A appears at 9 μs, and by 20 μs the arc is fully re-established at ∼200 A. During the early stages of re-ignition, the core voltage remains close to zero while the sheath voltage stabilises at ∼16 V, indicating that conduction is driven primarily by near-electrode processes.

Physics of the phenomena: As shown in Figure 5.11, at $t = 8$ μs the boundary layer remains in a metastable thermal state with a temperature of about 6000 K. Although this is cooler than in Case 2, it still provides insufficient dielectric strength (∼200 V/mm) to withstand the applied recovery voltage. The residual ionisation enables electron emission under the sheath field, and once the local electric field exceeds ∼100 kV/m, breakdown occurs. Compared with Case 2,

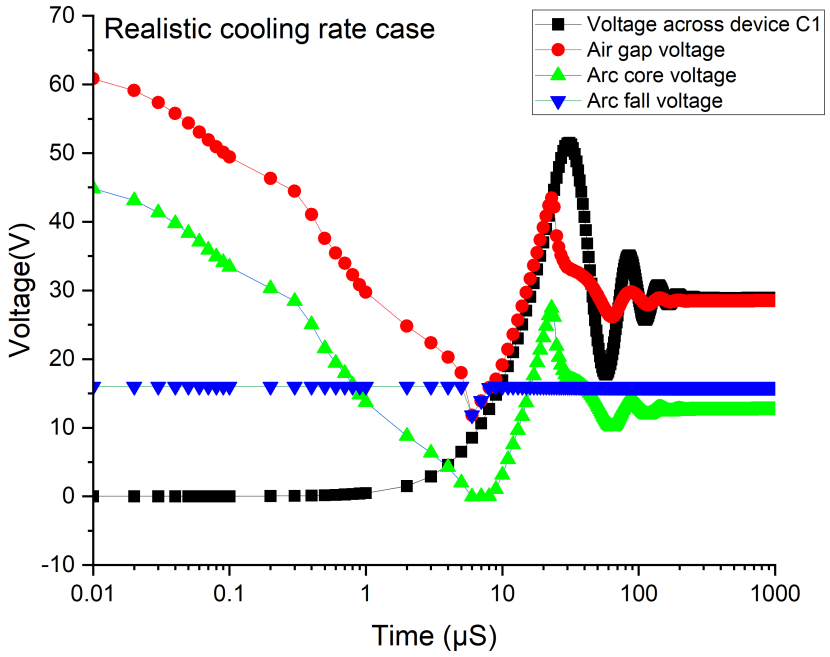

FIGURE 5.9: Voltage profile goes through the air gap and capacitor for realistic cooling rate example $h = h_3$

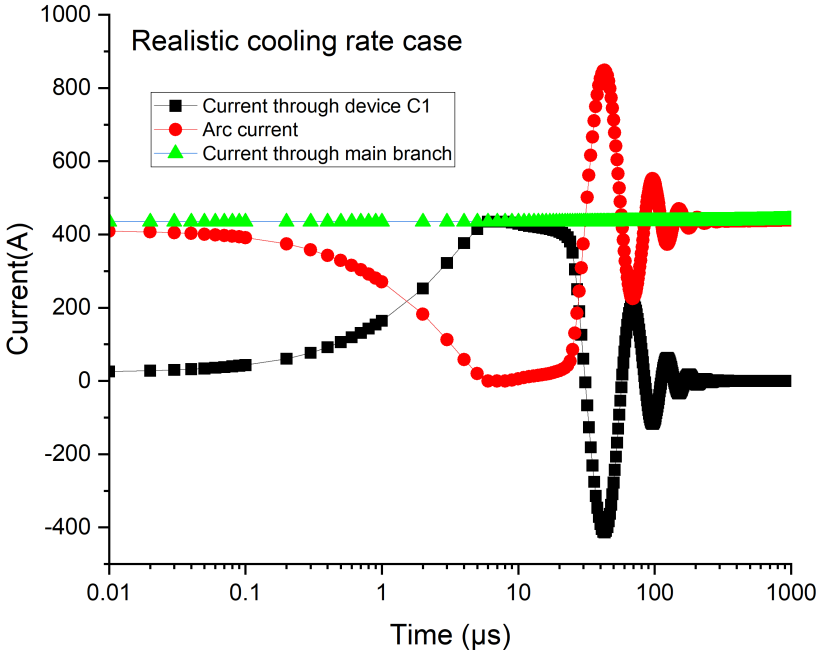

FIGURE 5.10: Current profile goes through the air gap and capacitor for realistic cooling rate example $h = h_3$

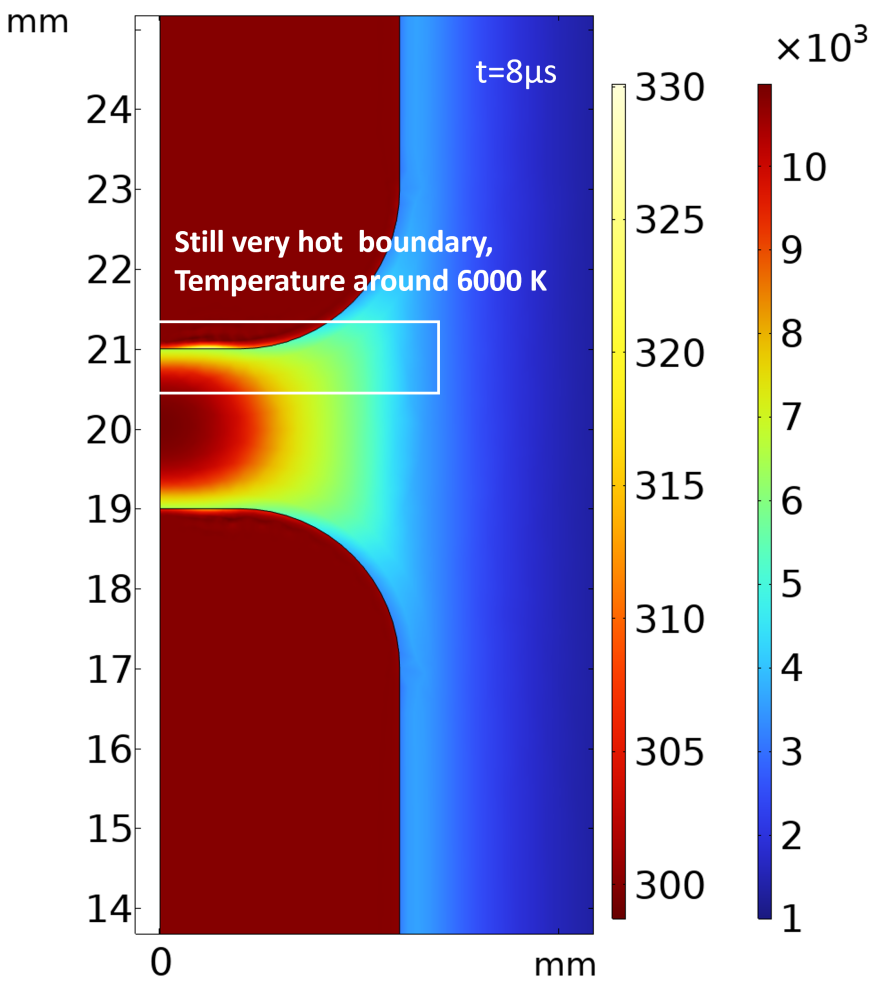

FIGURE 5.11: Temperature distribution for realistic cooling case ($h = h_3$) at $t = 8$ μs. The $\sim$6000 K boundary layer retains enough residual ionisation to trigger delayed re-ignition under the sheath field.

where the hot boundary layer ($\sim$9000 K) sustains high conductivity and causes almost immediate reignition, the cooler but still conductive layer in Case 3 delays breakdown, resulting in a longer metastable period before re-ignition.

In summary, the realistic cooling case shows that even with initial commutation and a brief zero-current period, incomplete cooling leaves the boundary layer marginally conductive. Compared to Case 2, where breakdown occurs almost immediately after the sheath threshold is reached, Case 3 experiences a longer delay due to its lower boundary-layer temperature. Nonetheless, this metastable state ultimately fails to maintain dielectric strength, and delayed re-ignition occurs.

5.3 Mitigation of Re-ignition based on T_{plasma}

Observations from the Case 3 showed that, even after successful current commutation, the near-electrode boundary layer can remain hot ($T_{\text{plasma}} \approx 5000\,\text{K}$). This residual heat preserves a weakly ionised channel and reduces the dielectric strength of the gap, so that a rising recovery voltage during capacitor charging may trigger delayed re-ignition. In contrast to the well-cooled case (Figure 5.4), effective mitigation should limit both the peak value and the rate-of-rise of the air-gap voltage during recovery, thereby extending the zero-current interval and allowing the boundary layer to cool down and the breakdown voltage does not exceed the modelled arc gap voltage so the re-ignition does not take place in practice. Referring to the case 3 voltage profiles in Figure 5.9, adjustments could include slowing done the voltage rise rate (decreasing the capacitor charging rate.)

Motivated by this hypothesis, we assess two circuit-oriented mitigation strategies while retaining the plasma model unchanged: (i) increasing the arc-fall (sheath) voltage ΔV : to raise the conduction threshold imposed by the boundary layer model, and (ii) increasing the commutation capacitance C_c : to reduce the recovery dv/dt according to $i_C = C_c\,\mathrm{d}V/\mathrm{d}t$, thereby providing more cooling time before the gap experiences a critical field.

5.3.1 Strategy 1: Increasing the Arc-Fall Voltage (ΔV)

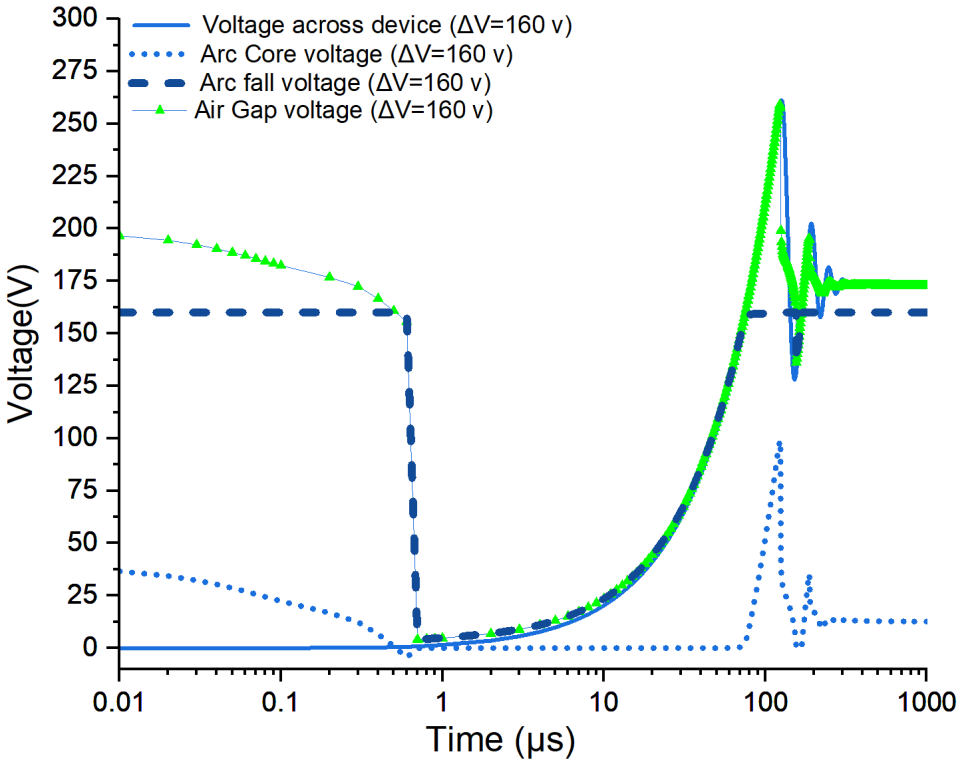

FIGURE 5.12: Comparison of voltage profile across the air gap and capacitor by increasing the arc fall voltage

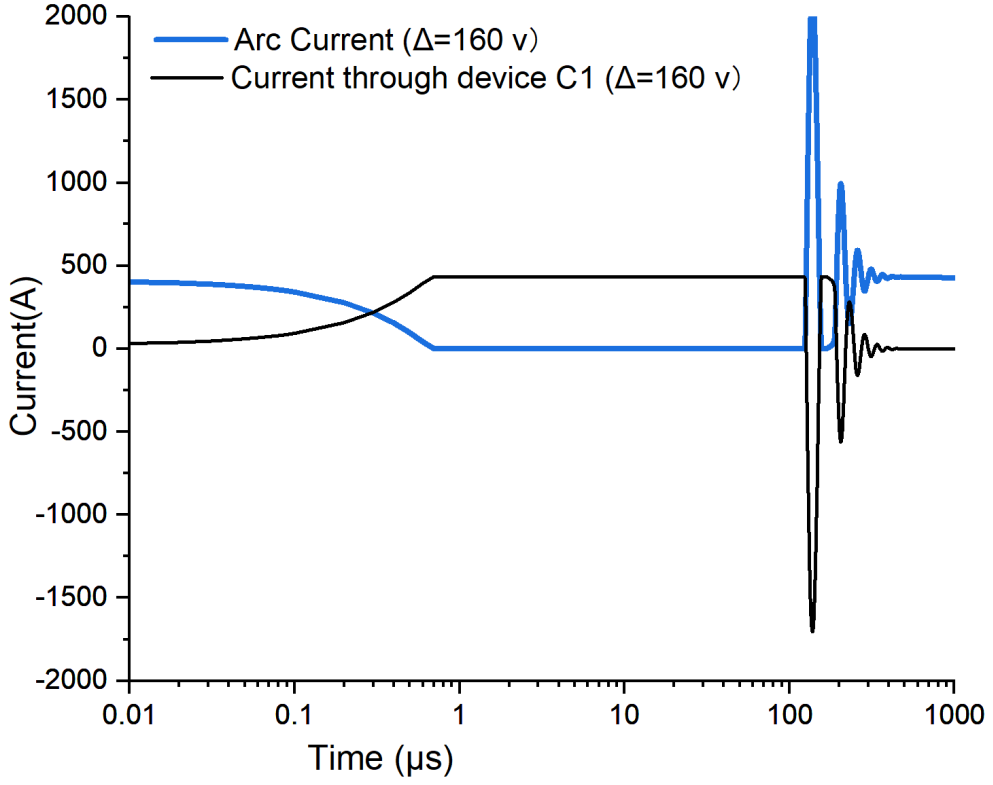

FIGURE 5.13: Current profiles across the air gap and capacitor by increasing the arc fall voltage

To gauge the benefit of a higher conduction threshold, we performed a sensitivity test by raising the sheath drop in the boundary-layer model from $\Delta V = 16$ V to 160 V while keeping the realistic-cooling (Case 3) parameters unchanged. As shown in Figure 5.12 and 5.13, after commutation the breaker is open and the air gap tracks the capacitor recovery ($V_{\text{gap}} \approx V_{C_1}$). For $t < 1$ μs the LC counter-current forces $I_{\text{arc}} \to 0$; in our (conductive-only) sheath model $V_{\text{sheath}} = I_{\text{arc}} \frac{\Delta V}{|I_{\text{arc}}|+10^{-3}\,\text{A}}$, so $V_{\text{sheath}} \to 0$ as $I_{\text{arc}} \to 0$ (here ΔV acts as a conduction threshold, not a static bias). During recovery the open gap is charged by C_1, hence V_{gap} increases and crosses the elevated threshold at ~ 70 μs; this crossing does not immediately yield conduction because the near-electrode layer, although cooling, is still carrier-poor and highly resistive, so the field mainly drives displacement current with negligible Joule heating. Around ~ 126 μs the accumulated recovery field gradually heats the metastable boundary layer, a conductive sheath reforms, I_{arc} begins to rise, and V_{sheath} jumps back toward ΔV, leading to a *delayed* re-ignition (peak near ~ 160 μs). Thus increasing ΔV defers rather than eliminates reignition; the practical implication is to emulate a higher effective threshold by limiting the recovery $\mathrm{d}V/\mathrm{d}t$ (e.g., via larger C_c), which is pursued next in Strategy 2.

5.3.2 Strategy 2: Increasing the Commutation Capacitance C_c

To reduce the recovery $\mathrm{d}V/\mathrm{d}t$ and lengthen the post–commutation cooling window, we increased the commutation capacitance while keeping the plasma model unchanged (Case 3 realistic cooling). Three values were assessed: the base $C_1 = C_c$, a fourfold increase $C_2 = 4C_c$, and a tenfold increase $C_3 = 10C_c$.The voltage and current traces in Figures 5.14–5.15 show that, once the breaker is open, the air-gap voltage essentially follows the capacitor voltage, $V_{\mathrm{gap}} \simeq V_{C_1}$. For a given branch current i_C, the relation $i_C = C_c\,\mathrm{d}V_{C_1}/\mathrm{d}t$ implies $\mathrm{d}V_{C_1}/\mathrm{d}t \propto 1/C_c$; therefore a larger C_c slows the recovery of V_{gap}, deferring (and for the largest C_c preventing) the moment at which it reaches the sheath threshold ΔV. Quantitatively (Table 5.2), re-ignition occurs for C_1 at $t \approx 20$ μs with $V_{\mathrm{gap}} \approx 50$ V, is deferred to $t \approx 100$–120 μs with $V_{\mathrm{gap}} \approx 65$ V for C_2, and no re-ignition is observed for C_3 as summarised in Table 5.2.

TABLE 5.2: Comparison of parameters for different capacitor values

Capacitor Value	**C1 = C_c**	**C2 = 4*C_c**	**C3 = 10*C_c**
Re-ignition voltage (V)	50	65	x
Surface temperature at re-ignition point (K)	10000	7000	x
Re-ignition time (μs)	20	100	x
Commutation time (μs)	5	5	5

A key observation is that the commutation time is about 5 μs for all three capacitances. This is because the first current zero is governed by the rapid rise of arc resistance and the *L–R* dynamics; the capacitor value hardly affects this early stage. The temperature profiles (in Figure 5.16) at $t = 5$ μs (just after commutation) are therefore almost identical for C_c, $4C_c$ and $10C_c$, with peak values around 12–14 kK. By $t = 20$ μs, the bulk gap temperature has dropped to about 8 kK in all cases, and a near-electrode boundary layer becomes visible: it is ~ 6 kK for $4C_c$ and $10C_c$, but still ~ 7 kK for C_c, which explains why the C_c case reignitions immediately at ~ 20 μs. At $t = 100$ μs the divergence is clear: for C_c the arc has already re-established and the temperature climbs back to ~ 13 kK; for $4C_c$ the overall gap is near 5 kK but the boundary layer near the axis remains at ~ 6 kK, consistent with the delayed reignition at 100–120 μs; for $10C_c$ a fully cooled boundary layer is formed and no reignition occurs.

It is worth noting (in Figure 5.16) that at $t = 20$ μs the boundary-layer temperatures of $4C_c$ and $10C_c$ (about 6 kK) are still high enough to be potentially conductive; however, the gap field is not yet large and a conductive sheath does not form, so current does not resume. This confirms that effective cooling of the boundary layer is crucial, but temperature alone is not a sufficient predictor: re-ignition is governed by the combined thermal and electric conditions. In practice, the boundary layer should be cooled below the conduction threshold of the gap and the recovery field must be kept below the level that can trigger breakdown. A complete description therefore calls for integrating electric breakdown with the thermal model, which we pursue in the next chapter.

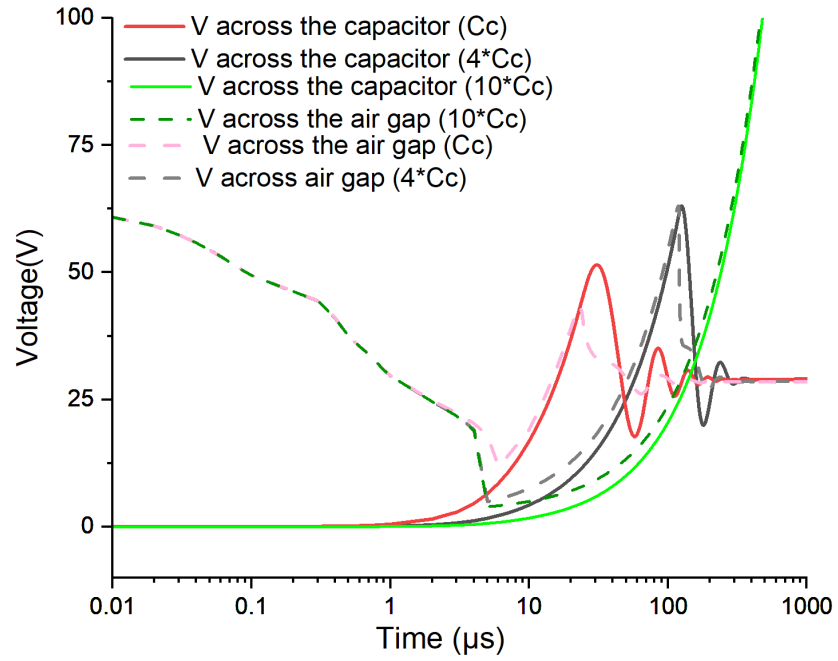

FIGURE 5.14: Comparison of voltage profile across the air gap and capacitor by increasing the capacitor value (C2,C3)

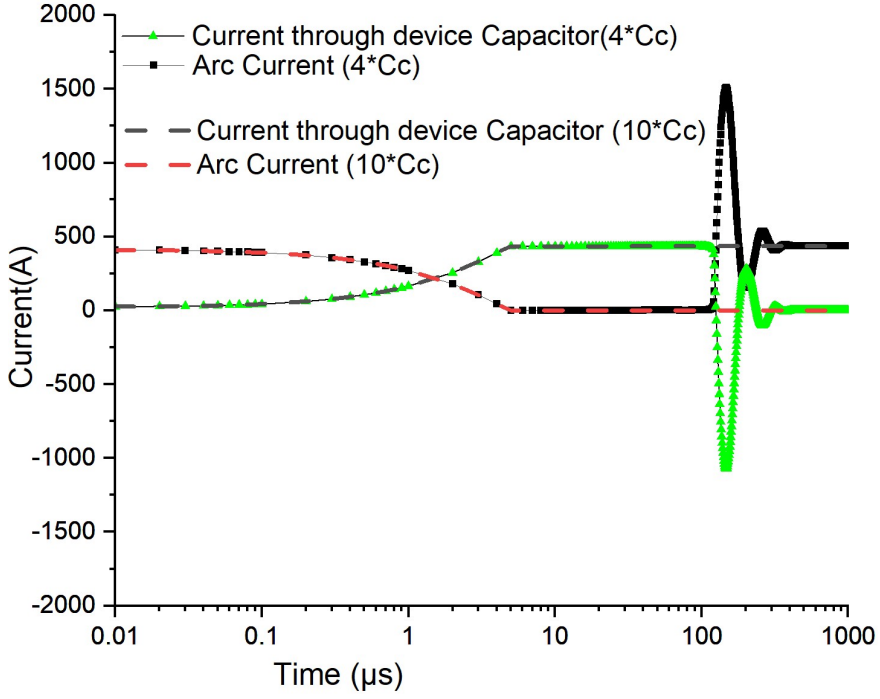

FIGURE 5.15: Comparison of current profiles across the air gap and capacitor by increasing the capacitor value (C2,C3)

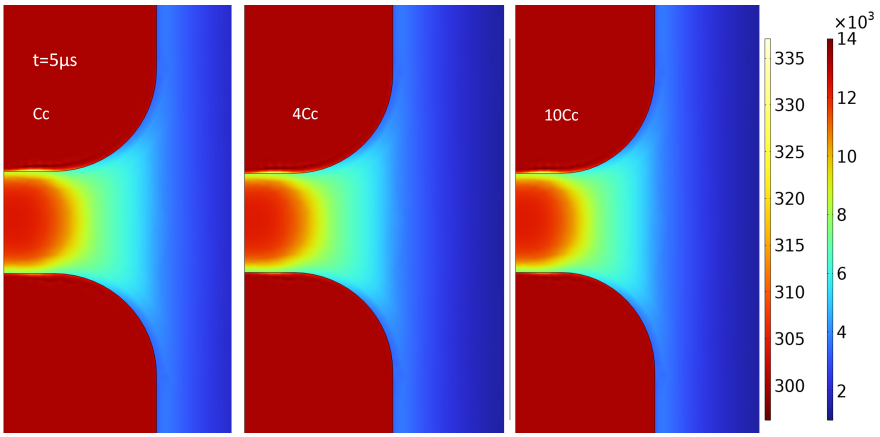

(A) At 4×10^{-6} s

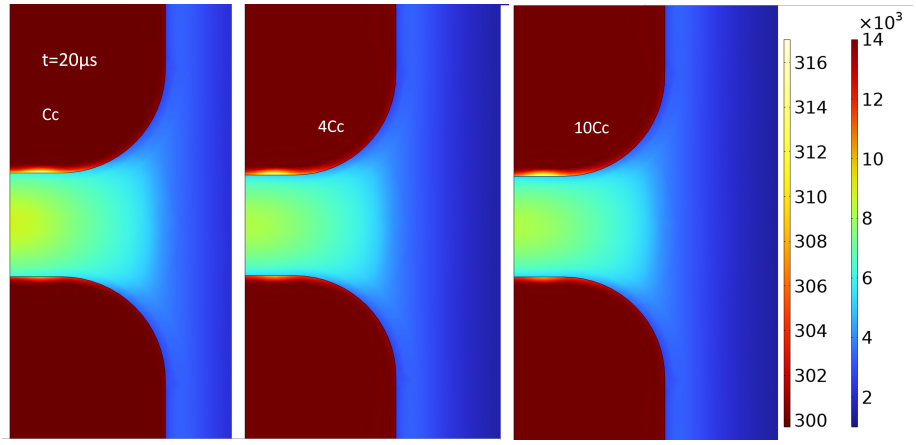

(B) At 2×10^{-5} s

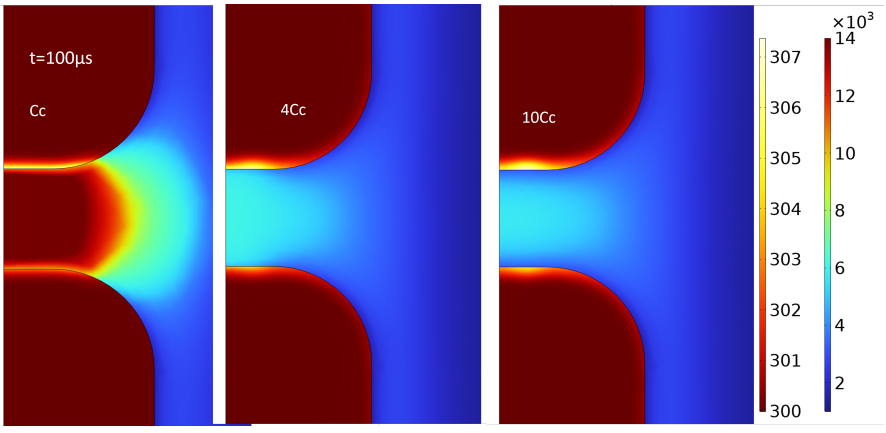

(C) At 1×10^{-4} s

FIGURE 5.16: The demonstration of boundary layer formation as time evolution by increasing the capacitor value

5.4 Summary

Figure 5.17 summarises an overview of Chapter 5: Section 5.1 formulates the LC-commutator arc–circuit model and justifies the three cooling scenarios, Section 5.2 diagnoses the re-ignition mechanism from these cases, and Section 5.3 proposes mitigation while highlighting model limits that motivate Chapter 6.

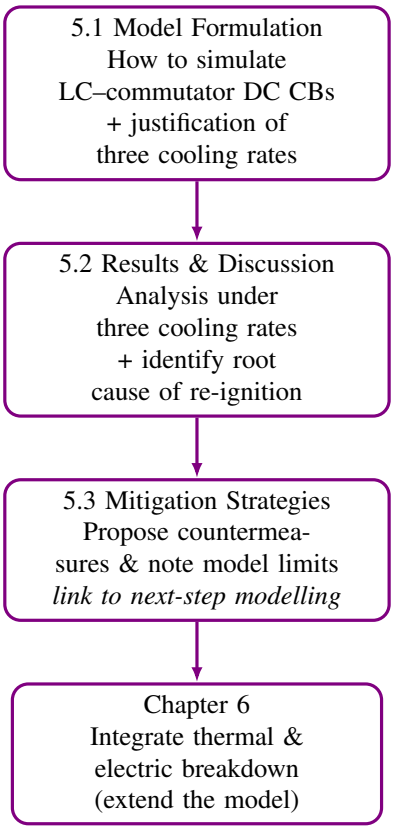

FIGURE 5.17: Overview of Chapter 5 sections and the link to Chapter 6.

This chapter coupled the validated Local Thermodynamic Equilibrium (LTE)–MHD thermal plasma core with an LC commutation network to investigate arc re-ignition in compact DC circuit breakers. Three cooling scenarios were examined via the electrode heat-transfer coefficient: strong (h_1), weak (h_2), and realistic temperature-dependent (h_3). The simulations show that, under strong cooling, a $\sim 0.05\,\mathrm{mm}$, $\approx 2000\,\mathrm{K}$ cold boundary layer forms at current zero and provides sufficient dielectric strength, so reignition does not occur; under weak cooling the near-electrode gas remains hot ($\sim 9000\,\mathrm{K}$) and re-ignites almost immediately once the sheath threshold is reached; under realistic cooling a $\sim 6000\,\mathrm{K}$ metastable layer, together with the recovering gap field, produces delayed re-ignition after a longer zero-current interval.

Two mitigation strategies were assessed: raising the arc-fall voltage ΔV (a sensitivity upper bound that defers but does not eliminate reignition) and increasing the commutation capacitance C_c, which lowers the recovery $\mathrm{d}V/\mathrm{d}t$, extends the cooling period, and can prevent re-ignition. For Strategy 2, three capacitor sizes were tested. Commutation itself completes in $\approx 5\ \mu\mathrm{s}$ for all cases—set by the rapid rise of arc resistance and the loop L–R dynamics—whereas the subsequent recovery is governed by the interplay between boundary-layer cooling and the field imposed by the charging capacitor. The analysis also shows that temperature alone is not a sufficient predictor; re-ignition is thermo-electric and should be predicted with a model that integrates thermal and electrical breakdown, which motivates the next chapter.

Chapter 6

Development of Temperature-Segmented Hybrid Breakdown Model and application in LC Commutator-based DC Circuit Breakers

The previous chapter focused on thermal effects in arc re-ignition and assumed that breakdown would not occur before sufficient cooling was achieved. This simplification limits predictive accuracy, as in heated short gaps electrical breakdown often initiates earlier than thermal re-ignition as shown in some experiment [113, 145].

As highlighted in Research Gap 3 (Section 3.2.5), conventional models such as Paschen's law and Critical Field Theory fail to provide reliable predictions under elevated temperatures and short-gap conditions. To overcome these limitations, this chapter introduces a temperature-segmented hybrid breakdown model that integrates electrical and thermal mechanisms. The model applies Paschen's law in the low-temperature regime, transitions through an interpolation zone, and adopts a Critical Field-based formulation at high temperatures. Section 6.1 introduced the theoretical foundations of the thermal runaway criteria and breakdown mechanisms; Section 6.2 details the hybrid model formulation, and Section 6.3 is the model validation, followed by a short summary of this Chapter in Section 6.4.

6.1 Model Formulation

6.1.1 Thermal Runaway Criteria: Derivation, and Validation

The thermal runaway phenomenon may occur when the air of low conductivity, already warm, is further heated by a low current [146–148]. Particularly during the post-commutation stage, the temperature across the air gap remains elevated as the circuit begins to recover voltage, there may some small leaking current around the gap. In such instances, thermal runaway can manifest, absent of breakdown, due to insufficient cooling, thereby increasing conductivity. To mitigate this, it is essential to suppress the heating process. The Equation 6.1 outlines a balance between power input and thermal losses within the system:

$$\frac{V^2}{R} = C_p \rho \frac{\Delta T}{\Delta t} \cdot \mathrm{Vol} - \left(\frac{T_g - T_s}{\Delta z} \right) \lambda(T_g) \cdot A \tag{6.1}$$

where V is the voltage applied across the air gap, R represents the resistance of the air gap, C_p denotes the specific heat capacity, ρ is the density, $\frac{\Delta T}{\Delta t}$ signifies the temperature rise driving thermal accumulation, T_g and T_s are the temperatures of the gas and the surface temperature of the electrode. Δz is the thickness of the boundary layer, $\lambda(T_g)$ is the thermal conductivity of the gas at temperature T_g, and A, Vol represents the contact area of arc on electrodes and gap volume respectively.

The term on the left-hand side represents the power input due to the applied voltage, indicative of how much heat is injected into the system at a given moment. The first term on the right side accounts for enthalpy accumulation within the system, while the subtracted term denotes cooling across the boundaries, highlighting the heat exchange dynamics.

The condition for thermal runaway requires air heating, $\frac{\Delta T}{\Delta t} > 0$, suggesting that thermal runaway occurs when the power input exceeds the cooling effect across the boundary layer of thickness Δz.

$$\frac{V^2}{R} > \left(\frac{T_g - T_s}{\Delta z} \right) \lambda(T_g) A \tag{6.2}$$

Simplifying the condition for thermal runaway involves finding the formula for resistance R of the gap, which relates resistance to the electrical conductivity $\sigma(T_g)$. The most resistive place is at the surface, so approximately the T_g is the plasma temperature close to the surface, length of the resistance path is equal to the gap distance d_{gap} and the area is A.

$$R = \frac{1}{\sigma(T_g)} \left(\frac{d_{\mathrm{gap}}}{A} \right) \tag{6.3}$$

Substituting this expression into the thermal runaway criteria yields a simplified equation for the critical voltage necessary to initiate the thermal runaway.

$$V_{\mathrm{th\_run}} = \sqrt{\frac{(T_g - T_s)\,\lambda(T_g)}{\sigma(T_g)} \cdot \frac{d_{\mathrm{gap}}}{\Delta z}} \tag{6.4}$$

The derived critical voltage $V_{\text{th\_run}}$ in Equation (6.4) encapsulates the competition between Joule heating and thermal dissipation to the electrodes. Specifically:

The numerator represents the heat dissipation capability through the boundary layer, while the denominator reflects the gas's tendency to convert electrical energy into heat. At high temperatures, the rapid increase of $\sigma(T_g)$ due to ionization outpaces the moderate rise of $\lambda(T_g)$, leading to an exponential drop in $V_{\text{th\_run}}$. This behavior indicates a positive feedback loop, where higher temperature leads to higher electrical conductivity and thus more Joule heating, further increasing the temperature.

6.1.2 Breakdown Mechanisms in Gases for High Temperature

Paschen's Law and Its Limitations in High-Temperature Scenarios

For a basic configuration involving two plane electrodes separated by a gas gap, Paschen's law describes the breakdown voltage (V_B) required to initiate electrical discharge in a uniform electric field. This analytical relationship expresses the breakdown voltage as a function of the gas pressure (P), the electrode gap distance (d), and the gas composition [25]:

$$V_B = \frac{Bpd}{\ln(Apd) - \ln\left[\ln\left(1 + \frac{1}{\gamma_{se}}\right)\right]} \tag{6.5}$$

In this equation, γ_{se} represents the secondary electron emission coefficient, which depends on the electrode material. The empirical constants A and B are specific to each gas. For air, these values are given as $A = 15$ [1/cm/Torr], $B = 365$ [V/cm/Torr], and $\gamma_{se} = 0.01$ [24].

At moderate gap distances and pressures, the breakdown voltage is approximately proportional to the product of pressure and gap distance (pd). However, at extremely low values of pd, Paschen's law suggests that a discharge might never occur. In practice, however, breakdown can still take place due to additional effects such as field emission or temperature variations, which are not initially accounted for in Paschen's law [112].

To address the limitation at high temperatures, we introduce a modified version of Paschen's law that incorporates thermal effects:

$$V_{B_1} = \frac{Bpd\frac{T_0}{T_g}}{\ln(Apd\frac{T_0}{T_g}) - \ln\left[\ln\left(1 + \frac{1}{\gamma_{se}}\right)\right]} \tag{6.6}$$

Here, $T_0 = 300K$ is the reference temperature, and T_g represents the gas temperature in the air gap. Despite this modification, experimental results indicate that Paschen's law remains valid only up to at temperatures around 2200K [113]. However, in arcing conditions, even after current commutation to the LC branch, the gas temperature in the gap is non-uniformed and may

remain above 2200K. This necessitates the exploration of alternative breakdown mechanisms for higher temperatures.

Note that the conventional use of Paschen's law for predicting breakdown voltage becomes unreliable for micrometer-scale gaps. This discrepancy arises because, in such very small gaps, the dominant breakdown mechanism transitions from the secondary electron to field emission, as discussed in [114]. But in circuit breakers the commutation time constant is large enough leading to a sub-mm gaps at the breakdown point, and Equation 6.6 is considered to be applicable.

Transition to Streamer Dominance

When the breakdown mechanism transitions from the Townsend avalanche to streamer, the local electron number density in the streamer head is so high that it sustains the ionization front by its own electric field. The breakdown behaviour becomes solely dependent on the inception electric field across the gap which is self-sustained by the streamer. This inception field can be estimated approximately as the critical field, i.e. the field at which the local production of electrons starts to exceed their losses (the electron attachment and detachment processes are balanced) [24]. Calculations indicate that the reduced critical dielectric strength of dry air remains relatively constant up to temperatures of 2000K. This observation is supported by published experimental data [26].

TABLE 6.1: Reduced critical electric field E_{cr}/N versus gas temperature (interpolated from [26])

Temperature (K)	E_{cr}/N **(Td)**
500 – 2000	≈ 115
3000	100
3500	85
4000	70
4500	60
5000	50

The relationship between the reduced critical field E_{cr}/N and gas temperature can be derived from experimental data and represented as an interpolation table. The corresponding data scatter is shown in Table 6.1:

This field strength is typically measured in Townsend (Td), where one Townsend is defined as:

$$1Td = 1 \times 10^{-21} \left[V \cdot m^2\right]$$

The breakdown field E_0 [V/m] can be determined as follows:

$$E_0 = E_{rd} \cdot N(T_g) \cdot \text{Td} \tag{6.7}$$

For a given temperature E_{rd} could be obtain from the Table 6.1 and the neutral particles number density $N(T_g)$ is given by:

$$N(T_g) = \frac{P}{K_b \cdot T_g} \quad [1/m^3] \tag{6.8}$$

where P is the pressure, K_b is the Boltzmann constant, T_g is the gas temperature.

It is reasonable to expect that for the breakdown at any point on the streamer path (which may have a different temperature) the local electric field at least exceeds E_0. The breakdown voltage can be found as a minimum of an integral taken along an arbitrary path connecting cathode and anode.

$$V_{B_2} = \min\left(-\int_{\text{anode}}^{\text{cathode}} \mathbf{E_0}(\mathbf{r}) \cdot \mathbf{dl}\right) \tag{6.9}$$

For short gaps the breakdown voltage can be approximately evaluated along the straight shortest path connecting the electrodes. In this case, the vector field $\mathbf{E}_0$ is aligned with the path **dl**, so the dot product simplifies.

$$V_{B_2} = \min\left(-\int_{\text{anode}}^{\text{cathode}} \mathbf{E}_0(\mathbf{r}) \cdot \mathbf{dl}\right) \approx \int_0^d E_0(z)\, dz \tag{6.10}$$

where $E_0(z)$ represents the **magnitude of the critical electric field strength** at any position z within the gap given by Equation 6.7, and d denotes the total electrode gap distance.

Although Equation (6.9) theoretically allows to find the breakdown path for the streamer, it is not practical to use it. Photoionization is known to have a strong effect on the streamer propagation including branching and in practice Equation 6.9 is only an indicator for the overall breakdown voltage. Under these circumstances, the simpler Equation **??** has the similar accuracy and Equation **??** is recommended.

Comparison of Thermal Runaway Criteria and the Breakdown mechanisms

The results presented in Figures 6.1 compare the breakdown voltage predicted by thermal runaway theory against Paschen's law (Fig 6.1a) and critical field theory (Fig 6.1b) across different gap distances (0.1–3 mm) and a wide gas temperature range (500–5000 K),assuming plane electrodes uniform temperature and electric field. The simulations reveal that: Based on the results shown in the Figures 6.1, when comparing Paschen's law and the thermal runaway model, it is evident that at temperatures below approximately 3000 K, the Paschen model predicts lower breakdown voltages than the thermal runaway model. This indicates that in the low-temperature region, breakdown is primarily governed by electron avalanche ionization, and typical gaps at initial stage of contacts separation more susceptible to Paschen-type breakdown. However, for high temperature above 3000 K, especially for small gaps ($\leq$0.5 mm), the critical voltage for thermal runaway drops sharply below the Paschen prediction, demonstrating that thermal instability becomes the dominant breakdown mechanism in short gaps at elevated temperatures.

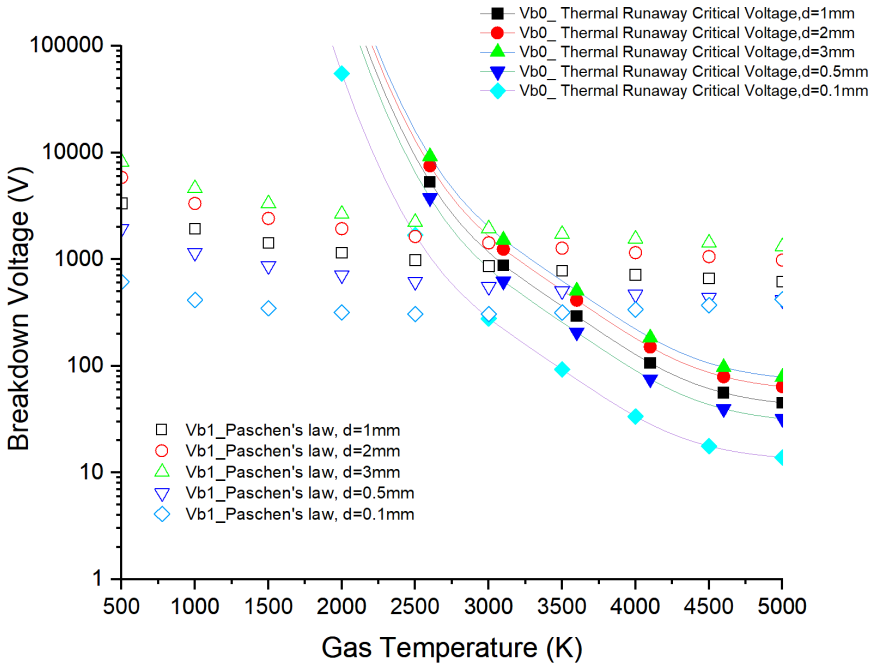

(A) Paschen's law vs Thermal Runaway Criteria

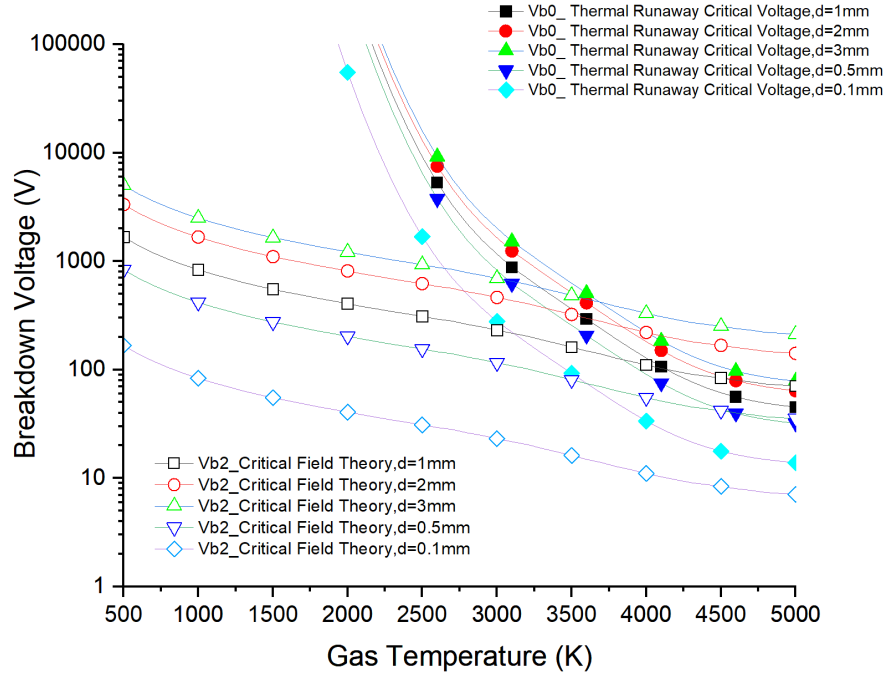

(B) Critical Field Theory vs Thermal Runaway Criteria

FIGURE 6.1: The comparison of the critical voltage from thermal runaway and breakdown voltage based on two breakdown mechanisms.

Therefore, it is essential to consider both mechanisms in simulations: the thermal simulation mainly captures the thermal runaway behavior, as we are concerned about the residual temperature distribution along the gap; but it is also crucial to monitor the potential for Paschen-type breakdown, because if breakdown occurs, it is simulated by artificially reducing the resistance

at the arc root once the breakdown voltage exceeds the arc root voltage, the implementation will be introduced in Equation 6.18. Additionally, according to the critical field model, breakdown can still occur at temperatures above 3000 K, meaning that in the intermediate-to-high temperature range, streamer inception driven by the critical field should also be considered to avoid underestimating the risk of breakdown in simulations.But the mechanism for such breakdown may deviate from Paschen law and has to be analysed.

6.2 Unified Breakdown Voltage Model

6.2.1 Experimental Verification of Paschen and Critical Field Breakdown Mechanisms

Based on the experimental data [113], the measured breakdown voltages are plotted against predictions from two classical models: a modified Paschen's law (V_{B1}) and the Critical Field Theory (V_{B2}), as shown in Figure 6.2. The comparison reveals a temperature- and gap-dependent transition between the two mechanisms. For temperatures below approximately 1000–1250 K, across all tested gap distances (0.1 cm, 0.3 cm, and 0.5 cm), the breakdown behaviour closely follows the Paschen curve. This is particularly evident in the 0.3 cm case, where data below 2000 K show excellent agreement with the modified Paschen model. However, as the temperature increases, deviations from Paschen behaviour emerge. For the 0.1 cm case, in the 2000–3500 K range, several data points (black square markers) fall between the Paschen and Critical Field predictions, other points are placed in between them, suggesting same sort of an intermediate regime. Similar transitions are observed in the 0.5 cm case, where breakdown behaviour begins to deviate from Paschen's law above 1500 K and shifts toward the critical field prediction around 2200 K.

These observations suggest that temperature plays a critical role in determining the dominant breakdown mechanism. While low-temperature breakdown is governed by the Townsend mechanism and follows the Paschen curve, higher-temperature cases exhibit signatures of streamer formation, which is better explained by the Critical Field Theory. To understand this regime shift, we further analyse the breakdown conditions using the Meek criterion and examine the physical parameters driving streamer inception.

6.2.2 Physical Interpretation of the Transition Between Breakdown Regimes

To interpret this transition quantitatively, we adopt the Meek-Loeb theory for streamer inception. The condition for an electron avalanche to transition into a streamer is that the head of the avalanche reaches a critical electron density N_e, sufficient to cause field distortion by to drive strong ionization in front of the head. The Equation (6.10) can be derived as shown in [24, 149]:

$$N_e = \frac{\varepsilon_0 \, \alpha_{\text{eff}}(E) \, E}{e} \tag{6.10}$$

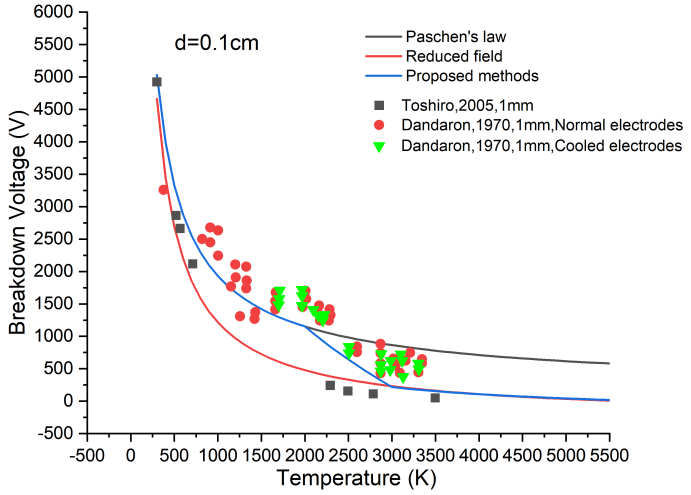

(A) 0.1cm

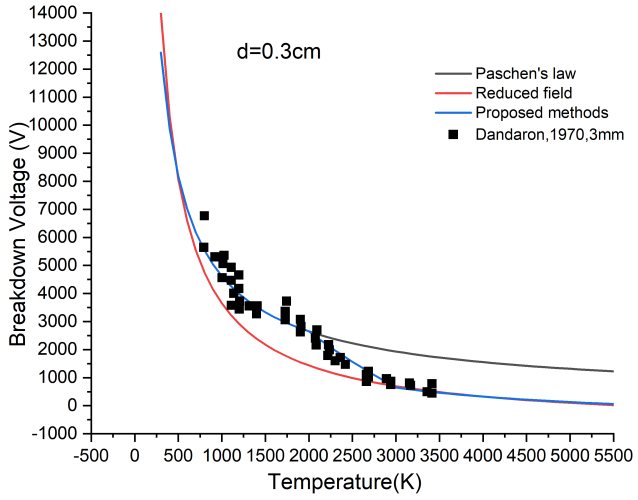

(B) 0.3cm

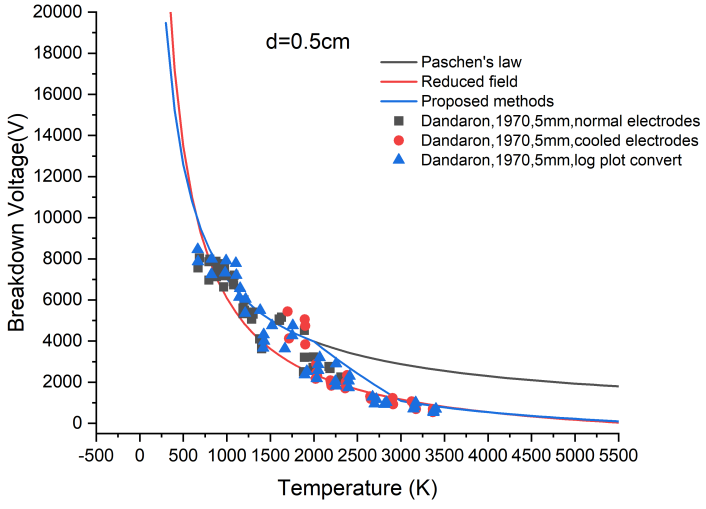

(C) 0.5cm

FIGURE 6.2: Experimental breakdown voltage [113] plotted against predictions from modified Paschen's law, Critical Field Theory, and the proposed unified model, for various gap distances (0.1–0.5 cm) over a temperature range of 300–5000 K

where N_e is the electron density required for streamer initiation (in m^{-3}), ε_0 is the vacuum permittivity, α_{eff} is the effective ionization coefficient (m^{-1}) defined as $\alpha(E) - \nu(E)$, with α the first Townsend ionization coefficient (m^{-1}) and ν the electron attachment coefficient (m^{-1}), E is the electric field strength (V/m), and e is the elementary charge (1.6×10^{-19} C).

Given that both α_{eff} and E are commonly described as functions of the reduced electric field E/N, where N is the neutral particle density (m^{-3}), and applying the general scaling laws [150], the Meek criterion can be rewritten in reduced form as: [150]

$$N_e = N^2 \frac{\varepsilon_0}{e} \left(\frac{\alpha_{\text{eff}}}{N} \cdot \frac{E}{N} \right) \tag{6.11}$$

In our calculations, the value of α_{eff} is taken from the data presented in Fig.9 and Fig.10 of [26], and N is the neutral particle density, which decreases with increasing temperature according to the ideal gas law ($N \propto 1/T$).

This form shows that the required electron density for streamer initiation scales with the square of the neutral particle density. Therefore, as temperature increases, $N_e \propto 1/T^2$ decreases rapidly, making it easier to form streamers at high temperatures.

For example, at $T = 300$ K, $N \approx 2.4 \times 10^{25}$ m^{-3}, and the required N_e is known to be around 10^{18} m^{-3}. Applying the scaling law:

$$N_e(T) = N_e(300\ \mathrm{K}) \left(\frac{300}{T} \right)^2$$

At $T = 3000$ K, we obtain:

$$N_e(3000\ \mathrm{K}) \approx 10^{18} \left(\frac{300}{3000} \right)^2 = 10^{16}\ \mathrm{m}^{-3}$$

This aligns well with the Local Thermodynamic Equilibrium (LTE) electron density in air at high temperatures reported in the literature [149], indicating that streamer formation becomes spontaneous at elevated temperatures due to sufficient thermally generated charge carriers.

To incorporate the enhanced field at the avalanche tip, Raizer's textbook [24] suggests that the ionization coefficient should be taken at $E = E_0 + E' \approx \frac{4}{3}E_0$, where E_0 is the critical field and E' represents the local field enhancement.

The equilibrium electron density N_e^{eq} for air plasma can be estimated from LTE simulations. According to calculations [149], a strong increase in equilibrium electron density N_e^{eq} beyond 2750–6000 K is observed. To estimate the equilibrium electron density at lower temperatures (2000–2500 K), we referred to Figure 1-1 in [149], and the required electron densities are given in Table 6.2. Streamer inception occurs immediately when:

$$N_e^{\text{eq}} > N_e \tag{6.12}$$

TABLE 6.2: Calculated streamer threshold densities using the above formulation. Ne is calculated from (12) with α_{eff} is taken as suggested in [26]. N is calculated from (8) at P=1atm.

Gas Temperature T**(K)**	**Natural Desity** N**(m^{-3})**	**Enhanced Field** E**(Td)**	**Req. Electron Density** N_e**(m^{-3})**
300	2.4×10^{25}	153	4.88×10^{17}
2000	3.66×10^{24}	153	1.13×10^{16}
2500	2.93×10^{24}	140	6.65×10^{15}
2750	2.56×10^{24}	133	4.82×10^{15}
3000	2.4×10^{24}	127	4.05×10^{15}

If Equation (6.12) is not satisfied, the avalanche travels some distance d_{tran} before converting itself to the streamer, given by:

$$\alpha_{\text{eff}} \cdot d_{\text{tran}} \approx \ln\left(\frac{N_e}{N_e^{\text{eq}}}\right) \tag{6.13}$$

TABLE 6.3: Threshold analysis for streamer breakdown: required vs. equilibrium electron density at various temperatures.

Gas Temperature T (K)	**Req. Electron Desity** N_e (m^{-3})	**Equilibrium Electron Density** $N_e^{eq}(m^{-3})$	**Streamer Breakdown? & Req. Distance**
2000	1.13×10^{16}	3×10^{12}	No, $d_{\text{tran}} \sim 11mm$
2500	6.65×10^{15}	1×10^{15}	No, $d_{\text{tran}} \sim 4mm$
3000	4.05×10^{15}	5×10^{16}	Yes, $d_{\text{tran}} = 0mm$

After comparing the results at 2000 K, 2500 K, and 3000 K, the equilibrium electron density N_e^{eq} is significantly lower than the required threshold N_e, indicating an increasing probability that streamer will not be formed. At 3000 K, however, the equilibrium density exceeds the threshold, which suggests spontaneous streamer formation. It means that at $T > 3000$K, 1atm, the critical field theory should be used to determine breakdown voltage.

In addition to the electron density threshold, the Meek criterion as expressed in Equation (6.14) includes a spatial condition: the avalanche must develop over a sufficient length to accumulate enough ionization. For room temperature, this spatial growth condition is typically given by:

$$\alpha_{\text{eff}} \cdot d_{\text{tran}} \geq 20 \tag{6.14}$$

This relation implicitly assumes a low initial electron density n_0, typically on the order of 1–10 particles/cm^3, as commonly found in cold ambient air [24]. However, at elevated temperatures (e.g., 3000 K), the gas may become partially ionized even before any electrical avalanche develops. This process is driven by increased electron-neutral collisions, excitation, and molecular dissociation, leading to a rise in the equilibrium electron density N_e^{eq}.

Due to this high background ionization, the avalanche process may be shortened or even rendered unnecessary for generating a large number of electrons through exponential growth. Instead, the required charge density at the streamer head is already present within the gap. As a result, streamer inception can occur almost instantaneously, without requiring an extended avalanche development distance. It agrees well with experiments [113]. For small gaps of 1mm Paschen law works even at 2500K but for 5mm gaps the critical field theory (streamer) is more applicable at the same temperature. The experiment [113, 114], observed consistent streamer breakdowns at 3000 K occurring in small air gaps (e.g., 0.1–0.5 cm), extending the applicability of the proposed model to sub-millimeter gaps (e.g., <0.1 cm), where thermal pre-ionization enables streamer inception without the need for extended avalanche development.

However, at intermediate temperatures such as 2500 K, this condition is not always satisfied. As shown by the black dot markers in Figure 6.2a, some experimental data at very short distances deviate from the predictions of the critical field theory. This suggests that at these temperatures, streamer inception may still require a minimum avalanche length to meet the Meek criterion, and thermal pre-ionization alone is insufficient to trigger breakdown in all cases. Therefore, while the streamer model remains valid across a broad range of gap distances and temperatures, its direct applicability to sub-millimeter gaps depends on whether the equilibrium electron density exceeds the critical threshold for streamer formation.

6.2.3 Unified Predictive Model for Breakdown Voltage Across Multi-Regimes Conditions

To improve the predictability of breakdown behavior across a broad temperature range, two dominant regimes governing breakdown phenomena in air gaps are selected:

Low-temperature regime (below $T_1 = 2000$ K): The breakdown follows Paschen's law, with minimal thermal ionization and dominant electron-neutral collisions, marking the onset of electrical breakdown via the Townsend mechanism.

High-temperature regime (above $T_2 = 3000$ K): Thermal pre-ionization leads to elevated equilibrium electron density, and the breakdown transitions to a critical field-dominated mechanism, as predicted by the Meek criterion and streamer theory.

Based on this analysis, the full temperature range is segmented into four regimes:

- When $T_g < T_1(2000K)$, the breakdown voltage V_{break} is governed by V_{B1}, following Paschen's law.
- When $T_g > T_2(3000K)$, the breakdown voltage V_{break} is determined by V_{B2} based on the critical field theory.
- When $T_g > 5000$ K, the gas becomes quasi-conductive and the breakdown voltage rapidly approaches zero, where $V_{\text{break}} \approx 0$ V.

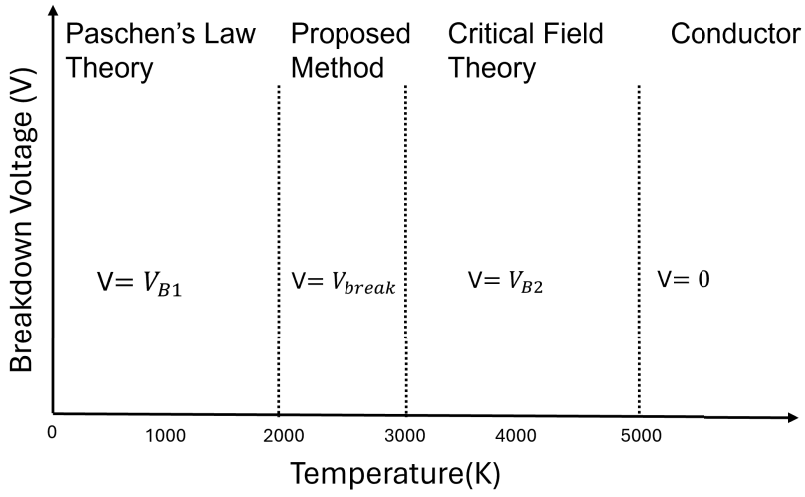

FIGURE 6.3: Schematic representation of breakdown voltage prediction.

- For intermediate temperatures within the range $T_1 \leq T_g \leq T_2$, the breakdown process is in transition, and both mechanisms contribute. It corresponds to an initial Townsend avalanche followed by a streamer.

To smoothly interpolate between V_{B1} and V_{B2} in the transitional regime, a linear weighting model is proposed:

$$V_{\text{break}} = A \times V_{B1} + B \times V_{B2} \tag{6.15}$$

where the weighting factors A and B are functions of temperature, defined as:

$$A = \frac{T_2 - T_g}{T_2 - T_1}, \quad B = \frac{T_g - T_1}{T_2 - T_1} \tag{6.16}$$

with the condition:

$$A + B = 1 \tag{6.17}$$

This interpolation ensures a smooth and physically consistent transition between the Townsend avalanche and streamer-driven breakdown mechanisms, enabling accurate prediction of breakdown voltages across the full range of the post-commutation stage for compact circuit breakers. A schematic illustration of the temperature-dependent behavior is provided in Figure 6.3, which categorizes the breakdown regimes and marks the transition thresholds based on the experimental and theoretical data in [113].

6.2.4 Experimental Comparison and Error Analysis

As shown in Figure 6.2, the proposed method maintains good accuracy across a wide temperature range. For instance, for the 0.3 cm gap case at 2700 K, the predicted breakdown voltage (1186 V) closely matches Dandaron's experimental value (1222 V) [113], yielding an error of only 2.9%. Across different gap sizes, Figure 6.3 demonstrates the adaptability of the temperature-dependent model. In high-temperature regions, such as 3500 K, traditional

Paschen's law significantly overestimates the breakdown voltage (1718 V) compared to the experimental value (449 V). In contrast, the proposed method reduces the prediction error to within 3.5% (predicted value 465 V).

In summary, the comparison between experimental breakdown voltage data and the model predictions for a gap of $d = 0.5$ cm is listed in Table 6.3. The selected temperatures correspond to available experimental data within the transition regime:

At 2100 K, the modified Paschen law remains reasonably applicable, with an error of approximately 13.7%. Although it slightly overestimates the breakdown voltage, it still captures the general trend, as thermal ionization is relatively weak and the breakdown process remains largely governed by electron-neutral collisions.

At 2400 K, the error of the modified Paschen law increases to approximately 13.7%, continuing to slightly overestimate the breakdown voltage but still capturing the trend due to limited thermal ionization.

At 2900 K, the discrepancy becomes more pronounced. The modified Paschen model yields a breakdown voltage more than twice the experimental value, with an error close to 59%. Meanwhile, the proposed model maintains good accuracy with only 9.7% deviation, demonstrating its capability to capture the correct breakdown behavior in the high-temperature transition zone approaching 3000 K.

These results validate the effectiveness of the proposed model in bridging the prediction gap across multiple temperature regimes, particularly where neither traditional Paschen's law nor the critical field theory alone is sufficient.

TABLE 6.4: Comparison of breakdown voltage predictions in transition regime

T_g **(K)**	**Experimental (V)**	**Modified Paschen Law (V)**	**Present Model (V)**	**Error (%)**
2100	3208	3830	3649	13.7%
2400	2302	3440	2716	18%
2900	1222	2958	1341	9.7%

6.3 Application in LC Commutation-Based Breakers

While the previous section (Section 6.3) focused on the theoretical foundation and validation of breakdown models under controlled conditions, the practical relevance of these models depends on their behaviour under realistic switching scenarios. In LC commutation-based Direct Current (DC) circuit breakers, voltage recovery dynamics and thermal non-uniformities strongly influence reignition behaviour. Therefore, in this section, the proposed hybrid breakdown model (Equation 6.15)is implemented to control the arc sheath within an LC commutation framework to assess reignition risk and evaluate the influence of circuit and cooling parameters on dielectric recovery.

TABLE 6.5: Circuit Parameters for LC commutator based CBs

Parameter	Value	Unit	Description
V1	1000	[V]	Power supply
L1	10	[mH]	Line inductance
R1	2.1	[Ω]	Line resistance
R2	0.0075	[Ω]	LC circuit resistance
L2	227	[nH]	Commutation inductor
C1	208/104	[μF]	Commutation capacitor
R3	0.001	[Ω]	Electrodes resistance
L_{arc}	50	[nH]	Arc core inductance
R4	Equation 6.18	[Ω]	Arc fall resistance
R5	0.01	[Ω]	Ground resistance

6.3.1 Model Implementation

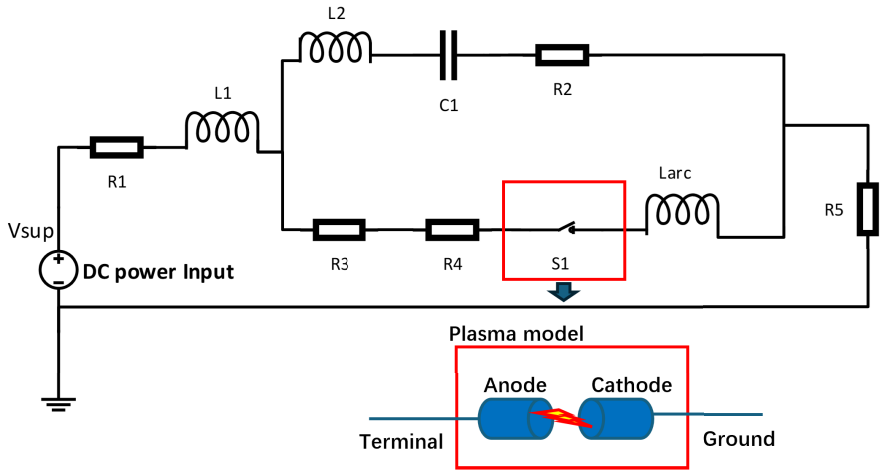

FIGURE 6.4: Schematic of the equivalent electric circuit of circuit breaker coupled with physic arc model

Circuit Working principle

In this study, a conventional DC commutation-type circuit breaker is used, following the design proposed in [17]. The equivalent circuit is shown in Figure 6.4, and the main parameters are listed in Table 6.5. The system includes a DC power source, an LC commutation loop, a physical arc model, and several resistive elements for damping and energy dissipation. The power supply ($V_1 = 1000\,\mathrm{V}$) feeds the current through the line inductance $L_1 = 10\,\mathrm{mH}$, which stores energy before the interruption. This corresponds to an initial current of about 435 A flowing in the main loop. The resistance $R_1 = 2.1\,\Omega$ in series with the inductor accounts for the line impedance and helps to dampen the circuit response.

At the moment of contact separation ($t = 0$), an arc is struck between the anode and cathode. The current continues to flow through the arc path, which includes the electrode resistance

$R_3 = 0.001\,\Omega$, the arc core inductance $L_{\text{arc}} = 50\,\text{nH}$, and a nonlinear sheath resistance R_4 defined in Equation 6.18. Meanwhile, the pre-charged capacitor $C_1 = 208/104\,\mu\text{F}$ is switched into the circuit in series with a small commutation inductor $L_2 = 227\,\text{nH}$ and resistance $R_2 = 0.0075\,\Omega$. Together, they form an LC loop that produces a high-frequency oscillation. Since the polarity of C_1 is opposite to the source, the resulting oscillation injects a reverse current into the arc.

As this commutation loop works, the oscillating current adds to the arc current. When the oscillation becomes strong enough to cancel out the DC component, the total current reaches zero. This provides the condition for the arc to extinguish. However, because the DC voltage is still present, the insulation must recover quickly to prevent reignition. The sheath resistance R_4 plays an important role here. It decreases under high current and increases sharply as the current nears zero, which helps dissipate energy and raises the sheath voltage to prevent re-ignition.

After the arc is extinguished, the remaining energy in the circuit is released through the resistors R_1 and $R_5 = 0.01\,\Omega$. This allows the circuit to return to a stable, non-conductive state.

Implementation of Nonlinear Sheath Resistance R4

The nonlinear sheath resistance $R4$ is introduced to capture the voltage saturation and negative resistance characteristics of the near-electrode sheath region. Its mathematical formulation is expressed as:

$$R4 = \frac{\mathbf{V}_{\text{break,sh}} \cdot (4 \cdot \mathbf{I}_{cr})}{(|IR4| + \mathbf{I}_{cr})^2} + \frac{V_{\text{sheath}}}{|IR4| + \mathbf{I}_{cr}} \tag{6.18}$$

Here, $\mathbf{V}_{\text{break,sh}} = V_B(T_u) + V_B(T_l)$ represents the total breakdown voltage across the sheath, calculated using the hybrid breakdown model (Equation 6.15) based on the temperatures T_u and T_l measured near the upper and lower electrode edges, respectively. The term $V_{\text{sheath}} = 16\,\text{V}$ denotes the intrinsic voltage drop across the sheath, as experimentally validated in [106, 151], while the critical current $\mathbf{I}_{cr} = 0.01\,\text{A}$ reflects the transition point between conduction regimes in the sheath, derived from the inflection point in the V-I characteristics presented by Najam et al. [151].

This expression comprises two additive components that together reproduce the essential physics of sheath behavior. The first term models voltage saturation effects. When the current $|I_{R4}|$ equals $\mathbf{I}_{cr}$, this term simplifies to $\mathbf{V}_{\text{break,sh}}/\mathbf{I}_{cr}$, producing a voltage drop of exactly $\mathbf{V}_{\text{break,sh}}$. This design ensures that the sheath reaches its characteristic voltage peak at the critical current, mimicking the transition from a high-resistance state to a conductive state. The scaling factor of 4 is chosen to achieve this matching condition and has no standalone physical meaning.

For current values much smaller than $\mathbf{I}_{cr}$, this first term yields a high resistance, representing the poorly conducting state of the sheath. Conversely, as the current increases beyond $\mathbf{I}_{cr}$, the term decreases rapidly (proportional to $1/I^2$), capturing the rapid drop in sheath impedance observed during high-current conduction.

The second term accounts for the intrinsic voltage drop across the space-charge-dominated region of the sheath, contributing a current-dependent resistance that decreases linearly with current (i.e., $\propto 1/I$). This reflects the classic negative resistance behavior where higher currents reduce the effective resistance of the sheath. The use of $|I_{R4}| + \mathbf{I}_{cr}$ in the denominator of both terms ensures numerical robustness, avoiding singularities at zero current and smoothing the transition across different conduction states.

Overall, this composite resistance expression enables accurate modeling of the sheath's nonlinear dynamic response. At low currents, the resistance is high, representing the difficulty in sustaining conduction; near $\mathbf{I}_{cr}$, the sheath voltage peaks due to saturation effects; and at high currents, the resistance falls rapidly, allowing enhanced conduction.

6.3.2 Dynamic Coupling Between Arc Reignition, Near-electrode Cooling and Circuit Parameters

To investigate the dynamic correlations between reignition (or successful interruption), near-electrode cooling rate and circuit parameters in mechanical DC circuit breakers, two capacitance values, 104 μF and 208 μF, were selected to represent cases with different commutation speeds, similar to experiments in [17]. These values of the capacitance C was chosen because C directly determines the duration of the commutation current decay and the slope of the capacitor voltage rise: a smaller capacitance (104 μF) produces faster commutation with a steeper voltage increase, while a larger capacitance (208 μF) results in slower commutation with a more gradual voltage rise, allowing a systematic comparison of their impact on gap insulation recovery.

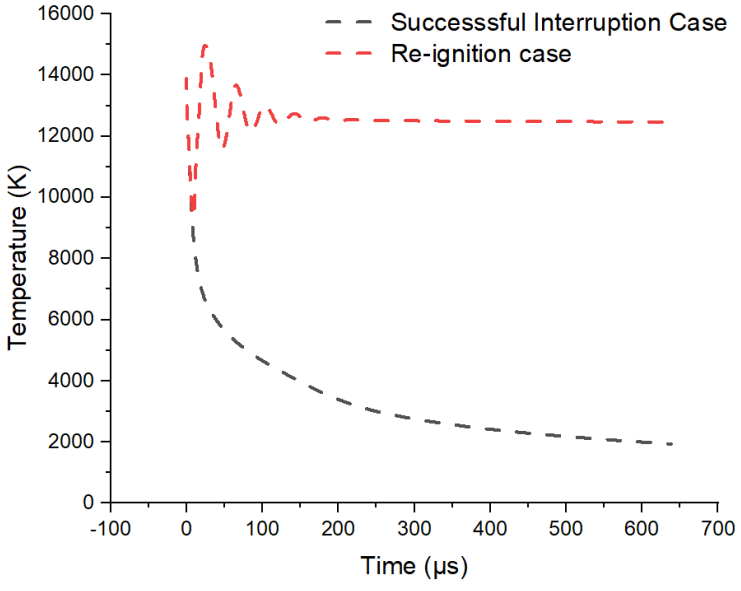

FIGURE 6.5: Average Temperature distribution along the centreline of Gap via different time instances

Theoretical breakdown voltage curves were derived by substituting the average temperature profile based on our simulation, as shown in Figure 6.5, into the respective breakdown voltages

for R4 (Table 6.5), while the integrated gap+sheath breakdown voltage, based on Equation (**??**), considered the entire non-uniform temperature field along the gap to capture the local variations in insulation strength and plotted on Figure 6.6 and Figure 6.8 (A).

In the voltage profiles as shown in Figure 6.6 and Figure 6.8 (A), the black solid line represents the voltage across the commutation capacitor (C1), the red line shows the arc core voltage (reflecting the sustaining potential of the plasma column), and the blue line indicates the arc fall voltage (corresponding to the sheath voltage drop near the electrodes). The green scatter points represent the combined breakdown voltage of the gap and sheath calculated by integrating the non-uniform temperature distribution across the gap, providing an accurate threshold for reignition. Additionally, dashed red, black, and blue lines correspond to theoretical breakdown voltages calculated from the time-evolving average gap temperature using Paschen's law, critical field theory, and thermal runaway models, respectively.

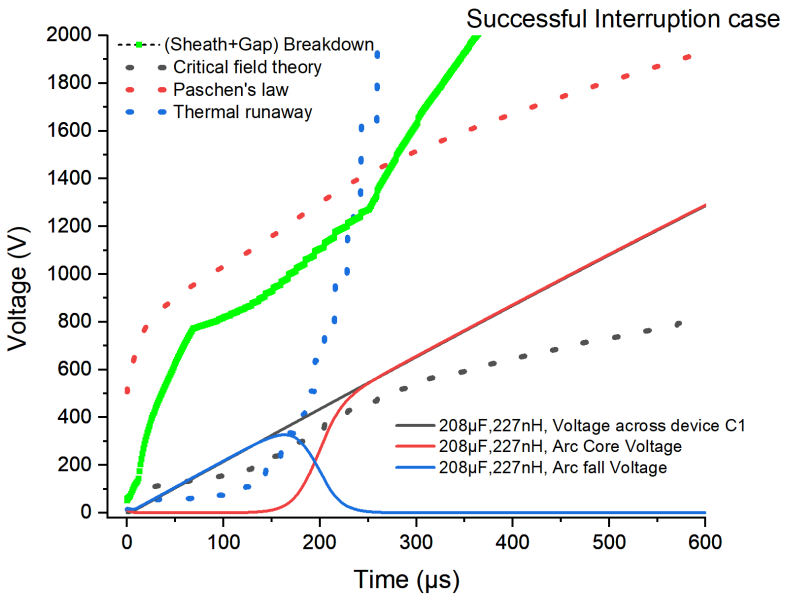

FIGURE 6.6: Case 1: Voltage profile across each device from 0.01 μs to 600 μs, when $C_1 = 208[\mu F]$, $L_2 = 227[nH]$

Case 1: 208 μF (Successful Interruption)

In the 208 μF case, the current waveform (in Figure 6.7) shows that the commutation process is initiated immediately at the simulation start (0 μs) because the model includes an initial contact gap and the arc already exists at the start of the simulations, and the arc current rapidly decays to zero within approximately 9 μs. Meanwhile, the capacitor current rises smoothly to take over the main current, indicating effective commutation. The voltage plot (in Figure 6.7 (A)) shows the capacitor voltage (black solid line with square marker) rising linearly from the start, while the arc fall voltage (blue solid line with triangular marker) increases during 150 μs. It indicates that the small current still flows through the hot plasma gap as shown in Figure 6.7 (B) (as the thermal runaway voltage is low than voltage of capacitor), although the impedance of this gap is high and the main current goes to the capacitor C_1. But between 150-250 μs the fall voltage

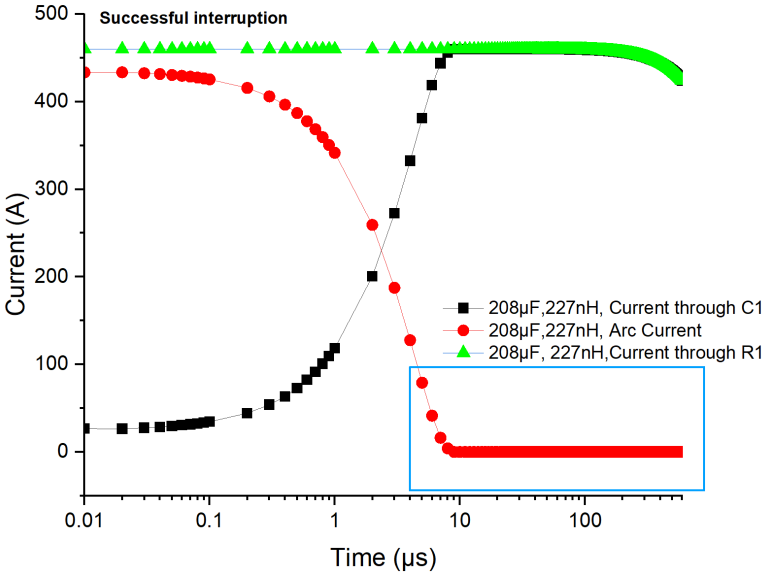

(A) Current profile goes through each device from 0.01 μs to 600 μs, when $C_1 = 208[\mu F]$, $L_2 = 227[nH]$

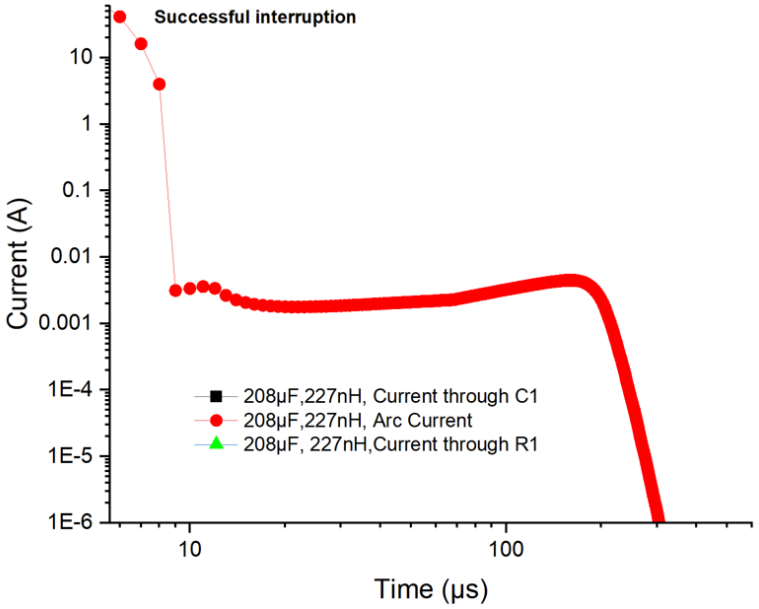

(B) Enlarge Current profile for 5 μs to 600 μs, when $C_1 = 208[\mu F]$, $L_2 = 227[nH]$

FIGURE 6.7: Case 1 Current profile goes through each device from 0.01 μs to 600 μs

drops to zero because the gap is cold enough to become dielectric air. During this transition, the current goes to almost completely zero as commutation completes, and the gap core voltage (red solid line with circular marker) continues to rise becoming equal to C_1 voltage. After 250μs, the air gap is dielectric without any sheath. Crucially, the integrated breakdown voltage (black dash-dotted line with green diamond marker) remains significantly higher than the actual gap voltage (sum of arc fall and arc core voltages) throughout the commutation process, ensuring no reignitions occur. At time 150-250 μs, the transition between arc core and arc sheath is

observed. The average temperature curve (Figure 6.5) during this period shows rapid cooling of the gap, with the temperature falling from 4000 K to 3000 K within these 100 μs. This indicates that the slower voltage rise resulting from the larger capacitor allows sufficient time for the boundary layer and gap to cool, enabling the insulation strength to recover before the gap voltage can exceed the breakdown threshold, ensuring successful interruption.

Case 2: 104 μF (reignition):

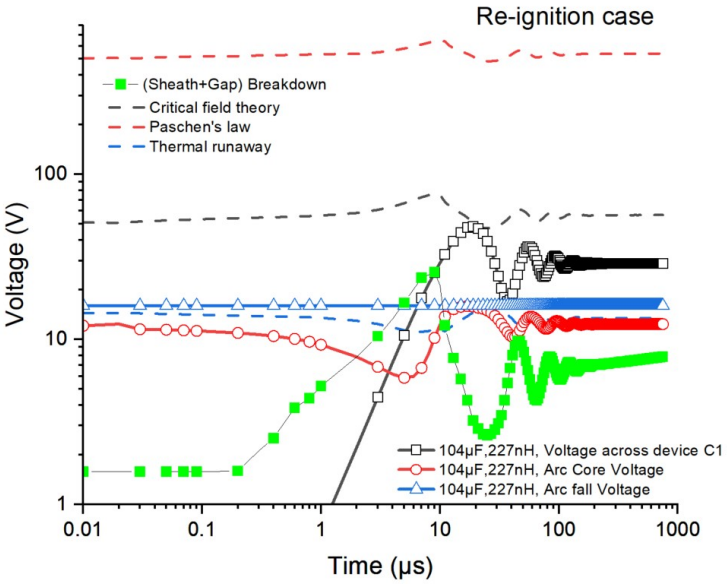

(A) Voltage profile across each device from 0.01 μs to 1000 μs, when $C_1 = 104[\mu F]$, $L_2 = 227[nH]$

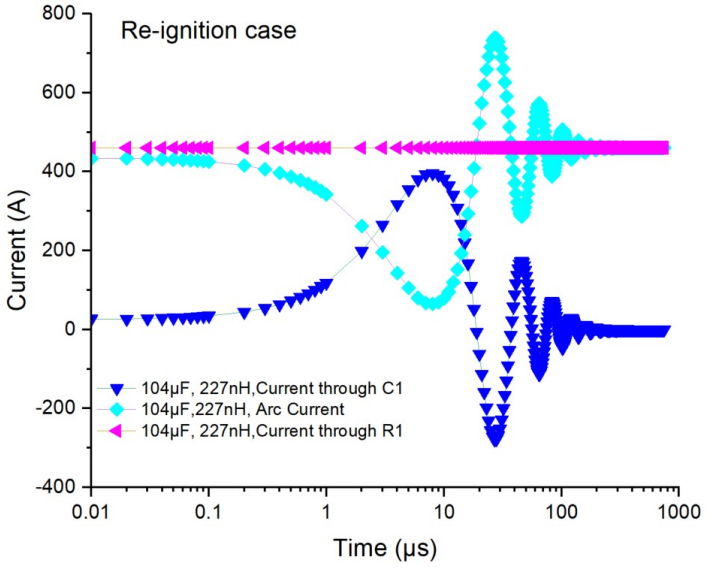

(B) Current profile goes through each device from 0.01 μs to 1000 μs, when $C_1 = 104[\mu F]$, $L_2 = 227[nH]$

FIGURE 6.8: Case 2 Voltage and Current waveform

In the 104 μF case, although the commutation starts normally and arc current briefly drops

between 1–8μs, it soon undergoes pronounced oscillations, returning to the initial current magnitude, indicating unsuccessful commutation. At t is around 8μs, the gap voltage (equal to C_1) exceeds breakdown voltage (green dots) breaking through the gap, the current starts to rise and the arc re-establishes. The voltage rise and current going through. The voltage plot reveals a steeper rise in capacitor voltage due to the smaller capacitance, causing the actual gap voltage to exceed the integrated and breakdown voltages while the average gap temperature remains above 10,000 K (the main cooling happens at thin surface layers). This mismatch between the rapid voltage increase and the slow cooling rate of the gap leads to the reignitions. Particularly, the crossings of the actual gap voltage with the predicted breakdown voltage (green points) as shown in Figure 6.8 (A) clearly demonstrate the time of the reignition and that the insulation strength recovery lags far behind the rapid voltage rise, confirming the root cause of the reignition.

The key insight from these cases is that the capacitor value C governs the duration of the commutation current decay and the voltage rise rate across the gap, while the gap insulation strength recovery depends on the thermal dissipation time constant of the gas and surface boundary layers. When the capacitance is too small (104 μF in this example), the gap voltage increases much faster than the cooling rate of the gap can reduce the temperature, causing the gap voltage to exceed the breakdown threshold before the insulation recovers, leading to reignitions. Conversely, with a larger capacitance (208 μF), the commutation duration is sufficiently long to allow the sheath and gap to cool synchronously with the voltage rise, preventing reignitions.

6.3.3 Temperature Evolution from Arc Phase to Fully Insulating Gap

Figure 6.9 illustrates the spatial temperature distribution at two representative time points: $t = 125\,\mu s$ and $t = 225\,\mu s$, capturing the physical transition from an arc phase with a cold boundary layer (and small leaking current through the gap) to a fully insulating dielectric gap at 250 μs, see Figure 6.7. At $t = 125\,\mu s$, a thin cold layer is clearly formed at the electrodes surfaces, while the central region remains relatively hot. This temperature gradient corresponds to the electrical condition where the central region is a good conductor, but the cold boundary layer demands high arc full voltage while the capacitor voltage continues to rise slowly remaining below the breakdown threshold of the gap.

By $t = 225\,\mu s$, the entire gap temperature falls below $4000\,K$, indicating that the originally hot ionized core has fully cooled. This transition aligns with the voltage evolution shown in earlier figures: the increasing capacitor voltage is no longer sufficient to drive even low current through the gap, and also it cannot re-ignite the arc due to the significant rise in breakdown voltage caused by whole gap cooling. Consequently, the gap enters a dielectric phase capable of withstanding higher voltages without electrical breakdown.

This result confirms the capability of the model to capture the full transition from plasma conduction to dielectric insulation. It also provides quantitative guidance for interrupting devices with smaller capacitance. For instance, when the capacitor value is reduced (e.g., to 104 μF), the commutation occurs too quickly, and the surface boundary layer does not have enough time to

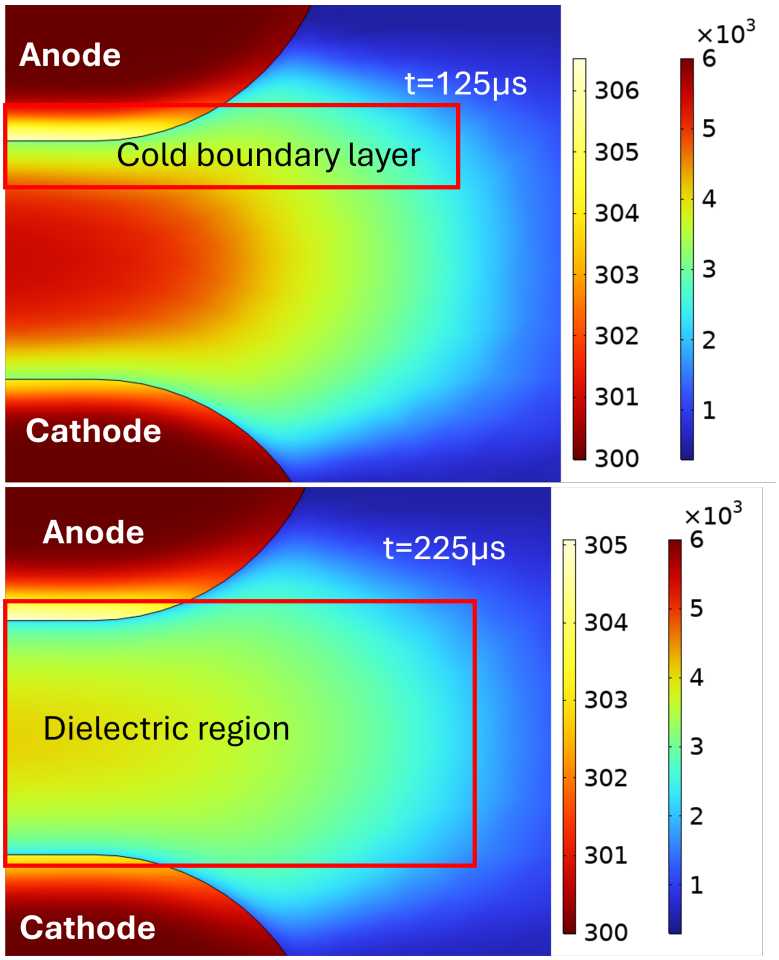

FIGURE 6.9: Simulation results of physic transformation from thin cold layer to a whole dielectric gap,example of C=208μF

fully cool, leading to reignition. However, based on the physical evolution seen here, extending the cooling window by approximately 100 μs is sufficient to ensure complete arc quenching. This could be achieved either by slightly increasing the snubber capacitance, or by enhancing thermal conductivity through electrode material selection or surface treatments that accelerate boundary layer cooling.

6.4 Summary

This Chapter, as shown in Figure 6.10 developed a comprehensive framework for predicting electrical breakdown in heated short air gaps by combining theoretical models and experimental evidence. The analysis began with the derivation of the thermal runaway criterion, highlighting the competition between Joule heating and boundary heat dissipation, which dominates at elevated temperatures. Subsequently, the applicability of classical Paschen's law was assessed, and a modified formulation incorporating thermal effects was introduced. While Paschen's law effectively describes breakdown behaviour at low temperatures and moderate pd values, its accuracy deteriorates when the gas becomes rarefied above approximately 2200 K.

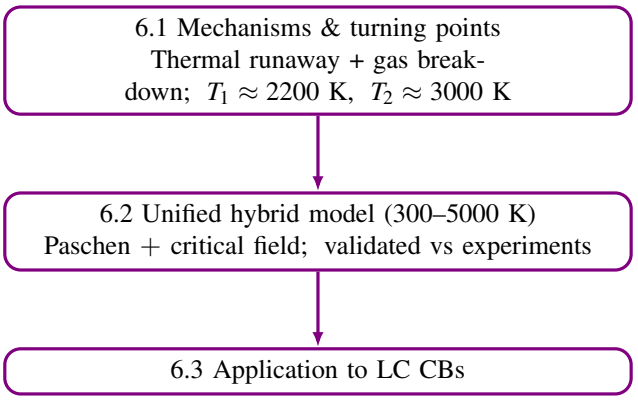

FIGURE 6.10: Chapter 6 Overview

To address this limitation, the Critical Field Theory and the transition from Townsend avalanche to streamer were investigated. Using Meek's criterion and electron density analysis, it was shown that streamer inception becomes increasingly probable as temperature rises, owing to the strong reduction in the required electron density and the exponential drop in breakdown field strength. Experimental comparisons confirmed a temperature-dependent shift in the dominant mechanism: Paschen-type breakdown governs low-temperature regimes, whereas thermal instability and field-driven streamer processes dominate beyond 3000 K, particularly for sub-millimetre gaps.

Building on these findings, a unified hybrid model was formulated to combine the strengths of the Paschen approach and the Critical Field method through a temperature-segmented interpolation. Validation against experimental data demonstrated that the proposed model significantly reduces prediction error compared with conventional methods, ensuring reliable estimates across 300 K–5000 K and various gap distances. Then it introduced the application of temperature-segmented hybrid breakdown model and implemented it within an LC commutation framework to assess reignition risk under practical operating conditions. Two post-commutation regimes were identified: an initial sheath-controlled phase and a subsequent dielectric-dominated phase as the gap cools. The analysis revealed that the dynamic matching between near-electrode cooling and capacitor-driven voltage recovery is critical for preventing arc reignition. Specifically, larger commutation capacitors slow the voltage rise, allowing sufficient cooling time and increasing the breakdown threshold, while smaller capacitors accelerate voltage recovery and heighten the risk of premature breakdown.

The combined findings provide both a mechanistic understanding of post-arc behaviour and a predictive tool for breaker design. They highlight the importance of enhancing dielectric recovery—either by prolonging the cooling interval (e.g., beyond 100 μs) or by increasing the arc fall voltage through design measures. These results offer practical guidelines for selecting capacitance values, optimising electrode configurations, and improving reliability in compact DC circuit breakers.

Chapter 7

Application of Multiphysics Arc Modelling to Low-Voltage DC Switches: Effects of Magnetic Fields and Contact Motion

While the previous chapter focused on re-ignition phenomena and hybrid breakdown modelling in LC commutation-based breakers, these findings primarily addressed in middle range of Direct Current (DC) applications (1-5kV). To fully demonstrate the versatility and practical relevance of the developed modelling framework, this chapter investigates arc dynamics in low-voltage DC switching devices, where compact geometries, permanent magnets, and fast contact motion create unique challenges for arc extinction. As highlighted in Research Gap 2 (Section 2.2.4), the combined influence of magnetic forces and variable-speed contacts remains poorly understood. Here, we apply a multiphysics arc simulation approach, coupled with experimental validation, to elucidate the stage-dependent roles of magnetic fields and contact velocity, and to identify design parameters that accelerate interruption in low-voltage switches.

7.1 Model Formulation

7.1.1 Assumption and Justification

The simulation setup of the entire system of Figure 2.18 in Chapter 2 involves several sub-models. These include the thermal plasma model, which is coupled to an external circuit, and a simplified near-electrode model designed for computational efficiency. While these simplifications reduce computational cost and allow for parametric studies, they inevitably introduce certain limitations in representing near-electrode non-equilibrium effects and 3D flow. However, the model retains the dominant physicals mechanisms controlling arc dynamics—such as Joule

heating, Lorentz force, and convective cooling—required to capture the essential arc dynamics observed experimentally. The following key assumptions enable this simplification:

Thermal Arc Model

The plasma is treated as a continuum and the arc column region is assumed to be in a state of Local Thermodynamic Equilibrium (LTE). In this open configuration, pressure variations are relatively small, and prior studies [129], [21, 37, 108, 152] have shown that assuming thermodynamic properties at 1 atmosphere is a valid approximation for modelling arc behavior in similar conditions.

Due to the complexity of modelling arc initiation via the molten bridge, the initial processes at the contact separation are not modelled, but instead, a Gaussian temperature distribution is used to approximate the initial conditions for a 200 μm air gap,similar to [37, 93].

The flow pattern is assumed to be laminar as in [119, 129, 143, 152]. This assumption is supported by the relatively low Reynolds number in the arc region, which arises from the moderate flow velocities and high gas viscosity at elevated temperatures.

Radiation losses are simplified by using a Net Emission Coefficient (NEC) approach [144] rather than solving the full radiative transfer equation,same as in chapter 3.

The modelling of the arc column is based on a conventional Magnetohydrodynamic (MHD) equations, which combines the conservation laws governing plasma fluid dynamics with Maxwell's equations to describe the electromagnetic field [93, 108]. Buoyance force and Lorentz force are also included as additional terms in the momentum equation, same as in Chapter 3.

The arc root phenomena were ignored and replaced by a simplified near-electrode boundary layer model, as detailed in the following section.

Near-electrode Boundary layer model

In [96] and [93], it was determined that a thin boundary layer provides a reasonable description of the thermal arc interaction with the electrodes. Within this boundary layer, all ionization processes occur. The layer is not modelled directly, but instead it is approximated as a fixed voltage drop across the sheath, as described in [24], representing the non-equilibrium region near the electrode surface. Rather than explicitly resolving the complex physics of the sheath, including charge separation and energy exchange, the model applies effective boundary conditions at electrodes and plasma domain that account for the net voltage drop and ensure conservation of charge and heat fluxes at the electrode interface.

The boundary layer thickness is set to 0.1 mm, consistent with previous studies [93]. Electrode heating is modeled based on conductive heat transfer from the adjacent plasma, where energy is primarily delivered by ions and neutral atoms. Arc cooling in this region is dominated by thermal conduction carried by heavy particles (i.e., ions and neutrals), which transport energy from the hot arc core to the cooler electrodes [93] during their collisions with the surfaces.

Geometry simplification

The model geometry is based on the experimental device described in [16]. The computational domain consists of an open-air region and solid AgSnO2 electrodes. The round electrodes are represented by their diametral cross-section of rectangular shape, measuring 4 mm in height and 1 mm in width. The edges of the electrodes are filleted with a radius of 0.2 mm to represent the curved edges. To facilitate a moving mesh, an outer enclosing rectangular region of 50 μm thickness is added. The background region itself is a rectangle with dimensions of 160 mm in width (x-axis) and 130 mm in height (y-axis), the electrodes are placed in the middle of the computational domain is shown in Figure 7.1.

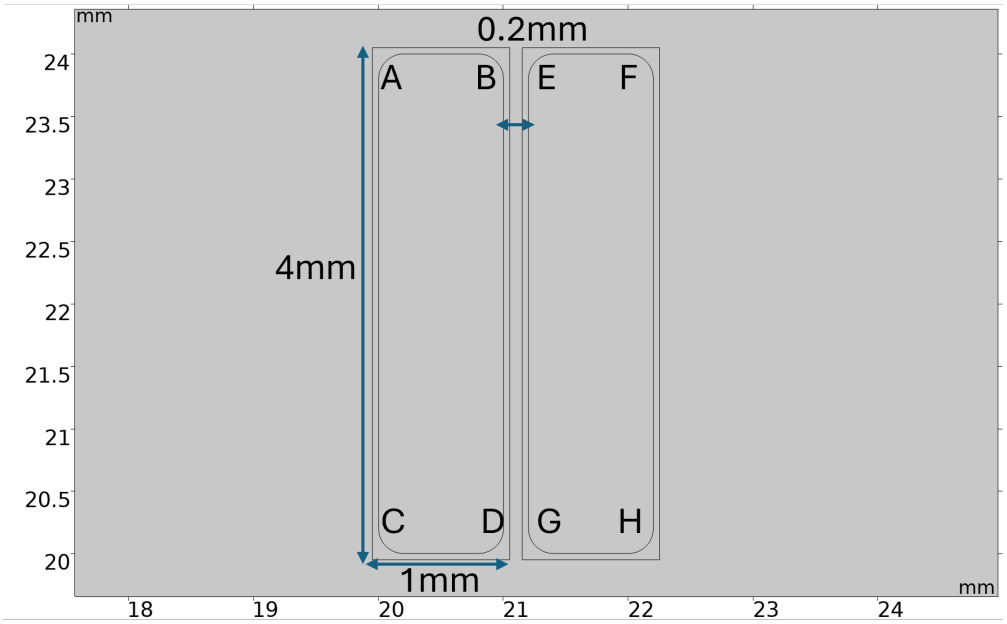

FIGURE 7.1: Details of the computational domain of two electrodes, with the external background region width of 160 mm and a height of 130 mm (the extend of this domain is not shown)

To balance computational accuracy and efficiency, the simulation employs a 2D axisymmetric model coupled with an out-of-plane thickness parameter to represent three-dimensional arc phenomena. As shown in Figure , the computation solves the electric potential and current continuity equations in the 2D plane while extending the results to 3D space through the specified depth parameter.

The coupling between the 2D computational model and the physical arc depth is mathematically established by incorporating the out-of-plane thickness parameter d into the physical equations. Specifically, the current density obtained from the 2D simulation $\mathbf{J}_{2D}$ is transformed into its 3D equivalent through the relation $\mathbf{J}_{3D} = \mathbf{J}_{2D} \cdot d$, effectively scaling the 2D results by the arc depth to represent the volumetric nature of the actual physical phenomenon. This approach extends to the calculation of total current, where the integration $I = \int \mathbf{J} \cdot d\mathbf{A}$ inherently contains the depth information within the differential area element $d\mathbf{A}$, ensuring that the computed current accurately reflects the three-dimensional conduction path through the arc region.

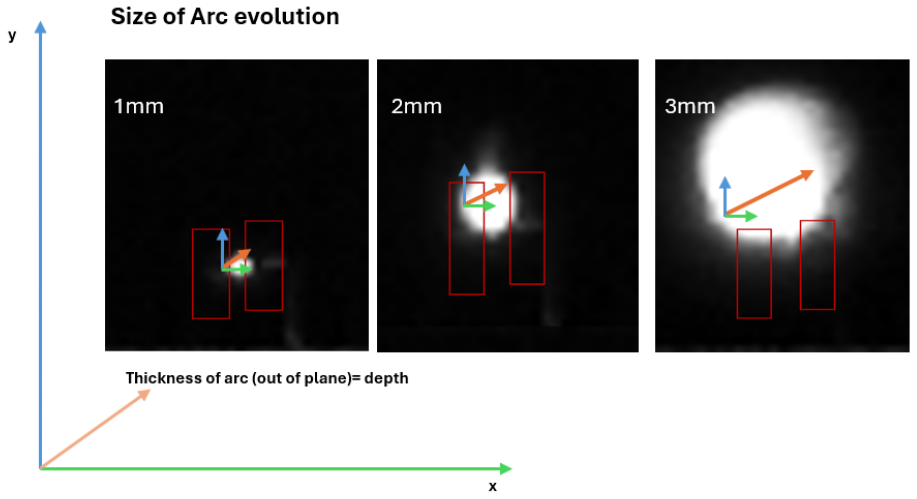

FIGURE 7.2: The key coupling mechanism is the incorporation of the **out-of-plane thickness (depth,** d), which represents the physical extent of the arc in the third dimension.

In the 2D model, all parameters have been translated into an equivalent thickness based on experimental data. In [16], variations in arc dimensions have been observed, with the arc depth ranging from 1 mm to 3 mm. To account for these variations, we introduce a time-dependent function for arc depth, which correlates with different stages of arc evolution. The timing of these stages is derived from experimental observations and depends on both time and moving velocity. Since these observations are based on specific experimental conditions, they may not be fully generalized to all scenarios, which presents a limitation of this study. To represent the arc depth variation in the 2D simulation, a time-dependent ramp function is introduced (Figure 7.3), where the initial arc depth (d_{ini}) is 1 mm, and the final depth (d_{fin}) reaches 3 mm. These values are not directly measured but inferred from experimental observations [16] under the assumption that the arc has a cylindrical shape, where the out-of-plane depth is approximated as equal to the observed 2D width. Although this introduces simplification, it provides a practical basis for capturing the effects of arc volume growth with electrode motion in a 2D model. The arc depth remain approximately constant at the later stages of the separation and taken as 3mm.

Coupled circuit

The arc model is coupled with the external power supply, and the parasitic parameters in the circuit are also considered. The value of each component is labeled in the Figure 7.4, and the minimal arc voltage is set to V_{sh} = 11 V based on the measurement from the experiments [16]. S1 represents the switching device model shown in Figure7.4, with the left contacts connected to the power supply circuit, and the grounded electrode moves with the fixed velocity.

Under a fixed voltage source with internal resistance R_s=R_n, two maximum power concepts are defined: (1) the maximum power that can be extracted from the power supply, given by $W_{\text{supply,max}} = \frac{V_{ps}^2}{R_s}$ when the circuit is effectively shorted (closed condition); and (2) the maximum power that can be deposited into the arc, given by $W_{\text{arc,max}} = \frac{V_{ps}^2}{4R_s}$ when the arc resistance matches

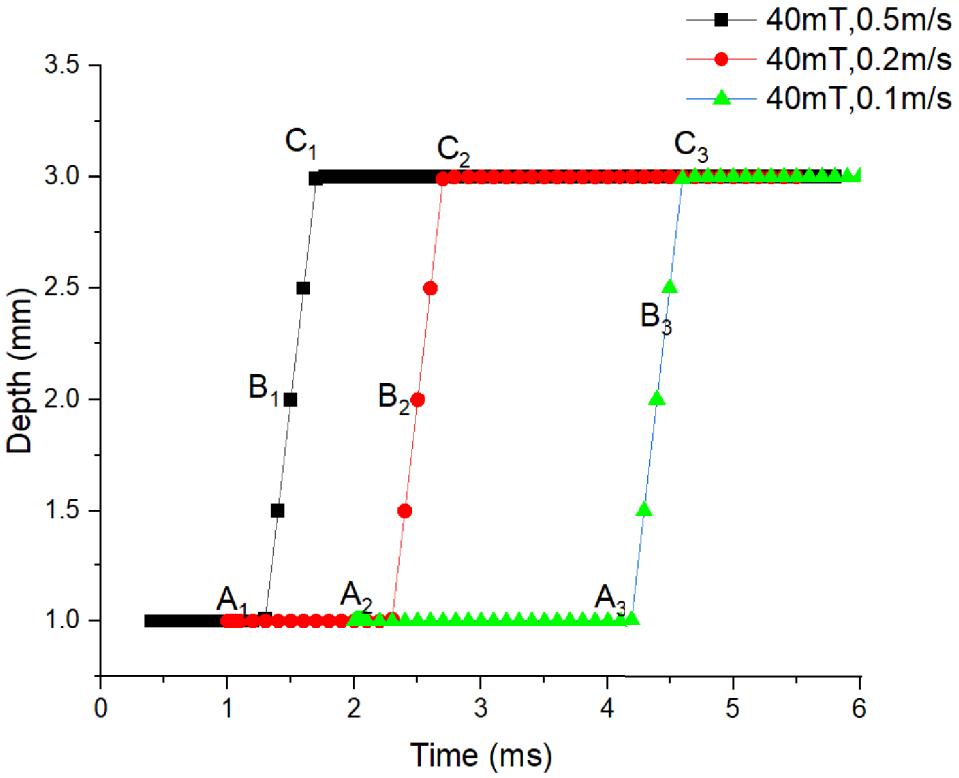

FIGURE 7.3: Arc depth implementation as a function of time and moving velocity based on the experiments observation, the marker is correlated to the different stages

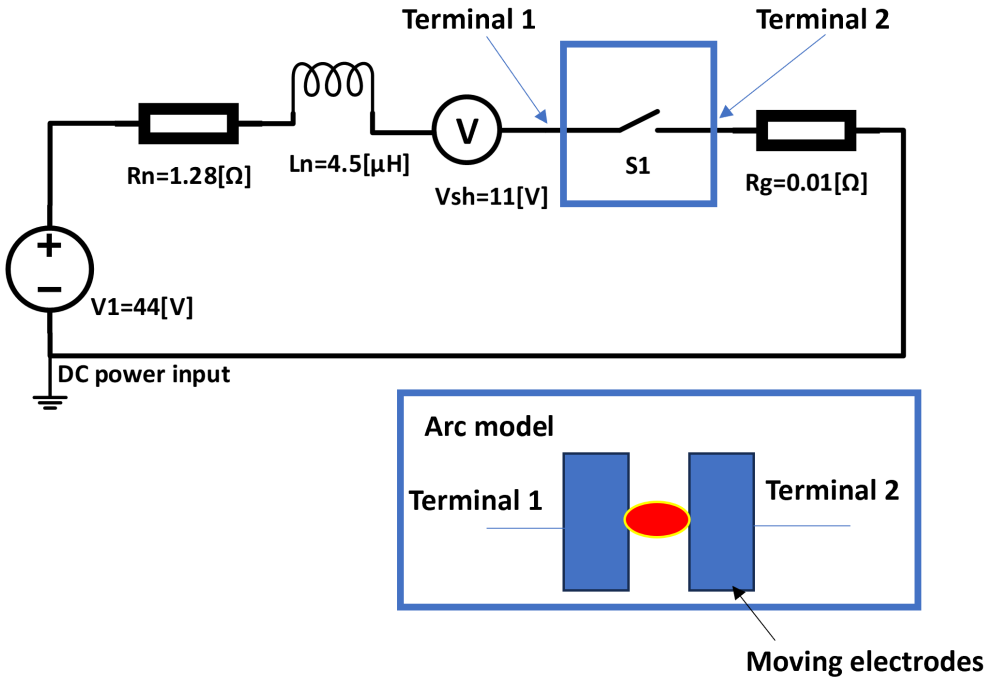

FIGURE 7.4: Equivalent electric circuit of the power supply coupled with the FEA model

the source resistance (open condition). This distinction clarifies that while the power supply has a theoretical maximum capacity, only a fraction of it can be transferred to the arc depending on

the arc resistance.

7.1.2 Boundary Conditions

The deformed geometry module is employed to implement the moving mesh for the moving boundary. Domain deformation is applied to the boundaries *AB*, *BD*, *DC*, and *CA* of the moving contacts, with the displacement defined as: $x = x_0 + v \times t$ where v represents the contact opening speed, and x_0 is the initial air gap, which is 0.2 mm. All other boundaries, as well as the remaining contact, are kept fixed.

Thermal Boundary Condition: The heat flux between the electrode surface and the plasma is defined using the heat transfer coefficient h_{heavy} [21]. Additionally, based on the observations in [93], the heat flux from heavy particles (ions and neutrals) to the electrode surface remains relatively small during the arc burning phase. Therefore, a heat transfer coefficient of $h_{\text{heavy}} = 250\ \text{W} \cdot \text{m}^{-2} \cdot \text{K}^{-1}$, evaluated at room temperature, is adopted in this study to estimate the net cooling effect at the electrode interface. Although h_{heavy} varies with temperature, this simplified treatment offers a worst-case scenario, representing the lowest convective cooling approximation within the boundary layer model. All other external boundaries are set to be thermally insulating.

Electric boundary: Boundary *AB*, *BD*, *DC* are grounded to small test resistor R_g and FE, EG, FG are terminated by the external circuit. The outside external boundaries are set as electrical insulation.

Fluid boundary: The solid material boundary is treated as a stationary wall with a no-slip velocity condition. All open boundaries are assumed to have a constant pressure condition 1 atm, allowing free outflow.

7.1.3 Domain Size and Mesh Selection

To verify that the chosen computational domain is sufficiently large, a sensitivity test was performed in which the outlet boundary was replaced by a wall. The results show negligible influence on arc behavior, indicating that boundary effects are minimal, and the selected domain is appropriate. Additionally, simulations were conducted with smaller domain size (e.g. 120 mm × 100 mm) and produced consistent arc voltage, current and temperature profiles within the region of interest, confirming independence of the predictions from the outer boundaries. The final domain, shown in Figure 7.1, is a rectangular box with the x-axis representing the horizontal direction. The computational domain consists of an open-air region and solid AgSnO2 electrodes. A hybrid meshing strategy was employed to balance the numerical accuracy and efficiency. In critical regions, particularly along electrode surfaces, a fine structured mesh with element size of 50 µm and 5 boundary elements as illustrated in Fig. 7.5 was applied to resolve steep thermal and air velocity gradients.

In less sensitive outer air regions, coarser triangular elements (200-500 µm) were used to reduce computational costs by approximately 40%. This mesh was refined further to check the effects

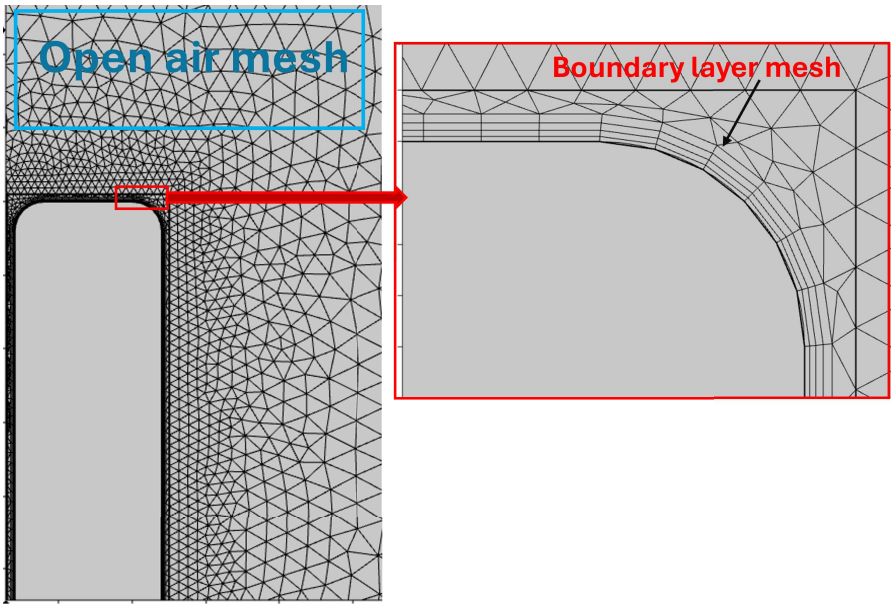

FIGURE 7.5: Simulation mesh with coarse elements in the open-air region and a refined boundary layer mesh near the electrode surfaces to capture temperature and velocity gradients.

of the size showed that peak temperature differences remained below 15% and arc extinction time deviations were within 20%, both falling with the margin of experimental uncertainty.

7.1.4 Time Step

Time-stepping was automatically controlled by the COMSOL solver within an absolute tolerance of 0.001. Although the time steps varied as the solution progressed, during the initial arcing phase (0–1 μs), a fine time step of 10 ns was typically used; in the arc propagation stage (2–100 μs), the step was increased to 1 μs; and in the later plasma decay phase (0.2–8 ms), a coarser step of 10 μs was applied.

7.1.5 Material Properties

The plasma domain is filled with air, electrical conductivity, thermal conductivity, specific heat capacity, and viscosity as functions of temperature taken from [122]. Thermodynamic properties of air are assumed at 1 atm, since pressure variations in the arc region are below 10% and considered negligible. The electrodes material is $AgSnO_2$ using properties from [138]; however, since the model does not include plasma-vapor interactions or surface emission, the electrode material only serves to define boundary thermal and electrical properties ($T_{surface} = 300K$).

7.2 Results and Discussions

7.2.1 Arc Stage Identification

Our model,supported by experimental observations in [16] as illustrated in Fig. 7.6, arc evolution is identified into three stages: Stage 1 (arc confined within electrodes), Stage 2 (arc expansion

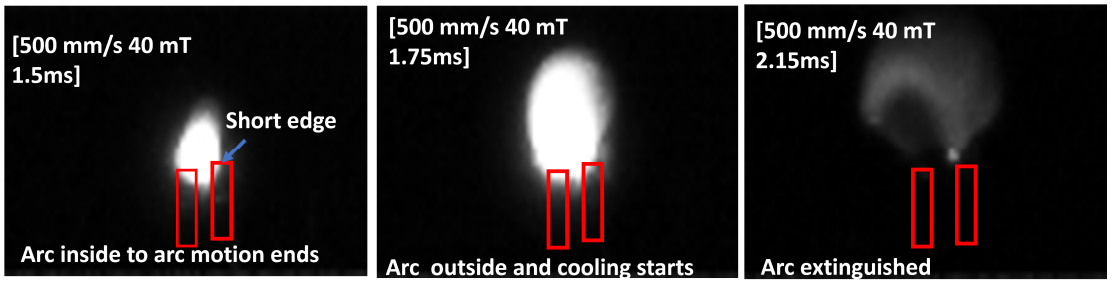

(A) Moving speed 0.5 m/s

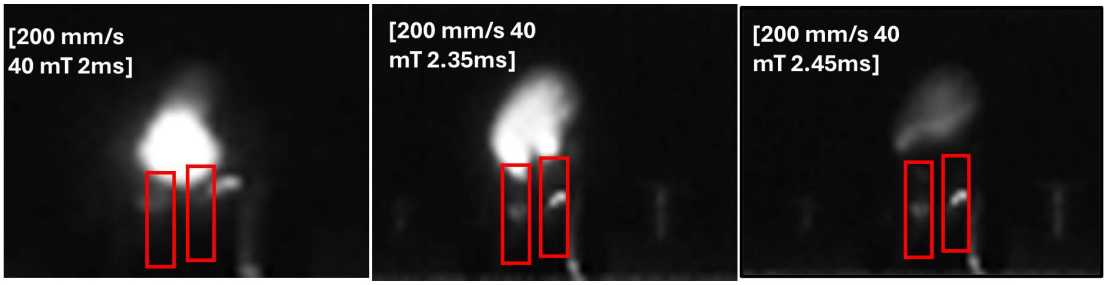

(B) Moving speed 0.2 m/s

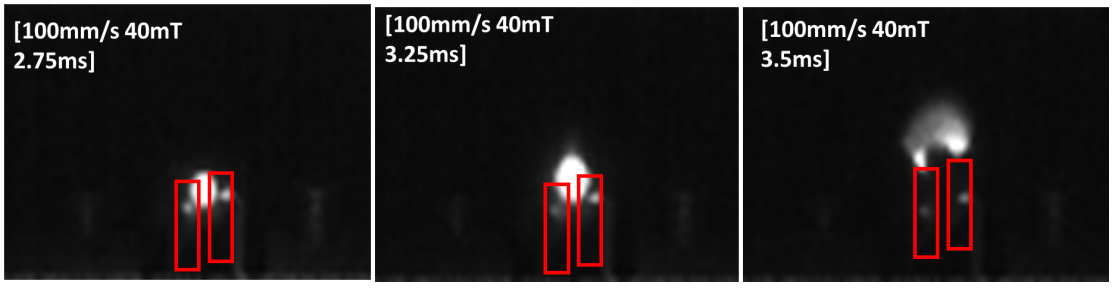

(C) Moving speed 0.1 m/s

FIGURE 7.6: Arc images at different stages for three opening speeds under 40 mT external magnetic field. Applied voltage: 55 V; current: 45 A.

outside the contact gap), and Stage 3 (rapid elongation and extinction). Fig. 7.7 shows simulated temperature distributions for these stages, with Columns A, B, and C corresponding to Stages 1–3 across opening speeds of 0.5, 0.2, and 0.1 m/s.

In Stage 1 (from initiation to t_1), the arc remains confined, current decreases slightly (33 A to 32.5 A) and voltage rises modestly (11 V to 12.5 V), reflecting arc elongation. The model underestimates voltage rise compared to experiments (15–18 V), mainly due to simplified boundary layer treatment omitting sheath formation and localized energy exchange significant in short arcs [38]. Assuming spatially uniform arc depth neglects local contraction near electrodes, possibly overestimating conductive cross-section and underestimating arc resistance, consistent with early trends in Figs. 7.8–7.10.

Stage 2 (t_1 to t_2) shows steeper voltage rise and faster current drop: simulations predict current decreasing from 32.5 A to 25 A with voltage rising to 25 V, matching experimental trends

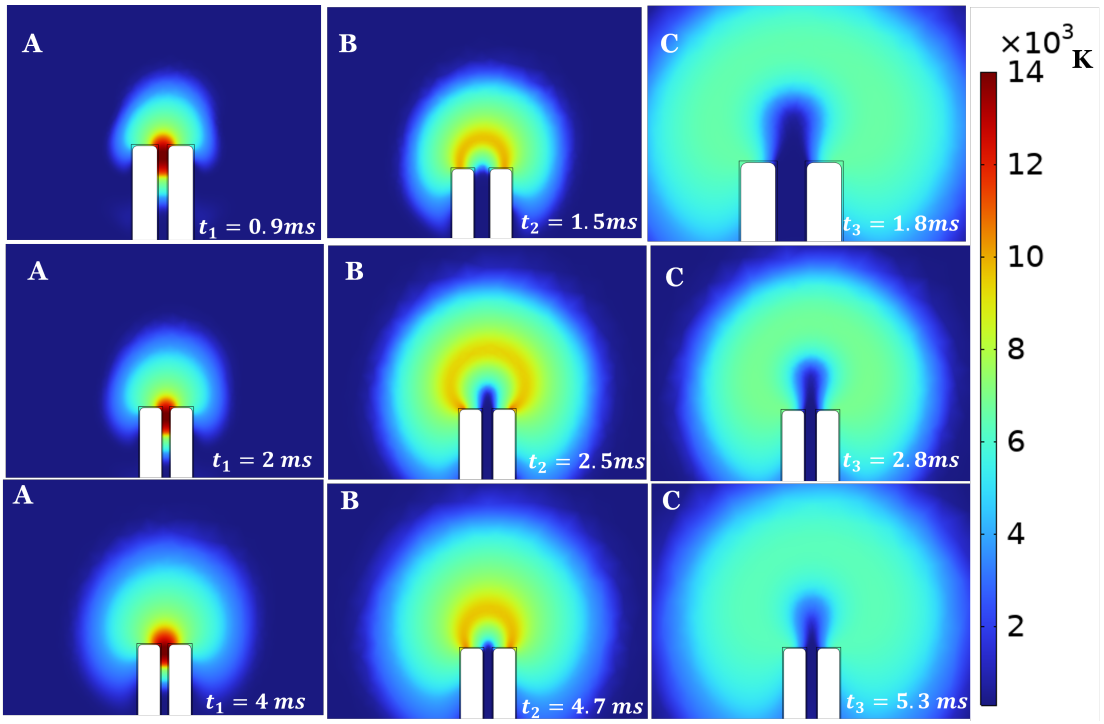

FIGURE 7.7: Simulated temperature distributions for three arc stages under different speeds at 40 mT field. Columns A, B, C: Stages 1–3; rows: 0.5, 0.2, 0.1 m/s from top to bottom. Applied voltage: 55 V; current: 45 A.

(18–22 V). Arc expands into open space, reducing near-electrode boundary effects. Fig. 7.7 (column B) shows mushroom-like arc profiles, with hottest region near the top contact edge.

In Stage 3 (t_2 to t_3), rapid arc elongation leads to current collapse and extinction: current falls from 25 A to 2 A, voltage peaks at 51 V. Predicted decay rates depend on speed: 40 A/ms (0.1 m/s), 65 A/ms (0.2 m/s), 80 A/ms (0.5 m/s) per Figs. 7.8–7.10. Fig. 7.7 (column C) shows a horseshoe-shaped arc; average temperature drops below 5000 K, and air gap conductivity decays rapidly. The consistent arc shape and maximum temperature at each stage across different **B** (applied external magnetic field) and **v** (moving velocity of contacts) indicate self-similar arc behavior, with external conditions mainly affecting stage durations rather than core processes.

7.2.2 Model Validation

Simulated voltage and current waveforms were compared with experiments at 0.5, 0.2, and 0.1 m/s speeds. Key points A–C mark arc stages in Fig. 7.6, and typical experimental data sets G1 and G2 correspond to identical conditions in [16]. For 0.5 m/s (Fig. 7.8), predicted extinction at 1.8 ms aligns well with G1 data. At 0.2 m/s (Fig. 7.9), predicted 2.8 ms extinction falls between experimental 2.4–3.1 ms; simulated Stage 1 shows higher current due to simplified arc root modeling neglecting near-electrode energy exchange. At 0.1 m/s (Fig. 7.10), discrepancies are largest: slower predicted arc migration leads to overestimated Stage 1 current.

Additional simulations placing arc seeds at various initial positions (from center to edges) showed negligible differences, suggesting discrepancies stem from some details missing in the

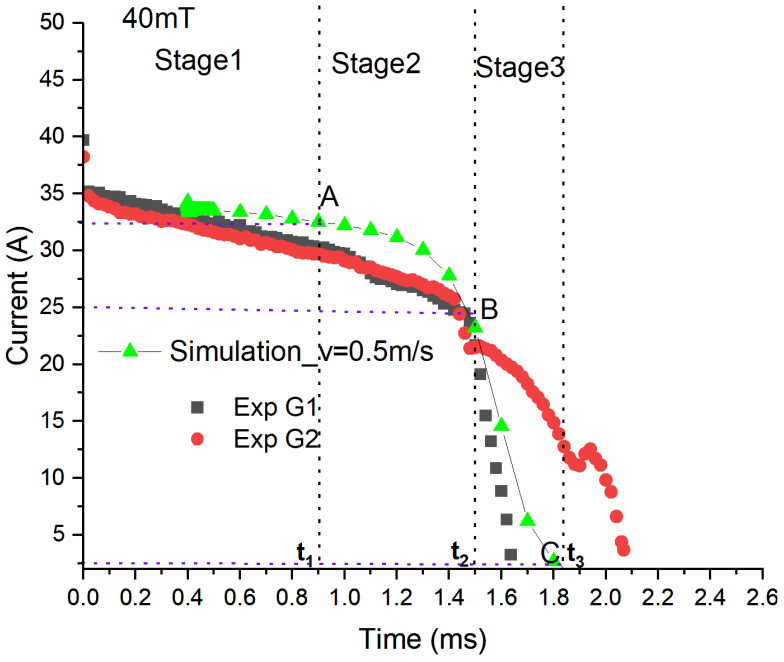

(A) Current waveform

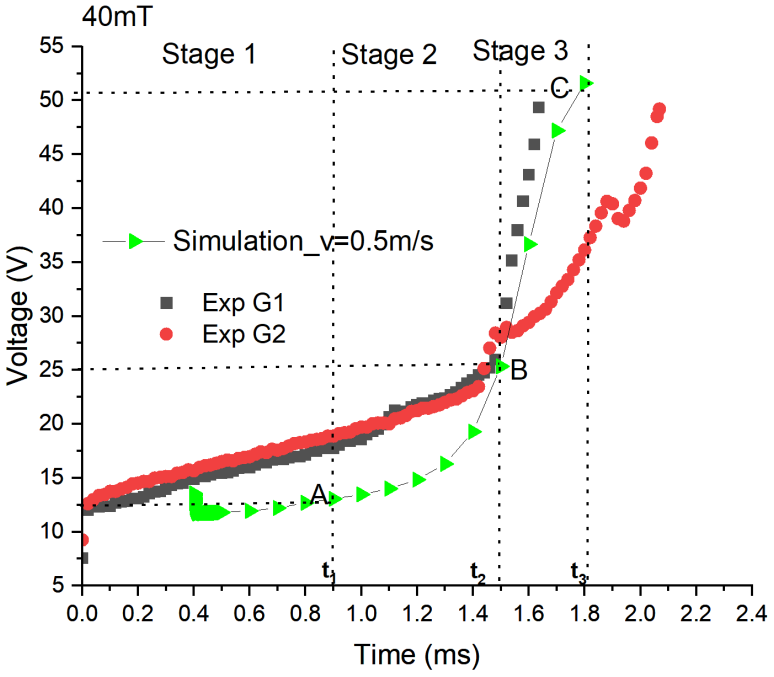

(B) Voltage waveform

FIGURE 7.8: Simulated and measured arc current (a) and voltage (b) at 0.5 m/s. 55 V, 45 A, 40 mT.

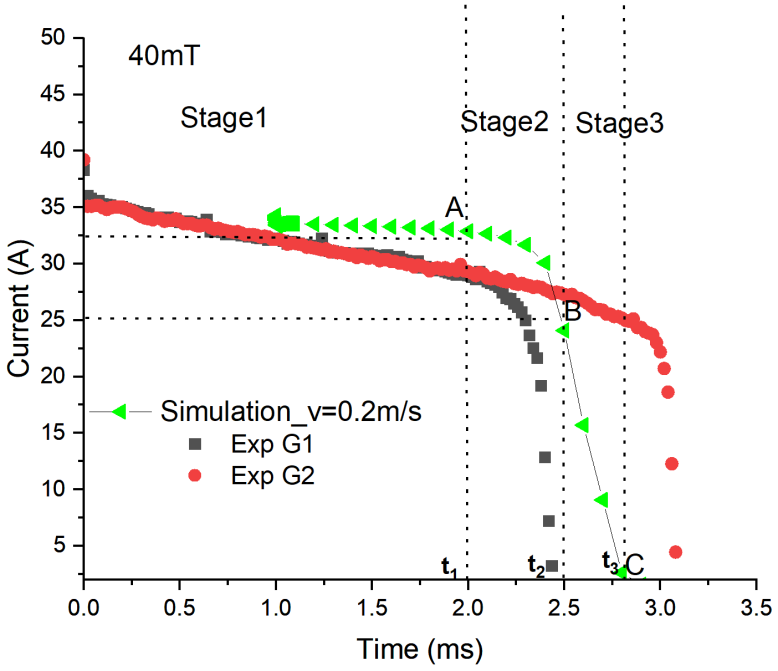

(A) Current waveform

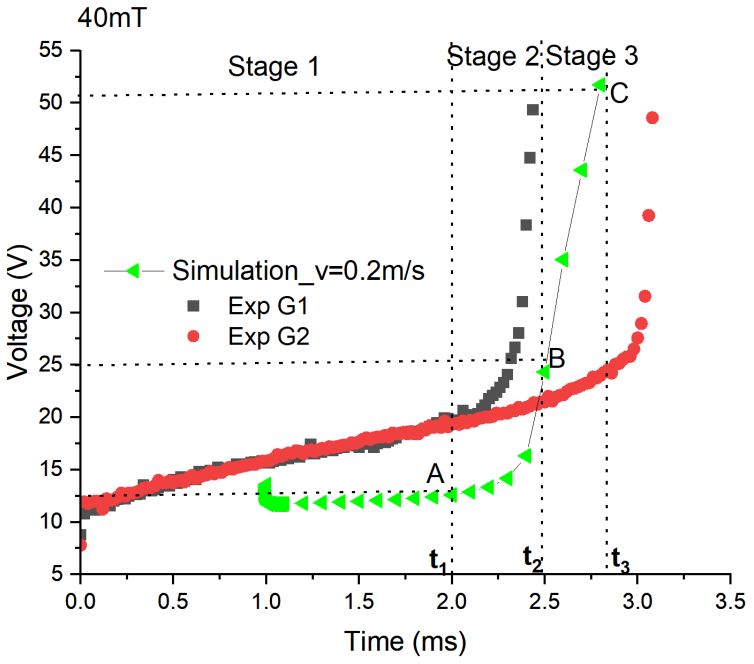

(B) Voltage waveform

FIGURE 7.9: Simulated and measured arc current (a) and voltage (b) at 0.2 m/s.

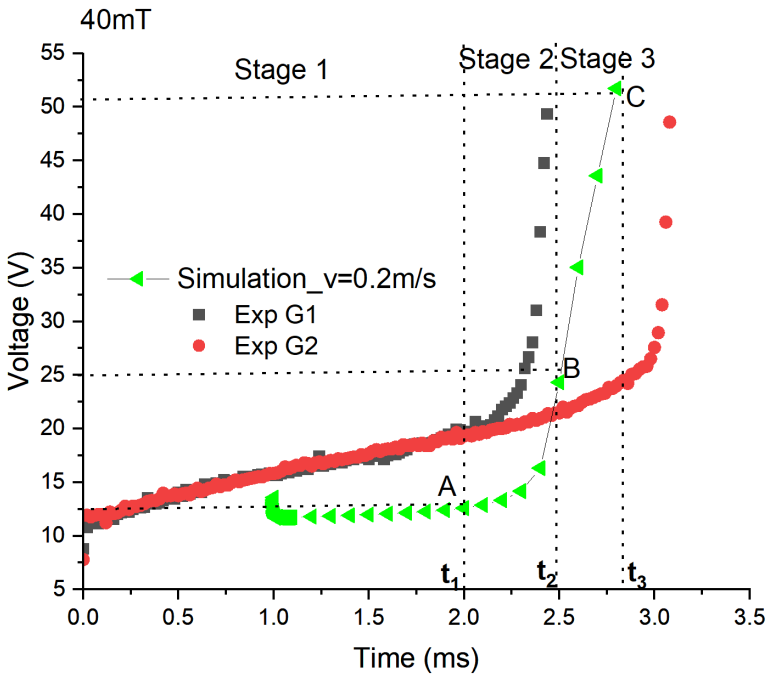

(A) Current waveform

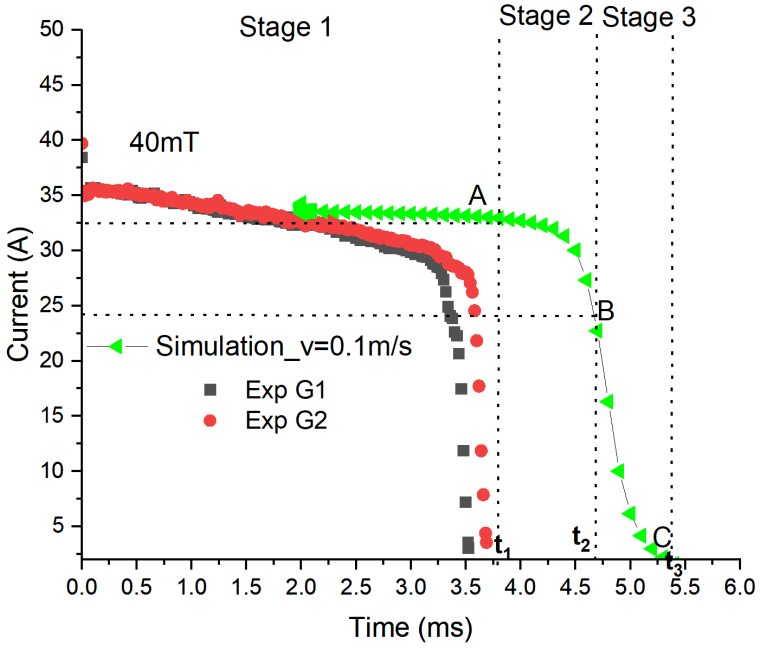

(B) Voltage waveform

FIGURE 7.10: Simulated and measured arc current (a) and voltage (b) at 0.1 m/s.

model—specifically neglection of early arc dynamics and crossflow effects. Simplified 2D assumptions miss side airflow shown in 3D studies [90, 153], as illustrated in Fig. 7.11, which can enhance cooling near the arc column and accelerate current decay.

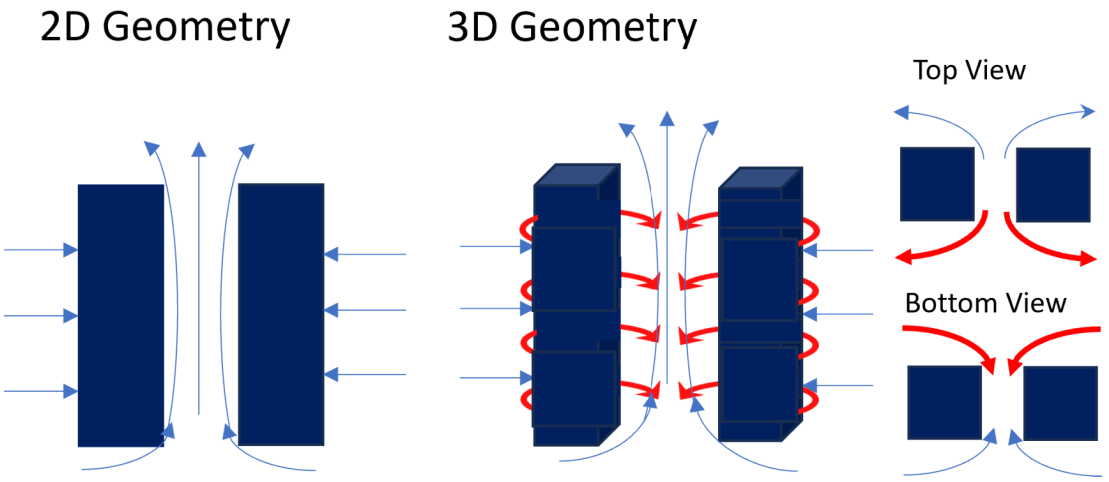

FIGURE 7.11: Comparison of airflow patterns: current 2D model (left) vs. realistic 3D flow (right). Red arrow shows side inflow missing in 2D simulation.

In conclusion, the model reliably captures key dynamics of Stages 2 and 3, with good agreement in extinction times above 0.2 m/s. Main discrepancies occur in Stage 1 at low velocities due to simplified boundary assumptions, but overall, the model provides a robust framework for evaluating arc extinguishment performance in low-voltage DC switches.

7.2.3 Effect of Key Factors on Arc Dynamics at Each Stage

The experimental data indicate that both moving velocity and the magnetic field accelerate the arc extinction process [16]. However, their specific influence on each stage remains unclear. The duration of each stage under different contacts moving speeds (0.5m/s,0.2m/s,0.1m/s) and magnetic field strengths (5mT,10mT,20mT,30mT,40mT, 50mT,60mT,80mT) is calculated and presented in Figure 7.12. The detailed analysis is as follows.

As shown in Figure 7.12a, defined as the time interval during which the arc remains confined between the contact is determined by tracking the temperature peak in the simulation. Stage 1 ends when the arc core, identified by the maximum temperature region, reaches the edge of the electrodes and begins to extend into the expansion zone, time decreases significantly with increasing magnetic field strength. For a given electrode moving speed, shortening the duration of Stage 1 by a factor between 5 and 6 as the magnetic flux density increases from 5mT to 80 mT. The opening velocity also strongly effects the Stage 1 duration. Effects of $\mathbf{v}$ and $\mathbf{B}$ appeared to be following power law dependences. The slopes of the corresponding curves for each B remain nearly equal across different magnetic field strengths. Referring to Figure 7.13a, for a range of contact speeds, the size of the arc and the arc temperature distribution remain localized and comparable, with the arc acceleration being approximately proportional to the applied magnetic flux density B. The primary role of B is to drive the arc toward the

contact edges. Increase in B results in proportional increase in Lorentz force, illustrated in Figure 7.13b. The Lorentz force induced by the external magnetic field exerts a volumetric force density on the arc column, enhancing its displacement towards the contact edges. For very large magnetic fields, the additional effect on Stage 1 becomes limited, though Stage 2 still shows a proportional response. As shown in Fig. 11(a), diminishing returns appear at higher magnetic fields: for example, at a 0.5 m/s opening speed, increasing B from 40 mT to 80 mT reduces Stage 1 duration only slightly (from 0.9 ms to 0.7 ms), whereas increasing B from 5 mT to 20 mT reduces it more significantly (from 4.4 ms to 1.1 ms). This indicates that at higher contact velocities, the benefit of stronger magnetic fields decreases. Conversely, for a given magnetic field, increasing the contact velocity also shortens Stage 1, but the reduction factor is only about 2.5–5 times when speed increases by a factor of 5. The primary effect of higher contact speed is to elongate the arc horizontally, creating a larger air gap and increasing resistance—especially important in low magnetic fields, where self-induced magnetic forces are insufficient to drive the arc towards the contact edges.

Overall, while both magnetic field and contact velocity influence Stage 1 duration, enhancing the magnetic field is generally more effective from a practical standpoint.

In Stage 2, the duration is primarily controlled by arc expansion, which becomes only weakly dependent on the contact opening speed, as shown in Figure 7.12b. The predicted variation range of Stage 2 for different B remains nearly unchanged for different v, indicating that increasing the contact velocity does not effectively reduce the Stage 2 duration. Once the arc exits the contact gap, arc dynamics and cooling airflow become crucial. In this stage, arc motion and its cooling are mainly affected by the magnetic field B. Unlike Stage 1, the arc is now fully exposed to the surrounding flow and can expand freely. Consequently, the surrounding gas stream converts heat away and stretches the arc column, as shown in Figure 7.14b. A higher flow velocity for higher Bs elongates and cools the arc more aggressively, promoting faster voltage rise and accelerating cooling of the plasma. This makes the arc harder to sustain, tending to shorten the Stage 2 duration. The effectiveness of the induced convective cooling can be quantified by comparing the arc's motion with the airflow velocity. Once exposed to the open space, the arc displacement from y_1=24mm at end of Stage 1 to the y_2=25.2mm.at end of Stage 2 (tracked by the position of the hottest arc region marked with a black dashed line in Fig.7.15) occurs over 0.19ms in the B=80mT, v=0.5m/s case. This corresponds to an arc motion velocity of approximately 6 m/s. In comparison, the average airflow in Fig.7.14b is around 55m/s thus, the fast convective flow of cold air though the arc region significantly enhances cooling. This intensified convective effect is the key factor in shortening Stage 2 duration under higher magnetic fields.

In Stage 3, the data indicates that both the magnetic field and the electrode moving velocity have a little influence on the arc behavior. As shown Figure 7.14c, the airflow distribution remains similar across cases and does not significantly contribute to cooling. This suggests that arc decay in this stage is governed by other factors. A deeper analysis of the underlying mechanisms will be provided through an energy analysis in later discussions.

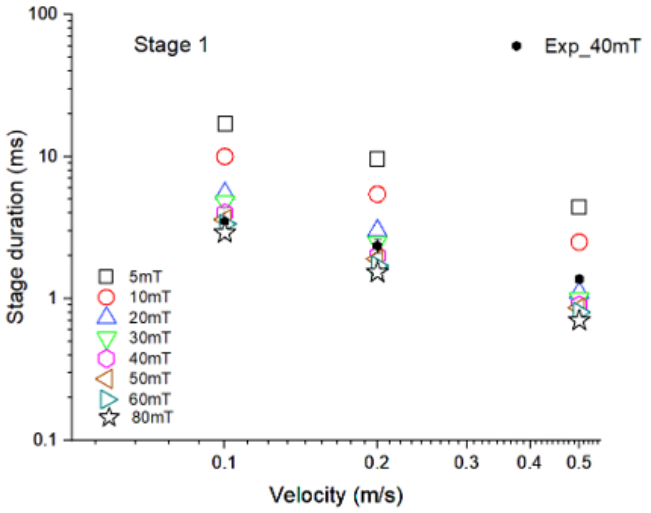

(A) Stage 1

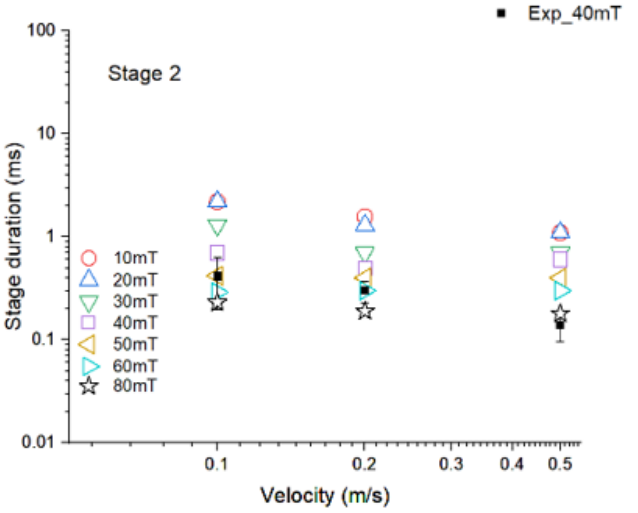

(B) Stage 2

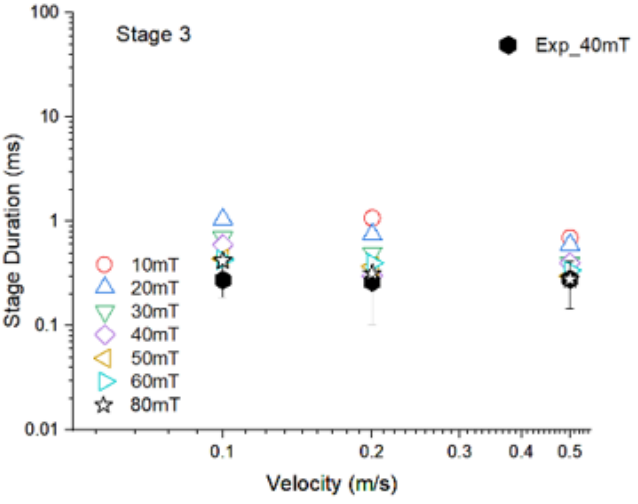

(C) Stage 3

FIGURE 7.12: Duration of arc behavior across three stages as a function of moving speed (0.5m/s, 0.2m/s. 0.1m/s) under different magnetic field

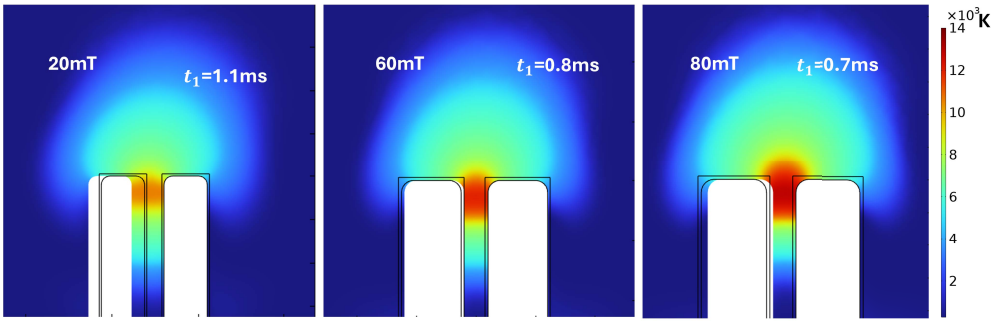

(A) Temperature distribution in K

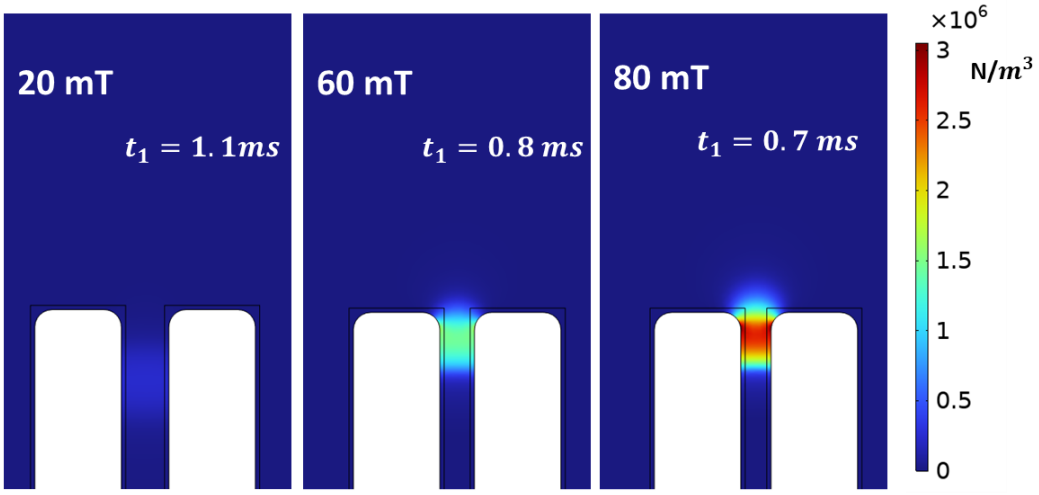

(B) Lorentz Force density in N/m^3

FIGURE 7.13: Comparison of Temperature in K (a) and Lorentz Force density in N/m^3, vertical component (b) under different applied magnetic field(20/60/80 mT) at the end of Stage 1 time instance, moving speed is 0.5 m/s

7.2.4 Correlations between the arc decay time and the parameters (B,v)

Based on simulation results under varying magnetic field strengths B and contact velocities v, an empirical analytical expression for arc extinguishing time was developed. The power-law fitting was based on the observation from simulation results, as shown in Fig.7.16.The empirical formula is:

$$t_{\text{extinguish}} = K \cdot v^{-\alpha} \cdot B^{-\beta} \tag{7.1}$$

The coefficients K and the exponents α and β were obtained via log-log linear regression, capturing the dominant trends across a wide range of simulation scenarios. Here, K is dependent on the electrode geometry, material, and power supply, whereas the power constants were found to be $\alpha = \beta = 0.7$.

Figure 7.17 presents the comparison the predicted values from this empirical model with simulation results over the range (20–80 mT, 0.1–0.5 m/s), with over 85% of the data points falling within a $\pm 10\%$ error margin. The coefficient of determination (R^2) of the log-log fitting is approximately 0.987, indicating a strong correlation between the fitted surface and the observed data.

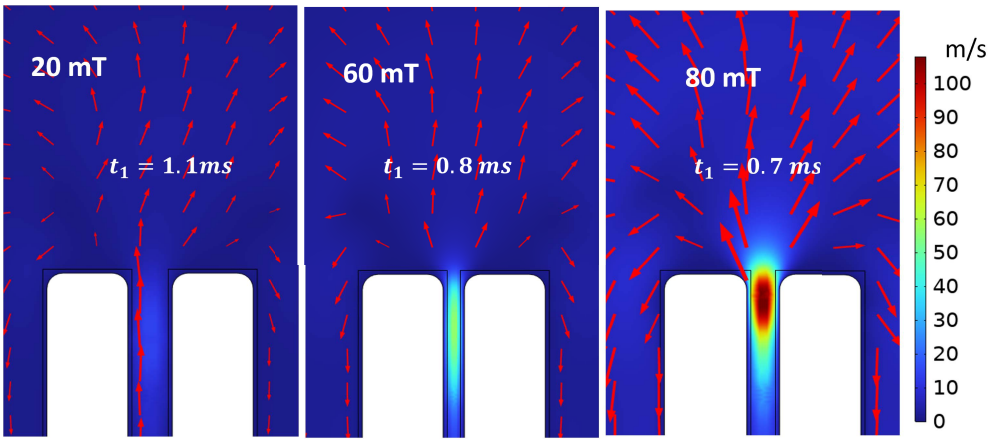

(A) Stage 1 (Legend scale is from 0-120m/s)

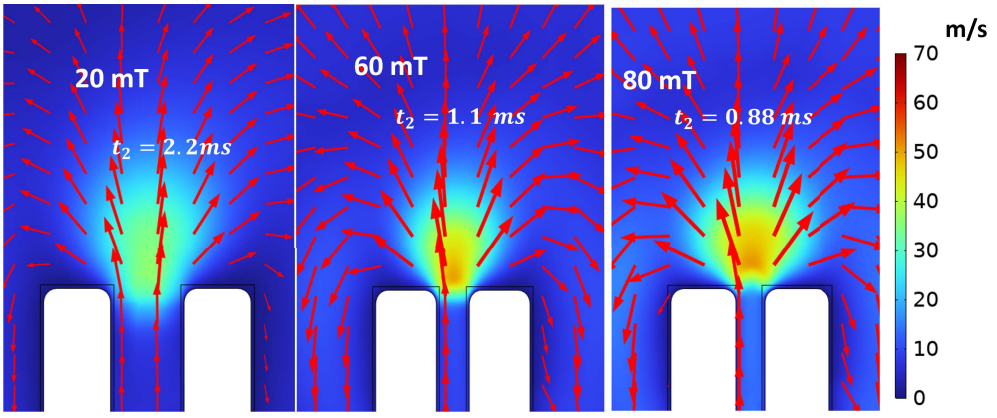

(B) Stage 2 (Legend scale is from 0-70m/s)

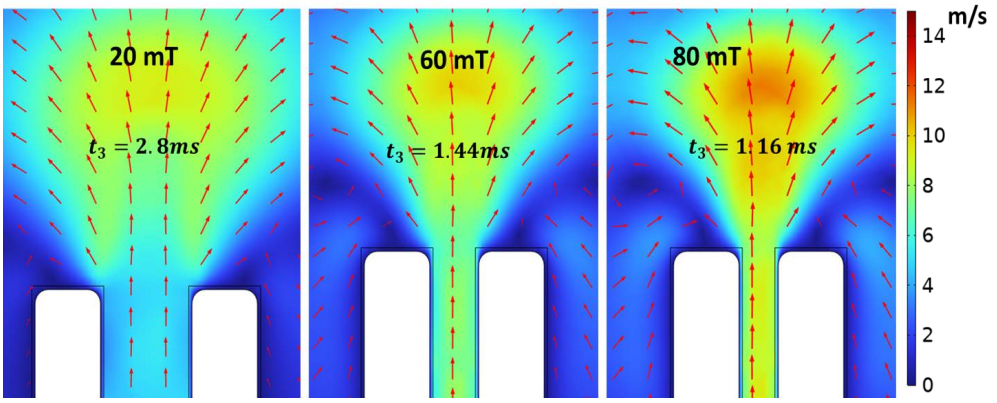

(C) Stage 3 (Legend scale is from 0-15m/s)

FIGURE 7.14: Airflow distribution at same stage under different applied magnetic fields at each stage when the contact velocity is 0.5m/s

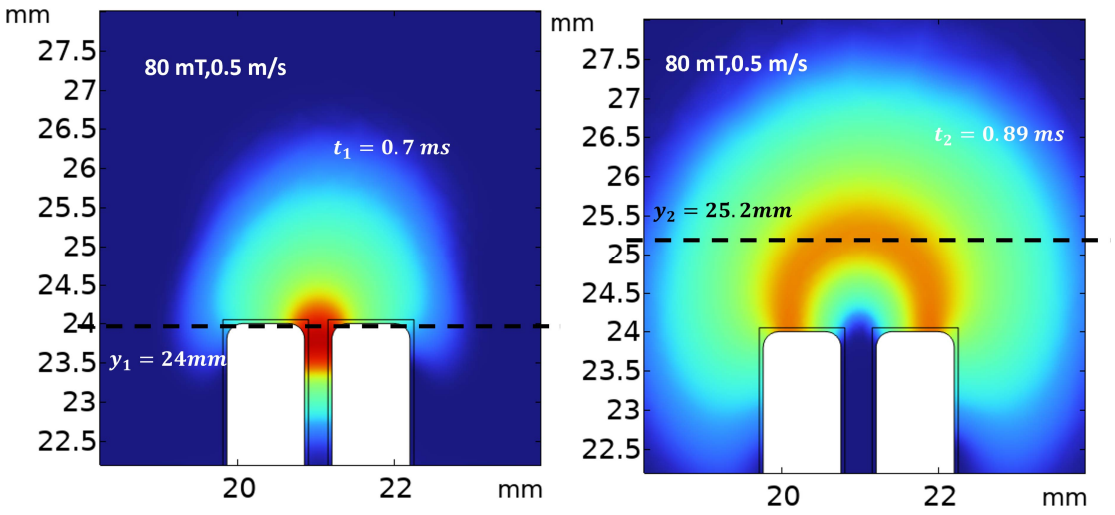

FIGURE 7.15: Temperature distribution in the arc. Arc motion (position) from Stage 1 to Stage 2 when the applied magnetic field is 80 mT, contact speed is 0.5m/s.

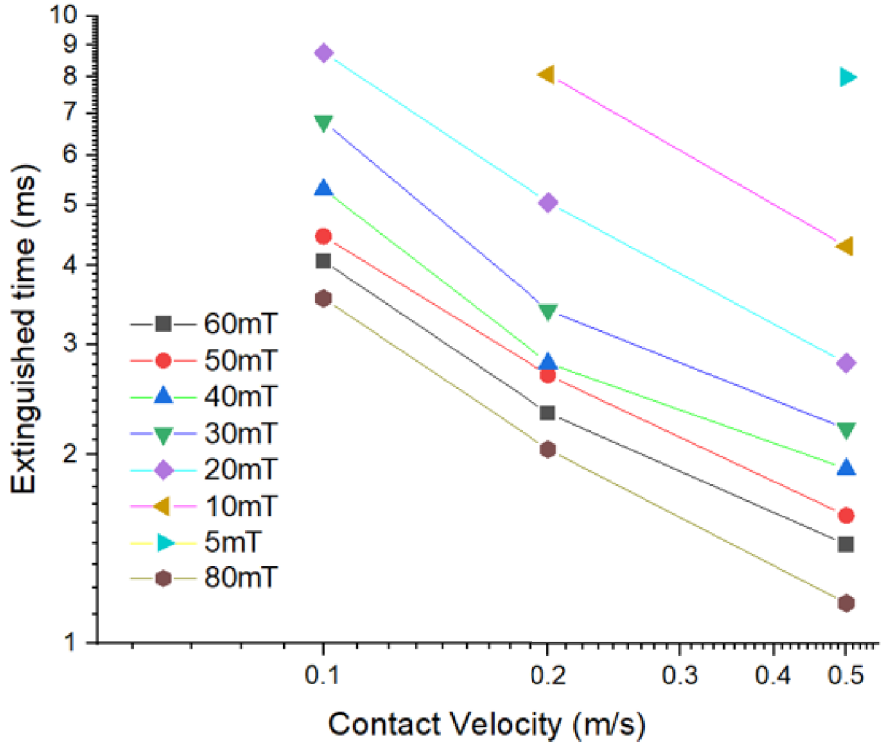

FIGURE 7.16: Log-log plot of arc extinction time (t_3) versus magnetic field strength (B) under different electrode velocities.

From the design perspective, this empirical relation can assist in predicting arc extinction time for a given contact geometry under varying magnetic fields and velocities. By running a limited set of simulations, the geometry-dependent constant K in the scaling law (with $\alpha = \beta = 0.7$) can be extracted. While this relation is derived from a specific experimental setup, it offers a practical framework that can be adapted to similar device configurations.

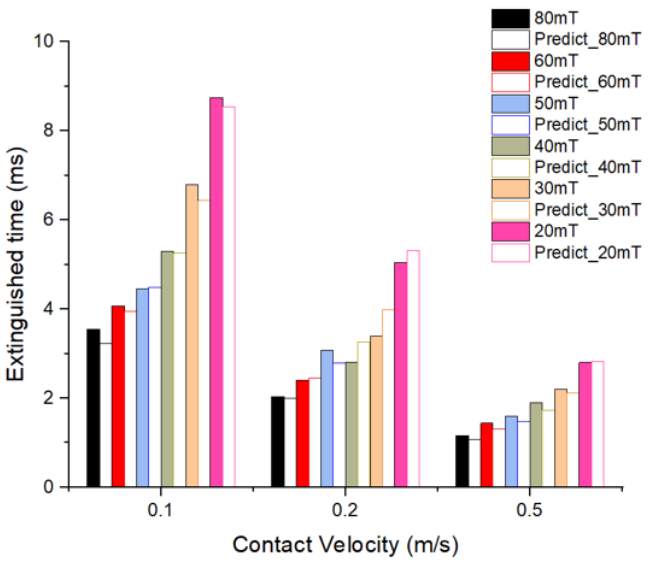

FIGURE 7.17: The comparison with the simulation results and the analytical fitting equation prediction

7.2.5 Energy Balance Analysis

To understand the mechanism driving the arc decay in Stage 3 and the empirical fitting relations, one must examine the physical origin of the coefficients K, α, and β. This section investigates whether these coefficients are system-specific or governed by more universal principles. The approach is based on analysing the detailed power balance during the arc extinguishment and tracing how the system dissipates energy. The total supplied power balance can be written as follows:

$$P_{\text{supply}} = V_{\text{supply}} \cdot I = V_{\text{arc}} \cdot I + I^2 R_{\text{s}} \tag{7.2}$$

The power consumed by the arc itself, $P_{\text{arc}} = V_{\text{arc}} \cdot I$, is composed of two mechanisms:

$$P_{\text{arc}} = Q_{\text{joule}} + V_{\text{sheath}} \cdot I \tag{7.3}$$

$$Q_{\text{joule}} = \iiint \sigma(T)|\vec{E}|^2 \, dV \tag{7.4}$$

$$\vec{J} \cdot \vec{E} = \sigma(T)|\vec{E}|^2 \tag{7.5}$$

Following [93], we assume that the sheath losses (associated with charged particles) are fully consumed by electrode heating, and they are ignored in our simulation of the arc core. Therefore, the plasma energy balance can be written as:

$$Q_{\text{joule}} = Q_{\text{rad}} + Q_{\text{boundary}} + Q_{\text{internal}} + Q_{\text{kinetic}} \tag{7.6}$$

where Q_{rad} is the radiation loss, Q_{boundary} is the conductive heat flux to the wall through neutral gas, and $Q_{\text{internal}} + Q_{\text{kinetic}}$ are the convective power losses due to heating of the surrounding

environment and gas flow.

$$Q_{\text{rad}} = \iiint 4\pi \cdot \text{NEC}(T_{\text{plasma}})\, dV \tag{7.7}$$

$$Q_{\text{boundary}} = \iint h(T_{\text{plasma}} - T_{\text{surface}})\, dA \tag{7.8}$$

Here, the temperature difference is across the boundary layer, and the heat transfer coefficient h is taken at room temperature for air (Section 8.1.3). The integration is performed over all electrode surfaces assuming $T_{\text{surface}} = 300$ K. Heating of electrodes over a few milliseconds is neglected.

$$Q_{\text{kinetic}} = \frac{d}{dt} \iiint \frac{1}{2} \rho(T) u^2\, dV \tag{7.9}$$

$$Q_{\text{internal}} = \frac{d}{dt} \iiint \rho(T) C_v(T) T\, dV \tag{7.10}$$

where V denotes the arc plasma volume, ρ is the gas density, A is the total electrode surface area, C_v is the gas specific heat, and u is the local airflow velocity. We analyze these contributions at three key time instances (t_1, t_2, t_3), corresponding to the end of Stage 1 (the arc being pushed to the edges), Stage 2 (onset of arc decay), and final arc extinction. The energy dissipation process during arc extinguishment dynamics under the same contact opening speed (0.5 m/s) but different magnetic fields (40 mT and 20 mT), and under the same magnetic field (40 mT) but different contact opening speeds (0.5 m/s and 0.2 m/s), exhibits significant stage dependence, as shown in Figure 7.18.

In Stage 1, the arc is moving toward the upper edge of the contacts long side while still confined between the electrodes. During this phase, the power in the arc varies slowly, exhibiting a near-linear trend. The dominant energy losses are sheath losses followed by boundary losses at the electrodes. Initially the convective cooling is limited. But at the end of Stage 1 this trend changes: convective losses overtake boundary cooling. It is interesting to look inside the phenomenon. As shown in Figure 7.6, the arc temperature and size do not change significantly in this stage. So, the arc volume remains approximately constant. However, there is a noticeable increase in the rate at which the internal and kinetic energy of plasma increases as shown in Figure 7.18. This increase primarily results from very fast air flow through the arc and associated convective cooling, where airflow effectively carries away arc heat and dissipates it in the surrounding space. In spite of the increase, these losses are moderate at the beginning of Stage 2 compared to the power losses in the arc sheath, and they are not sufficient to produce any arc decay. However, at the moment when the arc escapes, from the gap convective losses become more pronounced, and at the end of Stage 2 account for approximately 50% of the total power loss.

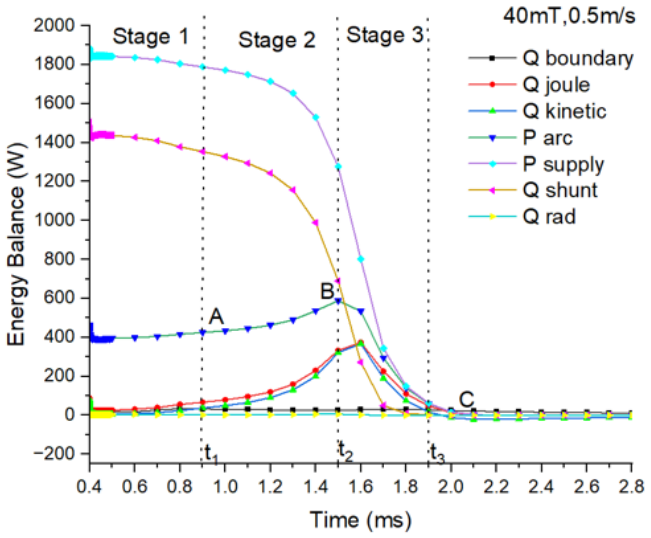

(A) 0.5 m/s,40 mT

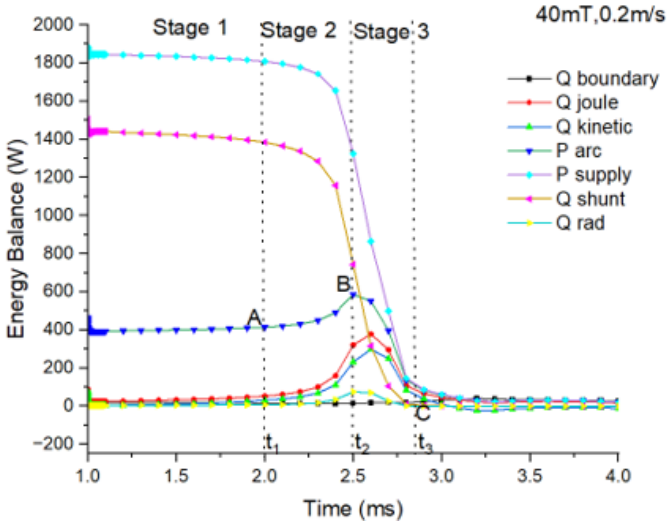

(B) 0.2 m/s,40 mT

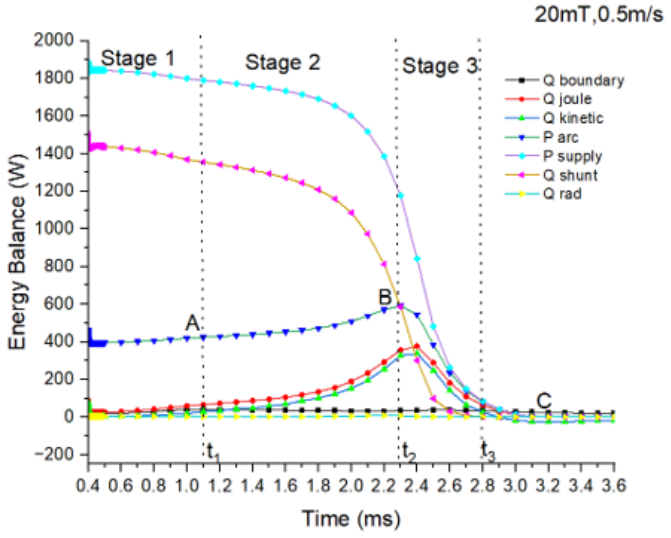

(C) 20 mT, 0.5 m/s

FIGURE 7.18: Energy balance analysis for three different cases at each stage

Arc decays at stage 2 while attached to the top side of the electrodes. During this phase, the total power in the arc exhibits a non-linear increase, echoing the changes in the v-i characteristics, as shown in the previous sections. The power supply injects more heat into the arc, but at the same time, significant convective losses persist due to the high airflow velocity and the larger volume of the arc core.

As shown in Figure 7.6, the air velocity reaches approximately 55 m/s, and the effective cross-sectional area through which these losses occur increases substantially by a factor of 10 or even more. This explains the rapid increase in energy losses from the arc core, particularly via convection and radiation, which ultimately accelerates arc extinction. By examining the arc behavior under varying contact velocities and air gaps as shown in Figure 7.19, we observe that arc extinction—or collapse—may occur at different spatial gap distances. However, these extinction points consistently correspond to the same power level, which aligns with the maximum power available from the power supply (with the given load connected series). This suggests that while increasing the contact velocity accelerates the system's progression toward this power threshold, arc extinction itself does not occur until the system reaches this maximum power. In other words, arc extinguishment is not solely governed by the rate of input energy, but by achieving a critical power condition—imposing a fundamental limit on the extinguishing process that cannot be bypassed by simply increasing field or speed.

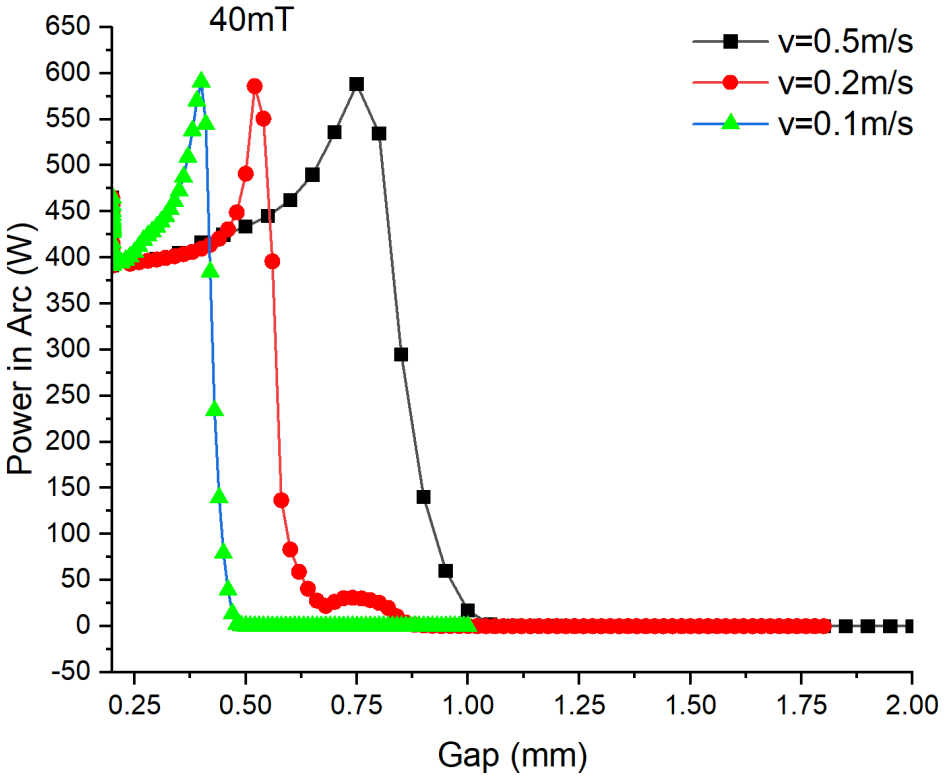

FIGURE 7.19: Gap-based arc behavior suggests velocity-invariant dissipation trend

For example, Fig.7.18a shows that Stage 2 ends at 1.5 ms (Point B), when the arc receives

maximum power from the supply. At this point, the arc resistance equals the effective circuit resistance, and the arc power reaches quarter of the total power available. As the arc grows further and its resistance increases, the system passes the maximum power point, causing power delivery to the arc to decline and marking the onset of arc collapse. Controlling Stage 2 is therefore critical, as it governs the transition from sheath-dominated to core-loss regimes. These findings suggest strategies for improving arc extinguishment performance, such as ensuring strong convective flow during Stage 2 and tailoring electrode geometry to support arc elongation, which can help reduce reignition risk. Circuit-level measures like adding snubber networks could further limit transient energy delivery; although these strategies require validation, they offer promising directions for enhancing low-voltage DC circuit breaker reliability. The consistency of power balance across different contact velocities, as shown in Figure 7.18a and Figure 7.18b, and across different magnetic field strengths as shown in Figure 7.18a and Figure 7.18c, indicates that arc motion mainly affects the timing of maximum power demand but not the overall power evolution or collapse mechanism. Energy analysis shows that some cooling occurs during Stage 1 between the electrodes, but it is insufficient for arc extinction. For successful interruption, the arc must progress to Stage 2, where airflow enhances convective cooling—a key factor in accelerating energy dissipation. Notably, arc collapse consistently begins when arc resistance matches that of the supply, underscoring the need to increase arc resistance rapidly by improving convective cooling. Since arc extinction was not observed in any simulation before the onset of maximum power, this highlights the importance of enhancing convective cooling mechanisms to trigger arc extinguishment more effectively.

7.3 Summary

Figure 7.20 summarises Chapter 7: Section 7.1 builds the model, Section 7.2 identifies arc stages and quantifies the stage-dependent roles of magnetic field B and contact velocity v with an energy-balance view of extinction, and Section 7.3 condenses the design guidance.

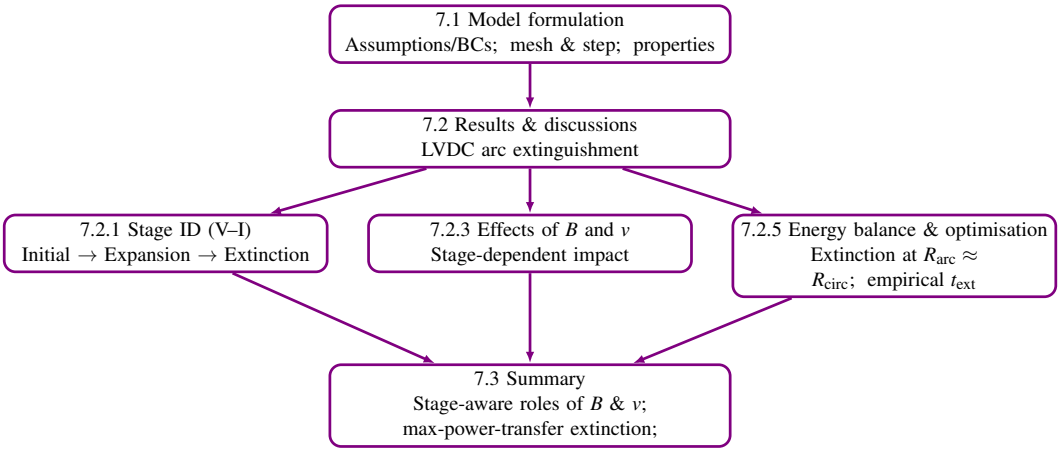

FIGURE 7.20: Chapter 7 Overview

This chapter systematically investigated the arc extinguishment process in low-voltage DC switches/circuit breakers through three critical perspectives: (1) proposed stage identification based

on voltage-current characteristics, (2) analysed stage-dependent roles of magnetic fields and contacts opening velocity, and (3) discussed energy balance driven extinction mechanisms and engineering optimization. The key findings and implications are summarized as follows:

The arc evolution is classified into three stages based on voltage–current characteristics. In Stage 1 (Initial), the arc remains confined between the electrodes and gradually migrates toward the edges under magnetic force and buoyancy, accompanied by a slow voltage rise and current decay. During this phase, power consumption remains relatively stable, with losses dominated by the sheath region. In Stage 2 (Expansion), the arc transitions into open air and adopts a hemispherical shape. The arc volume increases significantly, and high-velocity airflow enhances convective cooling, leading to accelerating current decay and voltage rise. In Stage 3 (Extinction), the arc forms a stretched horseshoe profile, followed by a sharp voltage surge and rapid current collapse. At this point, the arc resistance approaches the circuit resistance, and the power delivered reaches its maximum before the arc extinguishes.

The influence of magnetic field and contact velocity varies across the three arc stages. In Stage 1, the magnetic field governs arc displacement through the Lorentz force, while contact velocity aids arc elongation and resistance growth, especially under low-field conditions. In Stage 2, magnetic-field-induced convective cooling dominates, and the effect of contact velocity becomes negligible. In Stage 3, arc extinction occurs as arc resistance increases and the power delivered by the supply reaches its peak, triggering rapid collapse.

An empirical formula is proposed to estimate arc extinguishing time. A small number of simulations can be used to identify the geometry-dependent constant, aiding the selection of magnetic fields and contact velocities for a given design. This relation is based on specific experimental conditions and may not be directly generalizable to other configurations.

Arc extinction consistently occurs near the maximum power transfer point, where the arc resistance matches the circuit's effective resistance. Increasing the magnetic field or contact velocity accelerates the approach to this condition but does not alter the extinction threshold. Stage 2 governs the transition from sheath-dominated to core-loss regimes. Effective control—through enhanced airflow, optimized arc elongation, and rapid resistance rise—is essential to accelerate the approach to extinction.

Chapter 8

Conclusion and Future Work

This final chapter concludes the thesis by reflecting on the research conducted and summarising the key findings. It also outlines potential avenues for future work that could build upon the results presented in this study.

8.1 Conclusions

This thesis was motivated by the need to improve the understanding and predictive capability of arc behaviour in compact DC circuit breakers and low-voltage DC switches. Current research shows two notable gaps. First, in compact LC commutator-based DC circuit breakers, there is a lack of magnetohydrodynamic (MHD) models capable of accurately capturing the mechanisms of arc reignition, particularly the breakdown behaviour in millimetre-scale non-uniformly heated air gaps, which has not been fully modelled or explained. Second, in low-voltage DC switches, the combined influence of magnetic fields and contact motion speed across different arcing stages has not been systematically investigated via simulation.

To address these gaps, a multi-physics model was developed and validated to capture arc dynamics, breakdown phenomena, and post-arc dielectric recovery. A hybrid breakdown voltage prediction model applicable to the 300–5000 K temperature range was proposed, with the underlying mechanism transitions explained using electron density analysis. For low-voltage DC switch modelling, the effect of electrode motion-induced airflow was introduced, and arc behaviour was classified into distinct stages according to its position relative to the electrodes. The influence of magnetic fields and airflow in each stage, as well as energy distribution patterns, were analysed, and parametric studies on different contact velocities and magnetic field strengths were performed. The validated model can serve as a predictive tool to support practical circuit breaker design and is applicable across different voltage levels and operating conditions.

In the model verification stage, welding arcs were selected as a reference case. Steady-state simulations confirmed the validity of the LTE plus average-temperature-based heavy particle heat flux boundary treatment. Comparisons with N-LTE and 2T models showed that, despite

neglecting metal vapour and particle collisions, the simplified model produced results within the bounds of the two more accurate models, demonstrating a balanced trade-off between accuracy and computational efficiency. Furthermore, a Gaussian temperature distribution was used to initialise short-gap arcs, and formation times were tested under various initial currents (100–1000 A). All cases produced formation times of approximately 0.1 ms, far shorter than the interruption time in circuit breakers, confirming the reasonableness of the initialisation. Grid independence analysis ensured that the selected mesh balanced computational cost and accuracy.

When coupled with an LC commutation circuit, simulations with different cooling rates (strong cooling, weak cooling, and a realistic temperature-dependent cooling profile) revealed that near-electrode boundary layer cooling plays a decisive role in arc reignition. Under realistic cooling, the boundary layer temperature becomes a key factor in determining reignition; however, increasing the arc sheath voltage alone can only delay, not prevent, reignition. In contrast, increasing the commutation capacitor size (e.g., ten times the baseline value) can effectively suppress reignition. Detailed analysis showed that boundary layer temperature alone is insufficient to explain the phenomenon, highlighting the need to consider the interplay between electric field recovery and breakdown conditions.

Building on these findings, Chapter 6 compared and derived the mechanisms of thermal breakdown and streamer breakdown, identifying 2000 K and 3000 K as two transition points. Electron density calculations revealed the physical origins of these transitions. A hybrid breakdown model covering 300–5000 K was developed, which outperformed the traditional Paschen's law when validated against published experimental data. The model was further applied to explain the dynamic matching between dielectric recovery and capacitor-driven voltage recovery, showing that such matching is critical to preventing reignition.

To assess the model's applicability, the arc dynamics of low-voltage DC switches were also studied. Arc depth was reconstructed from experimental images, and contact geometry and motion were adjusted accordingly. Arc evolution was divided into three stages (constrained migration, hemispherical expansion, horseshoe-shaped extinction) and mapped to characteristic features on the V–I curve. Stage 1 is influenced jointly by magnetic field and contact velocity, with the former dominating arc displacement and the latter promoting elongation and resistance growth under low-field conditions. Stage 2 is governed primarily by magnetic-field-induced convective cooling, with negligible contact velocity influence. Stage 3 is determined by the matching between power supply capability and arc impedance. Energy distribution analysis revealed that Stage 2 plays a critical role in the transition from sheath-dominated to core-loss regimes. Based on these findings, an empirical formula for arc extinction time was proposed, enabling geometry-dependent constants to be determined with a small number of simulations, thus providing a basis for magnetic field and contact velocity selection across different switch designs. Although the relation depends on experimental conditions, it can be extended to other configurations via parameter calibration.

Theoretical Advances and Engineering Relevance

Theoretically, this work proposes a hybrid breakdown model that unifies the description of different temperature-regime mechanisms, quantitatively explains the mechanism transitions between thermal breakdown and streamer breakdown in non-uniformly heated gaps, and links cooling rate, electric field recovery, and dielectric breakdown thresholds into a coherent framework. A stage-based analysis methodology is established, systematically describing the roles of magnetic field and contact motion across different arc stages. Energy distribution analysis further clarifies the relationship between extinction conditions and the maximum power transfer point.

From an engineering perspective, the study provides a comprehensive set of design guidelines applicable to a wide range of DC switching devices, including but not limited to compact DC circuit breakers. The model enables rapid early-stage prediction of key performance indicators such as reignition risk, extinction time, and parameter sensitivities, reducing the need for iterative experimental trials. Based on the quantitative stage-specific analysis, systematic recommendations are made for component selection (e.g., commutation capacitor sizing) and structural optimisation (e.g., electrode geometry, opening angle). The modelling approach is inherently extensible and can be integrated with power electronic control strategies (e.g., coordinated operation with IGBT/SiC MOSFET devices) to develop intelligent DC protection schemes, thereby supporting future designs of high-reliability, modular, and customisable DC switching equipment.

The developed modelling framework demonstrates excellent scalability, enabling accurate prediction of arc behaviour across varying voltage and current levels, as well as different breaker geometries. A key insight from this work is that effective thermal management of the arc boundary layer significantly reduces the risk of arc re-ignition. Furthermore, the proposed mathematical model for predicting breakdown voltage in non-uniformly heated air gaps provides valuable guidance for practical DC circuit breaker design, including optimal selection of circuit parameters, electrode materials, and contact geometries. Collectively, these contributions establish a solid foundation for the development of compact DC circuit breakers in future multi-terminal HVDC grid applications as introduced in Chapter 2.

8.2 Future Research

Future improvements to the model can be made from both physical and numerical perspectives. One promising direction is to extend the current axisymmetric model to a fully three-dimensional formulation, enabling a more accurate representation of asymmetric gas flow patterns. This would enhance the predictive accuracy of the arc initiation stage (Stage 1), where lateral flows can influence cooling between the contacts. Additionally, some boundary assumptions remain idealized; for instance, the average temperature of the arc column and the electrode is currently used to estimate the heat transfer from heavy particles ($\mathbf{q}_h$) to the boundary layer. This can be refined by introducing a weighted temperature function, such as $T = f \cdot T_g + (1-f) \cdot T_s$,

where f adjusts the relative influence of the gas and surface temperatures. Moreover, the current model does not include the effect of metal vapor evaporation, which may significantly influence arc quenching behavior. Future work could incorporate evaporation rates based on electrode material properties to further improve simulation fidelity.

From an application standpoint, the model provides a foundation for exploring design strategies to accelerate arc extinction in low-voltage DC switching devices. For example, further studies could examine how arc runners or variations in the electrode opening angle (e.g., 15–90 influence the duration of Stage 2, where rapid cooling is essential. Additionally, based on the model's predictions of arc behavior, coordinated control with power electronic components—such as snubber circuits or the gate timing of IGBTs—can be explored. For example, IGBT switching actions could be synchronized with arc motion to enable more intelligent DC protection schemes.

Appendix A

List of Academic Publications

Journal Articles

1. **J. Nan**, G. Chen, I. Golosnoy,
   Temperature-Segmented Hybrid Arc Model for Breakdown Voltage Prediction from 300K to 5000K: Arc-to-Gas Phase Transition Analysis and Sheath Cooling Effects for Reignition Suppression in Air Circuit Breakers, Accepted, in **IET High Voltage**, first author.

2. **J. Nan**, M. Yan, S. M. Sharkh, J. W. Mcbride, G. Chen, I. Golosnoy,
   Impact of Moving Velocity and Magnetic Field On Arc Interruption Dynamics in Low-Voltage DC Switching Devices, Minor Revision, **IEEE Transactions on Plasma Science**, first author.

3. M. Yan, **J. Nan**, I. Golosnoy, G. Chen, S. M. Sharkh, J. W. Mcbride,
   Arc Cooling by an External Magnetic Field in Low Voltage DC Switching, Major Revision, to **IEEE Transactions on Components, Packaging and Manufacturing Technology**, second author.

Conference Papers

1. **J. Nan**, G. Chen, I. O. Golosnoy,
   Analysis of Breakdown Mechanisms in Heated Short Air Gaps During Contact Opening in Compact DC Circuit Breakers,
   In *2024 IEEE 69th Holm Conference on Electrical Contacts (HOLM)*, IEEE, 2024.

2. **J. Nan**, G. Chen, I. O. Golosnoy,
   Identification of Key Mechanism Behind Arc Re-Ignition in LC Commutator-Based DC Circuit Breakers,
   In *2024 7th International Conference on Electric Power Equipment – Switching Technology (ICEPE-ST)*, IEEE, 2024.

3. **J. Nan**, G. Chen, I. Golosnoy,
   Modelling of Arcing Phenomenon During Contact Opening in Novel Circuit Breaker,
   In *Proceedings of the International Symposium on High Voltage Engineering (ISH 2023)*,
   IET, 2023.

Awards

- **National Grid Prize for Best Student Poster**, 14th Universities High Voltage Colloquium (UHVnet), Cardiff, UK, 2022
- **Finalist, Young Investigator Award**, 32nd ICEC and 69th IEEE Holm Conference, Annapolis, MD, USA, 2024
- **Wang Jimei Best Young Investigator Award**, 7th International Conference on Electric Power Equipment – Switching Technology (ICEPE-ST), Xiamen, China, 2024
- **Best Student Oral Presentation Prize**,17th Universities High Voltage Colloquium (UHVnet), Liverpool, UK, 2025
- **Chinese Government Scholarship**, full PhD funding (36 months), Sep 2022 – Sep 2025

References

[1] A. Sauer, *The DC-Factory: Energy Efficient, Robust, Forward-looking*. München: Hanser, 2020.

[2] H. Köpf, E.-D. Wilkening, C. Klosinski, and M. Kurrat, "Breaking performance of protection devices for automotive DC powertrains with a voltage of 450 V," in *Proceedings of the 27th International Conference on Electrical Contacts*, (Dresden, Germany), pp. 1–6, June 2014.

[3] P. Meckler, F. Gerdinand, R. Weiss, U. Boeke, and A. Mauder, "Hybrid switches in protective devices for low-voltage DC grids at commercial used buildings," in *Proceedings of the 27th International Conference on Electrical Contacts*, (Dresden, Germany), pp. 1–6, June 2014.

[4] F. Mohammadi, K. Rouzbehi, M. Hajian, K. Niayesh, G. B. Gharehpetian, H. Saad, M. H. Ali, and V. K. Sood, "HVDC circuit breakers: A comprehensive review," *IEEE Transactions on Power Electronics*, vol. 36, no. 12, pp. 13726–13739, 2021.

[5] C. M. Franck, "HVDC circuit breakers: A review identifying future research needs," *IEEE transactions on power delivery*, vol. 26, no. 2, pp. 998–1007, 2011.

[6] A. Raza, A. Mustafa, U. Alqasemi, K. Rouzbehi, R. Muzzammel, S. Guobing, and G. Abbas, "HVDC Circuit Breakers: Prospects and Challenges," *Applied Sciences*, vol. 11, p. 5047, Jan. 2021.

[7] R. P. Smeets and N. A. Belda, "High-voltage direct current fault current interruption: A technology review," *High Voltage*, vol. 6, no. 2, pp. 171–192, 2021.

[8] L. Tang and B.-T. Ooi, "Locating and isolating DC faults in multi-terminal DC systems," *IEEE transactions on power delivery*, vol. 22, no. 3, pp. 1877–1884, 2007.

[9] D. Jovcic and B. Wu, "Fast fault current interruption on high-power DC networks," in *IEEE PES General Meeting*, pp. 1–6, IEEE, 2010.

[10] M. Hajian, D. Jovcic, and B. Wu, "Evaluation of Semiconductor Based Methods for Fault Isolation on High Voltage DC Grids," *IEEE Transactions on Smart Grid*, vol. 4, pp. 1171–1179, June 2013.

[11] R. Smeets, L. Van der Sluis, M. Kapetanovic, D. F. Peelo, and A. Janssen, *Switching in electrical transmission and distribution systems*. John Wiley & Sons, 2014.

[12] D. Jovcic, "AC fault current limiting using LC DC circuit breaker," in *2023 IEEE PES GTD International Conference and Exposition (GTD)*, pp. 104–108, 2023.

[13] D. Gonzalez, R. Methling, S. Gortschakow, S. Franke, and D. Uhrlandt, "Spectroscopic investigation of DC-arcs between parallel rails under the influence of external magnetic fields," in *2019 IEEE Holm Conference on Electrical Contacts*, (Milwaukee, WI, USA), pp. 115–121, 2019.

[14] A. Vassa *et al.*, "Magnetic blowing of break arcs up to 360 V DC," in *2010 Proceedings of the 56th IEEE Holm Conference on Electrical Contacts*, (Charleston, SC, USA), pp. 1–5, 2010.

[15] LSEMS, "EV Relay Catalog." https://www.lsems.com/en/business/ev-relay/info/download/catalog/EV_Relay_Catalog_EN_230327.pdf, 2023. Accessed: Jun. 23, 2025.

[16] M. Yan, S. M. Sharkh, and J. W. McBride, "An experimental study of the influence of a uniform external magnetic field on electric arcs in low voltage DC switching," in *2024 IEEE 69th Holm Conference on Electrical Contacts (HOLM)*, (Annapolis, MD, USA), pp. 40–48, 2024.

[17] D. Jovcic, "Fast commutation of DC current into a capacitor using moving contacts," *IEEE Transactions on Power Delivery*, vol. 35, no. 2, pp. 639–646, 2019.

[18] K. Tahata, S. El Oukaili, K. Kamei, D. Yoshida, Y. Kono, R. Yamamoto, and H. Ito, "HVDC circuit breakers for HVDC grid applications," in *11th IET international conference on AC and DC power transmission*, pp. 1–9, IET, 2015.

[19] D. Jovcic, "Series LC DC circuit breaker," *High Voltage*, vol. 4, no. 2, pp. 130–137, 2019.

[20] D. Shin, I. O. Golosnoy, and J. W. McBride, "Experimental study of reignition evaluators in low-voltage switching devices," *IEEE Transactions on Components, Packaging and Manufacturing Technology*, vol. 8, no. 6, pp. 950–957, 2018.

[21] J. Nan, G. Chen, and I. O. Golosnoy, "Identification of key mechanism behind arc reignition in LC commutator-based DC circuit breakers," in *2024 IEEE 69th Holm Conference on Electrical Contacts (HOLM)*, pp. 1–8, 2024.

[22] W. Hauer and X. Zhou, "Re-ignition and post arc current phenomena in low voltage circuit breaker," in *27th International Conference on Electrical Contacts (ICEC)*, (Dresden, Germany), pp. 398–403, VDE Verlag, 2014.

[23] L. Babich and T. V. Loiko, "Generalized Paschen's Law for Overvoltage Conditions," *IEEE Transactions on Plasma Science*, vol. 44, pp. 3243–3248, Dec. 2016.

[24] Y. P. Raizer, *Gas Discharge Physics*. Berlin, Heidelberg: Springer, 1991.

[25] K. Burm, "Calculation of the townsend discharge coefficients and the paschen curve coefficients," *Contributions to Plasma Physics*, vol. 47, no. 3, pp. 177–182, 2007.

[26] H.-J. Jang, Y.-H. Oh, K.-D. Song, and Y.-I. Kim, "Prediction of reduced critical electric field strength of hot dry air in the temperature range 300–5000 K at 0.1 MPa for medium-voltage switchgear," *AIP Advances*, vol. 10, p. 045103, 04 2020.

[27] "LVDC: Electricity for the 21st century – technology report," tech. rep., International Electrotechnical Commission (IEC), Geneva, Switzerland, 2017. IEC Technology Report TR LVDC, IEC SyC LVDC.

[28] W. Javed and D. Chen, "Low voltage DC microgrid protection system-a review," in *2018 53rd International Universities Power Engineering Conference (UPEC)*, pp. 1–6, IEEE, 2018.

[29] D. Jovcic, D. van Hertem, K. Linden, J.-P. Taisne, and W. Grieshaber, "Feasibility of DC transmission networks," in *2011 2nd IEEE PES International Conference and Exhibition on Innovative Smart Grid Technologies*, pp. 1–8, Dec. 2011.

[30] M. Muniappan, "A comprehensive review of DC fault protection methods in HVDC transmission systems," *Protection and Control of Modern Power Systems*, vol. 6, p. 1, Jan. 2021.

[31] C. Du and C. Wang, "Review of DC Circuit Breaker Technology for HVDC Application," in *2019 22nd International Conference on Electrical Machines and Systems (ICEMS)*, pp. 1–6, 2019.

[32] O. Cwikowski, J. Sau-Bassols, B. Chang, E. Prieto-Araujo, M. Barnes, O. Gomis-Bellmunt, and R. Shuttleworth, "Integrated HVDC circuit breakers with current flow control capability," *IEEE Transactions on Power Delivery*, vol. 33, no. 1, pp. 371–380, 2018.

[33] Y. Wang and R. Marquardt, "Performance of a new fast switching DC-breaker for meshed HVDC-grids," in *2015 17th European Conference on Power Electronics and Applications*, (Geneva, Switzerland), pp. 1–9, 2015.

[34] M. H. Rashid, *Power electronics handbook*. Butterworth-heinemann, 2017.

[35] M. Barnes, D. S. Vilchis-Rodriguez, X. Pei, R. Shuttleworth, O. Cwikowski, and A. C. Smith, "HVDC Circuit Breakers–A Review," *IEEE Access*, vol. 8, pp. 211829–211848, 2020.

[36] J. Hafner, "Proactive hybrid hvdc breakers-a key innovation for reliable HVDC grids," in *Proc. CIGRE Bologna Symposium*, pp. 1–8, 2011.

[37] D. Shin, *A study of re-ignition phenomena and arc modelling to evaluate switching performance of low-voltage switching devices*. PhD thesis, University of Southampton, June 2018.

[38] P. G. Slade, *Electrical Contacts: Principles and Applications*. Boca Raton, London, and New York: CRC Press Taylor & Francis Group, second edition, first issued in paperback ed., 2017.

[39] T. E. Browne, *Circuit interruption: theory and techniques*. M. Dekker, 1984.

[40] M. Backman, L. Liljestrand, F. Rafatnia, and R. Du, "Passive DC neutral breaker for bipolar HVDC schemes," *2017 4th International Conference on Electric Power Equipment - Switching Technology*, pp. 347–351, 2017.

[41] N. A. Belda, C. A. Plet, and R. P. P. e. a. Smeets, "Full power short-circuit tests of hvdc circuit breakers using ac generators operated at reduced power frequency," in *CIGRE Conference*, 2018.

[42] Z. Zhang, X. Li, M. Chen, J. He, Y. Li, and S. Xu, "Research and development of 160kV ultra-fast mechanical HVDC circuit breaker," *Power System Technology*, vol. 42, no. 7, pp. 2331–2338, 2018.

[43] S. Tokoyoda, T. Inagaki, and H. e. a. Sadakuni, "Development and testing of EHV mechanical DC circuit breaker," in *5th International Conference on Electrical Power Equipment - Switching Technology*, 2019.

[44] Y. Niwa, K. Yokokura, and J. Matsuzaki, "Fundamental investigation and application of high-speed VCB for DC power system of railway," in *24th International Symposium on Discharges and Electrical Insulation in Vacuum*, pp. 125–128, 2010.

[45] D. Jovcic and S. Kovacevic, "Experimental evaluation of 5 kV, 2 kA, DC circuit breaker with parallel capacitor," *IEEE Transactions on Power Delivery*, vol. 37, no. 5, pp. 3510–3520, 2021.

[46] W. Gu, D. Feng, and Z. Guo, "Development of high-speed mechanical switchgear with vacuum interruption technology and application in HVDC circuit breaker," in *3rd IEEE International Electrical And Energy Conversion Conference*, 2019.

[47] A. N. Greenwood, P. Barkan, and W. C. Kracht, "HYDC vacuum circuit breakers," *IEEE Transactions on Power Apparatus and Systems*, vol. PAS-91, no. 4, pp. 1575–1588, 1972.

[48] S. Tokuyama, K. Arimatsu, Y. Yoshioka, S. Yanabu, and T. Horiuchi, "Development and interrupting tests on 250 kV 8kA HVDC circuit breaker," *IEEE Transactions on Power Apparatus and Systems*, vol. PAS-104, no. 9, pp. 2453–2458, 1972.

[49] S. Tokoyoda, T. Inagaki, and K. e. a. Tahata, "DC current interruption tests with HV mechanical DC circuit breaker," in *CIGRE Winnipeg 2017 Colloquium*, 2017.

[50] N. A. Belda, R. P. P. Smeets, and R. M. Nijman, "Experimental investigation of electrical stresses on the main components of HVDC circuit breakers," *IEEE Transactions on Power Delivery*, vol. 35, no. 6, pp. 2762–2771, 2020.

[51] Z. Shi, Y. Zhang, Q. Wang, S. Jia, and L. e. a. Wang, "Numerical investigation on residual axial magnetic field in vacuum interrupter in DC interruption based on artificial current zero," *IEEE Transactions on Power Delivery*, vol. 32, no. 4, pp. 1915–1923, 2017.

[52] X. Li, Z. Yuan, J. Fu, Y. Wang, T. Liu, and Z. Zhu, "Nanao multi-terminal VSC-HVDC project for integrating large-scale wind generation," *IEEE Power and Energy Society General Meeting*, vol. 2014, p. 5, Oct 2014.

[53] Z. Jie, L. Haibin, X. Rui, L. Li, N. Wenhai, S. Kun, H. Feiyang, and L. Dapeng, "Research of DC circuit breaker applied on zhoushan multi-terminal VSC-HVDC project," in *2016 IEEE PES Asia-Pacific Power and Energy Engineering Conference*, pp. 1636–1640, 2016.

[54] H. Pang and X. Wei, "Research on key technology and equipment for zhangbei 500kV DC grid," in *2018 International Power Electronics Conference*, pp. 2343–2351, 2018.

[55] W. Wen, Y. Huang, B. Li, Y. Wang, and T. Cheng, "Technical assessment of hybrid DCCB with improved current commutation drive circuit," *IEEE Transactions on Industry Applications*, vol. 54, no. 5, pp. 5456–5464, 2018.

[56] International Electrotechnical Commission, "Low-Voltage Switchgear and Controlgear-Part 2: Circuit Breakers," no. 60947-2, 2006.

[57] B. Bachmann, G. Mauthe, E. Ruoss, H. Lips, J. Porter, and J. Vithayathil, "Development of a 500kV Airblast HVDC Circuit Breaker," *IEEE Transactions on Power Apparatus and Systems*, vol. PAS-104, pp. 2460–2466, Sept. 1985.

[58] A. Lee, P. G. Slade, K. H. Yoon, J. Porter, and J. Vithayathil, "The Development of a HVDC SF6 Breaker," *IEEE Transactions on Power Apparatus and Systems*, vol. PAS-104, no. 10, pp. 2721–2729, 1985.

[59] Y. Wang and R. Marquardt, "A fast switching, scalable DC-Breaker for meshed HVDC-SuperGrids," in *PCIM Europe 2014; International Exhibition and Conference for Power Electronics, Intelligent Motion, Renewable Energy and Energy Management*, pp. 1–7, 2014.

[60] A. Mokhberdoran, A. Carvalho, N. Silva, H. Leite, and A. Carrapatoso, "A new topology of fast solid-state HVDC circuit breaker for offshore wind integration applications," in *2015 17th European Conference on Power Electronics and Applications*, pp. 1–10, Sept. 2015.

[61] K. A. Corzine, "A New-Coupled-Inductor Circuit Breaker for DC Applications," *IEEE Transactions on Power Electronics*, vol. 32, no. 2, pp. 1411–1418, 2017.

[62] D. Keshavarzi, T. Ghanbari, and E. Farjah, "A Z-Source-Based Bidirectional DC Circuit Breaker With Fault Current Limitation and Interruption Capabilities," *IEEE Transactions on Power Electronics*, vol. 32, pp. 6813–6822, Sept. 2017.

[63] A. Maqsood, A. Overstreet, and K. A. Corzine, "Modified Z-Source DC Circuit Breaker Topologies," *IEEE Transactions on Power Electronics*, vol. 31, no. 10, pp. 7394–7403, 2016.

[64] J. Josefsson, "ABB HVDC circuit breaker," in *HVDC circuit breaker workshop, CIGRE Conference*, 2018.

[65] B. Yang, D. Cao, W. Shi, and et al., "A novel commutation-based hybrid HVDC circuit breaker," in *CIGRE Winnipeg Colloquium paper A3-15*, 2017.

[66] T. An, "HVDC breaker experience in SGCC," in *HVDC circuit breaker workshop, CIGRE Conference*, 2018.

[67] C. Meyer, M. Kowal, and R. De Doncker, "Circuit breaker concepts for future high-power DC-applications," in *14th IAS Annual Meeting. Conference Record of the 2005 Industry Applications Conference*, vol. 2, pp. 860–866, 2005.

[68] W. Xiang, Y. Hua, J. Wen, M. Yao, and N. Li, "Research on fast solid state DC breaker based on a natural current zero-crossing point," *Journal of Modern Power Systems and Clean Energy*, vol. 2, pp. 30–38, Mar. 2014.

[69] G. Liu, F. Xu, Z. Xu, Z. Zhang, and G. Tang, "Assembly HVDC Breaker for HVDC Grids With Modular Multilevel Converters," *IEEE Transactions on Power Electronics*, vol. 32, pp. 931–941, Feb. 2017.

[70] W. Lin, D. Jovcic, S. Nguefeu, and H. Saad, "Modelling of high-power hybrid DC circuit breaker for grid-level studies," *IET Power Electronics*, vol. 9, no. 2, pp. 237–246, 2016.

[71] M. Callavik, A. Blomberg, J. Häfner, and B. Jacobson, "The hybrid HVDC breaker," *ABB Grid Systems Technical Paper*, vol. 361, pp. 143–152, 2012.

[72] C. C. Davidson, R. S. Whitehouse, C. D. Barker, J.-P. Dupraz, and W. Grieshaber, "A new ultra-fast HVDC circuit breaker for meshed DC networks," in *11th IET International Conference on AC and DC Power Transmission*, pp. 1–7, 2015.

[73] D. Döring, D. Ergin, K. Würflinger, J. Dorn, F. Schettler, and E. Spahic, "System integration aspects of DC circuit breakers," *IET Power Electronics*, vol. 9, no. 2, pp. 219–227, 2016.

[74] W. G. Cigré, "B4. 52,"," *HVDC Grid Feasibility Study," WG Brochure*, 2013.

[75] C. international des grands réseaux électriques. Joint working group B4-A3-B3, *Technical Requirements and Specifications of State-of-the-art HVDC Switching Equipment*. CIGRÉ, 2017.

[76] B. Pauli, G. Mauthe, E. Ruoss, G. Ecklin, J. Porter, and J. Vithayathil, "Development of a high current HVDC circuit breaker with fast fault clearing capability," *IEEE Transactions on Power Delivery*, vol. 3, pp. 2072–2080, Oct. 1988.

[77] B. Damsky, I. Imam, and W. Premerlani, "A New HVDC Circuit Breaker System Design For -+ 400 kV," in *1979 7th IEEE/PES Transmission and Distribution Conference and Exposition*, pp. 230–236, Apr. 1979.

[78] M. Rahimo, A. Kopta, U. Schlapbach, J. Vobecky, R. Schnell, and S. Klaka, "The Bi-mode Insulated Gate Transistor (BIGT) a potential technology for higher power applications," in *2009 21st International Symposium on Power Semiconductor Devices & IC's*, pp. 283–286, June 2009.

[79] D. Bösche, E.-D. Wilkening, H. Köpf, and M. Kurrat, "Hybrid DC Circuit Breaker Feasibility Study," *IEEE Transactions on Components, Packaging and Manufacturing Technology*, vol. 7, pp. 354–362, Mar. 2017.

[80] W. Grieshaber, J. P. Dupraz, D. L. Penache, and L. Violleau, "Development and test of a 120 kV direct current circuit breaker," *45th CIGRÉ Session*, pp. 1–11, 2014.

[81] W. Zhou, X. Wei, S. Zhang, G. Tang, Z. He, J. Zheng, Y. Dan, and C. Gao, "Development and test of a 200kV full-bridge based hybrid HVDC breaker," in *2015 17th European Conference on Power Electronics and Applications*, pp. 1–7, Sept. 2015.

[82] A. Vassa *et al.*, "DC-arc blowing under pulsed magnetic field," in *26th International Conference on Electrical Contacts (ICEC)*, (Beijing), pp. 23–29, 2012.

[83] H. Manhart, W. Reider, and C. Veit, "Arc mobility on new and eroded Ag/CdO and Ag/SnO2 contacts," in *IEEE Holm Conference on Electrical Contacts*, (San Francisco, CA, USA), pp. 47–56, 1988.

[84] W. Widmann, "Arc commutation across a step or a gap in one of two parallel copper electrodes," *IEEE Transactions on Components, Hybrids, and Manufacturing Technology*, vol. 8, no. 1, pp. 21–28, 1985.

[85] S. Tokumitsu and M. Hasegawa, "Effective shortening of break arc duration s of Ag and several Ag-based contacts in DC load conditions with increased contact opening speeds and external magnetic field," in *2018 IEEE Holm Conference on Electrical Contacts*, pp. 87–94, 2018.

[86] R. Ma, M. Rong, F. Yang, Y. Wu, H. Sun, D. Yuan, H. Wang, and C. Niu, "Investigation on arc behavior during arc motion in air DC circuit breaker," *IEEE Transactions on Plasma Science*, vol. 41, no. 9, pp. 2551–2560, 2013.

[87] A. K. Leuthold, "Design and operation of high-voltage axial air-blast circuit breakers," *Electrical Engineering*, vol. 61, no. 12, pp. 1073–1074, 1942.

[88] S. Tokumitsu and M. Hasegawa, "Relationships between break arc behaviors of AgSnO2 contacts and lorentz force to be applied by an external magnetic force in a DC inductive load circuit up to 20V-17A," *IEICE Transactions on Electronics*, vol. 102, no. 9, pp. 641–645, 2019.

[89] M. Hasegawa and S. Tokumitsu, "Influences of contact opening speeds up to 200 mm/s and external magnetic field application on break arc duration characteristics of AgSnO2 contacts in DC 14 V load conditions up to around 10 A," *IEEE Transactions on Components, Packaging and Manufacturing Technology*, vol. 8, no. 3, pp. 375–382, 2018.

[90] J. J. Shea, E. Heckman, and J. C. S. Guevara, "DC arc properties in a DC magnetic field," in *2018 IEEE Holm Conference on Electrical Contacts*, (Albuquerque, NM, USA), pp. 195–203, 2018.

[91] J. W. McBride and S. M. A. Sharkh, "The influence of contact opening velocity on arc characteristics," in *16th International Conference on Electrical Contacts*, (Loughborough, UK), pp. 395–400, 1992.

[92] M. Lindmayer, "Simulation of switching arcs under transverse magnetic fields for DC interruption," *IEEE Transactions on Plasma Science*, vol. 44, pp. 187–194, 2016.

[93] M. Lisnyak, *Theoretical, numerical and experimental study of DC and AC electric arcs*. PhD thesis, Université Orléans, April 2018.

[94] M. Lisnyak, M. Cunha, J.-M. Bauchire, and M. Benilov, "Numerical modelling of high-pressure arc discharges: matching the lte arc core with the electrodes," *Journal of Physics D: Applied Physics*, vol. 50, no. 31, p. 315203, 2017.

[95] N. A. Almeida, M. S. Benilov, and G. V. Naidis, "Unified modelling of near-cathode plasma layers in high-pressure arc discharges," *Journal of Physics D: Applied Physics*, vol. 41, no. 24, p. 245201, 2008.

[96] M. S. Benilov, "Understanding and modelling plasma–electrode interaction in high-pressure arc discharges: a review," *Journal of Physics D: Applied Physics*, vol. 41, p. 144001, July 2008.

[97] N. A. Almeida, M. S. Benilov, and M. J. Faria, "Modelling near-anode layers in high-pressure arc discharges: effect of plasma pressure and anode surface temperature," *Journal of Physics D: Applied Physics*, vol. 50, no. 38, p. 385203, 2017.

[98] V. I. Kolobov and R. R. Arslanbekov, "Electron kinetics in low-temperature plasmas: Toward PIC-MCC/DSMC modeling of non-equilibrium flows," *Journal of Computational Physics*, vol. 231, no. 3, pp. 839–869, 2012.

[99] R. F. Ammerman, T. Gammon, P. K. Sen, and J. P. Nelson, "DC-arc models and incident-energy calculations," *IEEE Transactions on Industry Applications*, vol. 46, no. 5, pp. 1810–1819, 2010.

[100] J. Mentel, M. Ieee, J. Luhmann, and D. Nandelstadt, "Experimental investigation of electrodes for high pressure discharge lamps," in *Industry Applications Conference*, pp. 3293–3300, 2000.

[101] M. Lindmayer and H. Stammberger, "Application of numerical field simulations for low-voltage switchgear," in *Proceedings of IEEE Holm Conference on Electrical Contracts*, pp. 65–77, Oct. 1994.

[102] A. Mutzke, T. Rüther, M. Lindmayer, and M. Kurrat, "Arc behavior in low-voltage arc chambers," *The European Physical Journal-Applied Physics*, vol. 49, no. 2, p. 22910, 2010.

[103] M. Lindmayer, E. Marzahn, A. Mutzke, T. Ruther, and M. Springstubbe, "The process of arc splitting between metal plates in low voltage arc chutes," *IEEE Transactions on Components and Packaging Technologies*, vol. 29, pp. 310–317, June 2006.

[104] P. A. Jeffery, *The motion of short circuit arcs in low-voltage current limiting miniature circuit breakers*. PhD thesis, University of Southampton, 1999.

[105] J. L. Zhang, J. D. Yan, A. Murphy, W. Hall, and M. Fang, "Computational investigation of arc behavior in an auto-expansion circuit breaker contaminated by ablated nozzle vapor," *IEEE Transactions on Plasma Science*, vol. 30, pp. 706–719, Apr. 2002.

[106] M. Rong, Q. Ma, Y. Wu, T. Xu, and A. B. Murphy, "The influence of electrode erosion on the air arc in a low-voltage circuit breaker," *Journal of Applied Physics*, vol. 106, no. 2, 2009.

[107] Y. W. Charles, K. Eric, K. A. Rachid, K. Zacharie, and Z. François, "Study of the composition of a plasma of dry air contaminated by Al2O3, CO, Fe2O3 and SiO2," *Advances in Materials Physics and Chemistry*, vol. 12, no. 8, pp. 177–193, 2022.

[108] M. Rong, F. Yang, Y. Wu, A. B. Murphy, W. Wang, and J. Guo, "Simulation of arc characteristics in miniature circuit breaker," *IEEE Transactions on Plasma Science*, vol. 38, pp. 2306–2311, September 2010.

[109] J. Wendelstorf, *Ab initio modelling of thermal plasma gas discharges (electric arcs)*. PhD thesis, Technical University of Braunschweig, 2000.

[110] A. Fridman, *Plasma Chemistry*. Cambridge University Press, 2008.

[111] K. Ollegott, P. Wirth, C. Oberste-Beulmann, P. Awakowicz, and M. Muhler, "Fundamental properties and applications of dielectric barrier discharges in plasma-catalytic processes at atmospheric pressure," *Chemie Ingenieur Technik*, vol. 92, no. 10, pp. 1542–1558, 2020.

[112] D. B. Go and D. A. Pohlman, "A mathematical model of the modified paschen's curve for breakdown in microscale gaps," *Journal of Applied physics*, vol. 107, no. 10, 2010.

[113] G. Dandaron, G. Y. Dautov, and G. Mustafin, "Effect of gas temperature on breakdown potential," *Journal of Applied Mechanics and Technical Physics*, vol. 11, no. 1, pp. 140–143, 1970.

[114] A. M. Loveless, G. Meng, Q. Ying, F. Wu, K. Wang, Y. Cheng, and A. L. Garner, "The transition to paschen's law for microscale gas breakdown at subatmospheric pressure," *Scientific reports*, vol. 9, no. 1, p. 5669, 2019.

[115] M. Seeger, G. Naidis, A. Steffens, H. Nordborg, and M. Claessens, "Investigation of the dielectric recovery in synthetic air in a high voltage circuit breaker," *Journal of Physics D: Applied Physics*, vol. 38, p. 1795, May 2005.

[116] F. Karetta and M. Lindmayer, "Simulation of the gasdynamic and electromagnetic processes in low voltage switching arcs," in *Electrical Contacts-1996. Proceedings of the Forty-Second IEEE Holm Conference on Electrical Contacts. Joint with the 18th International Conference on Electrical Contacts*, pp. 35–44, IEEE, 1996.

[117] K. C. Hsu, K. Etemadi, and E. Pfender, "Study of the free-burning high-intensity argon arc," *Journal of Applied Physics*, vol. 54, pp. 1293–1301, Mar. 1983.

[118] R. Bini, M. Monno, and M. I. Boulos, "Numerical and experimental study of transferred arcs in argon," *Journal of Physics D: Applied Physics*, vol. 39, pp. 3253–3266, July 2006.

[119] M. Claessens, K. Möller, and H. G. Thiel, "A computational fluid dynamics simulation of high-and low-current arcs in self-blast circuit breakers," *Journal of Physics D: Applied Physics*, vol. 30, pp. 1899–1907, July 1997.

[120] R. Huang, H. Fukanuma, Y. Uesugi, and Y. Tanaka, "Simulation of Arc Root Fluctuation in a DC Non-Transferred Plasma Torch with Three Dimensional Modeling," *Journal of Thermal Spray Technology*, vol. 21, pp. 636–643, June 2012.

[121] R. Devoto, *The Transport Properties of a Partially Ionized Monoatomic Gas*. PhD thesis, Stanford University, CA, USA, 1965.

[122] A. B. Murphy, "Transport coefficients of air, argon-air, nitrogen-air, and oxygen-air plasmas," *Plasma Chemistry and Plasma Processing*, vol. 15, pp. 279–307, 1995.

[123] A. B. Murphy and E. Tam, "Thermodynamic properties and transport coefficients of arc lamp plasmas: argon, krypton and xenon," *Journal of Physics D: Applied Physics*, vol. 47, no. 29, p. 295202, 2014.

[124] M. S. Benilov, "Theory and modelling of arc cathodes," *Plasma Sources Science and Technology*, vol. 11, pp. A49–A54, Aug. 2002.

[125] M. Baeva, M. S. Benilov, N. A. Almeida, and D. Uhrlandt, "Novel non-equilibrium modelling of a DC electric arc in Argon," *Journal of Physics D: Applied Physics*, vol. 49, no. 24, p. 245205, 2016.

[126] H. R. Griem, "Validity of local thermal equilibrium in plasma spectroscopy," *Physical Review*, vol. 131, no. 3, pp. 1170–1176, 1963.

[127] M. Numano, "Criteria for local thermodynamic equilibrium distributions of populations of excited atoms in a plasma," *Journal of Quantitative Spectroscopy and Radiative Transfer*, vol. 43, no. 4, pp. 311–317, 1990.

[128] Y. Enami and M. Sakata, "Simulation of arc in molded-case circuit breaker with metal vapor and moving electrode," *2nd International Conference on Electric Power Equipment - Switching Technology*, pp. 1–4, 2013.

[129] F. Yang, Y. Wu, M. Rong, H. Sun, A. B. Murphy, Z. Ren, and C. Niu, "Low-voltage circuit breaker arcs—simulation and measurements," *J. Phys. D. Appl. Phys.*, vol. 46, p. 273001, 2013.

[130] P. Freton and J.-J. Gonzalez, "Overview of current research into low-voltage circuit breakers," *The open plasma physics journal*, vol. 2, no. 1, 2009.

[131] R. T. C. Choo, J. Szekely, and R. C. Westhoff, "Modeling of high-current arcs with emphasis on free surface phenomena in the weld pool," *Welding Journal*, vol. 69, no. 9, pp. 346–361, 1990.

[132] X. Ye, M. Dhotre, *et al.*, "CFD simulation of transonic flow in high-voltage circuit breaker," *International Journal of Chemical Engineering*, vol. 2012, 2012.

[133] B. Peyrou, L. Chemartin, P. Lalande, B. G. Chéron, P. Rivière, M.-Y. Perrin, and A. Soufiani, "Radiative properties and radiative transfer in high pressure thermal air plasmas," *Journal of Physics D: Applied Physics*, vol. 45, p. 455203, Oct. 2012.

[134] A. Gleizes, Y. Cressault, and P. Teulet, "Mixing rules for thermal plasma properties in mixtures of argon, air and metallic vapours," *Plasma Sources Science and Technology*, vol. 19, no. 5, p. 055013, 2010.

[135] H.-P. Li and M. S. Benilov, "Effect of a near-cathode sheath on heat transfer in high-pressure arc plasmas," *Journal of Physics D: Applied Physics*, vol. 40, pp. 2010–2017, Mar. 2007. Publisher: IOP Publishing.

[136] Y. Cressault, A. Murphy, P. Teulet, A. Gleizes, and M. Schnick, "Thermal plasma properties for Ar-Cu, Ar-Fe and Ar-Al mixtures used in welding plasmas processes: II. Transport coefficients at atmospheric pressure," *Journal of Physics D Applied Physics*, vol. 46, p. 5207, Oct. 2013.

[137] N. Mitrofanov and S. Shkol'nik, "Two forms of attachment of an atmospheric-pressure direct-current arc in argon to a thermionic cathode," *Technical Physics*, vol. 52, no. 6, pp. 711–720, 2007.

[138] COMSOL AB, *COMSOL Multiphysics Material Library*, 2023. Version 6.1, Stockholm, Sweden.

[139] A. Gleizes, J.-J. Gonzalez, and P. Freton, "Thermal plasma modelling," *Journal of Physics D: Applied Physics*, vol. 38, no. 9, p. R153, 2005.

[140] J. Lowke and M. Tanaka, "'lte-diffusion approximation'for arc calculations," *Journal of Physics D: Applied Physics*, vol. 39, no. 16, p. 3634, 2006.

[141] M. Irie and M. R. Barrault, "Flow velocity measurement in high-current arcs using doppler-shifted plasma scattering," *Journal of Physics D: Applied Physics*, vol. 10, no. 12, pp. 1599–1605, 1977.

[142] M. Benilov, L. Benilova, H.-P. Li, and G.-Q. Wu, "Sheath and arc-column voltages in high-pressure arc discharges," *Journal of Physics D: Applied Physics*, vol. 45, no. 35, p. 355201, 2012.

[143] J. Nan, G. Chen, and I. O. Golosnoy, "Analysis of breakdown mechanisms in heated short air gaps during contact opening in compact DC circuit breakers," in *2024 IEEE 69th Holm Conference on Electrical Contacts (HOLM)*, (Annapolis, MD, USA), pp. 1–8, 2024.

[144] J. Lowke, "Predictions of arc temperature profiles using approximate emission coefficients for radiation losses," *Journal of Quantitative Spectroscopy and Radiative Transfer*, vol. 14, no. 2, pp. 111–122, 1974.

[145] H.-J. Jang, Y.-H. Oh, K.-D. Song, and Y.-I. Kim, "Prediction of reduced critical electric field strength of hot dry air in the temperature range 300–5000 K at 0.1 MPa for medium-voltage switchgear," *AIP Advances*, vol. 10, no. 4, 2020.

[146] D. Hu, S. Huang, Z. Wen, X. Gu, and J. Lu, "A review on thermal runaway warning technology for lithium-ion batteries," *Renewable and Sustainable Energy Reviews*, vol. 206, p. 114882, 2024.

[147] J. Mitterauer and P. Till, "Computer Simulation of the Dynamics of Plasma-Surface Interactions in Vacuum Arc Cathode Spots," *IEEE Transactions on Plasma Science*, vol. 15, pp. 488–501, Oct. 1987. Conference Name: IEEE Transactions on Plasma Science.

[148] E. Hantzsche, "Thermal runaway prevention in arc spots," *IEEE Transactions on Plasma Science*, vol. 11, no. 3, pp. 115–122, 2007.

[149] D. Packan, *Repetitive nanosecond glow discharge in atmospheric pressure air*. PhD thesis, Stanford University, 2004.

[150] S. Nijdam, J. Teunissen, and U. Ebert, "The physics of streamer discharge phenomena," *Plasma Sources Science and Technology*, vol. 29, no. 10, p. 103001, 2020.

[151] A. Najam, P. Pieterse, and D. Uhrlandt, "Electrical modelling of switching arcs in a low voltage relay at low currents," *Energies*, vol. 13, no. 23, 2020.

[152] J. Nan, G. Chen, and I. Golosnoy, "Modelling of arcing phenomena during opening contacts in novel circuit breaker," in *Proceedings of the 22nd International Symposium on High Voltage Engineering*, pp. 701–707, IET, 2023.

[153] M. Lindmayer, "Cooling mechanisms of switching arcs under transverse magnetic fields in comparison with arcs without magnetic blast," *IEEE Transactions on Plasma Science*, vol. 46, pp. 444–450, Feb. 2018.